SAMARIUM OXIDE AND SAMARIUM OXYNITRIDE THIN FILM GATE OXIDES ON SILICON SUBSTRATE

GOH KIAN HENG

THESIS SUBMITTED IN FULFILMENT OF THE REQUIREMENTS FOR THE DEGREE OF DOCTOR OF PHILOSOPHY

FACULTY OF ENGINEERING
UNIVERSITY OF MALAYA
KUALA LUMPUR

2017

UNIVERSITY OF MALAYA

ORIGINAL LITERARY WORK DECLARATION

Name of Candidate: **GOH KIAN HENG**

Registration/Matric No: **KHA 130084**

Name of Degree: **DOCTOR OF PHILISOPHY**

Title of Project Paper/Research Report/Dissertation/Thesis ("this Work"):

SAMARIUM OXIDE AND SAMARIUM OXYNITRIDE THIN FILM GATE OXIDES ON SILICON SUBSTRATE

Field of Study:

ADVANCE MATERIALS / NANOMATERIALS

I do solemnly and sincerely declare that:

(1) I am the sole author/writer of this Work;
(2) This Work is original;
(3) Any use of any work in which copyright exists was done by way of fair dealing and for permitted purposes and any excerpt or extract from, or reference to or reproduction of any copyright work has been disclosed expressly and sufficiently and the title of the Work and its authorship have been acknowledged in this Work;
(4) I do not have any actual knowledge nor do I ought reasonably to know that the making of this work constitutes an infringement of any copyright work;
(5) I hereby assign all and every rights in the copyright to this Work to the University of Malaya ("UM"), who henceforth shall be owner of the copyright in this Work and that any reproduction or use in any form or by any means whatsoever is prohibited without the written consent of UM having been first had and obtained;
(6) I am fully aware that if in the course of making this Work I have infringed any copyright whether intentionally or otherwise, I may be subject to legal action or any other action as may be determined by UM.

Candidate's Signature Date: **18 Jan 2017**

Subscribed and solemnly declared before,

Witness's Signature Date:

Name:

Designation:

ABSTRAK

Lapisan logam samarium (Sm) tulen yang dipercitkan pada silikon telah dioksidakan dan dioksinitridakan bersama suhu pada pelbagai suhu (600 - 900 °C) dan tempoh (5 - 20 min). Kesan pengoksidaan bersama suhu dalam ambien gas oksigen (O_2) dan nitrus oksida (N_2O) ke atas sifat - sifat fizikal dan elektrik yang dimiliki oleh samarium oksida (Sm_2O_3) dan samarium oksinitrida ($Sm_xO_yN_z$) telah disiasat. Bagi sampel dioksida dalam ambien gas O_2, corak XRD menunjukkan penghabluran tidak meningkat dengan tempoh pengoksidaan. Dengan penalaan tempoh pengoksidaan, proses penghabluran lapisan Sm_2O_3 meningkat apabila suhu pengoksidaan meningkat. Kewujudan dua lapisan antara lapisan telah dikesan dalam gambar keratan rentas resolusi tinggi penghantaran elektron mikroskop (HRTEM). Kewujudan separuh polihabluran lapisan antara lapisan telah disokong oleh analisis pembelauan sinar-X (XRD), inframerah jelmaan Fourier (FTIR), Raman, dan analisis komposisi tenaga serakan sinar-X (EDX) spektroskopi. Kadar tenaga pengaktifan atau pertumbuhan pada setiap lapisan telah dikira daripada plot Arrhenius. Satu model fizikal yang berkaitan dengan lapisan separuh polihabluran Sm_2O_3 telah dicadangkan dan dijelaskan. Permukaan sampel 700 ºC yang licin telah menyumbangkan ciri arus-voltan (*I-V*) yang terbaik. Bagi sampel dioksida dalam ambien gas O_2, parameter optimum bagi suhu pengoksidaan dan tempoh pengoksidaan ialah 700 °C dan 15 min. Sampel yang dioptimum mempamerkan sifat elektrik yang terbaik iaitu mempunyai kebocoran ketumpatan arus yang terendah (1.15 x 10^{-4} A cm^{-2} pada 0.71 MV cm^{-1}), voltan kerosakan yang tertinggi (0.71 MV cm^{-1}), ketinggian halangan yang tertinggi (2.12 eV), tenaga perangkap yang tertinggi (7.485 x 10^{-4} eV), ketumpatan perangkap yang terendah (6.88 x 10^{21} cm^{-3}), malar dielektrik yang tertinggi (214), caj oksida berkesan yang terendah (2.81 x 10^{13} cm^{-2}), ketumpatan caj perangkap perahan yang terendah (5.56 x 10^{12} cm^{-2}), ketumpatan purata perangkap

lapisan antra lapisan yang terendah (~ 10^{14} eV^{-1} cm^{-2}), dan ketumpatan keseluruhan perangkap lapisan antara lapisan yang terendah (7.31 x 10^{13} cm^{-2}). Bagi sampel dioksinitrida dalam ambien gas N_2O, lapisan polihabluran $Sm_xO_yN_z$ telah dibentukkan. Satu lapisan silikat Sm ($Sm_aSi_bO_cN_d$) yang amorfus tertanam di antara lapisan $Sm_xO_yN_z$ dan silikon. Proses penghabluran lapisan Sm_2O_3 meningkat apabila suhu pengoksidaan meningkat dari 600 ºC hingga 700 ºC tetapi menurun apabila suhu pengoksidaan meningkat hingga 900 ºC. Intensiti Sm_2O_3 yang lemah juga dikesan dalam analisis FTIR dan analisis Raman. Berdasarkan gambar keratan rentas HRTEM dan analisis komposisi EDX, hanya satu lapisan antara lapisan ($Sm_aSi_bO_cN_d$) telah dibentukkan. Satu model fizikal yang berkaitan dengan lapisan separuh polihabluran $Sm_xO_yN_z$ dan amorfus lapisan antara lapisan $Sm_aSi_bO_cN_d$ telah dicadangkan dan dijelaskan. Sampel dioksinitrida pada 700 ºC mempamerkan sifat elekrik yang terbaik. Dengan penalaan tempoh pengoksinitridaan, kedua - dua lapisan separuh polihabluran $Sm_xO_yN_z$ dan lapisan amorfus $Sm_aSi_bO_cN_d$ telah dibentukkan. Berdasarkan analisis XRD, FTIR, dan Raman, sampel 15 min mempunyai penghabluran Sm_2O_3 yang terbaik dan tertanam dalam lapisan $Sm_xO_yN_z$. Prestasi elektrik yang optimum telah dicapai oleh sampel oksinitrida 15 min. Bagi sampel dioksinitrida dalam ambien gas N_2O, parameter optimum bagi suhu pengoksinitridaan dan tempoh pengoksinitridaan ialah 700 °C dan 15 min. Sampel yang dioptimum mempamerkan sifat elektrik yang terbaik iaitu mempunyai kebocoran ketumpatan arus yang terendah (9.54 x 10^{-7} A cm^{-2} pada 3.9 MV cm^{-1}), voltan kerosakan yang tertinggi (3.9 MV cm^{-1}), ketinggian halangan yang tertinggi (6.33 eV), tenaga perangkap yang tertinggi (0.005 eV), dan ketumpatan perangkap yang terendah (5.657 x 10^{21} cm^{-3}). Dengan membandingkan parameter optimum (700 ºC and 15 min) bagi kedua-dua sampel oksida dan oksinitrida, ia menunjukkan prestasi elektrik telah diperbaiki oleh campuran nitrogen kerana kekosongan valance nitrogen dapat berfungsi sebagai pembentuk rangkaian oleh itu stabilkan struktur oksida.

ABSTRACT

Sputtered pure samarium (Sm) metal films on silicon substrates were thermally oxidized and oxynitrided at various temperatures (600 – 900 °C) and durations (5 – 20 min). Effects of thermal oxidation ambient in oxygen (O_2) and nitrous oxide (N_2O) gas ambient on the physical and electrical properties of samarium oxide (Sm_2O_3) and samarium oxynitride ($Sm_xO_yN_z$) thin films were investigated. For all samples oxidized in O_2, the XRD patterns showed that crystallinity did not increase with oxidation duration. The crystallinity of Sm_2O_3 increased as the oxidation temperature increased. Two interfacial layers were observed in high resolution transmission electron microscopy (HRTEM) cross sectional images. The existence of semi-polycrystalline interfacial layers was supported by X-ray diffraction (XRD), Fourier transform infrared (FTIR), Raman analysis, and energy dispersive X-ray (EDX) spectroscopy composition analysis. The activation energy or growth rate of each stacked layer was calculated from Arrhenius plots. A physical model related to semi-polycrystalline interfacial layer is proposed and explained. The smoothest surface of the 700 °C sample showed the best current-voltage (*I-V*) characteristic. For thermal oxidation in O_2, the optimum parameters of oxidation temperature and duration were 700 °C and 15 min, respectively. The optimized sample yielded the best electrical properties with the lowest leakage current (1.15×10^{-4} A cm^{-2} at 0.71 MV cm^{-1}), highest electrical breakdown field (0.71 MV cm^{-1}), highest barrier height value (2.12 eV), highest trap energy (7.485×10^{-4} eV), lowest trap density (6.88×10^{21} cm^{-3}), highest effective dielectric constant (214), lowest effective oxide charge (2.81×10^{13} cm^{-2}), lowest slow trap charge density (5.56×10^{12} cm^{-2}), lowest average interface trap density (~ 10^{14} eV^{-1} cm^{-2}), and lowest total interface trap density (7.31×10^{13} cm^{-2}). For all the samples oxynitrided in N_2O, polycrystalline $Sm_xO_yN_z$ was formed. Amorphous Sm-silicate ($Sm_aSi_bO_cN_d$) was embedded between the $Sm_xO_yN_z$ film and the Si substrate.

The crystallinity of Sm_2O_3 increased when the oxynitridation temperature increased from 600 ºC to 700 ºC but decreased as the oxynitridation temperature increased to 900 ºC. The weak intensities of Sm_2O_3 were also detected in FTIR and Raman analysis. According to HRTEM cross sectional images and EDX compositional analysis, only one interfacial layer ($Sm_aSi_bO_cN_d$) was formed. Similarly, the activation energy or growth rate of each stacked layer was calculated from Arrhenius plots. A physical model related to formation of semi-polycrystalline $Sm_xO_yN_z$ thin film and amorphous $Sm_aSi_bO_cN_d$ interfacial layer is suggested and explained. The sample oxynitrided at 700 ºC for 15 min exhibited the best electrical properties with the lowest leakage current (9.54×10^{-7} A cm^{-2} at 3.9 MV cm^{-1}), highest electrical breakdown field (3.9 MV cm^{-1}), barrier height value (6.33 eV), highest trap energy (0.005 eV), and lowest trap density (5.657×10^{21} cm^{-3}). By comparing the optimized parameters (700 ºC and 15 min) of both oxidized and oxynitrided samples, it showed that the electrical performance is improved by incorporation of nitrogen. The high valance vacancy of nitrogen acts as network former hence stabilizing the oxynitrided structures.

ACKNOWLEDGEMENTS

Firstly, I would like to thank the god for his blessings so that my research works can be finished in time successfully. For sure, I would like to thank my supervisor, **Ir. Dr. Wong Yew Hoong** and co-supervisor, **Prof. Dr. A.S.M.A Hasseb**. They helped me a lot throughout the research studies. They are very kind and patient during suggesting me the outline of this project and correcting my doubts. Their advices, suggestions and supports are very useful for me to finish my research.

Special thanks are given to Dean (**Prof. Ir. Dr. Noor Azuan Bin Abu Osman**), Head of Mechanical Department (**Assoc. Prof. Dr. Mohd. Faizul**), all academic and administrative staffs of Faculty of Engineering for their supports and assistances. Besides that, grateful thanks to **Dr. Goh Boon Tong (Physic Department, Faculty of Science)** and all involved technicians from **Malaysian Institute of Microelectronic System (MIMOS)** for providing physical and electrical characterization services during my research studies.

Furthermore, I would like to thank my fellow colleagues for their physical and mental assistance at countless occasions. A great appreciation to my family members for their supports and encouragements. Last but not least, I would like to acknowledge the financial support provided by University of Malaya Research Grant (UMRG) (Grant No.: RP024A-13AET) and Postgraduate Research Grant (PPP) (Grant No.: PG048-2014A).

Thank you!!

TABLE OF CONTENTS

LIST OF FIGURES

LIST OF TABLES

LIST OF SYMBOLS AND ABBREVIATIONS

Φ_B	:	Barrier height (eV)
Φ_s	:	Surface potential (eV) : Permittivity of free space (F m^{-1})
Φt	:	Trap energy (eV)
ε	:	Mircrostrain
λ	:	Wavelength (cm^{-1})
A	:	Capacitor area (cm^2)
C	:	Capacitance (pF)
C_{IL}	:	Capacitance of interfacial layer (IL) (pF)
C_{ox}	:	Oxide capacitance (pF)
C_{total}	:	Total capacitance (pF)
C_{Sm2O3}	:	Capacitance of Sm_2O_3 (pF)
D	:	Crystallite size (nm)
d	:	Interplanar spacing (nm)
D_{it}	:	Interface trap density (eV^{-1} cm^{-2})
D_{total}	:	Total interface trap density (cm^{-2})
E	:	Electric field (MV cm^{-1})
E_{BD}	:	Dielectric breakdown field (MV cm^{-1})
I	:	Current (A)
J	:	Leakage current density (A cm^{-2})
m	:	Free electron mass
m_{ox}	:	Effective electron mass in the oxide
N_t	:	Trap density (cm^{-3})

q	:	Electronic charge (C)
Q_{eff}	:	Effective oxide charge (cm^{-2})
STD	:	Slow trap charge density (cm^{-2})
T	:	Oxidation/oxynitridation temperature (^oC)
t	:	Oxidation/oxynitridation time (min)
t_{ox}	:	Oxide thickness (nm)
V_{FB}	:	Flatband voltage (V)
V_g	:	Gate voltage (V)
Θ	:	Diffraction angle
κ	:	Dielectric constant
κ_{eff}	:	Effective dielectric constant
AFM	:	Atomic force microscopy
C-V	:	Capacitance-Voltage
HRTEM	:	High resolution transmission electron microscopy
FN	:	Fowler-Nordheim
FTIR	:	Fourier transform infrared
ICSD	:	Inorganic Crystal Structure Database
IL	:	Interfacial layer
I-V	:	Current-Voltage
J-E	:	Leakage current density-Electric field
EOT	:	Equivalent oxide thickness
MOS	:	Metal-Oxide-Semiconductor
TAT	:	Trap-assisted tunneling
XPS	:	X-ray photoelectron spectroscopy
XRD	:	X-ray diffraction

CHAPTER 1

INTRODUCTION

1.1 Theoretical Background

Nowadays, electronic devices require superior characteristic and performances such as high speed, low cost, small size, high reliability, high package density, and low power consumption due to the rapid development of the semiconductor industry (Casady & Johnson, 1996; Chalker, 1999; Elford & Mawby, 1999; Wong & Cheong, 2010). Several evolutions of integration which started from medium scale integration (MSI), large scale integration (LSI), very large scale integration (VLSI), up until the ultra-large scale integration (ULSI) were seen in semiconductor devices (Buchanan, 1999; Wilk, Wallace, & Anthony, 2001). The limitations of each previous stages were eventually hit and subsequently overcome by researchers or scientists (Buchanan, 1999; Houssa *et al.*, 2006; Leong, Doris, Kedzierski, Rim, & Yang, 2004).

As predicted by Moore's Law, the density of integrated circuits and number of devices will increase exponentially and double every two to three years (Arden, 2006; Robertson, 2004; Robertson & Wallace, 2015; Wilk *et al.*, 2001). This significant development of technology requires ultrathin gate oxide (~ 1.5 nm or 4 atomic layers) (Gordon, Becker, Hausmann, & Suh, 2001; Ranuarez, Deen, & Chen, 2006; Robertson & Wallace, 2015; Wilk *et al.*, 2001). In the last few decades, silicon dioxide (SiO_2) layer was used as primary gate oxide on silicon (Si) substrates in microelectronic industries because of its excellent insulator properties (Hirose *et al.*, 2000; Robertson & Wallace, 2015; Wilk *et al.*, 2001). However, physically thicker but the same electrically equivalent thickness is required for future nanoscale metal oxide semiconductor (MOS) technology.

An extremely thin film may lead to a large leakage current density owing to large amounts of quantum-mechanical tunneling through the gate oxide and low reliability of the gate oxide against electrical breakdown (Gordon *et al.*, 2001; Robertson & Wallace, 2015; Wilk *et al.*, 2001). This may cause unacceptable static power dissipation in the device (Houssa *et al.*, 2006; Robertson & Wallace, 2015; Wilk *et al.*, 2001). The gate leakage problem has occurred since late 1990s (Buchanan, 1999; Lo, Buchanan, Taur, & Wang, 1997; Robertson, 2004; Robertson & Wallace, 2015). However, this problem is not solved completely even though enormous ingenuity and efforts were done by numerous researchers due to continued downscaling trend.

For CMOS technology, a specific gate capacitance was designed to be proportional to the dielectric constant (κ) and inversely proportional to the thickness of the gate oxide (Wilk *et al.*, 2001; Y. H. Wong & Cheong, 2010). For the sake of reducing the leakage current density, a thicker film with high κ must be introduced to replace conventional SiO_2. In the former years, metal silicates and aluminates were investigated as they are thermodynamically stable on Si substrates and have high barrier height (Hubbard & Schlom, 1996; Robertson, 2000). Unfortunately, they have relatively low κ which is a limiting factor for future downscaling (Neumayer & Cartier, 2001). Various high κ oxides such as HfO_2 (Hsu, Su, & Yokoyama, 1992; Kuo, Kwor, & Jones, 1992; Ohmi *et al.*, 2000; Wong & Cheong, 2010), ZrO_2 (Hwang & Kim, 1993; Kalkur & Lu, 1992; Kim & Roh, 2006; Ohmi *et al.*, 2000; Wong & Cheong, 2010), ZrON (Atuchin, Kruchinin, Wong, & Cheong, 2013; Chew *et al.*, 2016; Wong, Atuchin, Kruchinin, & Cheong, 2014; Wong & Cheong, 2011, 2013; Wu, Cheng, Lai, & Pan, 2009), Al_2O_3 (George *et al.*, 1994; Kim & Roh, 2006; Wong & Cheong, 2010), TiO_2 (Houssa *et al.*, 2006; Kim & Roh, 2006; Wilk *et al.*, 2001; Wong & Cheong, 2010), Ta_2O_5 (Houssa *et al.*, 2006; Kim & Roh, 2006; Wilk *et al.*, 2001; Wong & Cheong, 2010), and Y_2O_3 (Choi,

Cho, Whangbo, Whang, Kang, *et al.*, 1997; Ng *et al.*, 2005; Onisawa *et al.*, 1990; Wong & Cheong, 2010) have been investigated over many years. However, the high κ is not the only selection criterion.

For most high κ oxides, the tunnel current is exponentially dependent upon the barrier height while the bandgap is inversely proportional to the dielectric constant. Thus, some choices of high κ oxide may be hampered by their lower barrier height and narrower bandgap. Moreover, some challenges such as elimination of fixed charges, suppression of charge trapping, improvement of electron mobility, and reduction of interface layer have to be overcome.

1.2 Problem Statement

Aggressive miniaturization that leads to high circuit density is demanded for current MOS industry. Greater devices functionality and performance at lower cost are required. This trend has forced the gate oxide thickness to decrease rapidly. However, the fundamental restriction on downscaling of the gate oxide in MOS applications is the leakage current density. Hence, a physically thicker oxides with the same electrically equivalent thickness is needed to replace the SiO_2.

In order to overcome this challenge, the high κ oxide was introduced and developed to supersede SiO_2. The new gate oxide candidate must exhibit better physical and electrical characteristics so that it can be used for future generations. For the purpose of finding new suitable high κ oxide thickness, it is convenient to develop an equivalent oxide thickness, *EOT* as

$$EOT = t_{high-\kappa} = \frac{\kappa_{high-\kappa}}{\kappa_{SiO_2}} \times t_{SiO_2} \qquad \text{(Equation 1.1)}$$

where $t_{high\text{-}\kappa}$ is the new high κ oxide thickness, $\kappa_{high\text{-}\kappa}$ is the κ of new high κ oxide, κ_{SiO2} is the κ of SiO_2, and t_{SiO2} is the SiO_2 thickness (Leskela & Ritala, 2003; Robertson, 2004; Wilk *et al.,* 2001; Wong & Cheong, 2010). Hence, it is convenient to refer the new high κ oxide thickness in terms of its equivalent thickness of SiO_2. Besides that, it facilitates more while developing high κ oxides, which allows continuous downscaling of lower *EOT* values.

Previously, several candidates for future high κ oxide were extensively investigated by different researchers to overcome the problems. However, each of them has their own drawbacks compared to SiO_2. Large interface trap density, flatband voltage shift, and fixed charge were observed in Al_2O_3 layers (Constantinescu, Ion, Galca, & Dinescu, 2012; Pan & Huang, 2010). Low conduction offsets with silicon conduction band and low thermodynamic stability were the main drawbacks of TiO_2 and Ta_2O_5 layers (Alers *et al.*, 1998; Autran, Devine, Chaneliere, & Balland, 1997; Son *et al.*, 1998). Low MOS fabrication process temperature was needed due to low crystallization temperatures of TiO_2 and Y_2O_3 layers. Besides that, Y_2O_3 layers have higher interface density compared to SiO_2 layers (Houssa *et al.*, 2006; Wong & Cheong, 2010).

Recently, some rare earth oxides (REOs) have been investigated due to their superior properties (Chin, Cheong, & Hassan, 2010; Paivasaari, Putkonen, & Niinisto, 2005; Sen *et al.*, 2007). Samarium oxide (Sm_2O_3) is one of the promising candidate materials among rare earth oxides because of some outstanding properties such as high κ (7-15), high breakdown electric field (5-7 MV/cm), large bandgap (4.33 eV), low leakage current, large conduction offset with Si, high thermal stability, small frequency dispersion, and low trapping rates (Chen, Hung, *et al.*, 2013; Chin *et al.*, 2010; Kao, Chen, *et al.*, 2010; Paivasaari *et al.*, 2005; Pan & Huang, 2010). Sm_2O_3 is also predicted to be

thermodynamically stable on Si substrates (Pan & Huang, 2010). Besides that, Sm_2O_3 is also less hygroscopic among REOs because of its smaller ionic radius and lesser electropositive properties (Zhao, Wang, Lin, & Wang, 2008).

In this work, formation of samarium oxide and samarium oxynitride on Si substrate by pure metal sputtering followed by thermal oxidation/oxynitridation were proposed. Both samarium oxide and samarium oxynitride thin film were formed by pure samarium metal thin film sputtering followed by thermal oxidation in oxygen (samarium oxide) and thermal oxynitridation in nitrous oxide (N_2O) (samarium oxynitride). The incorporation of nitrogen within oxide systems was believed to be able to improve and enhance the performance of gate oxides (Buchanan, 1999; Cheng, Chang-Liao, & Wang, 2006; Fenker, Kappl, Banakh, Martin, & Pierson, 2006; Hoffmann & Schmeisser, 2006; Karimi *et al.*, 2014; Mian & Flora, 1999; Stathis & Zafar, 2006; Tessier, Maillard, Orhan, & Chevire, 2010). Some research works reported that devices with nitrogen profile of hydrogen nitrogen species (e.g., NH_3) were less reliable compared to non-hydrogen nitrogen species (e.g., N_2O or NO) (Lucovsky, Niimi, Koh, & Green, 1998; Lucovsky, Niimi, Wu, Parker, & Hauser, 1998; Wong & Gritsenko, 2002). Enta *et al.* (Enta, Suto, Takeda, Kato, & Sakisaka, 2006) reported that NO gas was extremely toxic compared to N_2O gas.

Nevertheless, up to date, there is no report on the influences of either N_2O or NO gas on sputtered Sm thin film on Si substrates. Hence, the influences of thermal oxidation and oxynitridation of sputtered Sm/Si system on physical and electrical properties were investigated in this work. According to the results of characterization, a possible growth mechanism of oxidation and oxynitridation is proposed.

1.3 Research Objectives

The main objective of this research is to grow samarium oxide and samarium oxynitride thin films by pure samarium metal sputtering followed by thermal oxidation in oxygen (samarium oxide) and thermal oxynitridation in nitrous oxide (N_2O) (samarium oxynitride). Alongside this main objective, the following objectives are to be achieved.

1. To investigate the effects of thermal oxidation in O_2 gas ambient at different oxidation temperatures and durations on the physical and electrical properties of the oxidized sputtered pure samarium metal thin films on Si substrates.
2. To investigate the effects of thermal oxynitridation in N_2O gas ambient at different oxynitridation temperatures and durations on the physical and electrical properties of the oxynitrided sputtered pure samarium metal thin films on Si substrates.
3. To compare the physical, chemical, and electrical properties of oxidized and oxynitrided sputtered pure samarium metal thin films on Si substrates.
4. To establish a possible mechanism model of oxidation and oxynitridation to explain formation of the oxidized and oxynitrided sputtered pure samarium metal thin films on Si substrates.

1.4 Scope of Study

In this work, pure samarium metal thin film was sputtered on Si substrates followed by thermal oxidation process. Various parameters were investigated: (i) effects of thermal oxidation in O_2 gas ambient at different oxidation temperatures, (ii) effects of thermal oxidation in O_2 gas ambient at different oxidation durations, (iii) effects of thermal oxynitridation in N_2O gas ambient at different oxynitridation temperatures, (iv)

effects of thermal oxynitridation in N_2O gas ambient at different oxynitridation durations (v) comparison of the physical and electrical properties of oxidized and oxynitrided sputtered pure samarium metal thin films on Si substrates.

Physical and chemical characterizations of oxidized and oxynitrided Sm thin films were conducted by using X-ray diffraction (XRD), Fourier transformed infrared (FTIR) spectroscopy analysis, Raman analysis, high resolution transmission electron microscopy (HRTEM), energy dispersive X-ray (EDX) spectroscopy analysis, atomic force microscopy (AFM) analysis, and X-ray photoelectron spectroscopy (XPS) measurement. Besides that, semiconductor characterization system (SCS) was employed to investigate the electrical properties of the thin films.

1.5 Thesis Outline

This thesis is structured according to the structure below in order to provide better readability of the researched work. Chapter one begins with an overview of background, current issues and challenges faced in MOS-based devices, research objectives, and scope of study. Chapter two focuses on the literature review of existing gate oxide and REOs including their background, drawbacks, and deposition methods. The systematic methodology of the research is demonstrated in Chapter three. Chapters four presents the results and discussion of thermal oxidized samples while Chapters five presents the results and discussion of thermal oxynitrided samples. In Chapter six, this research work is concluded and summarized together with future recommendations of present work.

CHAPTER 2

LITERATURE REVIEW

2.1 Introduction

Rapid developments of complementary metal-oxide-semiconductor (CMOS) integrated circuit (IC) technologies are leading to superior requirements such as high speed or performance, low cost, small in size, high reliability, high package density, and low power consumption for electronic devices such as capacitors and transistors (Chalker, 1999; He, Zhu, Sun, Wan, & Zhang, 2011; Robertson, 2004; Wilk *et al.*, 2001; Wong & Cheong, 2010). According to Moore's law, the density of an integrated circuit would double every two to three years (Arden, 2006; Gordon *et al.*, 2001; Robertson & Wallace, 2015). His prediction is proven by large improvements and developments of semiconductor industry. These improvements were achieved by scaling down the dimension of the components of the devices. Reduction of component dimension is able to increase the speed and functionality of devices with lower power consumption (He *et al.*, 2011; Robertson, 2004).

However, aggressive size shrinking leads to some problems such as high leakage current density and low reliability of devices. Hence, the limitations of conventional SiO_2 gate oxide and the reasons of replacement of SiO_2 are reviewed. Since high κ oxides are suggested to replace SiO_2, the requirements and consideration in high κ oxide candidates are described. The next section begins by outlining the common high κ oxides. Following that, the common deposition methods are briefly enumerated. All the rare earth elements in the lanthanide group and their previous deposition methods are reviewed. After that,

the next section pays particular attention to the literatures of the Sm_2O_3 and its previous deposition methods. Lastly, the role of nitrogen in gate oxides is described.

2.2 Limitation of SiO_2 layer and scaling issues

So far, the scaling of Si-based MOS capacitors was achieved through the scaling of the SiO_2 gate oxide thickness. SiO_2 layers are mostly in amorphous form and have excellent interface with Si substrates (Hirose *et al*., 2000; Robertson, 2004; Robertson & Wallace, 2015; Wilk *et al*., 2001). Thus, SiO_2 layers are excellent insulators and good native oxides on Si substrates. It also can be patterned and etched into nanoscale (Robertson, 2004; Robertson & Wallace, 2015; Wilk *et al*., 2001). Other semiconductors such as Ge, GaAs, GaN, have a poor native oxide with poor properties. SiO_2 layers have a low concentration of electronic defects and can be grown by thermal oxidation. SiO_2 layers can re-bond the network and remove dangling bonds owing to their covalent bonds and low coordination number (Constantinescu *et a*l., 2012; He *et al.*, 2011; Robertson, 2004; Wilk *et al*., 2001).

Unfortunately, the limits of SiO_2 layers will soon be reached because of relentless miniaturization of MOS devices. A thickness of SiO_2 layer as thin as 2 nm and sometimes lower is required (Muller *et al*., 1999; Ng *et al*., 2005; Robertson, 2004; Wilk *et al*., 2001). When the thickness reaches about 1.5 nm, it is only 4 to 5 atomic layers which causes problems such as direct tunneling, variation of dielectric thickness, and impurity penetrations (Cheng *et al*., 2004; Kakushima *et al*., 2010). Such thin layers will cause undesirable circuit power dissipation and prohibitively high gate current leakage (> 1 A/cm^2 at 1 V) due to direct tunneling of electrons through the SiO_2 layer without going via the conduction band. For SiO_2 at a 1 V gate bias, the leakage current density increased

from 1 x 10^{-12} A cm^{-2} at 3.5 nm to 1 x 10 A cm^{-2} at 1.5 nm which is twelve orders of magnitude in current density (Lo, Buchanan, & Taur, 1999; Lo *et al.*, 1997). These remarkable increases in leakage current density are the primary motivation for the investigation of high κ oxides. In the fabrication process, this film thickness is hard to produce and measure accurately. Thus, replacement of SiO_2 gate oxide is required so that a physically thicker film can be used without reducing the capacitance of the gate oxide (Kim & Roh, 2006; Robertson, 2004; Vali & Hosseini, 2004; Wilk *et al.*, 2001; Wong & Cheong, 2010).

For example, one of the important electronic devices is a MOS capacitor. A simple illustration of stacking layers sequences is shown in Fig. 2.1. A gate oxide layer is embedded between the substrate and gate electrode layers. I_{in} refers to input current while I_{out} refers to output current. A capacitor operates based on capacitances. The tunneling current decreases exponentially with increasing thickness or distance.

Thus, the solution to solve tunneling problems is to use a new high κ oxide with same or lower oxide thickness which is able to maintain same oxide capacitance without the tunneling problems according to Equation 2.1.

$$C_{ox} = \frac{\kappa_{ox}\varepsilon_o A_{ox}}{t_{ox}} \qquad \text{(Equation 2.1)}$$

where C_{ox} is the oxide capacitance, κ_{ox} is the oxide dielectric constant, ε_o is the permittivity of free space (8.85 x 10^{-12} F/m), A_{ox} is the oxide area, and t_{ox} is the oxide thickness (Robertson, 2004; Wilk *et al.*, 2001; Wong & Cheong, 2010).

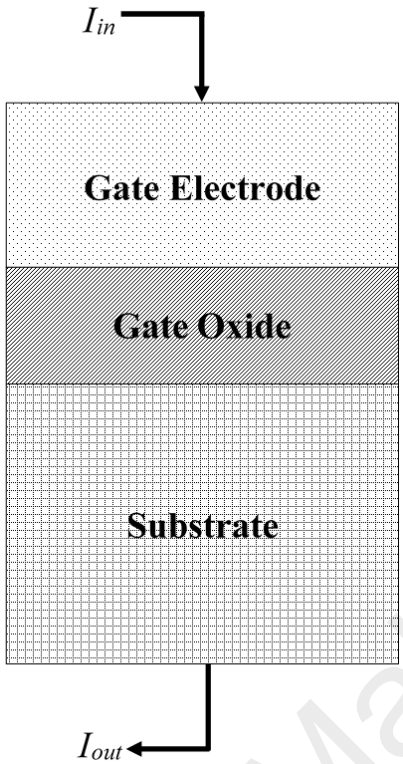

Figure 2.1: A simple illustration of stacking layers sequences of MOS capacitor.

2.3 Selection criteria and consideration in various gate oxides

As mentioned before, a high κ oxide is required to replace the SiO_2 layer so that a material with a larger thickness can be used without reducing the capacitance of components according to Eq. 2.1. However, there are numerous materials and processes to be considered before jumping to a decision. Decision making always requires a compromise between conflicting objectives. Conflict arises because the best choice is a compromise or optimization but not as optimum as their ability allows. Hence, a systematic, simple, and logical method or tool is needed to guide decision makers in considering various selection criteria and their interrelations.

Previously, several strategies of material selection were suggested and reported by Rao (Rao, 2006, 2008a, 2008b; Rao & Patel, 2010a, 2010b), Roth (Field, Kirchain, & Roth, 2007; Fuchs, Field, Roth, & Kirchain, 2008), and Ashby (Ashby, 1988, 1989, 2000;

Ashby, Brechet, & Cebon, 2002; Ashby, Brechet, Cebon, & Salvo, 2004; Ashby & Cebon, 1993; Ashby, Gibson, Wegst, & Olive, 1995). A number of materials which are used in mechanical or electronics engineering were selected and analyzed by Ashby's approach owing to his simple and straightforward type of method (Aditya & Gupta, 2012; Cebon & Ashby, 2006; Guisbiers *et al.*, 2010; Parate & Gupta, 2011; Pratap & Arunkumar, 2007; Quinn, Spearing, Ashby, & Fleck, 2006; Reddy & Gupta, 2010; Spearing, 2000; Srikar & Spearing, 2003). Basically, there are four steps in Ashby's approach as shown in Fig. 2.2: (1) translating design requirements, (2) screening using constraints, (3) ranking using objectives, and (4) seeking supporting information. Translation of design requirement is expressed as function, objective, constraint, and free variable as shown in Fig. 2.3. A selection process always starts with market needs which determines the objectives. The objective refers to the design criteria that must be maximized or minimized to optimize the performance of materials. The constraint is the design requirement that must be satisfied. Once the design requirements are defined, those unsuitable materials which cannot fulfill the constraints or requirements will be screened out. In this stage, bulk values are used for the screening process. After that, the screened materials will be ranked according to the objective. Finally, a high level of precision of supporting information such as experimental results and data sheets issued by the material manufacturer are required to decide on which material is confirmed as the final choice.

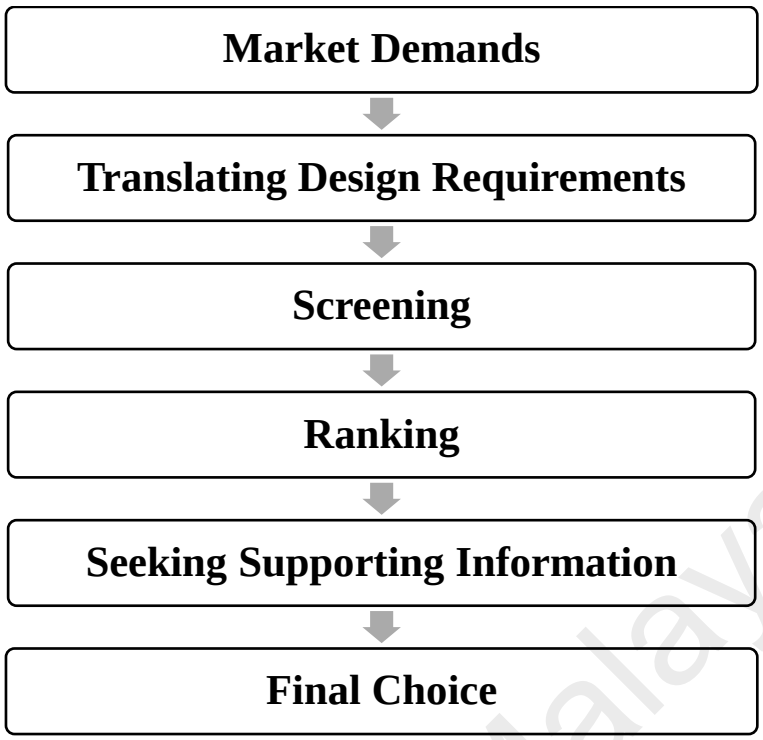

Figure 2.2: Procedures in Ashby approach (Ashby, 1990, 2000).

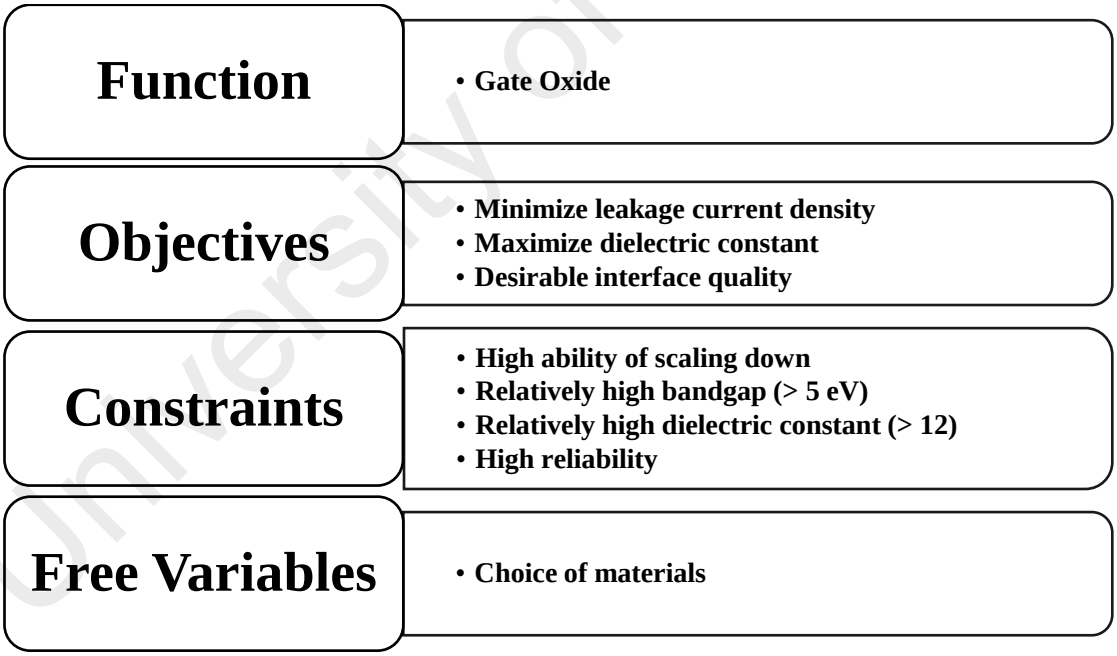

Figure 2.3: Translation of design requirement, which is expressed as function, objectives, constraints, and free variables (Ashby, 1990, 2000).

According to the information in Fig. 2.3, the interrelationship between dielectric constant and bandgap of lanthanide REOs is plotted as shown in Fig. 2.4. Fig. 2.4 is a simple material selection chart with one pair of material properties (bandgap and dielectric constant). Based on Fig. 2.4, it is obvious that only five REOs (black dotted)

satisfy the requirements as stated in Fig. 2.3. At first glance, it seems that La_2O_3 is the best candidate among the REOs. However, numerous previous works reported that it is very hygroscopic and less reliable after prolonged use (Chin *et al*., 2010; Engstrom *et al*., 2007; Frohlich *et al*., 2006; Leskela, Kukli, & Ritala, 2006). Hence, Sm_2O_3 gained a lot of interests to be investigated as the promising candidate.

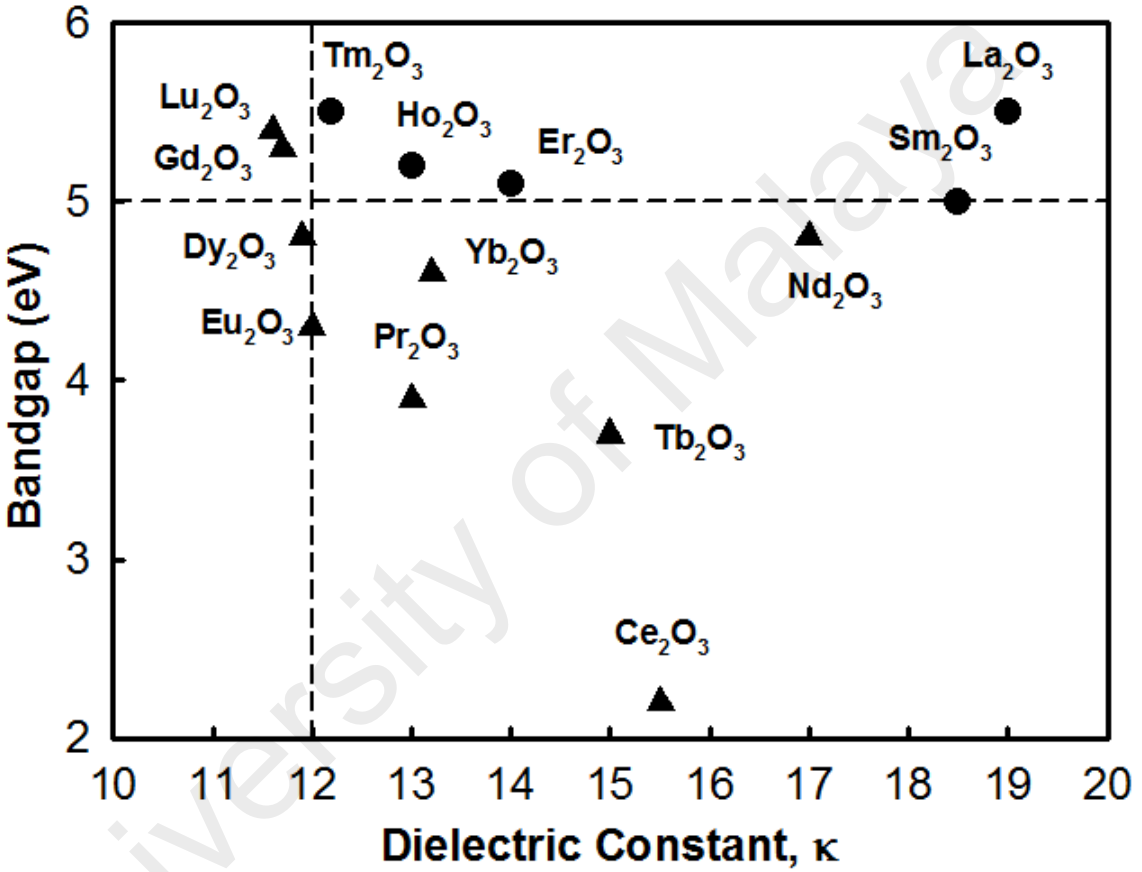

Figure 2.4: The interrelationship between dielectric constant and bandgap of lanthanide REOs (Chin *et al.*, 2010).

In Ashby's approach, the performance of materials were also measured and analyzed by performance metrics, *P*, which was described in terms of the control variables. The performance metrics (*P*) can be expressed in the following mathematical form (Ashby, 2000).

$$P = f(F, G, M) \qquad \text{(Equation 2.2)}$$

where *f* means "a function of". The control variables include the functional parameters (*F*), geometric parameters (*G*), and material indices (*M*). The control variables depend on one or sometimes multiple objectives. The functional parameters refer to functional requirements of the applications. The geometric parameters are the required dimensions while the material indices are the mechanical, thermal, or electrical properties of components for particular applications.

Besides Ashby's approach, many researches summarized and discussed the problems, which are faced during the process of finding high κ oxide. Some problems were: (1) EOT down scaling ability; (2) loss of carrier mobility; (3) gate voltage threshold shifting; (4) oxide defects (Gusev *et al*., 2001; Robertson, 2004; Robertson & Wallace, 2015; Wilk *et al*., 2001). Besides that, many parameters and factors should be considered including deposition methods, electronic structure designs, thermal stability, interface properties, and band offsets.

Hence, six requirements or selection criteria were required. The new oxide must: (1) have high enough κ (> 12), (2) be thermodynamically stable, (3) be kinetically stable, (4) act as insulator with over 1.0 eV band offsets, (5) form a good electrical interface with Si, and (6) have few bulk electrically active defects (Engstrom *et al*., 2007; He *et al*., 2011; Houssa *et al*., 2006; Leskela *et al*., 2006; Leskela & Ritala, 2003; Robertson, 2004; Wong & Cheong, 2010). The new oxide must have high enough κ, normally over 10, preferably 20-30 so that it can used for longer years of downscaling technology. However, the extremely high κ is not suitable in CMOS design due to its low band gap. This may cause undesirable strong fringing fields at source and drain electrodes. The κ value varies inversely with band gap in most of the cases (except La_2O_3, Sm_2O_3, and Nd_2O_3) as shown in Fig. 2.4. Besides that, the new oxide must be thermodynamically stable so that the

reactions with Si substrates and formation of SiO_2 or silicide layers can be avoided. SiO_2 layers will increase EOT values and affect the functions of new oxides while metallic silicides surface layers will short out the field effects. This can be avoided by choosing an oxide which possesses higher heat of formation than SiO_2 (He *et al.*, 2011; Houssa *et al.*, 2006; Robertson, 2004; Wong & Cheong, 2010).

Kinetically stable means the new oxide is compatible with existing process conditions. For example, if the new oxide is in amorphous form, then the new oxide must remain in amorphous form after annealing. The changes in crystallographic orientations and grain sizes may affect the κ values and then degrade the electronic properties. The new oxide must act as insulator with over 1 eV band offsets. Conduction due to Schottky emission of electrons and holes into oxide band should be avoided. However, it is difficult to find those band gaps over 5 eV because the valance band offset is normally bigger than the conduction band offset for most of the oxides (He *et al.*, 2011; Leskela & Ritala, 2003; Robertson, 2004; Wong & Cheong, 2010).

Since the oxide is in direct contact with Si substrates, the best interface quality in terms of roughness and interface defects is required. There are two methods to produce high quality interfaces, either to grow the crystalline oxide epitaxially or use an amorphous oxide. Normally, amorphous oxides are preferred for five reasons. Firstly, amorphous oxides are cheaper than crystalline oxides. Secondly, they have lower concentration of interface defects because it is able to configure its interface bonding. Thirdly, amorphous oxides can have a gradually varying composition such as nitrogen content without creating new phases. Fourthly, amorphous oxides are isotropic so that they will not scatter carriers during fluctuations in polarization from differently oriented oxide grains. Finally, amorphous oxides do not have grain boundaries which act as easy

diffusion paths. However, an epitaxial oxide has a more abrupt interfaces with lower EOT (He *et al*., 2011; Houssa *et al*., 2006; Leskela *et al*., 2006; Robertson, 2004).

Atomic configurations that affect electronic states in oxide bandgap contributed to electrically active defects. These electrically active defects may cause four main problems: (1) the charge trapped which causes gate threshold voltage shifting, (2) instable operating characteristics due to a changing threshold voltage changed over time, (3) decreasing carrier mobility due to scattering by trapped charges, and (4) unreliability owing to electrical failure and breakdown (He *et al*., 2011; Houssa *et al*., 2006; Robertson, 2004; Wong & Cheong, 2010).

2.4 Common high dielectric constant oxides

Many studies have been done to replace the SiO_2 layer as gate oxide, oxynitride and/or nitride such as HfO_2 (Hsu *et al*., 1992; Kuo *et al*., 1992; Ohmi *et al*., 2000; Wong & Cheong, 2010), ZrO_2 (Hwang & Kim, 1993; Kalkur & Lu, 1992; Kim & Roh, 2006; Ohmi *et al*., 2000; Wong & Cheong, 2010), ZrON (Atuchin *et al*., 2013; Chew *et al*., 2016; Wong *et al*., 2014; Wong & Cheong, 2011, 2013; Wu *et al*., 2009), Al_2O_3 (Cico *et al*., 2007; Gao et al., 2016; Lin *et al*., 2003; Shao *et al*., 2003), TiO_2 (Houssa *et al*., 2006; Kim & Roh, 2006; Wilk *et al*., 2001; Wong & Cheong, 2010), Ta_2O_5 (Houssa *et al*., 2006; Kim & Roh, 2006; Wilk *et al*., 2001; Wong & Cheong, 2010), and Y_2O_3 (Durand *et al*., 2005; Ioannou-Sougleridis *et al*., 2004; Kwo *et al*., 2001; Lee *et al*., 2014; Pan & Lee, 2007; Paumier, Gaboriaud, & Kaul, 2002; Quah & Cheong, 2011) as shown in Fig. 2.5. Unfortunately, each of them has their own limitations and disadvantages compared to SiO_2 layers.

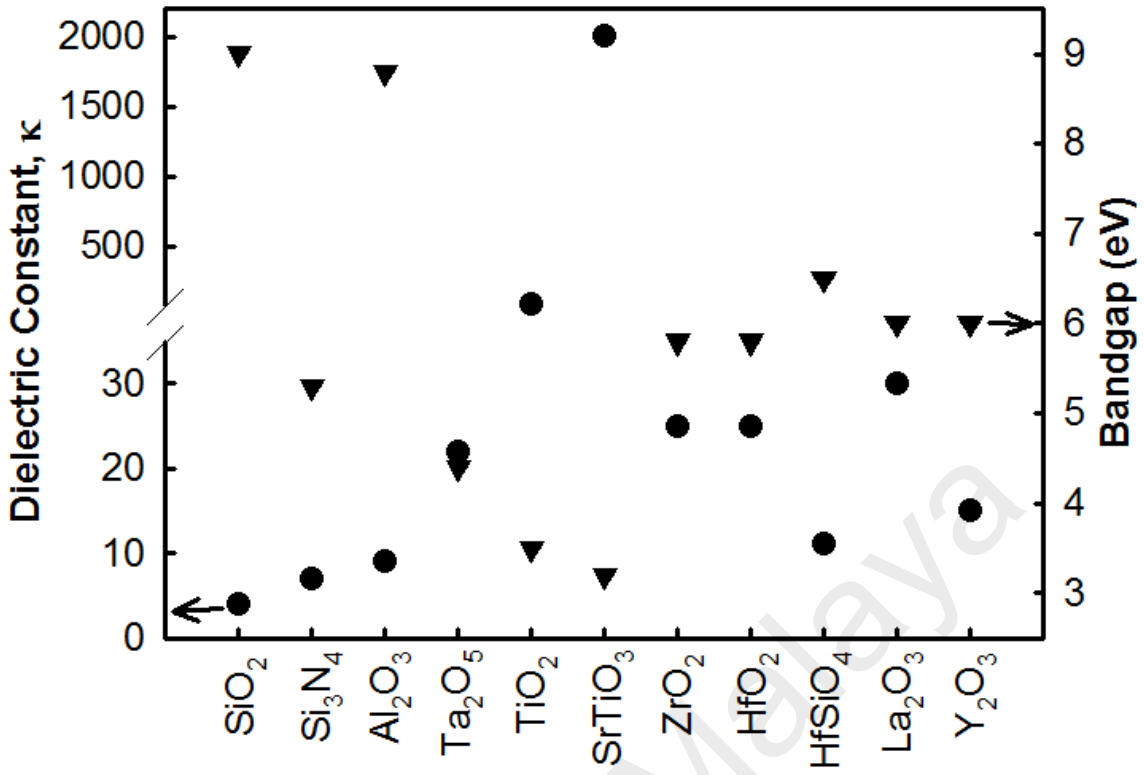

Figure 2.5: Dielectric constant and bandgap values of common high κ materials (Plummer & Griffin, 2001; Robertson, 2000, 2004).

Previous researches reported that Al_2O_3 has high κ value (~ 10), large bandgap (~ 9 eV), large band-offset (~ 2.16 eV), and high thermal stability (Cico *et al*., 2007; Kim, Fuentes-Hernandez, Potscavage, Zhang, & Kippelen, 2009; Kim *et al*., 2011; Lin *et al*., 2003; Quah & Cheong, 2014). However, Al_2O_3 layers have some problems such as large interface trap density, large flatband voltage shift, and large fixed charge (Cico *et al*., 2007; Constantinescu *et al*., 2012; Pan & Huang, 2010). TiO_2 and Ta_2O_5 layers are found to have low conduction offsets with the silicon conduction band and low thermodynamic stability (Alers *et al*., 1998; Autran *et al*., 1997; Shao *et al*., 2003; Son *et al*., 1998). TiO_2 has a smaller bandgap (~ 3.3 eV) than to HfO_2 and ZrO_2 (Robertson & Wallace, 2015). Y_2O_3 is considered a promising candidate due to its high κ (~ 18), large bandgap (~ 6 eV), large conduction band-offset (~ 2.3 eV), low lattice mismatch, and high thermal stability with silicon (Cheng *et al*., 2009; Cho *et al*., 2002; Choi, Cho, Whangbo, Whang, Hong, *et al*., 1997; Gaboriaud, Paumier, Pailloux, & Guerin, 2004; Kwon *et al*., 2008; Lin, Juan, Liu, Wang, & Chou, 2015; Quah & Cheong, 2011; Yu *et al*., 2011).

Low crystallization temperatures of TiO_2 and Y_2O_3 layers limit the MOS fabrication process temperatures. Moreover, Y_2O_3 layers have a higher interface density compared to SiO_2 layers (Houssa *et al*., 2006; Wong & Cheong, 2010). Undesirable interfacial layers (either Y-silicate or SiO_2) were formed easily between Y_2O_3 layers and Si substrate in any deposition or post deposition annealing (PDA) ambient (Durand *et al*., 2005; Evangelou, Wiemer, Fanciulli, Sethu, & Cranton, 2003; Ioannou-Sougleridis *et al*., 2004; Pan & Lee, 2007; Paumier *et al*., 2002). The presence of interfacial layers can be avoided by e-beam evaporation in vacuum ambient as reported by Kwo *et al.* (Kwo *et al*., 2001). Durand *et al.* (Durand *et al*., 2005) found that, the Y_2O_3 layers disappeared after annealing at 700 ºC owing to the instability of Y_2O_3 layers on SiO_2 layer. It has been reported that the leakage current density and capacitance decreased due to the formation of interfacial layer when the oxidation or annealing temperature were increased (Bethge *et al*., 2014; Gaboriaud, Pailloux, Guerin, & Paumier, 2001; Tang *et al*., 2006).

It has been reported that HfO_2 and ZrO_2 layers are quite suitable as replacement materials for SiO_2 because they not only fulfilled the six requirements of new oxide selection criteria but also have other beneficial properties (Chen, Hung, *et al*., 2013; Gao *et al*., 2016; Robertson & Wallace, 2015; Schamm, Scarel, & Fanciulli, 2007; Wong & Cheong, 2010). ZrO_2 and HfO_2 have very similar electronic structures (Robertson & Wallace, 2015). ZrO_2 has a high chemical durability, high corrosion resistance, and a high refractive index. HfO_2 has a high permittivity and low leakage current.

However, there were still some problems with HfO_2 and ZrO_2 layers (Chen, Hung, *et al*., 2013; Lee *et al*., 2014; Leskela *et al*., 2006; Wong & Cheong, 2010). The previous researches have placed the problems into six categories: (1) growth and formation of the interfacial layer during deposition and post deposition annealing, (2) microcrystal growth

after the heat treatment, (3) lateral oxidation at the gate edge, (4) existence of fixed charges and shifted flatband voltage, (5) existence of chemical vapor precursor contamination, and (6) higher interface state density (Chen, Hung, *et al*., 2013; Chen, Song, You, & Zhao, 2013; Chen, Lai, Cheng, Hsu, & Hsu, 2012; Chin *et al*., 2010; Gao *et al*., 2016; Maleto, Solovjeva, Turevskaya, Vorotilov, & Yanovskaya, 1994; Ohmi *et al*., 2000; Wong & Cheong, 2010). The growth of interfacial layers limits the downscaling of EOT values due to additional thickness. Moreover, HfO_2 has a high concentration of electronic structure defects such as oxygen vacancies and oxygen interstitials (Gao *et al.*, 2016; Robertson & Wallace, 2015). These defects cause a high interface state density owing to the large amount of trapped charges. Some metals or oxides such as Y, Yb, La, Dy, TiO_2, Al_2O_3, Y_2O_3, and La_2O_3 (Chen, Liu, Feng, Che, & Zhao, 2013; Chen *et al*., 2013; Cho *et al*., 2004; Gao *et al*., 2016; Kukli *et al*., 2007; J. S. Lee *et al.*, 2014; Lee *et al*., 2011; Park *et al*., 2007; Srivastava & Malhotra, 2011; Srivastava, Mangla, & Gupta, 2015) have been incorporated into HfO_2 to reduce leakage current density, reduce fixed charge, reduce interface charge, reduce oxygen vacancy concentration, and increase the crystallization temperature through oxygen vacancy passivation.

2.5 Common deposition methods of gate oxide films

Many deposition methods have been developed for REOs thin films but they can be divided into two main categories. The first one is chemical vapour deposition (CVD) such as metal organic-CVD (MOCVD), and atomic layer deposition (ALD), while the second one is physical vapour deposition (PVD) such as sputtering (radio frequency (RF) and direct current (DC)), vacuum evaporation, thermal evaporation, electron beam evaporation, and pulsed laser deposition (PLD) (Chin *et al*., 2010; He *et al*., 2011; Houssa *et al*., 2006; Leskela & Ritala, 2003; Wong & Cheong, 2010).

2.5.1 Chemical vapour deposition (CVD)

The MOCVD applies basic principles of both CVD and ALD processes. The main difference between them is that MOCVD uses a metal organic compound as precursor (Y. H. Wong & Cheong, 2010). A liquid precursor is advantageous to avoid or limit particle formation (Houssa *et al.*, 2006). ALD is also known as atomic layer chemical vapour deposition (ALCVD) or atomic layer epitaxy (ALE) (Wong & Cheong, 2010). ALD is a thin film deposition process which involves the chemical gas phases and two precursors are deposited and oxidized alternatively in a sequential manner at substrates, called surface controlled growth cycles. The first precursor is introduced in excess and a monolayer of reactant is chemisorbed onto the surface. Then, the first precursor is removed by inert gas before the second precursor is introduced. The second precursor reacts with the reactant on the surface and produces the desired film. Lastly, the second precursor is removed by inert gas again and the process is completed (Chin *et al.*, 2010; Jo, Ha, Park, Kang, & Kim, 2006; Leskela & Ritala, 2003). The precursor must be volatile, have high purity, nontoxic, have no gas phase reactions, no self-decomposition, and no etching of the existing oxide (Leskela & Ritala, 2003; Robertson, 2004). Good film quality, electrical properties, and low contamination of films can be produced by thermal and plasma enhanced ALD (Kim, Maeng, Moon, Myoung, & Kim, 2010). Both MOCVD and ALD are able to control the film thickness precisely with good uniformity and conformal coverage over complex shapes owing to the self-limiting growth mechanism of the precursors (Chin *et al*., 2010; Houssa *et al*., 2006; Jo *et al*., 2006; Leskela & Ritala, 2003; Robertson, 2004; Wong & Cheong, 2010).

The chemical deposition methods are more widely used because of the advantages as mentioned in the previous section such as large area depositions, uniform film, good

composition control, high film density, and deposition rates (He *et al*., 2011; Houssa *et al.*, 2006; Leskela & Ritala, 2003; Shalini & Shivashankar, 2005). However, there are still some concerns in chemical depositions such as molecular precursor availability, precursor stability, and volatility. High deposition temperatures and/or post deposition annealing are required to decompose metal organic precursors. Thus, large amount of carbon may be present which are detrimental to the electrical properties of the films (He *et al.*, 2011; Houssa *et al.*, 2006; Kosola, Paivasaari, Putkonen, & Niinisto, 2005; Robertson, 2004). As Wong and Cheong summarized (Wong & Cheong, 2010), ALD process has three main limitations: (1) too fine size of particles makes it difficult to be transported from source to the film, (2) poor nucleation on hydrogen terminated silicon, and (3) residues contaminations. A typical example is the carbon content was left in Nd_2O_3 film which was deposited by ALD process (Kosola *et al.*, 2005).

2.5.2 Physical vapour deposition (PVD)

For physical depositions, PLD requires a laser beam to ablate the target source and vaporize the materials that eventually sublimate on the substrates (Wong & Cheong, 2010). PLD is a clean and simple method to obtain a wide range of structures, compositions, and properties (Constantinescu *et al.*, 2012). In electron beam evaporation, an electron beam is used as power source to heat the target source to produce vapourized materials that sublimate condensed on substrates in high vacuum ambient (Wong & Cheong, 2010). Electron beam evaporation can produce ultrathin and smooth films with excellent electrical properties (Pan & Huang, 2010; Sen *et al.*, 2007; Wong & Cheong, 2010). Dense and compact films with low stress can be deposited by electron beam evaporations (Yang, Fan, Qju, Xi, & Fu, 2009). The substrates suffer little damage since

the electron beam sputters on the target source but not the substrates. However, it is not suitable as a conventional production method.

Sputtering is a process where source materials are ejected from the target source and deposited on the substrate in vacuum chamber (Chin *et al.*, 2010; Wong & Cheong, 2010). DC and RF sputtering are the most common types of sputtering process. DC sputtering is used for target materials with good electrical conductivity while RF sputtering is used for target materials with low electrical conductivity (Wong & Cheong, 2010). For RF magnetron sputtering, a magnet is involved to increase the concentration of electron ionizations and lengths of electron paths thus increase the ionization efficiency (Chin *et al.*, 2010). Sputtering has a high deposition rate, low substrate temperatures rise, good adhesion between films and substrates, and is broadly available (Robertson, 2004; Wu *et al.*, 2014). Even though straightforward sputtering of metal or metal oxide target is easier but it may oxidize the Si substrate and form thick a SiO_2 interlayer or metal silicate layer during deposition (Kim & Roh, 2006; Pampillon *et al.*, 2011). Besides that, sputtering only deposits in line of sight so it does not give good coverage on complex shape (Robertson, 2004).

2.6 Rare earth oxide (REO) as alternative gate oxide

Recently, some REOs have been investigated due to some superior properties such as high κ (between 7 and 30), large bandgap (between 4 and 6 eV), high breakdown electric field, high resistivity (among 10^{12} and 10^{15} Ω·cm), high conduction offset, low interface trap density, smooth surface, small lattice mismatch with silicon, high thermal and chemical stability. REOs have been widely used in electronic devices such as, frequencies switches, reprogrammable memory circuits, capacitors, transistors, and

varicaps (Andreeva, 1998; Constantinescu *et al*., 2012; Dakhel, 2004a; Kaya, Yilmaz, Karacali, Cetinkaya, & Aktag, 2015; Paivasaari *et al*., 2005; Pan & Huang, 2010; Rozhkov, Goncharov, & Trusova, 1995; Rozhkov, Trusova, & Berezhnoy, 1998; Schamm *et al*., 2007; Shalini & Shivashankar, 2005; Zhao *et al*., 2008).

With the lanthanide metal group of rare earth elements as shown in Fig. 2.6, Pm is an active radioactive element so it is not suitable as a gate oxide materials. Lanthanide has different oxidation states (+2, +3 and +4). Thus, lanthanide oxide exists as Ln_2O, Ln_2O_2, and Ln_2O_3. Ln_2O, it is unstable but Ln_2O_3 are stable. Thus, Ln_2O_3 is used to replace SiO_2 layers in MOS applications. In lanthanide oxides, La_2O_3 to Pr_2O_3 with stable hexagonal structure (lighter REOs) are suggested to be more suitable as replacement materials than heavier REOs (Sm_2O_3 to Lu_2O_3) with cubic and monoclinic structures. However, this cannot be proved because purity, deposition methods, and thickness are more influential on κ value (Chin *et al*., 2010).

Lanthanide													
La	Ce	Pr	Nd	Pm	Sm	Eu	Gd	Tb	Dy	Ho	Er	Tm	Yb	Lu

Figure 2.6: Lanthanide metal group of rare earth elements.

The lanthanide REOs have higher dielectric constant (κ = between 7 and 30) than SiO_2 (κ = 3.9). High κ allows reducing *EOT* for downscaling purposes (Gillen & Robertson, 2013; Schamm *et al*., 2007). Higher dielectric constant can avoid using ultrathin thickness of gate oxides which may lead to undesirable current leakage due to direct tunneling of electron through gate oxides (Engstrom *et al*., 2007). A high enough band gap is also required for insulating properties. Normally, the bandgap should be higher than 5 eV. Therefore, only five of these lanthanide REOs are higher than 5 eV as shown in Fig. 2.4 (Chin *et al*., 2010).

REOs are predicted to be chemically or thermodynamically stable when in contact with Si substrates because they are able to resist silicide formation after deposition. The oxygen tends to dissociate easily in air or oxygen during post deposition annealing. This will form SiO_x interfacial layers or rare earth silicates layers. Undesirable interfacial layers may degrade the electric properties due to a reduced κ value. Thus, optimization of deposition parameters of gate oxides is required to minimize formation of interfacial layers (Andreeva, 1998; Chin *et al*., 2010; Frohlich *et al*., 2006; Leskela *et al*., 2006; Schamm *et al*., 2007).

Another concern of REOs is the hygroscopic property (Frohlich *et al*., 2006; Leskela *et al*., 2006). Hydrate, Ln_2O_3-H_2O will be formed after moisture absorption which may lead to form hydroxide, $Ln(OH)_3$. Hydroxide may increase film thickness and reduce the κ value. The hygroscopic property may roughen the surface of gate dielectric and increase leakage current density. The moisture reactivity of REOs is increasing as lattice energy, ionic radius and cations electronegativity of REOs are decreasing. Thus, La_2O_3 is the most hygroscopic (lowest electronegativity and highest lattice energy) while Lu_2O_3 is the least hygroscopic (highest electronegativity and lowest lattice energy) as shown in Fig. 2.7 (Chin *et al*., 2010; Engstrom *et al*., 2007; Frohlich *et al*., 2006; Zhao *et al*., 2008).

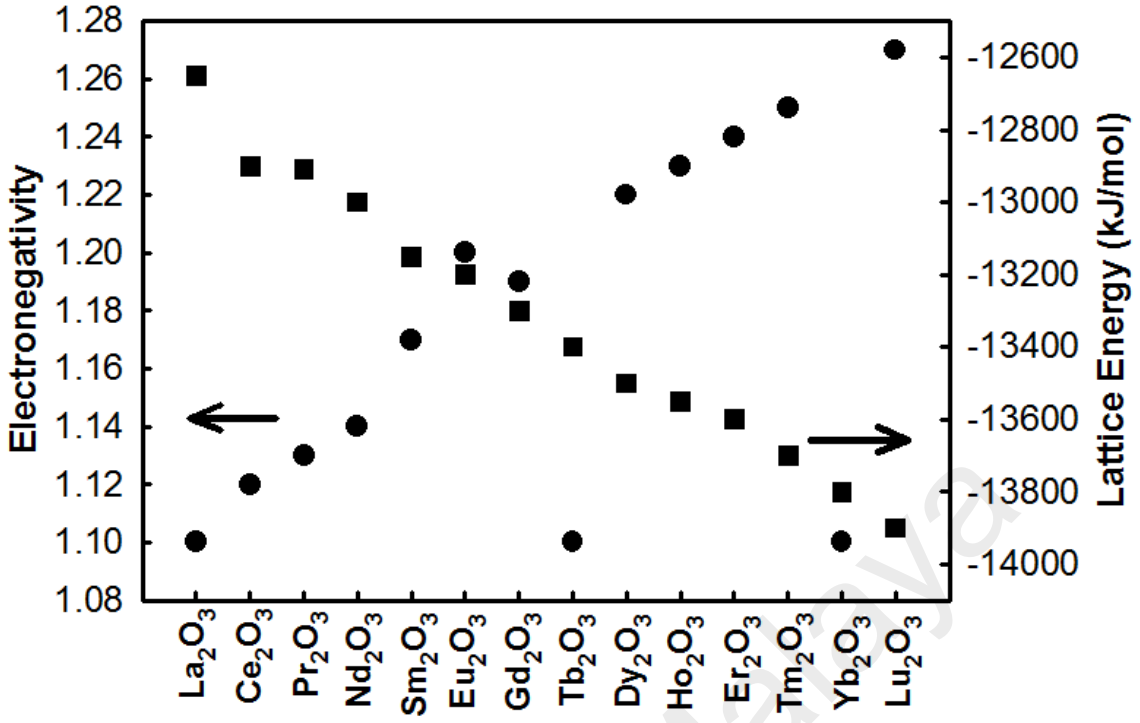

Figure 2.7: The electronegativity and lattice energy of lanthanide REOs (Chin *et al*., 2010; Zhao *et al.*, 2008).

2.7 Deposition methods of REO films and their performances

2.7.1 Lanthanum (La) oxide

Since lanthanum oxide (La_2O_3) has high κ (~ 27) and large interface barrier with Si substrates, it was seen as a suitable replacement for conventional SiO_2 layer as gate oxide (Cheng *et al*., 2004; Kakushima *et al*., 2010; Kim et al., 2010; Ng et al., 2005; Pisecny *et al*., 2004; Sen *et al*., 2007; Wong, Yang, Kakushima, Ahmet, & Iwai, 2012a). Based on previous works, La_2O_3 films have been deposited by e-beam evaporation (Kawanago *et al*., 2012; Ng *et al*., 2005; Sen *et al*., 2007; Wong *et al*., 2012a), MOCVD (Cheng *et al*., 2004; Pisecny *et al*., 2004), MBE (Kakushima *et al*., 2010), and ALD (Kim *et al*., 2010).

The formation of La-silicates at the La_2O_3 - Si substrates interface and fairly good MOSFET operations were observed (Kawanago *et al*., 2012). Kawanago *et al.*

(Kawanago *et al*., 2012) conducted 3 steps of annealing (annealing in oxygen ambient, forming gas annealing (FGA) at 800 º C, and 420 ºC) after La_2O_3 deposition by e-beam evaporation to solve the oxygen defects without degrading the interfacial properties. The binding energy was increased without increasing the La-silicate thickness (Kawanago *et al*., 2012). For La_2O_3 films by e-beam evaporation followed by PDA, film thicknesses were decreased before PDA at 300 ºC due to film densification while film thickness were increased after PDA at 300 ºC owing to growth of an interfacial silicate layer. A lower leakage current (6.67×10^{-7} A cm^{-2}) was observed if annealed at higher temperature (Ng *et al*., 2005). In Sen *et al.* (Sen *et al*., 2007) works, the trapping characteristics of La_2O_3 films deposited by e-beam evaporations were improved after annealing at 600 ºC due to removal of O vacancies and the formation of SiO_2 layers.

For CVD at a deposition temperature of 600 ºC at low pressure, smooth amorphous features were detected and RMS increased after PDA in oxygen ambient. A flatband voltage of 1.3 V and dielectric constant of 23.5 were reported in Cheng *et al.* works (Cheng *et al.*, 2004). The La_2O_3 thin films deposited at 250 ºC by e-beam evaporation were smoother than films deposited at room temperature. The leakage current density at 1.0 V was 1.7×10^{-8} A cm^{-2} with 1.26 nm of EOT (Ohmi *et al*., 2000). In Yang *et al.* works, smooth amorphous La_2O_3 films deposited by e-beam evaporation remained up to 900 ºC. The amorphous films have a smaller roughness and larger bandgap. With the increase of annealing time, the fixed charge density was increased significantly. The dielectric constant and leakage current density were determined to be 15.5 and 7.56×10^{-6} A cm^{-2} respectively (Yang *et al.*, 2009). The transconductance and drain current can be improved by scaling down the EOT which can suppress the formation of La-silicate layers (Kakushima *et al*., 2010). Relative low average interface trap density (2×10^{11} cm^{-2} eV^{-1})

and leakage current density (8 x10^{-7} A cm^{-2}) can be obtained by pulse enhanced PLD deposition (Kim *et al*., 2010).

For La_2O_3 films deposited by MOCVD, the dielectric constants, flatband voltages, and oxide charges density were improved after annealing at oxygen ambient. The flatband voltages and oxide charges density were further improved while the dielectric constant remained the same if FGA (Pisecny *et al*., 2004). In Wong *et al.* (Wong *et al*., 2012a) works, Al ions were introduced into La_2O_3 films by plasma immersion ion implantation. The flatband voltages of the samples annealed at 400 ºC shift to more negative side because implanted Al ions were not fully activated and interstitial atoms served as positives charges. The flatband voltages were reduce to -0.9 V after RTA at 600 ºC with PMA (Wong *et al*., 2012a).

2.7.2 Cerium (Ce) oxide

Cerium dioxide or ceria (CeO_2) has been widely used in catalytic applications and also in Si-based optoelectronics due to its unique physical properties, high κ (~ 26), high ability of oxygen storage, and high refractive index (~ 2.3) (Pagliuca, Luches, & Valeri, 2013; Wong, Yang, Kakushima, Ahmet, & Iwai, 2012b; Yamamoto, Momida, Hamada, Uda, & Ohno, 2005). CeO_2 is highly absorbing in the UV region and is optically transparent in the visible spectral regions (Logothetidis *et al.*, 2004). However, its lattice spacing may expand by 0.6 due to oxygen defect formations in oxygen poor conditions (Yamamoto, Momida, Hamada, Uda, & Ohno, 2005). Trivalent Ce^{3+} at grain boundaries and around O vacancies occurred as defective regions in amorphous Ce_2O_3 films. CeO_2 (Ce^{4+}) may reduce to Ce_2O_3 (Ce^{3+}) and the bandgap will reduce from around 6 eV to around 2 eV (Yamamoto *et al.*, 2005). Based on previous studies, CeO_2 films were

deposited by e-beam evaporation (Feng *et al*., 2014; Logothetidis *et al*., 2004; Mamatrishat *et al*., 2012; Pagliuca *et al*., 2013; Wong *et al*., 2012b; Yang, Wong, Kakushima, & Iwai, 2012), ion beam assisted deposition (IBAD) (Mamatrishat *et al*., 2012), reactive sputtering (Kao, Chen, Chen, *et al*., 2015; Kao, Chen, Liu, *et al*., 2014), and PLD (Balakrishnan *et al*., 2013).

In CeO_2 films grown by reactive evaporation, Ce silicates were formed between CeO_2 and both Si (111) and (100) substrates after annealing. Disappear of Ce^{4+} in XPS peaks may be due to formation of cerium silicates or Ce_2O_3 phases (Pagliuca *et al*., 2013). In Logothetidis *et al.* (Logothetidis *et al*., 2004) works, the CeO_2 films were deposited by e-beam evaporation and IBAD. IBAD produced films exhibited much larger grains compared to e-beam evaporation produced films. Amorphous interface layers were formed in all cases. However, interfaces of IBAD produced samples were rougher due to ions bombardment during deposition process (Logothetidis *et al*., 2004). For CeO_2 films deposited by sputtering followed by RTA, the intensity of XRD peaks and surface roughness were increased as the annealing temperatures increased owing to film crystallization. The CeO_2 films annealed at 950 ºC exhibit the largest memory window of 4.7 V (Kao, Chen, Chen, *et al*., 2015). For CeO_2/SiO_2 films deposited by sputtering followed by RTA, the samples annealed at 800 ºC have strongest crystallization, largest grain size, and highest RMS value.

Balakrishnan *et al.* (Balakrishnan *et al*., 2013) proposed deposition of CeO_2 films by PLD. The crystallite sizes and surface roughness increased as the substrate temperatures increased. The CeO_2 films deposited at 973 K exhibited better than those deposited at lower temperatures (Balakrishnan *et al*., 2013). Mamatrishat *et al.* reported that Ce silicate layers were formed after annealing. The energy bandgap and valence band

offset of Ce silicate with respect to silicon were determined to be at 7.67 and 4.35 eV, respectively. The concentration of Ce^{3+} ions decreased and that of Ce^{4+} ions increased at the interface between CeO_2 films and Si substrates (Mamatrishat *et al*., 2012).

Since 2012, CeO_2 films have been used as capping layer on La_2O_3 as gate dielectric layer (Feng *et al*., 2014; Wong *et al*., 2012b; Yang *et al*., 2012). The high oxygen vacancies of La_2O_3 films can be overcome by deposition of CeO_2 films on top. The CeO_2 films can be self-adapted and supply extra oxygen atoms to La_2O_3 films (Yang *et al*., 2012). The electrical performance was improved compared to single La_2O_3 films (Feng *et al*., 2014; Wong *et al*., 2012b; Yang *et al*., 2012). In Lim *et al.* (Lim, Cheong, & Lockman, 2011) works, $La_xCe_yO_z$ films were deposited by metal organic decomposition. The microstrains of $La_xCe_yO_z$ films reduced while the crystallite sizes increased when both annealing temperatures and time were increased. Si nanocrystal was found in the SiO_x interface layer owing to thermal decomposition of SiO_x at high temperature (Lim *et al*., 2011).

2.7.3 Praseodymium (Pr) oxide

Praseodymium oxide, Pr_2O_3 has been widely used in photocatalytic materials, anode of LED, CMOS, and DRAM technologies (Abrutis *et al.*, 2008; Lo Nigro, Toro, Malandrino, Fiorenza, *et al*., 2005; Lo Nigro *et al.*, 2006; Mane *et al*., 2005; Osten, Bugiel, & Fissel, 2003). Pr_2O_3 has an appropriate band offset to Si (> 1 eV), high κ (~ 30), middle bandgap energy (~ 3.9 eV), large energy of formation (- 12900 kJ mol^{-1}), ultra-low leakage current (< 10^{-8} A cm^{-2} at 1 V) and relatively low *EOT* (1.4 nm) (Abrutis *et al*., 2008; Kato *et al*., 2014; Kogler *et al*., 2007; Lo Nigro, Toro, Malandrino, Fiorenza, *et al*., 2005; Lo Nigro *et al*., 2006; Lo Nigro, Toro, Malandrino, Raineri, & Fragala, 2005; Osten

et al., 2003; Wang, Wu, Fang, & Zhang, 2004; Watahiki, Tinkham, Jenichen, Braun, & Ploog, 2007; Watahiki *et al*., 2008). Previously, Pr_2O_3 films were deposited by MOCVD (Abrutis *et al*., 2008; Kato *et al*., 2014; Lo Nigro, Toro, Malandrino, Fiorenza, *et al*., 2005; Lo Nigro *et al*., 2006; Lo Nigro, Toro, Malandrino, Raineri, *et al*., 2005), PLD (Wolfframm, Ratzke, Kouteva-Arguirova, & Reif, 2002), thermal evaporation (Wang *et al*., 2004), MBE (Mane *et al*., 2005; Watahiki *et al*., 2007; Watahiki *et al*., 2008), e-beam evaporation (Mussig *et al*., 2002; Osten *et al*., 2003; Osten, Liu, Bugiel, Mussig, & Zaumseil, 2001, 2002; Osten, Liu, Mussig, & Zaumseil, 2001), and ion beam synthesis (Kogler *et al*., 2007).

An amorphous PrO_x films were observed at low partial oxygen pressure of MOCVD. Pr_6O_{11} films tend to form at higher partial oxygen pressures (40 - 100 Pa) and lower growth temperatures while Pr_2O_3 films tend to form at lower partial oxygen pressures (0.027 – 0.6 Pa) and higher growth temperatures (Abrutis *et al*., 2008). Hexagonal Pr_2O_3 crystals of smaller grain size were formed in dominantly amorphous PrO_2 films at higher oxygen partial pressure of MOCVD. Cubic Pr_2O_3 and Pr silicates were formed after PDA in N_2 atmosphere while hexagonal Pr_2O_3 and Pr silicate were formed after PDA in vacuum atmospheres (Kato *et al.*, 2014). The Pr_2O_3 films were crystallized at 800 ºC in oxygen ambient but remain amorphous in argon ambient. However, the silicate layers were formed at 900 ºC in argon ambient. No Pr silicide was found in both ambient (Lo Nigro, Toro, Malandrino, Raineri, *et al.*, 2005).

Polycrystalline Pr_2O_3 films were deposited by MOCVD and multi interface layers (Pr_2O_3/Pr silicate/SiO_2/Si) were found. The dielectric constant, flatband voltage, and leakage current density of the Pr_2O_3/Pr silicate/Si stack were determined to be 26, 0.4 V, and 5 x 10^{-10} A cm^{-2}, respectively (Lo Nigro *et al*., 2006). The Pr oxide films were

amorphous if MOCVD deposition temperatures were lower than 600 ºC. The thickness of Pr silicate layers was increased with the deposition temperature. The leakage current density and breakdown electrical fields for 15 nm polycrystalline Pr_2O films were 1 x 10^{-7} A cm^{-2} and 4.5 MV cm^{-1}, respectively. A dielectric constant of 16 and flatband voltage of 0.1 V were reported (Lo Nigro, Toro, Malandrino, Fiorenza, *et al*., 2005). In Mane *et al.* (Mane *et al*., 2005) works, the $Pr_xSi_yO_z$ films were deposited by MBE. The dielectric constant, flatband voltage shift, and leakage current density were determined to be 12, -1.3 eV, and 10^{-7} A cm^{-2}, respectively (Mane *et al*., 2005). Si was added during growth of Pr_2O_3 by MBE. The added Si enhanced the nucleation at initial stages and restricted the atomic intermixing by forming the silicate interlayer. Hexagonal Pr_2O_3 was more stable at higher temperature than cubic Pr_2O_3 and restricted the oxygen diffusion through the layer due to its higher density. However, the overall leakage current density was still quite high (~10^{-1} A cm^{-2}) (Watahiki *et al*., 2007).

$PrSi_2$ films were formed in the as-deposited films under oxygen deficient atmosphere during MBE. Pr_2O_3 films disappeared for samples annealed at 900 ºC. However, the silicidation of Pr can be suppressed by supplying additional oxygen gas (Watahiki *et al*., 2008). PrO_2 phases were preferred to grow at initial stages due to lower lattice mismatch. SiO_2 layers may act as stress buffer during transformation of PrO_2 to Pr_2O_3 (Mussig *et al*., 2002). The Pr_2O_3 films grown epitaxially on Si (001) by MBE displayed high κ (~ 30), low leakage current (~ 10^{-4} A cm^{-2}) and high breakdown voltage field (43 MV cm^{-1}). The structural quality of epitaxially grown films degraded after being exposed to air due to oxygen diffusion through Pr_2O_3 and the formation of a SiO_x layer. However, this can be suppressed by aluminum capping on Pr_2O_3 films (Osten *et al*., 2003; Osten, Liu, Bugiel, *et al*., 2001; Osten *et al.*, 2002; Osten, Liu, Mussig, *et al*., 2001). For Pr_2O_3 films deposited by ion beam synthesis, Pr silicide was detected at lower annealing

temperatures while Pr silicates were detected at higher annealing temperatures (Kogler *et al*., 2007).

2.7.4 Neodymium (Nd) oxide

Neodymium oxide (Nd_2O_3) was selected for electronic applications not only because of its high κ but also good step coverage and good dielectric strengths (Kao, Chan, Chen, Chung, & Luo, 2010; Kao, Chen, Liao, *et al*., 2014). According to previous studies, Nd_2O_3 films were deposited by reactive RF sputtering (Kao, Chan, *et al*., 2010; Kao, Chen, Liao, *et al*., 2014), thermal evaporation (Dakhel, 2004d), and ALD process (Kosola *et al*., 2005).

Strong Nd_2O_3 film structures were formed on polycrystalline Si substrates by reactive RF sputtering after RTA at 900 ºC (Kao, Chan, *et al*., 2010; Kao, Chen, Liao, *et al*., 2014). The binding energies shifted to higher energies compared to as-deposited film. The RMS of as-deposited films improved from 5.61 nm to 4.81 nm after RTA at 900 ºC. Nd_2O_3 structures exhibited strongest intensity for (002)-, (102)-, and (110)-oriented structures. The annealed samples at 900 ºC have highest electrical breakdown fields (~ 6 MV cm^{-1}) and lowest gate voltage shift (~ 0.1 V) among the annealed samples (Kao, Chan, *et al*., 2010; Kao, Chen, Liao, *et al*., 2014).

Anne Kosola *et al.* (Kosola *et al.*, 2005) reported that Nd_2O_3 films deposited by ALD were crystallized at higher annealing temperatures. The residual contaminants or carbonates from precursors were detected in FTIR spectra. The RMS of annealed samples (1.0 nm) had increased compared to deposited samples (0.8 nm). The flatband voltages shifted to positive bias from - 2.5 V to - 2.2 V when AC frequencies increased from 100

kHz to 500 kHz. About 10.5 of dielectric constant of annealed samples were obtained by calculation. The leakage current of Nd_2O_3 films were very low, around 3.2 x 10^{-9} A cm^{-2} and the breakdown field strength were around 1.3 MV cm^{-1} (Dakhel, 2004d).

2.7.5 Europium (Eu) oxide

Europium oxide (Eu_2O_3) was used in optoelectronics, microelectronics, and laser applications owing to its high κ (~ 14), large bandgap energy (4.5 eV), chemical and thermal stability with Si substrates (Dakhel, 2004b, 2004c, 2005a; Singh *et al.*, 2008). In Singh *et al.* works, the thin Eu_2O_3 films were deposited by low pressure MOCVD methods. The dielectric constant of 600 ºC grown Eu_2O_3 films was about 12. The flatband voltages decreased when the grown temperatures increased owing to removal of Eu deficient parasitic phases and better crystallinity of the films (Singh *et al.*, 2008).

Based on previous works, europium (Eu) was widely used as doping element in indium oxide or indium-zinc oxide (IZO) by sol-gel spin coating technique (Ting, Li, Wang, & Yong, 2014) or thermal evaporation to form MOS structures (Dakhel, 2004b, 2004c, 2005a). Eu acted as carrier suppressor in IZO due to its low electronegativity (1.2) and standard electrode potential (-1.991 V). Furthermore, Eu^{3+} ions (0.095 nm) have similar ionic radius and same charges with In^{3+} ions (0.08 nm). Thus, extra free charge carriers were not produced if In^{3+} ions were replaced by Eu^{3+} ions. Lower RMS of EIZO samples (1.01 nm) were observed when compared to un-doped samples (1.88 nm) (Ting *et al*., 2014). For thermally evaporated Eu-In oxide films followed by RTA at 800 ºC in vacuum, dielectric constants as high as 29.4 and barrier heights of 3.9 were reported in Dakhel's works (Dakhel, 2004b, 2004c, 2005a).

2.7.6 Gadolinium (Gd) oxide

Gadolinium oxide, Gd_2O_3 has many applications in electronics, photonics, and nuclear industries (Gottlob *et al*., 2006; Grave *et al*., 2012; Her *et al*., 2014; Kao, Chen, & Lin, 2015; Kao, Chen, & Huang, 2013; Kuei & Hu, 2008; Mishra *et al*., 2015; Pampillon *et al*., 2011). Gd_2O_3 has high κ (~ 15), high bandgap energy (~ 6 eV), low lattice mismatch (~ 0.5%), high transparency in UV region, band offset with Si substrates (2.21 eV), thermally and chemically stable with Si substrates (Cheng *et al*., 2009; Grave *et al*., 2012; Guo *et al*., 2004; Her *et al*., 2014; Kao, Chen, & Lin, 2015; Kao *et al*., 2013; Kuei & Hu, 2008; Luptak *et al*., 2005; Pampillon *et al*., 2011; Pampillon, Feijoo, & San Andres, 2013; Yue *et al*., 2008). Based on previous researches, Gd_2O_3 films were deposited by sputtering followed by plasma oxidation (Pampillon *et al*., 2013), modified epitaxy process (Gottlob *et al*., 2006), PLD (Cheng *et al*., 2009; Mishra *et al*., 2015), sputtering (Her *et al*., 2014; Kao, Chen, & Lin, 2015; Pampillon *et al*., 2011; Yue *et al*., 2008), LP-CVD (Kao *et al*., 2013), thermal evaporation (Dakhel, 2004e, 2005c; Luptak *et al*., 2005), anodic oxidation (Kuei & Hu, 2008), EB-PVD (Grave *et al*., 2012), dual ion beam deposition (Zhou *et al*., 2004), sol-gel methods (Guo *et al*., 2004), e-beam evaporations (Lee *et al*., 2010; Wu, Landheer, Quance, Graham, & Botton, 2002), and ALD (Fang, Williams, Odedra, Jeon, & Potter, 2012).

Amorphous of 6 nm Gd_2O_3 films can be achieved by plasma oxidation. However, SiO_x and GdO_x layers formed between Si substrates and Gd_2O_3 films. The dielectric constants of Gd_2O_3 films were about 14. The interface state density and leakage current density were improved after annealing process (Pampillon *et al*., 2013). At RTA temperatures of 930 ºC after modified epitaxy process, the Gd were fully replaced or resolved by the TiN gates. No Gd_2O_3 films were shown and only thicker interfacial layers

were shown in HRTEM. The on/off current ratios and leakage current density were ~ 10^6 and ~ 10^{12} A cm^{-2}, respectively (Gottlob *et al*., 2006).

For PLD methods, Mishra *et al.* (Mishra *et al*., 2015) reported that the amorphous Gd_2O_3 films were formed at lower substrate temperatures and only monoclinic Gd_2O_3 films were observed when substrate temperatures were above 673 K. The surface roughness was mainly affected by substrate temperatures while no significant effects by various oxygen partial pressures (Mishra *et al*., 2015). Gd_2O_3 and TiN seed layers were deposited by PLD methods. TiN seed layers were able to prevent oxidations of Si substrates and diffusion between Gd and Si substrates. Existence of $Gd(OH)_3$ due to hygroscopic characteristics of REOs. High leakage currents occurred due to O vacancies at grain boundaries. Hence, relatively low dielectric constant (~ 6) and high leakage current density (0.1 A cm^{-2}) were observed (Cheng *et al*., 2009).

Hexagonal Gd films occurred at RTA between 100 ºC and 250 ºC after high pressure sputtering but disappeared at higher temperatures. Monoclinic Gd_2O_3 formed below 350 ºC while cubic Gd_2O_3 was observed at 500 ºC and above. However, hexagonal $GdSi_2$ was observed too. The leakage current densities improved when oxidation temperatures and FGA temperatures increased. The interface state density of samples FGA at 450 ºC (4 x 10^{10} eV^{-1} cm^{-2}) were lower compared to samples FGA at 300 ºC (1.7 x 10^{12} eV^{-1} cm^{-2}) (Pampillon *et al*., 2011). The preferable orientation of (401)-structures deposited by low pressure CVD possessed strong and well crystallizations which are suitable for sensing applications. The dielectric constants improved from 11.14 to 14.67 after as-deposited films annealed at 900 ºC. Relatively high leakage current density of ~ 7 MV cm^{-1} was observed (Kao *et al*., 2013).

For Gd_2O_3 films deposited by RF sputtering, the surface roughness increased with the increase in RTA temperatures. The electrical performances and overall storage capability improved after RTA (Kao, Chen, & Lin, 2015). The cubic phase of Gd_2O_3 films were observed at lower growth temperatures and monoclinic phases of Gd_2O_3 films dominated at higher growth temperatures of RF sputtering deposition. The cubic phase of Gd_2O_3 films exhibited better electrical properties compared to monoclinic phases of Gd_2O_3 films (Yue *et al*., 2008). Gadolinium silicates with thickness of 1.7 nm were observed at the interface layers between Gd_2O_3 films and Si substrates after thermal evaporation deposition of Gd_2O_3 films. The dielectric constants of Gd_2O_3 films were 11.4 (Luptak *et al*., 2005).

For anodic oxidation, the film structures were not affected by the magnitude of bias voltages instead by the oxidation times. The Gd-silicate layers did not form but SiO_2 interfacial layers were observed. For anodization voltages of 30 V, the electrical performances improved with the increase of anodization times while the electrical performances improved with the decrease of anodization times for 60 V. The Gd_2O_3 films dissipated and disappeared for samples anodized at 60 V and 40 min (Kuei & Hu, 2008).

For EB-PVD methods, cubic phases were observed at higher deposition temperatures and higher oxygen flow rates. However, monoclinic phases were observed for samples with thicker films. The grain sizes increased with the increase of films thickness and deposition temperatures. The dielectric constants increased with the decrease of oxygen flow rates. The samples with relatively low deposition temperatures (200 ºC) and oxygen flow rates (25 and 50 sccm) have highest dielectric constants of 20 (Grave *et al*., 2012). Monoclinic structures with lower grain sizes appeared at lower substrate temperatures for dual ion beam epitaxy deposition methods. Oxygen

deficiencies caused the ratio of Gd and O did not achieve 3:2. High flatband voltages of 9.0 V indicated high charge density in the oxide owing to oxygen deficiencies (Zhou *et al.*, 2004). Crystallization started at annealing temperature of 400 ºC after being deposited by sol gel method and the grain sizes increased with annealing temperatures (Guo *et al*., 2004).

The Zr incorporated Gd_2O_3 films deposited by e-beam evaporations have better crystalline structures by impeding the growth of Gd-silicate interfacial layers and reducing oxygen activation barriers. However, the Zr atoms may cause lattice constant shrinkages due to Zr radius being smaller than Gd radius (Lee *et al*., 2010). Amorphous of GdN films with low concentration of impurities and good uniformity were deposited at lower temperatures by ALD method (Fang *et al*., 2012). Smooth and uniform of orthorhombic $GdTiO_3$ films were deposited stoichiometry by reactive sputtering method. The dielectric constants and threshold voltages of $GdTiO_3$ films were determined to be ~ 15 and 0.14 V respectively. High I_{on}/I_{off} ratio of 4.2 x 10^8 was observed due to high electron mobility (32.3 $cm^2 V^{-1} s^{-1}$) and low leakage currents (~ 10^{-12}) (Her *et al*., 2014).

No interfacial layers were formed between as-deposited Gd silicate films and Si substrates after deposition by e-beam evaporation process. However, SiO_2 interfacial layer were formed after annealing in oxygen ambient (Wu *et al*., 2002). For Gd-In oxide films deposited by thermal evaporation, the Gd oxides crystallized alone and the grains growth of In_2O_3 were enhanced in atmosphere with higher oxygen concentration. The dielectric constants decreased from 7.47 to 4.46 due to formation of silicate layers when annealing temperatures increased from 400 ºC to 600 ºC (Dakhel, 2004e, 2005c).

2.7.7 Terbium (Tb) oxide

Terbium oxide (Tb_2O_3) was widely used in MOSFET device application such as optical glasses and colour TV tubes. It possesses relatively high κ (~14), large bandgap, low leakage current, and is stable with Si substrates up to 800 ºC (Kao, Liu, *et al*., 2012; Pan, Jung, & Chen, 2010; Pan & Li, 2010; Pan, Li, & Deng, 2010).

In Kao *et al.* (Kao, Liu, *et al*., 2012) works, the Tb_2O_3 films were formed on strained Si:C substrates by reactive RF sputtering followed by RTA. The crystallinity (higher intensity), binding energy (from 149 eV to 528.7 eV), RMS of surface (from 5.67 nm to 4.07 nm), RMS of interface (from 5.85 nm to 1.7 nm), gate voltage shift (from - 2.0 to - 0.5), leakage current (from 10^{-4} to 10^{-5}) and electrical breakdown voltages (from - 6 V to - 14 V) of annealed samples were improved compared to as-deposited films (Kao, Liu, *et al*., 2012).

2.7.8 Dysprosium (Dy) oxide

Dysprosium oxide, Dy_2O_3 has high κ (~ 12), large bandgap energy (~ 4.9 eV), and is chemically and thermally stable with Si substrates (Al-Kuhaili & Durrani, 2014; Dakhel, 2005b, 2006d; Hardy *et al*., 2009; Lawniczak-Jablonska *et al*., 2006; Pan, Chang, & Chiu, 2011). Its ionic radius was relatively larger which means it reacts poorly with Si substrates and has no or lesser formation of silicate layers (Dakhel, 2006d). These superior properties attracted many researchers to study and investigate its probability as gate oxide materials. Based on previous literatures, Dy_2O_3 films were deposited by reactive sputtering (Lawniczak-Jablonska *et al*., 2006; Pan *et al*., 2011; Pan & Lu, 2011), thermal

evaporation (Al-Kuhaili & Durrani, 2014; Dakhel, 2005b, 2006c, 2006d), MOCVD (Thomas *et al*., 2008), and ALD (Hardy *et al*., 2009).

Preferable orientation of (100)-planes of cubic dysprosium and (400)-planes of Dy_2O_3 were formed by reactive sputtering. The surface roughness increased with the increase of RTA temperatures. However, silicon atoms from substrates and oxygen from Dy_2O_3 moved to interface regions and formed low κ interfacial layer during RTA at 800 ºC. Thus, the amorphous silica layers were formed and leading to smaller surface roughness. The samples annealed at 700 ºC had better dielectric constant (10.41), lower leakage current density (9.81 nA cm^{-2}), and smaller interface state density (1.26 x 10^{12} eV^{-1} cm^{-2}) (Pan *et al*., 2011).

Fine grain structure and amorphous film can be achieved by lower deposition rate of reactive evaporation. Smooth Dy silicate interfaces were confirmed by good agreement between measured and stimulated C-V curves which indicated low density of interface traps. For oxygen annealing, there is more uniform distribution of crystallization compared to argon annealing (Lawniczak-Jablonska *et al*., 2006). Dahkel (Dakhel, 2006d) reported that [111]-orientation grains decreased by increasing PDA temperatures and in vacuum environment compared to atmosphere annealing after thermal evaporation of Dy_2O_3 films. In Al-Kuhaili *et al.* (Al-Kuhaili & Durrani, 2014) works, the Dy_2O_3 films were deposited by thermal evaporation followed by PDA at various temperatures (200 - 800 ºC). The Dy hydroxide and Dy hydroxide carbonates were converted into Dy_2O_3 after PDA at 800 ºC. The Dy_2O_3 films annealed at 600 ºC exhibited smoothest surface and best optical properties (Al-Kuhaili & Durrani, 2014).

$DyMnO_3$ started to crystallize at temperature more than 600 ºC after thermal evaporation which was better and higher than crystallization temperatures of the Dy_2O_3 (300 ºC) and Mn_2O_3 (500 ºC). The $DyMnO_3$ grains with [200]-orientations were grown with increasing of annealing temperatures. Samples annealed at 1000 ºC in air atmosphere have lower interface state density (1.85 x 10^{15} eV^{-1} m^{-2}) and higher dielectric constants (5.2) (Dakhel, 2005b, 2006c). Titanium adding of Dy_2TiO_5 by RF sputtering was able to suppress the hydroxide thickness. SiO_2 layers were almost unaltered at high temperature (≤ 800 ºC). However, oxygen atoms were moving from Dy_2TiO_5 to the interfacial layer to form silicate and SiO_2 at RTA temperatures of 900 ºC. The surface roughness increased with the increase of RTA temperatures. The Dy_2TiO_5 annealed at 800 ºC exhibited thinner CET of 2.02 nm, smaller interface state density of 7 x 10^{11} eV^{-1} m^{-2}, and lower hysteresis voltage of about 10 mV (Pan & Lu, 2011). Hardy *et al.* (Hardy *et al*., 2009) reported that HfO_2 layer can act as barrier layer to prevent Dy-silicate during ALD process. He also reported that Dy may prevent the monoclinic HfO_2 crystallization in $HfDyO_x$ (Hardy *et al.*, 2009). For $DyScO_3$ films deposited by MOCVD, the dielectric constants and breakdown fields were determined to be 22 and 2.3 MV cm^{-1}, respectively (Thomas *et al.*, 2008).

2.7.9 Holmium (Ho) oxide

Holmium oxide (Ho_2O_3) was attracted to be used in optoelectronics, logic devices, memory devices, and pH sensing films due to its high κ (~ 13), large bandgap energy, and chemical and thermal stability with Si substrates (Castan *et al.*, 2015; Kukli *et al*., 2014; Pan, Chang, & Chiu, 2010; Pan & Huang, 2011). In addition, Ho_2O_3 possess highest lattice energy, largest magnetic moment and susceptibility among the REO and easy to be crystallized prior to an annealing process (Heiba & Mohamed, 2015; Pan, Chang, *et*

al., 2010). According to previous literatures, Ho_2O_3 films were deposited by reactive RF sputtering (Pan, Chang, *et al*., 2010; Pan & Huang, 2011), sol-gel method (Heiba & Mohamed, 2015), and ALD (Castan *et al*., 2015).

In Pan *et al.* (Pan, Chang, *et al*., 2010; Pan & Huang, 2011) works, the poor crystallinity of Ho_2O_3 films were formed by reactive sputtering before RTA process. The crystallinity and binding energy improved after RTA process. However, the crystallinity decreased when the RTA reached at 900 ºC due to amorphous silica layers formation at the interface between Ho_2O_3 films and Si substrates. This trend was supported by binding energy of Ho-O bonds decreasing suddenly but Si-O bonds increasing for samples annealed at 900 ºC. The surface roughness increased when RTA temperatures increased, but the RMS decreased at 900 ºC. It may be due to holmium and oxygen atoms migrating to interface layers and forming amorphous silica layers with lower surface roughness at higher RTA temperature (900 ºC) (Pan, Chang, *et al*., 2010; Pan & Huang, 2011).

For Mn-doped Ho_2O_3 films deposited by sol-gel methods, the crystallite sizes decreased with the Mn contents but the strains increased with the Mn contents (Heiba & Mohamed, 2015). In Castan *et al.* works, the $HoTiO_x$ films were grown by ALD process. The higher Ho content of $HoTiO_x$ films have lower capacitance values but less leaky which have lower leakage current density (Castan *et al*., 2015).

2.7.10 Erbium (Er) oxide

Erbium oxide, Er_2O_3 was also an attractive candidate material as gate oxide due to its large conduction band offset to Si (~ 3.5 eV), high κ (~ 14), good thermal stability with Si, small lattice mismatch, large bandgaps energy (~ 7.5 eV), high transparency in

visible range (> 90%), and low interface trap density (4.2 x 10^{10} eV^{-1} cm^{-2}) (Adelhelm *et al.*, 2009; Chen, Her, *et al*., 2013; Kao, Chen, Pan, Chiu, & Lu, 2012; Paivasaari, Putkonen, Sajavaara, & Niinisto, 2004; Xu, Tao, Yang, & Takoudis, 2012). It also has small ionic radius and appropriate electronegativity which suppress the hydroxylation (Xu *et al*., 2012). According to previous literatures, Er_2O_3 films were deposited by ALD (Paivasaari *et al*., 2004; Xu *et al*., 2012), laser ablation (Queralt *et al*., 1995), cathodic arc deposition (Adelhelm *et al*., 2009), thermal evaporation (Dakhel, 2005d, 2006a, 2006b, 2008), LP-CVD (Kao, Chen, *et al*., 2012), reactive sputtering (Chang *et al*., 2008; Huang *et al*., 2008; Pan, Lin, Wu, & Lai, 2009; Wu *et al*., 2014; Zhu, Fang, & Liu, 2010; Zhu *et al*., 2011), and e-beam evaporation (Al-Kuhaili & Durrani, 2007).

In Xu *et al.* (Xu *et al*., 2012) and Paivasaari *et al.* (Paivasaari *et al*., 2004) works, the polycrystalline of Er_2O_3 films were deposited by ALD method. The grain sizes and surface roughness increased with the increase of annealing temperatures. Er-silicates were formed at 1000 ºC due to inter-diffusion between Er_2O_3 films and SiO_2 interfacial layers (Xu, Tao, Yang, & Takoudis, 2012). The dielectric constants increased from 9.8 to 11.8 while the flatband voltages decreased from 0.66 V to 0.3 V after annealed at 600 ºC. The hysteresis voltages decreased significantly indicated the trapped charges were reduced efficiently. The leakage currents were increased after annealed due to presence of grain boundaries which acted as leakage paths compared to amorphous as-deposited films (Xu *et al.*, 2012). Amorphous films can be obtained at low deposition temperatures and the SiO_2 layer hinders the heteroepitaxial Er_2O_3 film (Paivasaari *et al*., 2004). Smoother and highly textured surfaces can be deposited by laser ablation methods compared to electron beam evaporation techniques (Queralt *et al*., 1995).

In Adelhelm *et al.* (Adelhelm *et al*., 2009) works, the monoclinic B-phase Er_2O_3 films with dense structures were deposited by filtered cathodic arc deposition resulting from ion bombardment irradiation damages and high internal stress during particle formation. The Er_2O_3 films deposited by thermal evaporation followed by PDA in vacuum conditions suffered more structural oxygen vacancies compared to PDA in dry oxygen atmospheres. The samples annealed in vacuum exhibited better electrical results which have lower interface state density (1.3×10^{12} eV^{-1} cm^{-2}) and higher dielectric constant (~ 12.1) compared to samples annealed in dry oxygen atmospheres (Dakhel, 2005d, 2006a). The Er-silicate interfacial layer were formed after reactive sputtering deposition followed by RTA at 800 ºC resulting in the increase of surface roughness due to migration of Er atoms to interfacial layer and forming amorphous silicate layer (Pan *et al.*, 2009).

However, Kao *et al.* reported that RTA at 800 ºC after low pressure CVD had smoother surface roughness than samples before RTA due to increasing of grain size and well crystallization process. The dielectric constant of annealed Er_2O_3 films with EOT of 153 Å was 10.19. The reported leakage current density and breakdown electrical field of annealed at 800 ºC samples were ~ 10^{-7} A cm^{-2} and ~ 7 MV cm^{-1} (Kao, Chen, *et al*., 2012). In Wu *et al.* (Y. P. Wu *et al*., 2014) works, the effects of substrates temperatures during RF magnetron sputtering were investigated. The compressive stress becomes larger when the substrate temperatures increased from room temperature to 200 ºC (Y. P. Wu et al., 2014). The amorphous and stoichiometric Er_2O_3 films can be formed by RF sputtering of Er_2O_3 target in Ar ambient (Zhu *et al*., 2010; Zhu *et al*., 2011). Sub-stoichiometric Er_2O_3 films can be achieved by e-beam evaporation on 300 ºC of substrate temperature without oxygen atmosphere (Al-Kuhaili & Durrani, 2007).

The doped Er_2O_3 films or Er-doped films have attracted great attentions of researchers owing to their potential applications in MOS and integrated optics. During thermal evaporation deposition, Mn_2O_3 and Er_2O_3 do not crystallized each alone but $ErMnO_3$ compounds were preferable to form as reported in Dakhel's works (Dakhel, 2008). Stable crystalline solid solutions of Er-Gd oxides were detected in samples which were PDA in oxygen and vacuum atmospheres after thermal evaporation depositions (Dakhel, 2006b).

For reactive co-sputtering of Er and Ti, amorphous structures of $ErTi_xO_y$ films remained even after annealing process. The surface roughness increased with the PDA temperatures. The dielectric constant, field effect mobility, and threshold voltage of Er_2TiO_5 annealed at 400 ºC were determined to be 14.6, 8.24 $cm^2\ V^{-1}\ s^{-1}$, and 0.37 V, respectively (Chen, Her, *et al*., 2013). Er interlayer was found to increase the NiSi formation temperatures of ion beam sputtering process. However, Er interlayers did not significantly improve the Schottky barrier heights of Ni/Er/Si system (Huang *et al*., 2008). Er-silicate films were formed in $Er/SiO_2/Si$ stacking systems after RTA process. The oxygen atoms which were supplied by SiO_2 were diffused to Si substrates and formed the Er-silicate layers during RTA (Chang *et al*., 2008).

2.7.11 Thulium (Tm) oxide

Thulium oxide (Tm_2O_3) was one of the potential replacements of SiO_2 because of its high κ, large bandgap energy, lattice constant was two times the lattice constant of Si, chemical and thermal stability with Si substrates (Dakhel, 2009; Litta, Hellstrom, & Ostling, 2015; Pan & Yen, 2010a, 2010b; Wang, Fang, *et al*., 2012; Wang, Ji, Zhu, Fang, & Ren, 2012). Based on previous literatures, Ho_2O_3 films were deposited by reactive

sputtering (Pan & Yen, 2010a, 2010b), MBE (Ji *et al*., 2011; Wang, Fang, *et al*., 2012; Wang, Ji, *et al*., 2012), and ALD (Litta, Hellstrom, Henkel, & Ostling, 2014; Litta *et al*., 2015).

Single crystalline of Tm_2O_3 films can be achieved by atomic oxygen assisted MBE growth method followed by ultra-high vacuum annealing at 800 ºC. The dielectric constant (~ 10.8) and leakage current density (~ 2 x 10^{-3} A cm^{-2}) improved after annealing process. The higher oxygen partial pressure may degrade the crystallinity due to SiO_x interface layers becoming thicker and cannot be removed by in-situ UHV annealing. Thus, large orientation distributions of mosaic structures were formed (Ji *et al*., 2011; Wang, Fang, *et al*., 2012; Wang, Ji, *et al*., 2012). The bandgap of Tm_2O_3 was determined to be 5.76 eV (Wang, Ji, *et al*., 2012).

Preferable (400)-oriented was formed by reactive sputtering by RTA at 800 ºC in oxygen ambient. According to XPS spectra, the energy of SiO_2 layers increased and energy of Tm_2O_3 films decreased for samples which endured RTA at 800 ºC. The surface roughness increased with RTA temperature due to crystallization during annealing. The samples annealed at 700 ºC have lower leakage current density compared to 800 ºC due to leakage paths along the grain boundaries (Pan & Yen, 2010a, 2010b). The 2 nm of TmSiO films can be formed without presence of SiO_x by ALD following by PDA at 750 ºC in nitrogen ambient. The silicate layer thickness increased with the PDA temperature. The capacitance density, EOT, and interface state density of TmSiO films improved after PDA process (Litta *et al*., 2014).

2.7.12 Ytterbium (Yb) oxide

Ytterbium oxide (Yb_2O_3) was selected as gate oxide in CMOS devices not only due to its high κ (~ 15), high energy band (> 5 eV) but also due to it being thermally stable with Si substrates because of its high Gibb free energy (Dakhel, 2009; Lin, Wu, Wu, & Lee, 2014; Pan & Huang, 2009; Tseng *et al*., 2011). Yb_2O_3 possesses high quality of interfaces with Si substrates with low interface trap density (2.4×10^{11} cm^{-2} eV^{-1}) and low fixed oxide charge density (2.8×10^{11} cm^{-2}) (Lin *et al*., 2014). The most preferable (222)-oriented of Yb_2O_3 were obtained by RTA at 800 ºC after reactive sputtering. However, intensity of SiO_2 layers increased at higher RTA temperature (800 ºC) due to maintain the Yb-silicate structures by the SiO_2 interface layers (Pan & Huang, 2009).

According to previous researches, Yb was also used as dopant for transition metal oxides. The Yb dopants were able to stabilize the cubic phase and improve leakage current in HfO_2 (Chen, Liu, Feng, Che, & Zhao, 2014). Yb also had low solid solubility and formed well grain boundaries in In_2O_3 film (Dakhel, 2010). Chen Shuai *et al.* (Chen *et al.*, 2014) reported that Yb may lead to crystallographic change from monoclinic to cubic phase of HfO_2. Monoclinic HfO_2 was stable at room temperature but cubic only existed at high temperature environment due to oxygen vacancies presence by compensated Yb charge states. The dielectric constant increased from 16.1 to 28.4 compared to un-doped HfO_2 (Chen *et al.*, 2014). Dakhel (Dakhel, 2009) reported that if the presence of Yb_2O_3, Mn_2O_3 did not crystallized it was because Mn ions diffused into the inter-grain boundaries either in amorphous Yb_2O_3 structures or crystalline Yb_2O_3 structures. At high concentrations of Yb-doped In_2O_3, non-crystalline structures were formed with larger lattice parameters due to larger ionic radius of Yb^{3+} than In^{3+}. The dielectric constants reached about 81.6 for 8.5 wt. % of Yb-doped In_2O_3 (Dakhel, 2010).

2.7.13 Lutetium (Lu) oxide

Lutetium oxide (Lu_2O_3) has high lattice energy (- 13871 kJ mol^{-1}) and large bandgap (5.5 eV). It was predicted to show good insulating property, thermal stability, hygroscopic immunity, and lower leakage current (Chan *et al*., 2008; Darmawan, Yuan, & Lee, 2006; Pan, Chen, & Jung, 2012). Previously, Lu_2O_3 films were deposited by reactive sputtering (Pan *et al*., 2012) and PLD (Chan *et al*., 2008; Darmawan *et al*., 2006).

Amorphous of Lu_2O_3 films can be achieved by PLD techniques followed by PDA at 600 ºC in nitrogen ambient. The leakage current density at 1 V was 2.6 x 10^{-5} A cm^{-2} with EOT of 1.1 nm (Darmawan *et al*., 2006). RTA at 900 ºC after reactive sputtering may cause Lu-silicate formation. It was shown by higher intensity of Lu-silicate peaks in XPS and lower intensity of Lu_2O_3 in XRD peak compared to RTA at 800 ºC. The dielectric constants (from 9.1 to 12.8) and breakdown voltage fields (from 3.4 MV cm^{-1} to 3.53 MV cm^{-1}) were improved by RTA process. The samples annealed at 800 ºC exhibited highest flatband voltage shift of about 2.93 V (Pan *et al*., 2012). For Lu_2O_3 films deposited by PLD, Lu-silicate were formed after PDA process. However, the lattice strains were decreasing when the PDA temperatures increased (Chan *et al*., 2008).

Combinations of superior properties of both La (high crystallization temperatures and high dielectric constant) and Lu (low hygroscopic and reactivity) were investigated by forming $LaLuO_3$ film (Triyoso, Gilmer, Jiang, & Droopad, 2008). $LaLuO_3$ has high κ (~30) and is thermally stable up to 1000 ºC. $LaLuO_3$ deposited by MBE still remain amorphous after RTA at 700 ºC and 900 ºC. However, $LaLuO_3$-silicate and interfacial layer were formed and increased with RTA temperatures. The leakage current density was increased after annealed at 900 ºC (Triyoso *et al*., 2008). For the $LaLuO_3$ deposited

by ALD, as-deposited films were smooth and remain amorphous up to 1000 ºC. The dielectric constants were improved from 17 to 30 after annealing process (Roeckerath *et al.*, 2008). For the La_2O_3 doped SiO_2 (LSO) films deposited by e-beam evaporation remained amorphous up to 800 ºC. Interfacial layer of SiO_2 were formed due to diffusion of oxygen atom towards Si substrates (Shi *et al*., 2007).

Compared to single La_2O_3 gate stack, La_2O_3/Y_2O_3 double gate stack able to reduce the SiO_2 and silicate layer formation (Ahmet *et al*., 2008). For CeO_x/La_2O_3 gate stacks, oxygen vacancies in La_2O_3 films can be filled with oxygen from CeO_x due to reduction reaction of CeO_x (Wong *et al*., 2012b). La was also doped in Hf oxide which was able to remain amorphous at higher temperature, lower defect densities and lower lattice mismatch with Si (Cheng, Qi, Zhang, Zhang, & Pan, 2012). For CeO_x and La_2O_3 stacking gate oxides, the Ce^{3+} ions were reduced from Ce^{4+} ions releasing oxygen which diffused into La_2O_3 films. Ce_xO_y was able to store or release oxygen and reduce the defects during La_2O_3 formation because of its good oxygen storage capacity. The CeO_x/La_2O_3 stacks of transistors have larger transconductance, smaller subthreshold slope and better hot carrier robustness compared to single La_2O_3 stack of transistor (Wong *et al*., 2012b).

2.8 Samarium oxide, Sm_2O_3 as alternative gate oxide

Sm_2O_3 is one of the promising candidate materials among rare earth oxides because of some outstanding properties such as high κ (7-22), high breakdown electric field (5-7 MV/cm), large bandgap (4.33 eV), low leakage current, large conduction offset with Si, high thermal stability, small frequency dispersion, low trapping rate, and low hygroscopic characteristic (Chen, Hung, *et al*., 2013; Chin *et al*., 2010; Dakhel, 2004a; Huang *et al*., 2011; Kao, Chen, *et al*., 2010; Kaya, Yilmaz, Kahraman, & Karacali, 2015;

Kaya, Yilmaz, Karacali, *et al*., 2015; Pan & Huang, 2010; Rozhkov *et al*., 1995; Rozhkov *et al*., 1998; Shalini & Shivashankar, 2005).

Among the high bandgap (> 5 eV) lanthanide REOs, Sm_2O_3 has the lowest flatband voltage (0.1 V) and lowest leakage current (1.1 x 10^{-8} A/cm^2) (Chin *et al*., 2010; Paivasaari *et al*., 2005). Even though the Ho_2O_3 has low leakage current density (1.2 x 10^{-8} A/cm^2) but its high flatband voltage (6.9 V) is not preferred (Chin *et al*., 2010; Paivasaari *et al*., 2005). Besides that, some researchers have shown that Sm_2O_3 films have lower leakage current density (2.5 x 10^{-6} A/cm^2) than La_2O_3 (0.9 x 10^{-4} A/cm^2) (Chin *et al*., 2010; Jo *et al*., 2006; Pan, Huang, You, & Yeh, 2008).

Among the lanthanide REOs, Sm_2O_3 has the second highest κ value and has a relatively large bandgap as shown in Fig. 2.4 (Chen, Hung, *et al*., 2013; Chin *et al*., 2010; Huang *et al*., 2011; Kaya, Yilmaz, Kahraman, *et al*., 2015; Kaya, Yilmaz, Karacali, *et al*., 2015; Pan & Huang, 2010). Sm_2O_3 is also predicted to be thermodynamically stable on Si substrates (Chen, Hung, *et al*., 2013; Kao, Chen, *et al*., 2010; Kaya, Yilmaz, Kahraman, *et al*., 2015; Kaya, Yilmaz, Karacali, *et al*., 2015; Pan & Huang, 2010; Pan *et al*., 2008). Moreover, Sm_2O_3 is less hygroscopic than La_2O_3 because it has a smaller ionic radius and is less electropositive as shown in Fig. 2.7 (Chin *et al*., 2010; Kaya, Yilmaz, Karacali, *et al*., 2015).

In previous works (Pan & Huang, 2010; Shalini & Shivashankar, 2005), Shalini and Shivashankar reported that Sm_2O_3 films deposited by MOCVD were strongly oriented due to the small lattice mismatch (0.6%) between cubic Sm_2O_3 and Si substrates. Rozhkov *et al.* reported that relatively high barrier energy (2.72 eV) and breakdown field (5-7 MV/cm) were obtained at Si- Sm_2O_3 interfaces (Rozhkov *et al*., 1995; Rozhkov *et*

al., 1998). Constantinescu *et al.* measured dielectric constants ranging from 14 to 16 (Constantinescu *et al*., 2012). A relatively low threshold voltage (0.79 V) and large mobility (6.25 cm^2/V s) were reported in Chen *et al.* work owing to the smooth interface surface formed between the Sm_2O_3 and indium-gallium-zinc oxide (IGZO) layers (Chen, Hung, *et al*., 2013). A dielectric constant as high as 20 was obtained from calculations by Kaya *et al.* (Kaya, Yilmaz, Kahraman, *et al*., 2015). The resistivity of Sm_2O_3 films deposited under various sputtering power and temperatures were varied from $1.1x10^8$ Ω^{-1} cm^{-1} to $2.5x10^6$ Ω^{-1} cm^{-1} (Kaya, Yilmaz, Karacali, *et al*., 2015).

2.9 Previous deposition methods of Sm_2O_3 films

According to previous works, the Sm_2O_3 films were deposited by both PVD and CVD methods as summarized in Table 2.1. Fig. 2.8 shows the summary of leakage current density – electrical breakdown field (*J-E*) characteristic of Sm_2O_3 films deposited by various previous methods. Sputtering was the most common deposition method. The Sm_2O_3 films were deposited by direct sputtering of Sm_2O_3 target or pure samarium target followed by post deposition annealing or oxidation. Some researchers deposited the Sm_2O_3 films by RF magnetron sputtering with Sm_2O_3 and or Sm targets (Huang *et al*., 2011; Kao, Chen, *et al*., 2010; Kaya, Yilmaz, Kahraman, *et al*., 2015; Kaya, Yilmaz, Karacali, *et al*., 2015; Pan & Huang, 2010) while only one researcher deposited the Sm_2O_3 films by DC magnetron sputtering with Sm target (Chen, Hung, *et al*., 2013). In Kaya *et al.* works (Kaya, Yilmaz, Karacali, *et al*., 2015), effects of sputtering power and substrate temperature on composition and structural quality of Sm_2O_3 films were proven. The smoothest and best crystallinity of Sm_2O_3 films were formed at 200 W sputtering power and a substrate temperature of 200 ºC.

Table 2.1: Summary of thickness, surface roughness, and interfacial layer characterization methods of Sm_2O_3 films deposited by various previous methods.

No.	Deposition methods	Thickness (nm)	RMS (nm)	Interfacial layer characterization methods	Ref.
1	ALD	50	1.2	-	(Paivasaari *et al*., 2005)
2	RF sputtering	7.5 - 8.2	0.19 - 0.37	XPS	(Pan & Huang, 2010)
3	DC sputtering	120	3.43 - 7.81	XPS	(F. H. Chen, M. N. Hung, *et al*., 2013)
4	RF sputtering	25	-	XPS	(Kao, Chen, *et al*., 2010)
5	MOCVD	120	3.9 - 7.9	-	(Shalini & Shivashankar, 2005)
6	PLD	61.4	5 - 10	SEM	(Constantinescu *et al*., 2012)
7	Thermal evaporation	122.2	-	-	(Dakhel, 2004a)
8	Vacuum evaporation	230 - 300	-	-	(V. A. Rozhkov *et al*., 1998)
9	RF sputtering	61	-	TEM	(S. Y. Huang *et al*., 2011)
10	RF sputtering	120	-	-	(Kaya, Yilmaz, Kahraman, *et al*., 2015)
11	RF sputtering	110 - 125	5.2 - 19.5	-	(Kaya, Yilmaz, Karacali, *et al*., 2015)

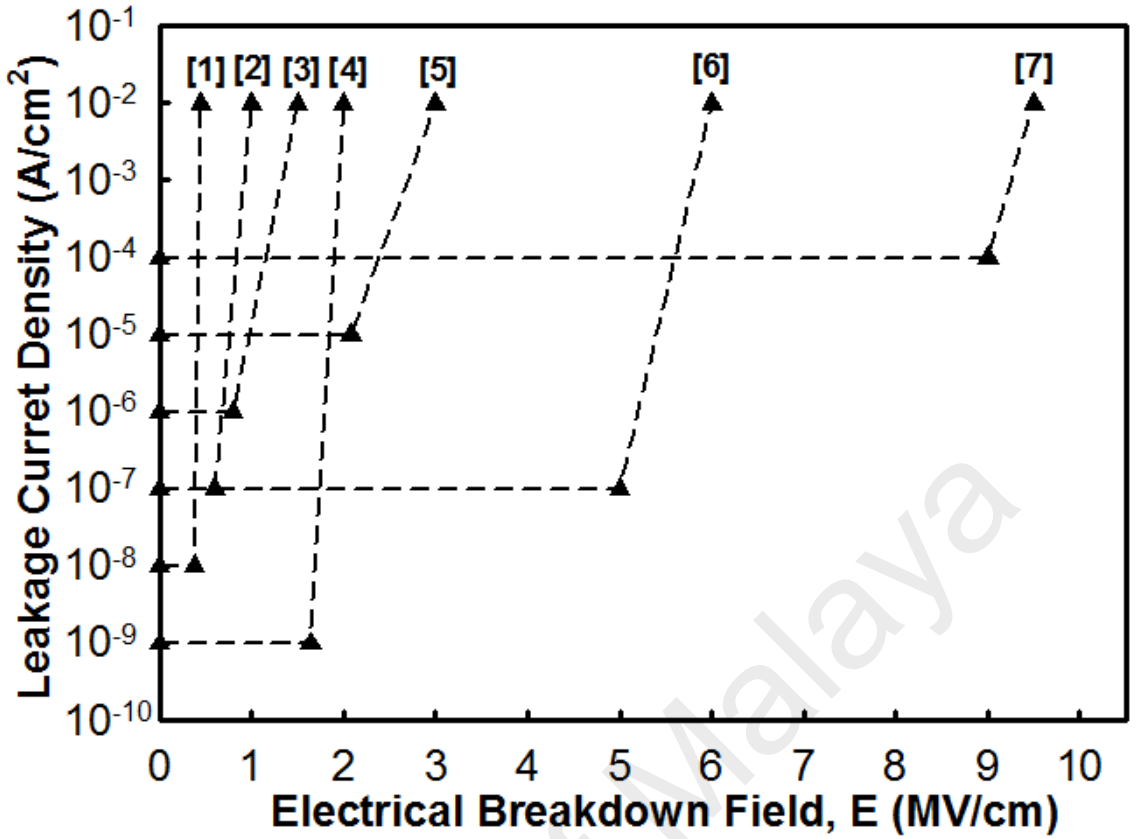

Figure 2.8: Summary of leakage current density – electrical breakdown field (*J-E*) characteristic of Sm_2O_3 films deposited by various previous methods.

References: [1] = Paivasaari *et al.*, 2005; [2] = Dakhel *et al.*, 2004; [3] = Constantinescu *et al.*, 2012; [4] = Huang *et al.*, 2011; [5] = Kaya *et al.*, 2015; [6] = Rozhkov *et al.*, 1998; [7] = Kao *et al.*, 2010.

Pan *et al.* concluded that RF magnetron sputtering was able to produce thin film (7 nm) with lower leakage current (10^{-7} Acm^{-2} at 1 V) (Pan *et al.*, 2010). Recently, some researchers proved that post deposition annealing (PDA) after RF magnetron sputtering can improve structural and electrical properties such as reduce leakage current, increase capacitance density, and reduce surface roughness (Henkel *et al.*, 2011; Pan *et al.*, 2008). In another study by Pan *et al.*, they reported that PDA can improve the electrical properties of Sm_2O_3 thin film on Si substrates. The optimum sample which is PDA at 700 ^{0}C which gives the highest dielectric constant and the lowest leakage current density while reducing the EOT values (Pan *et al.*, 2008).

Vacuum and thermal evaporation are another physical route of deposition methods (Dakhel, 2004a; Rozhkov *et al*., 1995; Rozhkov *et al*., 1998). In Rozhkov *et al.* works (Rozhkov *et al*., 1995; Rozhkov *et al*., 1998), Sm_2O_3 was evaporated onto Si substrates after thermal oxidation of samarium in air. The samarium was oxidized in air before evaporated on Si substrates. An effective dielectric constant of 42.7 was calculated from the Schottky current formula in Dakhel's work (Dakhel, 2004a). The Sm_2O_3 films can also be deposited by radio frequency-pulsed laser deposition (RF-PLD) which produced good quality and amorphous Sm_2O_3 films (Constantinescu *et al*., 2012). The laser ablation was involved in PLD where target material evaporated when irradiated by an intense laser beam and deposited on the substrate.

Besides that, highly crystalline Sm_2O_3 films with the low lattice mismatch had been grown by MOCVD using phenanthroline adducts of pentadionate complexes (Shalini & Shivashankar, 2005). In MOCVD, metal organic precursors are transported by carrier gas before decomposing and being deposited. The Sm_2O_3 films were also grown by ALD. The films produced by ALD had good electrical properties such as high κ (~ 29) and high bandgap (5 eV) (Henkel *et al*., 2011). In Paivasaari *et al.* work (Paivasaari *et al*., 2005), the 0.38 MV/cm^{-1} of breakdown field and $1.1x10^{-8}$ Acm^{-2} were reported for the Sm_2O_3 films deposited by ALD.

2.10 Role of nitrogen in gate oxide on Si substrate

In my work, not only samarium oxide thin film was formed but also samarium oxynitride. The incorporation of nitrogen within oxide systems was believed able to improve and enhance the performance of gate oxides. At first glance, replacing SiO_2 by the high κ oxides (Sm_2O_3) seems simple and straightforward. However, the electrical

properties of MOS are complicated by the involvement of low κ interfacial layers which are mostly not intentionally grown. The interfacial layers may limit the downscaling ability of *EOT* and downgrade the electrical performance of the gate oxide. Therefore, much research has been done to avoid or at least minimize the formation of low κ interfacial layers.

The incorporation of nitrogen within oxide systems is one of the viable methods which allow the improvement and enhancement of gate oxide performances (Buchanan, 1999; Cheng *et al*., 2006; Fenker *et al*., 2006; Hoffmann & Schmeisser, 2006; Karimi *et al*., 2014; Mian & Flora, 1999; Stathis & Zafar, 2006; Tessier *et al*., 2010). Nitride and oxynitride materials have attracted attention due to their interesting physical, chemical, optical, magnetic, and electrical properties (Chappe *et al*., 2007; Chappe *et al*., 2004; Chen *et al*., 2016; Diot, Larcher, Marchand, Kempf, & Macaudiere, 2001; Fenker *et al*., 2006; Tessier *et al*., 2010). Nitrogen also acts as a network former due to its higher valence (Wong & Gritsenko, 2002). It is believed that oxynitride can be used for bridging oxide and nitride and their interface to Si substrates (Wong & Gritsenko, 2002). A tighter and more linked structure may be produced if partial substitution of oxygen by nitrogen in the bonding network occurred (Lofaj, Satet, Hoffmann, & de Arellano Lopez, 2004). The physical properties such as density, hardness, Young's modulus, thermal expansion coefficient will be improved owing to property modification after introduction of N^{3-} within oxide anionic sub-networks (Diot *et al*., 2001; Kumar, Sundaresan, & Rao, 2011; Lofaj *et al*., 2004).

Oxynitride gate oxides have higher crystallization resistance and reliability because of incorporated nitrogen stabilizing the oxidized structures (Zhang, Lu, Onodera, & Maeda, 2007). Post annealing in N_2O gas may reduce the interface trap density by

passivation of excess interfacial carbon or silicon (Hoffmann & Schmeisser, 2006; Stathis & Zafar, 2006). Besides that, nitrogen in gate oxides acts as a good barrier to boron penetration from p^+ polysilicon (Mian & Flora, 1999; Tan, 2007). However, oxynitride also has some drawbacks such as reduced carrier mobility and enhanced electron trapping (Mian & Flora, 1999; Tan, 2007).

Previously, many oxynitride of high κ materials thin films such as $Ti_xO_yN_z$ (Chappe *et al*., 2007; Chappe *et al*., 2004), LaON (Sato *et al*., 2007), $SrTaO_2N$ (Masubuchi, Kawamura, Taniguchi, & Kikkawa, 2015), LiPON (Kim, Mun, Park, Jin, & Park, 2013), $Ta_xO_yN_z$ (Banakh, Csefalvay, Steinmann, Fenker, & Kappl, 2006; Cristea *et al*., 2015), $W_xO_yN_z$ (Nunez *et al*., 2015), $Nb_xO_yN_z$ (Fenker *et al*., 2006), $Hf_xO_yN_z$ (Cheng *et al*., 2006; Zhang *et al*., 2007) were investigated. These oxynitride of high κ materials were formed by either oxidation process or PDA in nitrogen-containing gases ambient such as NH_3, N_2O, or NO. The $Ti_xO_yN_z$ thin films displayed intermediate behavior between metallic TiN and insulator TiO_2 compounds (Banakh *et al*., 2006; Chappe *et al*., 2007). The $Ti_xO_yN_z$ thin films combine properties of metallic oxides (colour and optical properties) and nitrides (hardness, structural stability, oxidation, and wear resistance) (Banakh *et al*., 2006; Chappe *et al*., 2007; Nunez *et al*., 2015).

Kato *et al.* (Kato, Toyota, Jin, & Ono, 2008) reported that greater than a dielectric constant of 30 was achievable in $Ta_xO_yN_z$ film. TaN has lower resistivity which may reduce the contact resistance (Kim, Lee, Kim, & Kim, 2005). The Hf_xO_yN film has higher reliability and higher crystallization resistance than HfO_2 film owing to nitrogen in Hf_xO_yN film stabilizing the oxygen ions (Cheng, Chang-Liao, Wang, & Wang, 2004). The tunable N/O ratio leads to a large spectrum of compositions and microstructures leading to a range of potentially attractive properties (Chappe *et al.*, 2007; Cristea *et al*.,

2015; Fenker *et al*., 2006). It has been reported that devices with nitrogen profile of hydrogen nitrogen species (e.g., NH_3) were less reliable than non-hydrogen nitrogen species (e.g., N_2O or NO) (Lucovsky, Niimi, Koh, *et al.*, 1998; Lucovsky, Niimi, Wu, *et al*., 1998; Wong & Gritsenko, 2002). The introduction of N_2O and NO were more efficient in reducing the defects and increasing the reliability even though it may increase the thickness of gate oxide. It has been reported that the films oxidized or annealed in NO gas contained a higher nitrogen concentration than those in N_2O gas using the same process. Films grown or annealed in N_2O contained nitrogen concentration of less than 1 at. % (Carr & Buhrman, 1993; Carr, Ellis, & Buhrman, 1995; Ellis & Buhrman, 1996; Gusev *et al*., 1998; Gusev *et al*., 1997; Hegde, Maiti, & Tobin, 1997; Lu, Hussey, Graham, Cao, & Tay, 1996; Lu, Tay, Cao, & Pianetta, 1995; Wong & Gritsenko, 2002). The low concentration of nitrogen was desirable to control channel hot electron degradation effect at gate oxide/Si interface but was not able to efficiently reduce effect of boron penetration at poly-Si gate (Mian & Flora, 1999; Momose, Morimoto, Ozawa, Yamabe, & Iwai, 1994; Stathis & Zafar, 2006).

The incorporation of large amounts of nitrogen into the gate oxide may cause large flatband voltage and threshold voltage shifts, thus reducing electron mobility of the device (Joshi, Ahn, & Kwong, 1993; Ma *et al*., 1994; Mian & Flora, 1999; Momose *et al*., 1994; Pfiester *et al*., 1990; Tan, 2007). Hence, it is paramount to control the nitrogen concentration and its distribution. Therefore, many nitrogen-containing heating profiles were introduced and suggested by various researchers and scientists (Ellis & Buhrman, 1996; Gupta *et al*., 1998; Gusev *et al*., 1998; Lu, Gusev, Gustafsson, Brasen, *et al*., 1997; Lu, Gusev, Gustafsson, & Garfunkel, 1997; Lu *et al*., 1996; Lu *et al*., 1995; Mian & Flora, 1999).

CHAPTER 3

MATERIALS AND METHODOLOGY

3.1 Introduction

This chapter describes the materials used and the methodology employed in the present study. Fig. 3.1 presents an overview of this research via a flow chart. Fig. 3.2 shows a simple illustration of steps used for preparing sample in this research. Fig 3.3 shows an overview of characterization techniques employed in this research. This chapter mainly consists of three main parts:

(i) Materials,

(ii) Experimental procedures, and

(iii) Characterization techniques.

All materials and chemicals used in this work are enumerated and described. The descriptions of the materials are divided into four sub-groups.

(i) Substrate materials

(ii) Chemicals used in Si substrate and quartz tube cleaning process

(iii) Materials used in Sm and Al sputtering process

(iv) Materials used in thermal oxidation / oxynitridation process

The steps used in preparing the samples in this research are described in the experimental procedures section (Fig. 3.2):

(i) Si substrate cleaning

(ii) Sm thin film sputtering

(iii) Thermal oxidation / oxynitridation of sputtered Sm thin film on Si substrate in O_2 / N_2O gas ambient

(iv) MOS capacitor fabrication process via Al sputtering

Diverse characterization techniques employed in this work are presented in this chapter as well (Fig. 3.3). Physical, chemical, and electrical characterizations are explained. Physical and chemical characterization techniques include X-ray diffraction (XRD), Fourier transformed infrared (FTIR) spectroscopy analysis, Raman spectroscopy, high resolution transmission electron microscopy (HRTEM), energy dispersive X-ray (EDX) spectroscopy analysis, atomic force microscopy (AFM), and X-ray photoelectron spectroscopy (XPS). Besides that, capacitance–voltage (*C*-*V*) and current–voltage (*I*-*V*) measurement are carried out to analyze electrical properties.

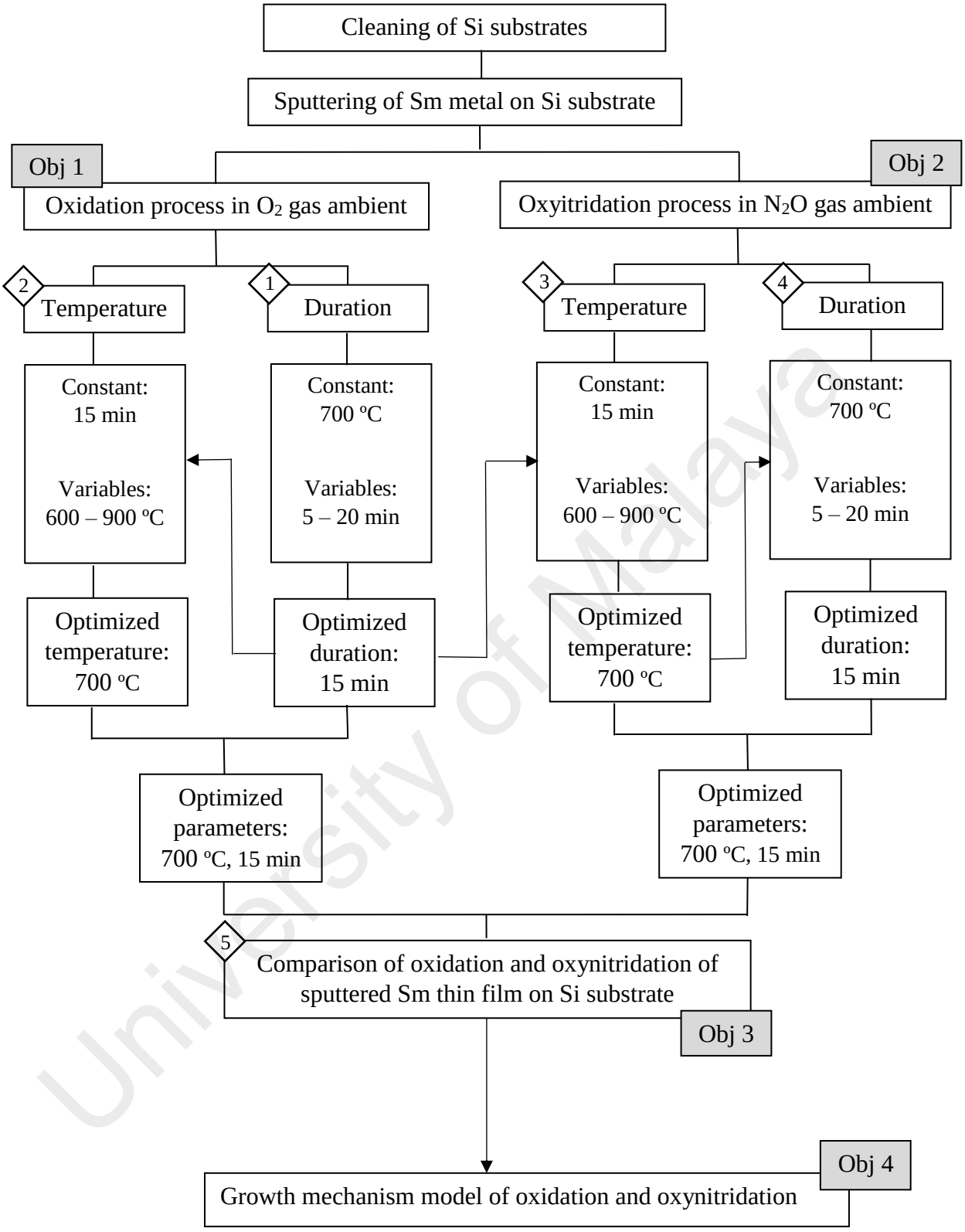

Figure 3.1: An overview of research methodology.

Notes:
(i) Obj 1, Obj, 2, Obj 3, and Obj 4 refer to the objectives numbered 1, 2, 3, and 4, respectively, in subsection 1.3 of Chapter 1.
(ii) Arabic numerals indicate the parameters that will be discussed in Chapter 4 and 5 sequentially.

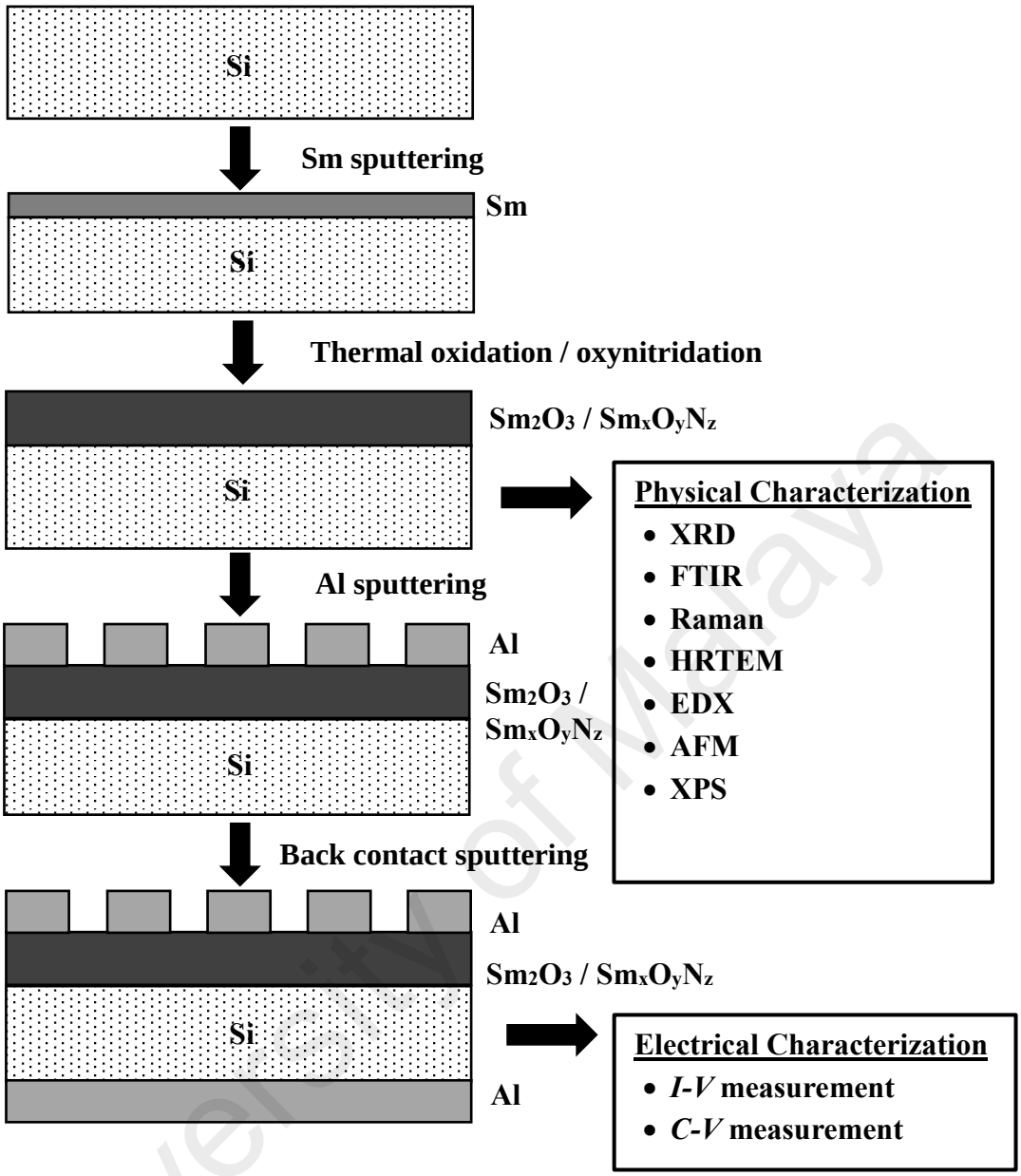

Figure 3.2: A simple illustration of steps used in preparing samples in this research.

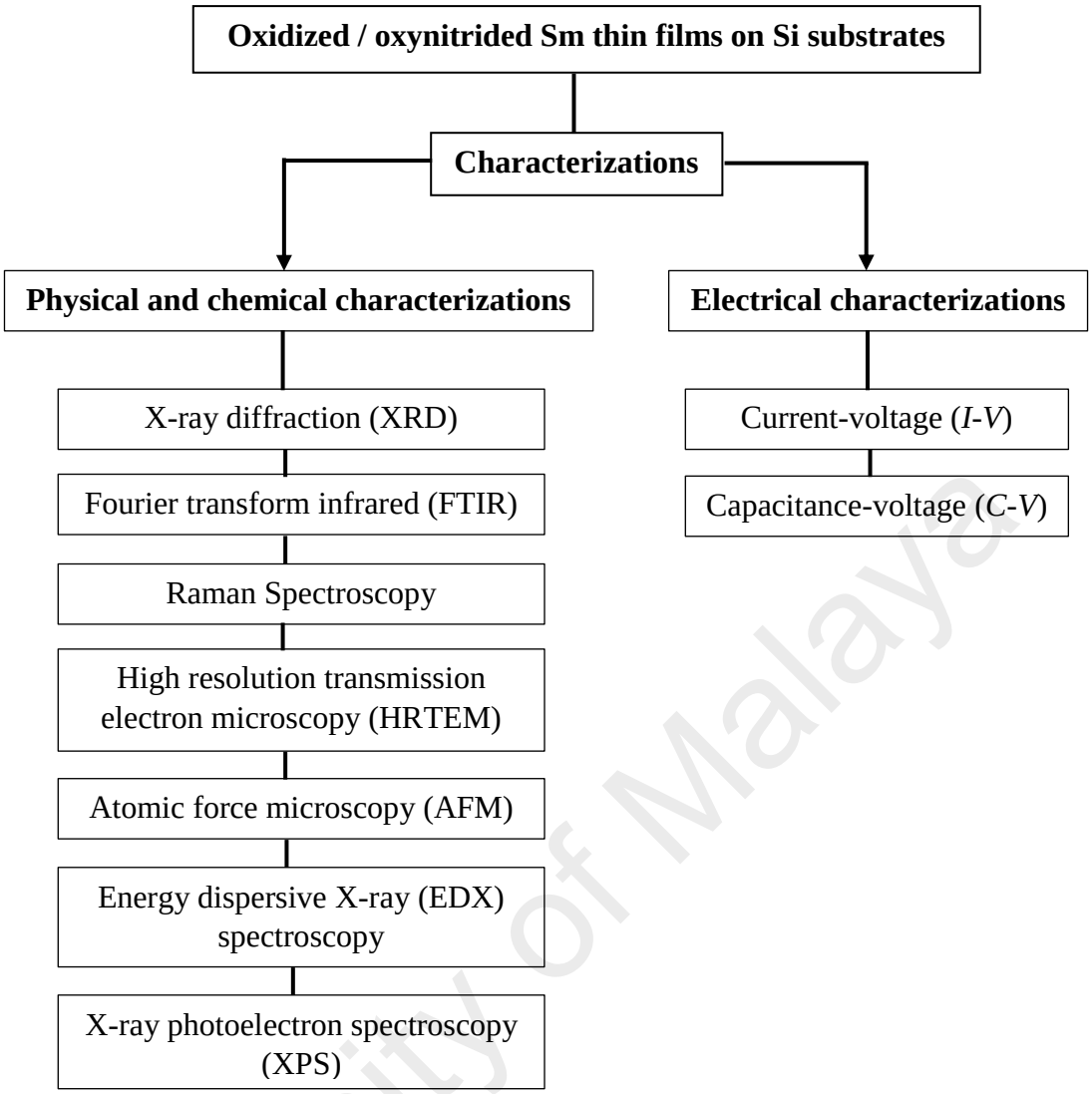

Figure 3.3: An overview of characterization techniques employed in this research.

3.2 Materials

3.2.1 Substrate Material

Si wafers were used as substrate materials. Si wafers were supplied by Meds Technologies Sdn Bhd. The Si wafers are *n*-type, (100)-oriented, 1 – 10 Ω cm of resistivity, and doped with phosphorus with a polished surface on one side.

3.2.2 Chemicals used in Si substrate and quartz tube cleaning process

The chemicals used in Si substrate and quartz tube cleaning are listed in Table 3.1 according to their chemical formula, assay percentages, supplier and Chemical Abstracts Service (CAS) numbers.

Table 3.1 List of chemicals used in Si substrate and quartz tube cleaning process

No	Chemical	Chemical Formula	Assay	Supplier / CAS No.
1	Hydrogen Peroxide	H_2O_2	30%	R&M Chemicals / 7722-84-1
2	Hydrogen Fluoride	HF	49%	R&M Chemicals / 7664-39-3
3	Hydrochloric Acid	HCl	37%	R&M Chemicals / 7647-01-0
4	Ammonia Hydroxide	NH_4OH	29%	R&M Chemicals / 1336-21-6
5	Acetone	$(CH_3)_2CO$	> 99%	R&M Chemicals / 67-64-1

3.2.3 Materials used in Sm and Al sputtering process

Argon gas, samarium target, and aluminum target were needed during Sm pure metal sputtering and metallization process. Acetone was used to clean the sputtering chamber. Table 3.2 is the details of the materials and chemicals for the sputtering process.

Table 3.2: List of the materials and chemicals for sputtering process.

No	Material	Chemical Formula	Supplier / CAS No.	Specification(s)
1	Samarium target	Sm	Kurt J. Lesker	Purity: 99.9% Diameter: 101.6 mm Thickness: 3.175 mm
2	Aluminium target	Al	Kurt J. Lesker	Purity: 99% Diameter: 101.6 mm Thickness: 3.175 mm
3	Argon gas	Ar	Gaslink / 7440-37-1	Purity: 99.99%
4	Acetone	$(CH_3)_2CO$	R&M Chemicals / 67-64-1	Purity: 99.99%

3.2.4 Materials used in thermal oxidation / oxynitridation process

The O_2, N_2O, and Ar gases were used during thermal oxidation / oxynitridation process. Table 3.3 gives the details of gases utilized in thermal oxidation / oxynitridation process.

Table 3.3: Gases utilized in thermal oxidation / oxynitridation process

No	Gas	Chemical Formula	Supplier / CAS No.	Purity
1	Oxygen	O_2	Gaslink / 7782-44-7	99.99%
2	Argon	Ar	Gaslink / 7440-37-1	99.99%
3	Nitrous oxide	N_2O	Gaslink / 10024-97-2	99.99%

3.3 Experimental Procedures

3.3.1 Si substrates cleaning process

Si wafers were cut into square shape with dimension of 1 cm x 1 cm using a diamond cutter. The Si wafers went through a series of cleaning processes. The cleaning processes include ultrasonic cleaning, standard procedure of Radio Corporation of America (RCA) cleaning, and HF dipping. The cleaning processes are described in Table 3.4.

Table 3.4: Cleaning process steps.

Process	Purpose	Procedures
Step 1 Ultrasonic cleaning	To remove physical and small particles from the substrate surface.	(i) The Si wafers were put in a sample holder and placed in a container which contained deionized (DI) water. (ii) The container was put into an ultrasonic bath for 10 min. (iii) Then, the Si wafers were rinsed with DI water.
Step 2 RCA-1	To remove organic contaminants from the substrate surface.	(i) The chemicals (NH_4OH : H_2O_2 : H_2O) were prepared with the ratio of 1:1:5. (ii) 100 ml of DI water was heated to 90°C on a hot plate. (iii) Once the temperature reached 90°C, 20 ml of NH_4OH was added into heated DI water. (iv) 20 ml of H_2O_2 was added into DI water when temperature decreased to 80°C. (v) The solution started to bubble after one minute. (vi) The Si wafers were soaked for 15 minutes and the temperature was maintained at 80°C. (vii) Then, the Si wafers were rinsed with DI water.

Table 3.4: Cleaning process steps. (continued)

Step 3 HF dipping	To remove native oxide from the substrate surface.	(i) Diluted HF solution was prepared with ratio 1:50 (HF : H_2O). (ii) The Si wafers were soaked in diluted HF solution for 10 seconds. (iii) After 10 seconds, the Si wafers were rinsed with DI water immediately.
Step 4 RCA-2	To remove metal ions from the substrate surface.	(i) The chemicals (HCl : H_2O_2 : H_2O) were prepared with the ratio of 1:1:6. (ii) 120 ml of DI water was heated to 90°C on a hot plate. (iii) Once the temperature reached 90°C, 20 ml of NH_4OH was added into heated DI water. (iv) 20 ml of H_2O_2 was added into DI water when temperature decreased to 80°C. (v) The solution started to bubble after one minute. (vi) The Si wafers were soaked for 15 minutes and the temperature was maintained at 80°C. (vii) Lastly, the Si wafers were rinsed with DI water and dried with air gun.

3.3.2 Sm thin films sputtering process

In this work, Sm thin films were deposited using a TF 450 physical vapour deposition (PVD) radio frequency (RF) sputtering system. Prior to sputtering, the sputter chamber, substrate holder, target holder, and shutter were cleaned with acetone. Then, the Sm target was fixed into the target holder while the cleaned Si wafers were placed on the substrate holder. Fig. 3.4 shows the sputtering system employed in this work. After locking the chamber, it was evacuated to a base pressure of 1.5×10^{-3} Pa. Then, inert Ar gas was introduced into the chamber and the RF power source was adjusted to 170 W. Before sputtering on Si substrates, pre-sputtering was done for about 3 minutes to remove

the native oxide on the Sm target surface. After pre-sputtering, the shutter was opened and Sm sputtering started at a working pressure of 3 x 10^{-3} Pa. The distance between the target and Si wafers was about 20 cm. A 150 nm of Sm thin film was sputtered on Si substrate for thermal oxidation process while a 20 nm of Sm thin film was sputtered on Si substrate for thermal oxynitridation.

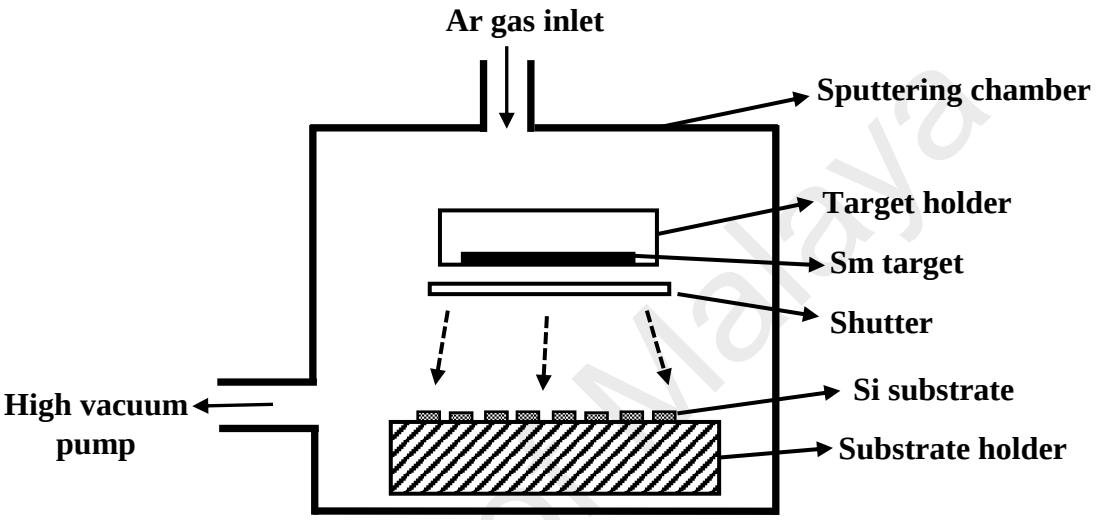

Figure 3.4: The working chamber of RF sputtering system used in this work

3.3.3 Thermal oxidation / oxynitridation of sputtered Sm thin film on Si substrate in O_2 / N_2O gas ambient

The thermal oxidation and oxynitridation processes were carried out in O_2 and N_2O gas ambient in a quartz tube which was placed in a horizontal tube furnace. Prior to the thermal oxidation and oxynitridation processes, the quartz boat and quartz tube were cleaned with diluted HF solution in order to avoid contaminants. Then, the quartz tube containing samples on a quartz boat was placed into a horizontal tube furnace as shown in Fig. 3.5. The section below describes the design of experiments (DOE):

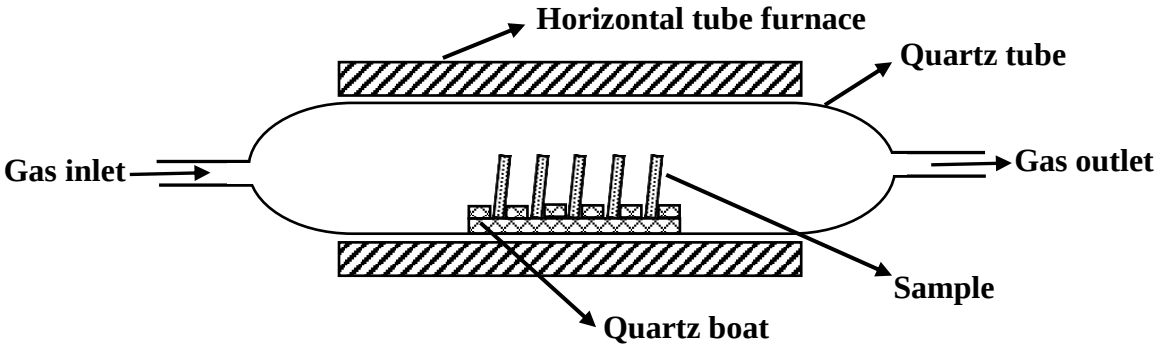

Figure 3.5: Setup for thermal oxidation / oxynitridation processes.

(i) Effects of thermal oxidation temperature on sputtered Sm thin film on Si substrate

The samples were heated up to one of a set of temperatures (600, 700, 800, and 900 °C) in Ar gas with a heating rate of 10 °C/min. Once the set temperature was reached, O_2 gas was introduced into the quartz tube with a flow rate of 150 ml/min for 15 min. The oxidized samples were then cooled down to room temperature in Ar gas ambient.

(ii) Effects of thermal oxidation duration on sputtered Sm thin film on Si substrate

The samples were heated to 700 °C in Ar gas with a heating rate of 10 °C/min. Once it reached 700 °C, O_2 gas was introduced into the quartz tube with a flow rate of 150 ml/min for one of a set of durations (5, 10, 15, and 20 min). The oxidized samples were then cooled down in Ar gas.

(iii) Effects of thermal oxynitridation temperature on sputtered Sm thin film on Si substrate

The samples were heated up to one of a set of temperatures (600, 700, 800, and 900 °C) in Ar gas with a heating rate of 10 °C/min. Once set temperature was reached, N_2O gas was introduced into the quartz tube with flow rate of 150 ml/min for 15 min. The oxynitrided samples were then cooled down in Ar gas.

(iv) Effects of thermal oxynitridation duration on sputtered Sm thin film on Si substrate

The samples were heated to 700 °C in Ar gas with a heating rate of 10 °C/min. Once reached 700 °C, N_2O gas was introduced into the quartz tube with a flow rate of 150 ml/min for one of a set of durations (5, 10, 15, and 20 min). The oxynitrided samples were then cooled down in Ar gas.

3.3.4 MOS capacitor fabrication process via Al sputtering process

The oxidized and oxynitrided samples were used to fabricate MOS capacitors in order to do electrical characterization. A 100 nm thick Al layer was deposited on both top and bottom of the sample by sputtering. The Al sputtering is similar with the Sm sputtering process as shown in Fig. 3.4. The base pressure, working pressure, RF power, distance between substrate the target, and argon gas flow rate were regulated at 1.5×10^{-3} Pa, 3×10^{-3} Pa, 170 W, 20 cm, and 25 cm^3/min, respectively. Before sputtering on the samples, pre-sputtering was done for about 3 minutes to remove the native oxide on the Al target surface. After the pre-sputtering process, the shutter was opened and Al layer was sputtered on the top of the sample. The same procedures were repeated for back contact metallization on the bottom of the samples.

3.4 Characterizations Techniques

3.4.1 XRD Analysis

XRD is a technique to identify the atomic or molecular structure of polycrystalline compounds which is a common technique used to characterize crystallinity of thin films (Escoubas, Brillet, Mesarotti, Raymond, Thomas, & Morin, 2008; Terasawa, Akimoto, Mizuno, Ichimiya, Sumitani, Takahashi, Toriumi, 2005). The diffraction process of X-ray is described by Bragg's law.

$$\lambda = 2d \sin\theta \qquad \text{(Equation 3.1)}$$

where λ is the wavelength of radiation beam (nm), d is the interplanar spacing in a crystal (nm), and 2θ is the angle between the diffracted and the transmitted beams (°). Since most of materials were not a single crystal, diffraction pattern is useful to identify various possible orientation of crystalline compounds. From the diffraction pattern, not only the atomic or molecular structure can be obtained, but also its composition, phases, and state of polycrystalline compounds.

The oxidized and oxynitrided Sm thin films were characterized by PANalytical Empyrean X-ray diffractometer (XRD) system in a scan range of 2θ = 10 – 90 ° and operating at 40 kV and 30 mA with a scan rate of 0.02° per second. Copper (Cu K_α) with wavelength (λ) of 0.15406 nm was used as X-ray source was used to identify crystallinity of oxidized and oxynitrided Sm thin films. A diffraction pattern plot (intensity of X-ray against angle 2θ) for each sample was obtained after they were scanned.

The crystallite size (D) and microstrain (Ɛ) due to crystal defects such as dislocations can be evaluated from XRD peak broadening (Venkateswarlu, Bose, &

Rameshbabu, 2010). The crystallite size (D) and microstrain (Ɛ) can be extracted through three methods: (1) simplified integral breadth method, (2) Fourier method, and (3) double Voigt method. The average value rather than the crystallite size distribution is given by the simplified integral breadth method among these methods (Herrmann, Forter-Barth, Kempa, & Krober, 2009; Mittemeijer & Welzel, 2008; Mote, Purushotham, & Dole, 2011; Santra, Chatterjee, & Sen Gupta, 2002; Vives, Gaffet, & Meunier, 2004). Basically, simplified integral breadth method consists of two basic approaches: (1) Debye-Scherrer analysis and (2) Williamson-Hall (W-H) analysis (Mittemeijer & Welzel, 2008; Mote *et al.*, 2011).

For the Debye-Scherrer analysis, Scherrer equation was used to estimate the crystallite size of Sm_2O_3 (Mote *et al.*, 2011; Venkateswarlu *et al.*, 2010). The crystallite size, *D* from Scherrer equation was given by:

$$D = \frac{K\lambda}{\beta_D cos\,\theta} \qquad \text{(Equation 3.2)}$$

where λ is the wavelength of the radiation, *K* is a constant, which is equal to 0.9, β_D was the peak width at half maximum intensity, and θ is the peak position.

The Williamson-Hall (W-H) analysis uses the broadening of multiple peaks to estimate crystallite size and microstrain. Apart from the crystallite size, lattice strain was also another independent factors that contribute to total peak broadening (Mote *et al.*, 2011; Venkateswarlu *et al.*, 2010; Zak, Majid, Abrishami, & Yousefi, 2011). Strain-induced broadening due to crystal distortion and imperfections was given by:

$$\mathcal{E} = \beta_S / 4\ tan\ \theta \qquad \text{(Equation 3.3)}$$

where β_S was the peak width at half maximum intensity and θ was the peak position. From Eq. 3.2 and 3.3, it is clear that peak width from the strain varies as *tan* θ (integral breadth of Gaussian component) whereas crystallite size varies as 1/*cos* θ (integral breadth of Lorentzian component) (Mittemeijer & Welzel, 2008; Mote *et al*., 2011; Zak *et al*., 2011). For the W-H analysis, assuming that crystallite size and strain contributions to peak broadening were independent and both have Cauchy-like profile (convolution of Gaussian and Lorentzian profile), the peak broadening was the sum of the Scherrer equation (Eq. 3.2) and strain-induced broadening (Eq. 3.3) (Mittemeijer & Welzel, 2008; Miyazaki, 2002; Mote *et al*., 2011; Venkateswarlu *et al*., 2010; Zak *et al*., 2011). Hence, sum of Eq. 3.2 and 3.3 yields:

$$\beta_{hkl} = \beta_D + \beta_S \qquad \text{(Equation 3.4)}$$

$$\beta_{hkl} = \frac{K\lambda}{D\ cos\theta} + 4\varepsilon\ tan\theta \qquad \text{(Equation 3.5)}$$

By rearranging the equations, W-H equation was given by

$$\beta_{hkl} cos\theta = \frac{K\lambda}{D} + 4\varepsilon\ sin\ \theta \qquad \text{(Equation 3.6)}$$

3.4.2 FTIR Analysis

The FTIR spectroscopy is a measurement technique to identify the presence of functional groups by obtaining an infrared spectrum of absorption or emission of a material (Grill & Neumayer, 2003; Schmitt & Flemming, 1998). The FTIR provides quantitative and qualitative analysis for organic and inorganic samples. The high spectral resolution data represents the intensity of light as a function of the position of the moveable mirror in an interferometer. A mathematical technique called the Fourier

Transform, then transforms the raw data into the spectrum of the sample, the optical signal, as a function of the wavenumber.

In this research, the FTIR analysis was conducted by using the Perkin Elmer Spectrum 400 Fourier Transform infrared (FTIR) spectrometer. The scanning range was 1300 – 400 cm^{-1} and transmittance mode was employed.

3.4.3 Raman Analysis

In Raman analysis, laser light is utilized as electromagnetic radiation, which contains an oscillating electric field that interacts with a molecule through its polarizability (Bernard, Goff, Thi, & Detorresi, 1993; Fernandes, Salome, & da Cunha, 2009; Kerr, Li, Canepa, & Sommer, 2007). The ability of electron cloud interacting with an electric field determines the polarizability. The radiation may be reflected, absorbed or scattered. The chemical and structural information were provided by the shift in wavelength of the inelastically scattered radiation. In this research, the Raman analysis was conducted using a Horiba Xplora One Raman spectrometer which is used to measure the chemical bonding stability upon thermal oxidation and oxynitridation processes. The scanning range was 0 - 4000 cm^{-1}.

3.4.4 HRTEM Analysis

HRTEM is a microscopy technique in which a high energy beam of electron is transmitted through an ultra-thin sample (Danterroches, 1984; Sinclair, 1985). The interaction between transmitted electrons and sample will produce an image. The image is magnified and focused onto an imaging device. High resolution makes it suitable for

imaging materials on the atomic scale. The HRTEM is able to simultaneously provide information in real space (in the imaging mode) and reciprocal space (in the diffraction mode).

Prior to HRTEM imaging, the cross sectioned film was prepared by lamella preparation (Helios NanoLab 650). Platinum (Pt) was deposited on surfaces of samples to protect the surface from ion bombardment damage caused by focused ion beam. In this research, the cross sectioned film was analyzed with a TECNAI G2 F20 high resolution transmission electron microscope (HRTEM). The microscope had accelerating voltage from 20 to 200 kV and standard magnification from 22 x to 930 kx. The illumination system consisted of a field emission gun with a Schottky Field emitter electron source. There were condenser lens, condenser apertures (C1 and C2), objective aperture (OA) and selective aperture (SA). A computerized stage with unique eccentric specification for maximized tilt of 30 ° with double tilt holder. The evacuation system was fully interlock differentially pump column with turbo molecular pump and oil-free pumping system for ultra clean evacuation. The ultimate pressure was 2.7 x 10^{-5} Pa (sample chamber). Images were acquired using SC1000 ORIUS CCD camera. CCD chip in this camera provides maximum resolution of 4008 x 2672 pixels with 14-bit dynamic range. The SC1000 ORIUS supports frame rates of more than 14 frames per second at 4x binning. This high frame rate is ideal for locating suitable sample segments directly on screen. The thickness of the oxide and interfacial layer were measured.

3.4.5 EDX analysis

In this research, EDX (Oxford Instrument X-Max^N 80T SDD detector) analysis was used in conjunction with HRTEM. The EDX analysis characterizes the elemental composition of materials by detecting emitted x-rays during bombardment by an electron beam. Both elemental composition of individual points and lateral distribution of elements can be determined by the EDX analysis. The EDX detector measures the relative abundance of emitted x-rays versus their energy by separating the characteristic X-rays of different elements into an energy spectrum. A typical EDX spectrum is plotted as X-ray counts versus energy (keV).

3.4.6 AFM Analysis

AFM is a technique which uses a sharp cantilever tip interacts with the sample surface sensing the local forces between the molecules of the tip and surface of the sample (Bhushan & Dandavate, 2000; D. W. Wang, Tsau, Wang, & Chow, 1995; Rugar & Hansma, 1990). The AFM not only provides image in three-dimensional topography, but also provides various types of surface measurements and atomic scale of height information with minimum sample preparation. The cantilever deflects towards the surface due to the attractive force between the surface and the tip when the tip approaches the surface. The cantilever deflections towards or away from the surface was detected by the laser beam. The surface measurements such as root-mean-square (RMS), average roughness (R_a), and surface topography images were generated in the computing system.

In this research, surface topography and the RMS of oxidized and oxynitrided Sm thin films were analyzed using a Veeco D3100 atomic force microscopy (AFM) in noncontact mode, with 1 μm x 1 μm scanned surface areas.

3.4.7 XPS Measurements

XPS is a technique which is used for investigating the surface chemistry of materials (Fadley, 2010; Levasseur, Vinatier, & Gonbeau, 1999; Opila *et al.*, 1999; Sharma, Tripathi, & Shripathi, 2009; Watts, 1994). It provides information from the top 10 nm of a sample with a spatial resolution from 3 μm to a few hundred micrometers. The composition and electronic state of the sample were investigated by utilizing photo-ionization and kinetic energy distribution analysis of the emitted photoelectrons. The ionization and the emission of a core (inner shell) electron occurr when a photon is absorbed by an atom. The photoelectron spectrum was generated and recorded by the electron energy analyzer.

Generally, the chemical compositions of the films were acquired from both survey and narrow scan. The survey scan was run with energy of 280 eV for 10 min to determine the elemental chemical states. The core-level spectra of six elements were detected. They were Sm 3*d*, Si 2*p*, O 1*s*, N 1*s*, and C 1*s*. After that, narrow scan was run with energy of 112 eV for 5 min to scan through each binding energy of the six elements. The detected C 1*s* peak was due to the carbon-based residues and contaminants on the surface. The binding energy of 284.6 eV was used as a reference to compensate for the shifting effect of the XPS spectra. Prior to deconvolution of XPS spectra, the linear background and surface charge were corrected by using CasaXPS software.

3.4.8 *I-V* Measurement

In this research, the current-voltage (*I-V*) measurements were conducted using a BPW-800 8" probe station along with a Keithley 4200 semiconductor characterization system (SCS). The sweep range and frequency were set to 0 - 20V and 50 Hz, respectively. The obtained *I-V* plot was converted to leakage current density versus electrical breakdown field (*J-E*). From the *J-E* plot, the current density at various electrical fields can be determined.

The current-voltage (*I-V*) measurement results were transformed into *J-E* plot. The *E* value was obtained from

$$E = (V_g - V_{fb})/t_{ox} \qquad \text{(Equation 3.7)}$$

where V_g is the gate voltage, V_{fb} is the flatband voltage, and t_{ox} is the oxide thickness (Kurniawan, Cheong, *et al*., 2011; Kurniawan, Wong, *et al*., 2011; Y. H. Wong & Cheong, 2011a, 2012a, 2012b). Two step oxide breakdowns were revealed in all characterized MOS capacitors. It was due to either one layer (Sm_2O_3 or IL) was pre-maturely broken down (E_S) at a lower electrical field. Another layer will block the carrier until it was broken down electrically (E_H) at a higher electrical field. The instantaneous increment of the leakage current density at E_S was relatively small and defined as a soft breakdown. For E_H, the instantaneous increment was larger and defined as hard breakdown method (Y. H. Wong & Cheong, 2011a, 2012a, 2012b; Depas, Nigam, & Heyns, 1996).

3.4.9 High Frequency of *C-V* Measurement

The same BPW-800 8" probe station along with the Keithley 4200 semiconductor characterization system (SCS) as mentioned above was used for capacitance-voltage (*C-V*) measurements. Both forward bias (from inversion to accumulation) and reverse bias (from accumulation to inversion) were swept by linear DC voltage ramp. This means that the bias sweep was run at - 20 V to + 20 V and + 20 V to - 20 V with sweep rate of 0.1 V per second. From *C-V* measurements, several characteristics can be acquired such as dielectric constant, flatband voltage, oxide capacitance, effective oxide charge, interface trap density, slow trap density, and total interface trap density.

CHAPTER 4

RESULTS AND DISCUSSION: THERMAL OXIDATION

4.1 Introduction

This chapter presents and discusses the experimental results of the physical, chemical, and electrical characterizations of the thermally oxidized sputtered Sm thin films on Si substrate. This chapter consists of two main parts: (i) effects of oxidation duration at 700 ^{o}C on sputtered Sm thin film on Si substrate and (ii) effects of oxidation temperature for 15 min on sputtered Sm thin film on Si substrate.

4.2 Effects of oxidation duration on sputtered Sm thin film on Si substrate

4.2.1 Physical and chemical properties

4.2.1.1 XRD analysis

Fig. 4.1 shows the XRD patterns of the oxidized samples for different durations (5 min, 10 min, 15 min, and 20 min). Three strong peaks at 28°, 69°, and 76° were detected in all samples which belong to the cubic phase of silicon (c-Si) (111), c-Si (004), and c-Si (331), respectively. These peaks were confirmed by Inorganic Crystal Structure Database (ICSD) with reference code 98-001-6569. The cubic phase of Sm_2O_3 (c-Sm_2O_3) was revealed at various diffraction angles of 17.6°, 19.9°, 38.9°, 46.4°, 47.2°, 54.4°, 56.4°, 58.2°, 61.8°, 74.6°, and 75.4° corresponding to the (002), (112), (233), (152), (334), (154), (226), (444), (064), (138), and (257) planes, respectively. These peaks were confirmed by ICSD with the reference code of 98-004-0475. According to the XRD results, it was observed that the peak intensities at 38.9°, 47.2°, 54.4°, 56.4°, 58.2°, and 74.6°, increased when the samples were oxidized within time period ranging from 5 min to 10 min but

decreased beyond 10 min of oxidation, as shown in Fig. 4.2. The peak intensity of Sm_2O_3 may have decreased due to the formation of an interfacial layer (samarium silicate, $Sm_xSi_yO_z$). It may be caused by the diffusion of oxygen from Sm_2O_3 film to the Si substrate during extended time (15 and 20 min) (Lim, Cheong, & Lockman, 2011; Tamboli, Puri, & Puri, 2010; S. Wang, Liao, Liu, & Liu, 2015). Thus, the peak becomes broader because of changes of intensity.

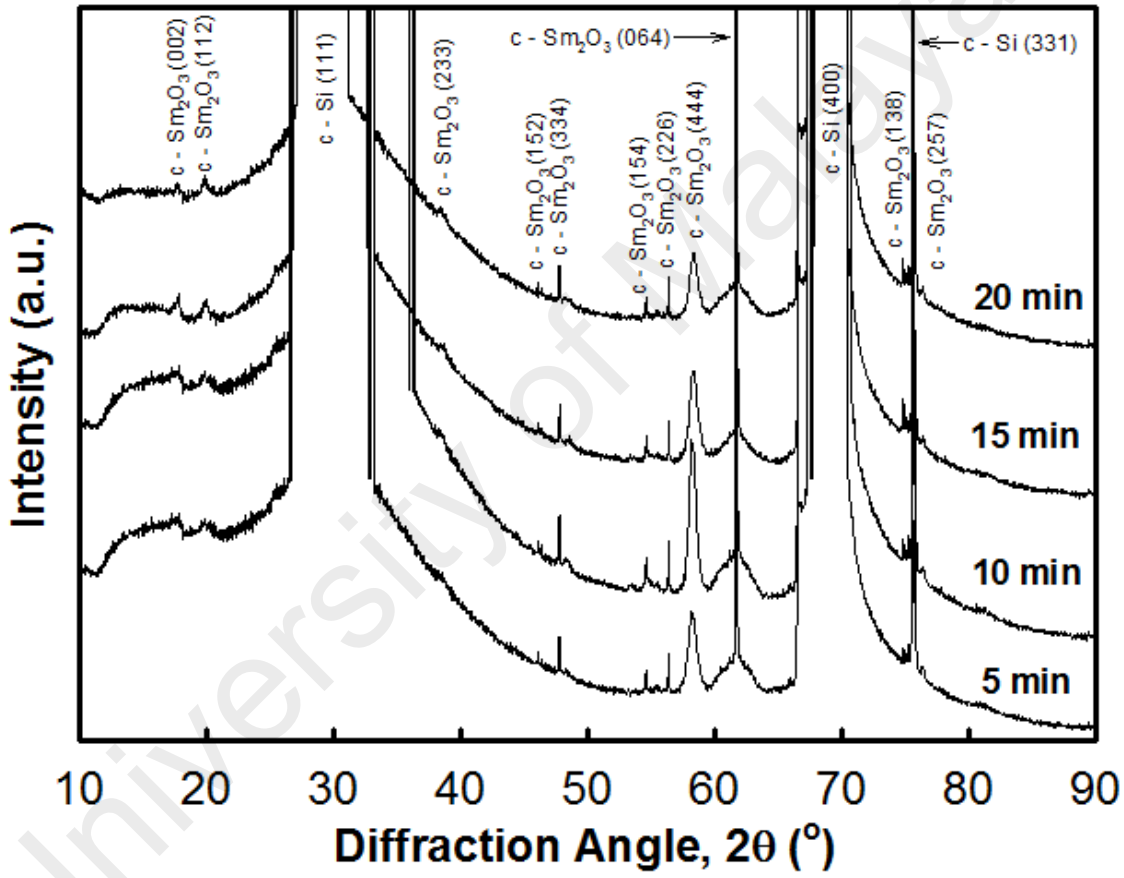

Figure 4.1: XRD patterns of oxidized samples at various oxidation durations (5 min, 10 min, 15 min and 20 min).

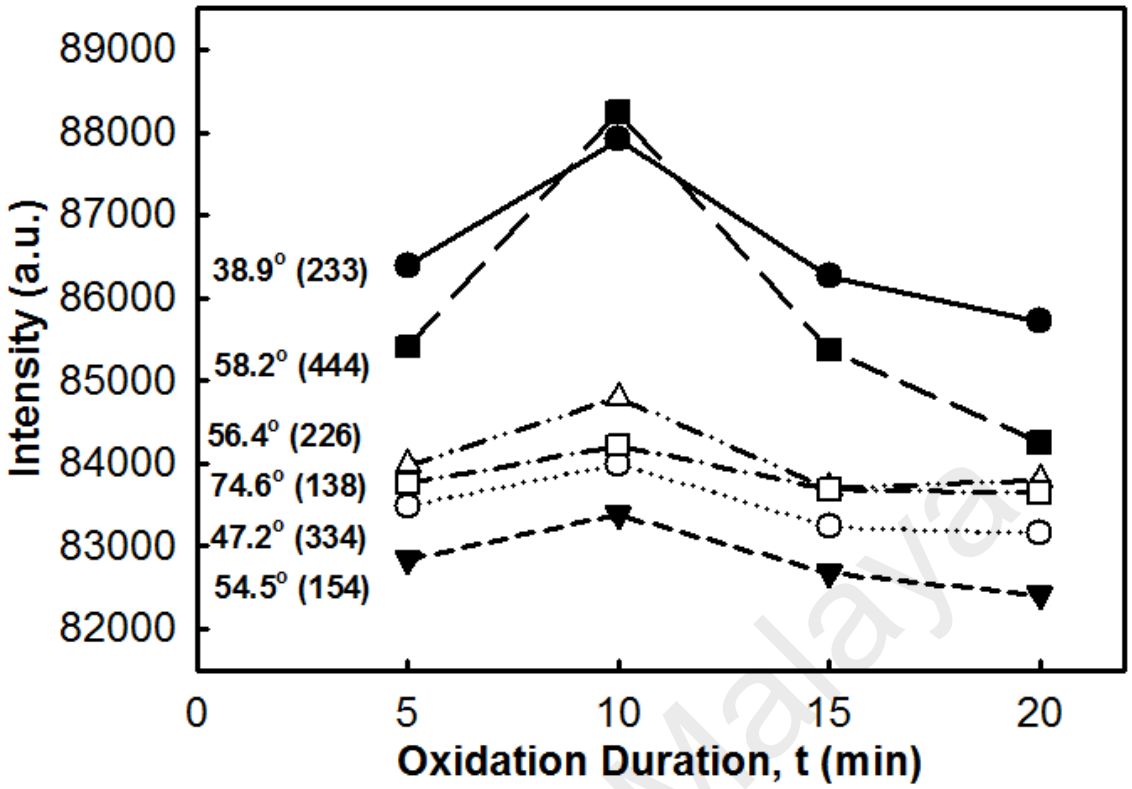

Figure 4.2: Intensities of Sm_2O_3 (233), (334), (154), (226), (444), and (138) at 38.9°, 47.2°, 54.5°, 56.4°, 58.2°, and 74.6°, respectively as a function of oxidation duration (5 min, 10 min, 15 min and 20 min).

For Scherrer analysis, the average crystallite size of the Sm_2O_3 was calculated from all peak positions. The average crystallite sizes of Sm_2O_3 for 5 min, 10 min, 15 min, and 20 min were 15.95 nm, 11.38 nm, 11.58 nm, and 15.13 nm, respectively (Fig. 4.3). These values were close to previous reported range of values which deposited by RF sputtering (Kaya, Yilmaz, Kahraman, & Karacali, 2015). It was shown that crystallite sizes of 10 min and 15 min gave smaller differences or distribution of size which may be due to more homogenous or well distributed crystallite size. Since the Scherrer equation only gives a lower bound of crystallite size plus the microstrain was not taken into account, the W-H analysis was conducted (Venkateswarlu *et al.*, 2010)

.

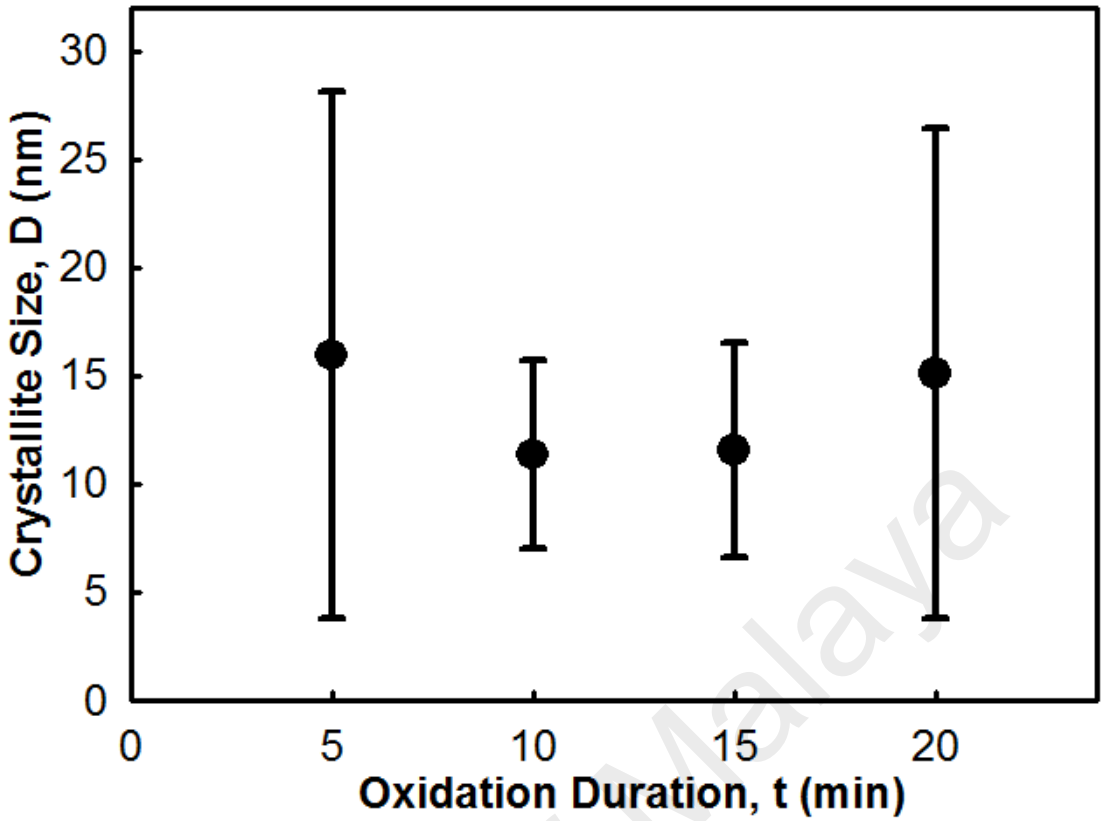

Figure 4.3: Calculated crystallite sizes by the Scherrer equation of Sm_2O_3 as a function of oxidation durations (5 min, 10 min, 15 min and 20 min).

A $\beta_{hkl} \cos \theta$ versus 4 $\sin \theta$ graph (Fig. 4.4) was plotted based on Eq. 3.6. Five points with goodness of fit (r^2) of ~ 0.9 were obtained from the distribution of values. $\mathcal{E}$ is the gradient of the graph while $K\lambda/D$ is the y-intercept of the graph and D can be calculated from the $K\lambda/D$. Based on the W-H analysis, the crystallite size of Sm_2O_3 decreased from 13.71 nm to 13.42 nm when the oxidation duration increased from 5 min to 10 min but, the crystallite size increased from 13.42 nm to 19.54 nm after extending the oxidation duration to 20 min. The microstrain of Sm_2O_3 for 5 min, 10 min, 15 min, and 20 min were 0.0363, 0.0358, 0.0364, and 0.0393. Both crystallite sizes and microstrain are shown in Fig. 4.5. The calculated crystallite sizes of Sm_2O_3 by both the Scherrer equation and W-H analysis did not have the same value and/or trend. However, the 10 min sample has the smallest crystallize size in both calculations.

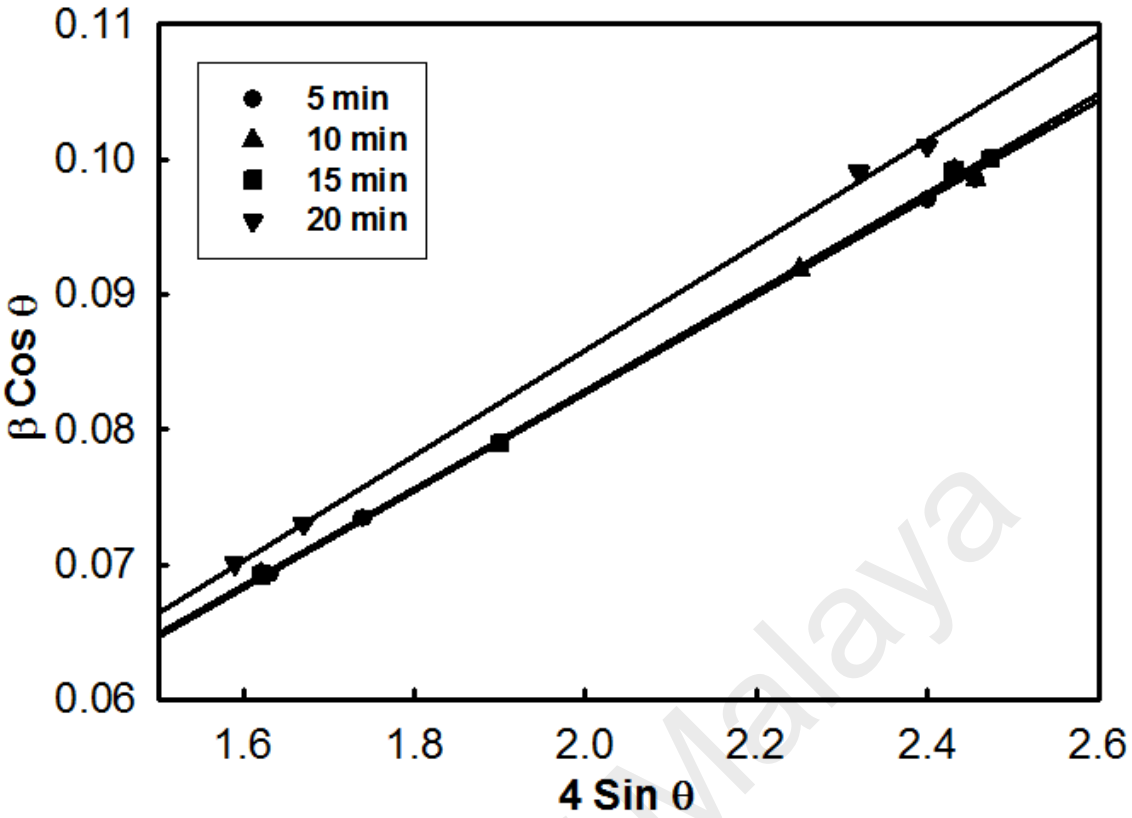

Figure 4.4: W-H plot of oxidized samples for various oxidation durations (5 min, 10 min, 15 min, and 20 min).

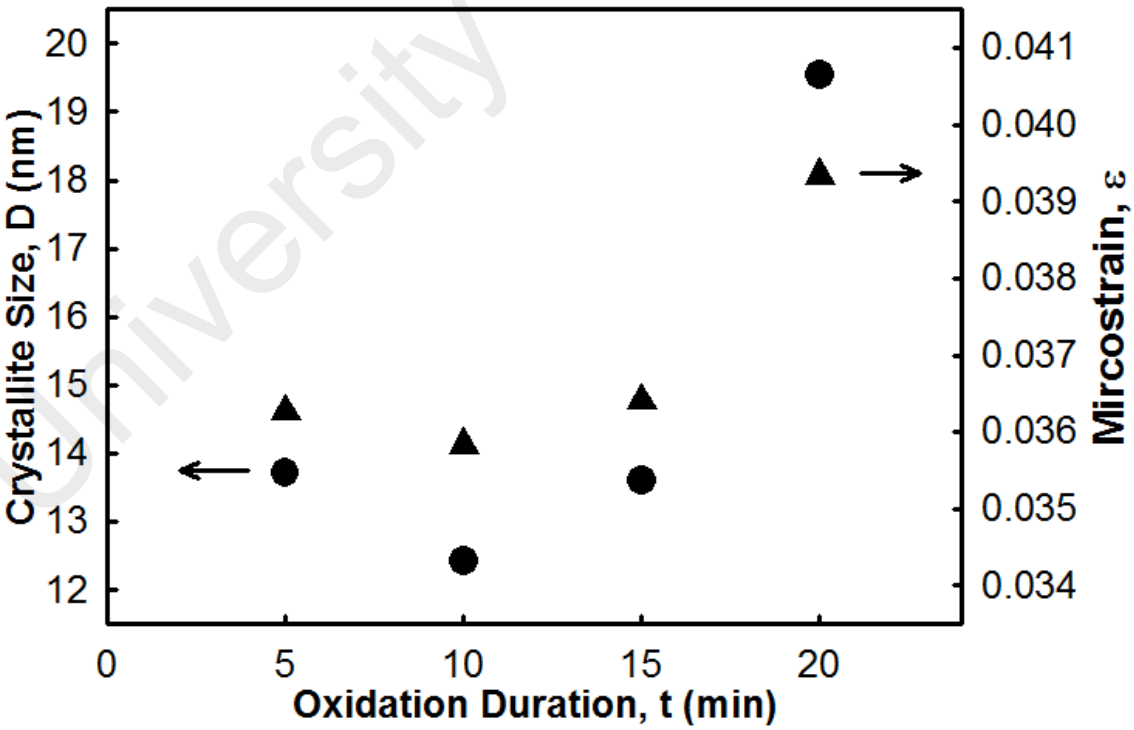

Figure 4.5: Relationship of calculated crystallite size and microstrain from W-H plot as a function of oxidation duration (5 min, 10 min, 15 min and 20 min).

4.2.1.2 FTIR analysis

Fig. 4.6 shows the FTIR transmittance spectra (700 - 400 cm^{-1}) of Sm sputtered on Si substrate and the thermally oxidized samples for different durations. The Si - Si vibration mode band was located at 567 cm^{-1} in all samples. The Si - Si peak shifted as oxidation duration increased. For 5 min sample, Sm - O vibration mode was detected at 403 cm^{-1} (Hussein *et al*., 2003), 416 cm^{-1} (Hussein *et al*., 2003; Ruiz-Gomez *et al*., 2014), 425 cm^{-1} (Hussein *et al*., 2003; Ismail, 1995), 437 cm^{-1} (Hussein *et al*., 2003; Ismail, 1995), 447 cm^{-1} (Hussein *et al*., 2003; Kusrini, Arbianti, Sofyan, Abdullah, & Andriani, 2014), 458 cm^{-1} (Hussein *et al*., 2003; Kusrini *et al*., 2014), 472 cm^{-1} (Kusrini *et al*., 2014; Ruiz-Gomez *et al*., 2014), 482 cm^{-1} (Hussein *et al*., 2003; Ruiz-Gomez *et al*., 2014), and 501 cm^{-1} (Hussein *et al*., 2003). At 501 cm^{-1}, the peak became sharper when the oxidization duration was increased from 5 min to 20 min. The peaks at 416 cm^{-1}, 425 cm^{-1}, and 458 cm^{-1} shifted as the oxidation duration increased. For both 437 cm^{-1} and 447 cm^{-1}, the peaks shifted and broadened as the oxidation duration increased. The intensity of 403 cm^{-1} decreased as the oxidation duration increased. For 472 cm^{-1} and 482 cm^{-1}, the peaks became sharper when the oxidation duration increased from 5 min to 10 min but became broadened after extending the oxidation duration. A similar phenomenon also occurred in the XRD results. The broadening and shifting of the peaks may be due to the formation or growth of interfacial layers which matched with inferences from the XRD results.

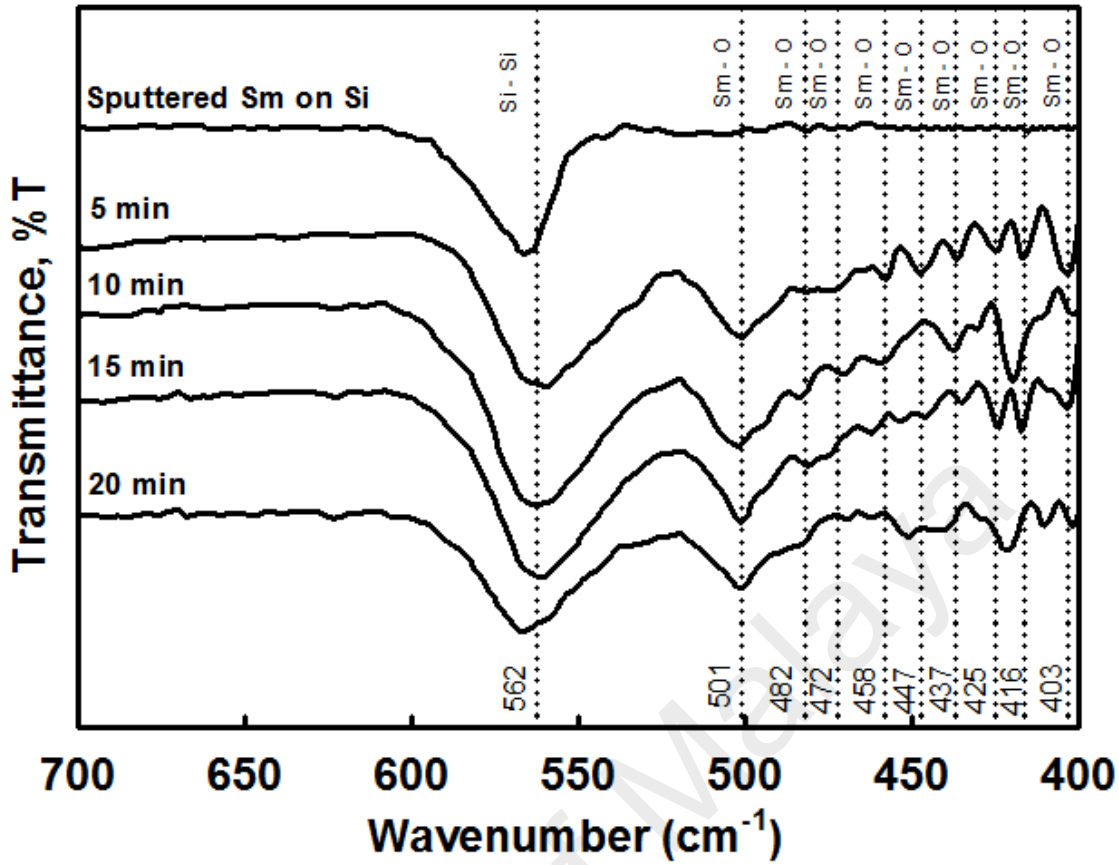

Figure 4.6: Transmittance spectra of oxidized samples for various durations (5 min, 10 min, 15 min, and 20 min).

4.2.1.3 Raman analysis

The Raman results for all oxidized samples are shown in Fig. 4.7. The peak at 520 cm^{-1} is assigned to the silicon substrate (Y. H. Wong & Cheong, 2011b). The peaks at 101 cm^{-1} (S. Jiang, Liu, Lin, Li, & Li, 2013), 111 cm^{-1} (S. Jiang *et al*., 2013), 120 cm^{-1} (S. Jiang *et al*., 2013), 145 cm^{-1} (S. Jiang *et al*., 2013), 168 cm^{-1} (Mandal, Sarkar, Deb, & Chakrabarti, 2014; S. Jiang *et al*., 2013), 177 cm^{-1} (S. Jiang *et al*., 2013), 238 cm^{-1} (Hongo, Kondo, Nakamura, & Atou, 2007; Mandal *et al*., 2014; S. Jiang *et al*., 2013), and 408 cm^{-1} (Hongo *et al*., 2007; Mandal *et al*., 2014; S. Jiang *et al*., 2013) are assigned to Sm_2O_3. Fig. 4.8 shows the intensities of mentioned peaks as a function of oxidation temperature and the 15 min sample had the highest intensity. However, this result did not match with the XRD results which recorded that 10 min sample has the highest intensities. This

phenomenon may be caused by high surface selectivity with about 100 nm sampling depth of the Raman analysis (Cuesta, Dhamelincourt, Laureyns, Martinez-Alonso, & Tascon, 1998; Lespade, Marchand, Couzi, & Cruege, 1984). According to the reports (Cuesta *et al.*, 1998; Lespade *et al.*, 1984), the Raman laser only penetrates about 100 nm depth of the film. Better crystallinity of the 15 min sample was detected at a near to surface region. This inference can be supported by a lower RMS of the 15 min sample (section 4.2.1.5) and both samples have almost the same range of crystallite size distribution as inferred in the Scherrer calculations. There are unknown peaks at 245 and 477 cm^{-1}, since they were neither belong to Sm_2O_3 nor Si, thus they were inferred to the formation of interfacial layer as inferred in the FTIR analysis.

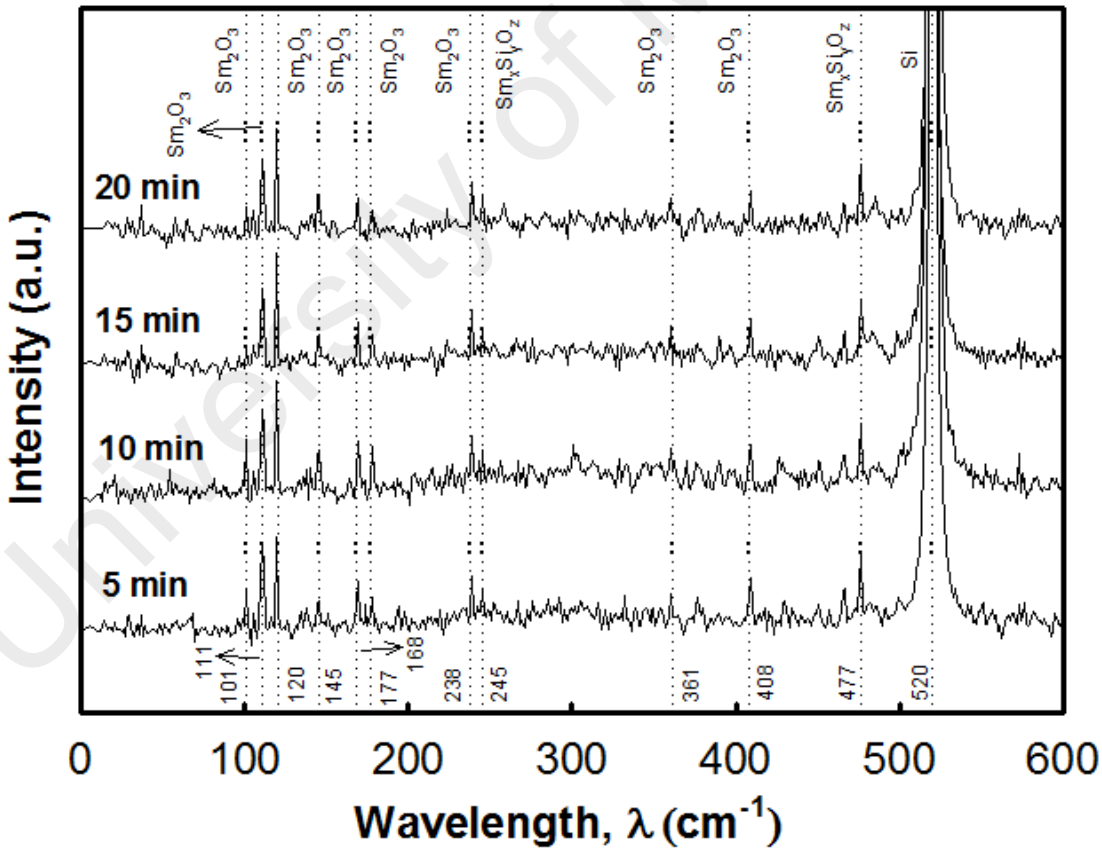

Figure 4.7: Raman spectra of oxidized samples for various durations (5 min, 10 min, 15 min, and 20 min).

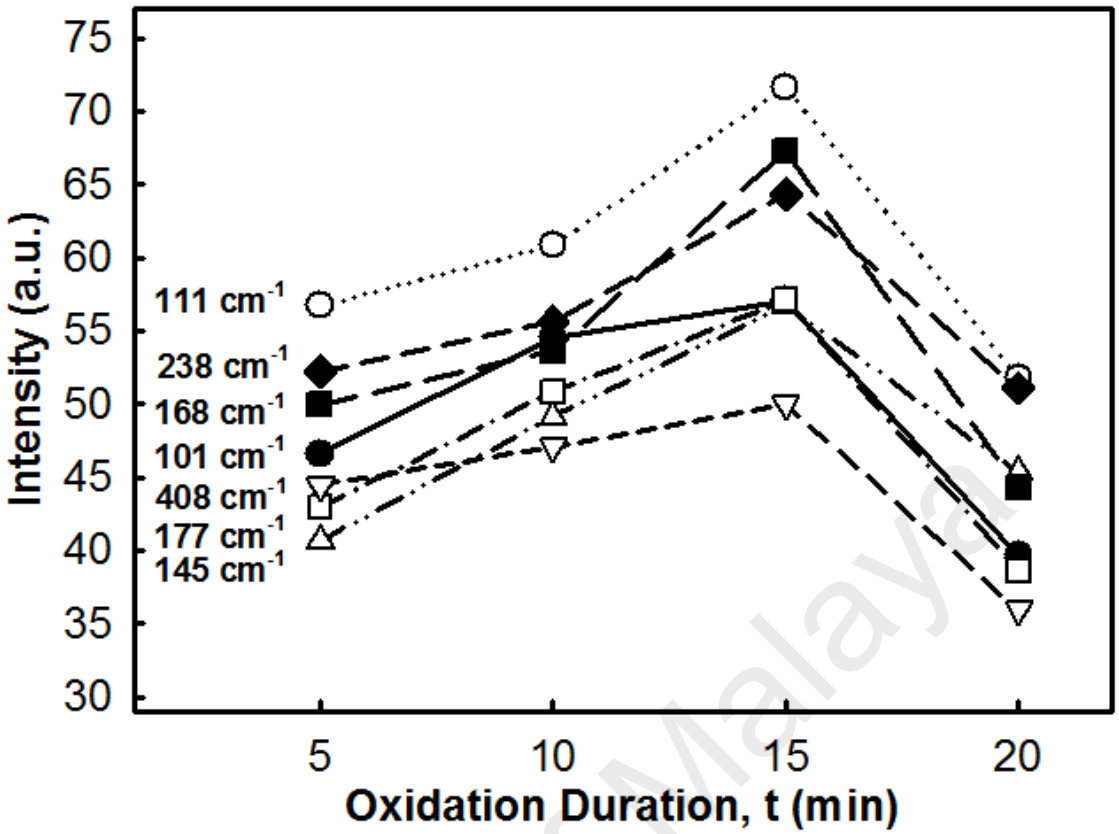

Figure 4.8: Intensities of Sm_2O_3 at 101 cm-1, 111 cm-1, 145 cm-1, 168 cm-1, 177 cm-1, 238 cm^{-1} and 408 cm-1 as a function of oxidation duration (5 min, 10 min, 15 min, and 20 min).

4.2.1.4 HRTEM and EDX analysis

Fig. 4.9 shows the EDX line scan of composition analysis of the 15 min sample. The inset shows the cross sectional HRTEM images of the 15 min sample. The total oxide layer thickness was 150 nm. It can be seen that not only Sm_2O_3 film was formed but an Sm-O-Si interfacial layer between Sm_2O_3 film and Si substrate was formed too. The presence of the Sm-O-Si interfacial layer in the EDX matched with the inference from the XRD, FTIR, and Raman analysis which inferred the formation of interfacial layer in between Sm_2O_3 film and Si substrate.

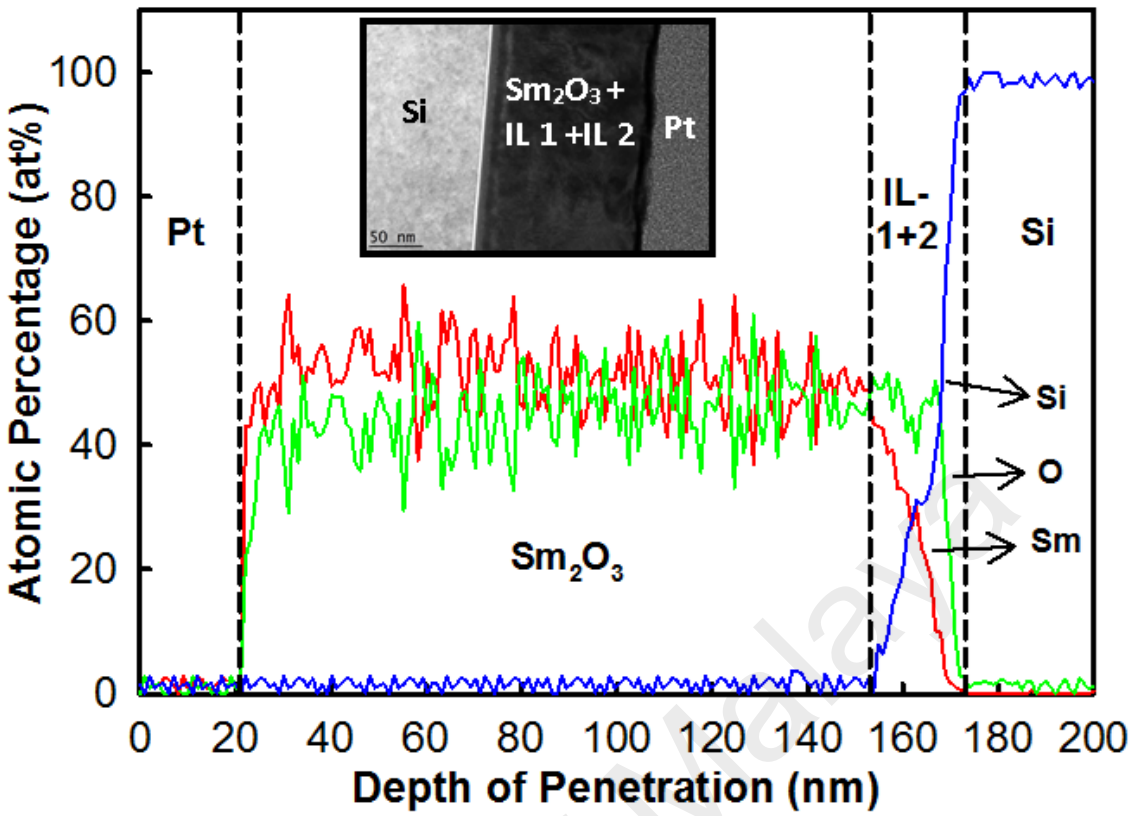

Figure 4.9: EDX composition analysis of 15 min sample. Pt was used as protective layer during lamella preparation before HRTEM and EDX analysis. The inset shows the cross sectional HRTEM image of the 15 min sample.

4.2.1.5 AFM analysis

Fig. 4.10 shows the two-dimensional surface topography of oxidized samples by atomic microscopy force (AFM). The scanned area was 1 μm x 1 μm. The 15 min sample had the smoothest surface (2.3 nm) among the samples (Fig. 4.11). The surface was smoother than deposited films of previous works which was 3.9 nm (MOCVD) (Shalini & Shivashankar, 2005), 5 nm (RF-PLD) (Constantinescu, Ion, Galca, & Dinescu, 2012), 3.34 nm (co-sputtering) (V. A. Rozhkov, Goncharov, & Trusova, 1995), and 5.2 (co-sputtering) (Kaya, Yilmaz, Kahraman, *et al.*, 2015). The fluctuation of the surface height will affect the local electrical field of the samples. The electrical field at the peak of surface is bigger than electrical field at the valley (Zhao, Wang, Lu, Palasantzas, & De Hosson, 1999). The reconstruction of grains and misalignment of crystallite domains caused grain clustering (dotted line in Fig. 4.10(a), (b), & (d)) to occur which contributed

to a rougher surface (Chabinyc *et al.*, 2007). The higher RMS (10 min) was observed during the process of grain reconstruction. During the extended time (20 min), the grains grew and become bigger (Chen, Hung, *et al.*, 2013; Pan & Huang, 2010). Thus, it was shown that the consolidation and formation of grains were most desirable at 15 min.

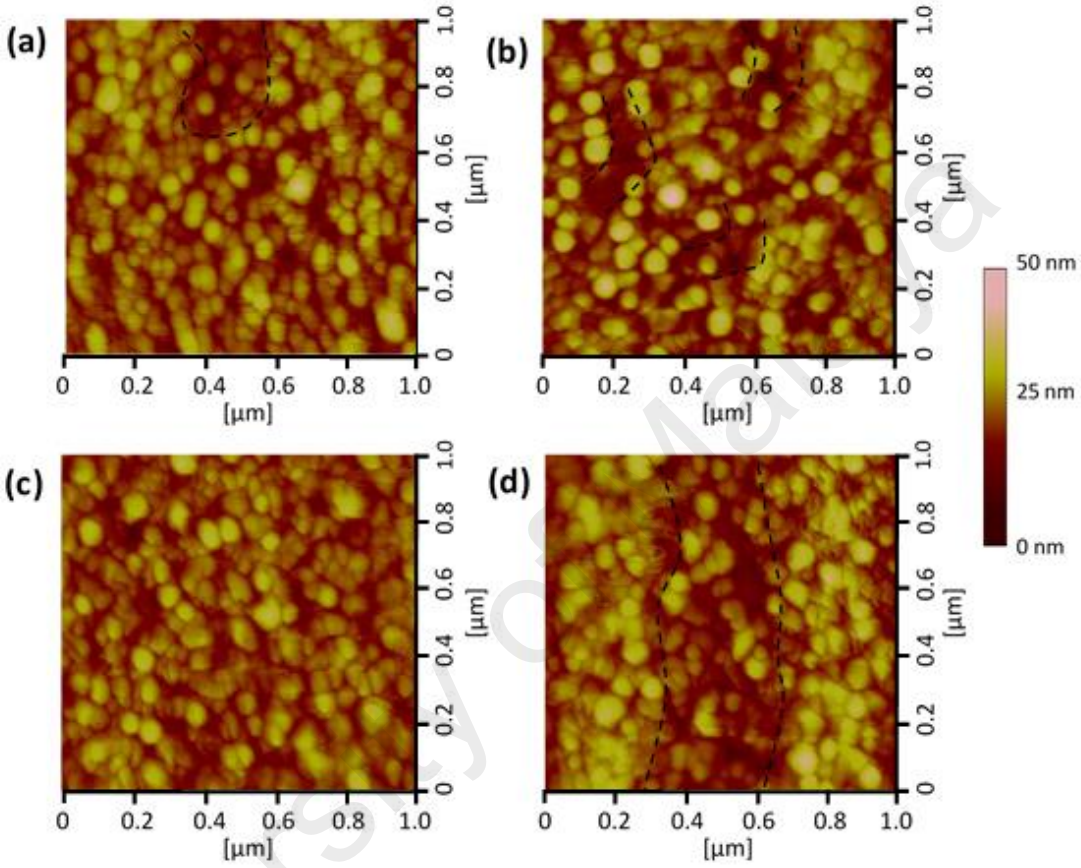

Figure 4.10: Two-dimensional surface topography of oxidized samples for various durations: (a) 5 min, (b) 10 min, (c) 15 min, and (d) 20 min.

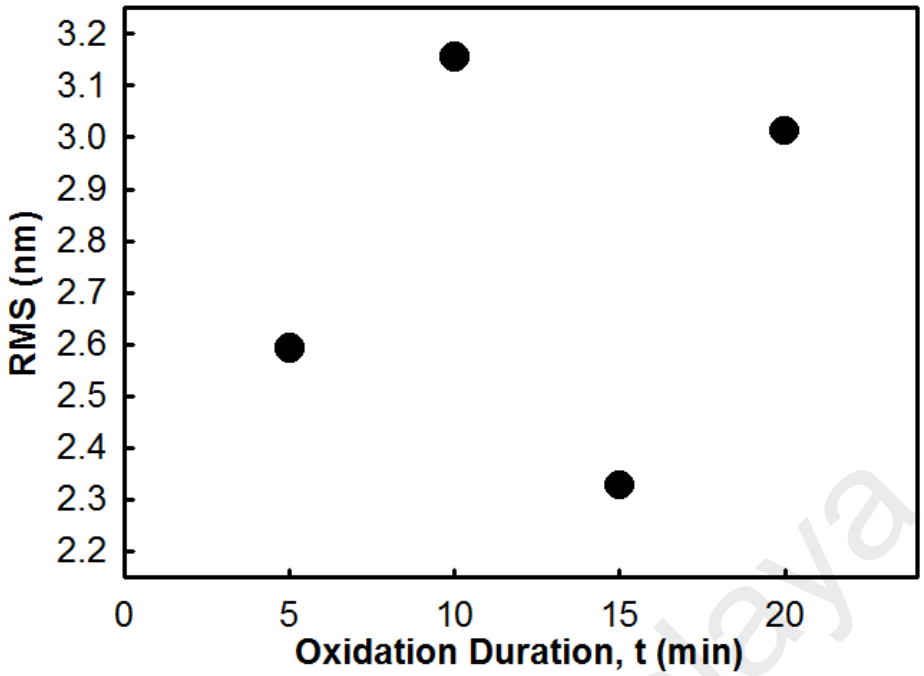

Figure 4.11: RMS values of oxidized samples for various durations (5 min, 10 min, 15 min, and 20 min).

4.2.2 Electrical properties

4.2.2.1 *J-E* characteristic

Fig. 4.12 shows the leakage current density-electric field (*J-E*) characteristic of investigated samples. The 5 min, 15 min, and 20 min samples, have almost the same *J* values. However, the 15 min sample has the highest E_H among them. Surface roughness may contribute as a factor affecting the electrical breakdown field in samples (Tak, Kim, Park, Lee, & Lee, 2009; Zhao, Wang, Lu, Palasantzas, & De Hosson, 1999; Meuris *et al*., 1992). The 15 min sample was the smoothest and had the highest electrical breakdown field. High roughness and large grain size may lead to a lower electrical breakdown field than low roughness and small grains (Meuris *et al*., 1992; Zhao, Wang, Lu, Palasantzas, & De Hosson, 1999). From the *J-E* measurements, time-zero dielectric breakdown (TZBD) reliability tests had been done at room temperature (25 °C). The cumulative failure percentage of 100 capacitors were presented in Fig. 4.13. According to the plot, the 15 min samples had the highest reliability.

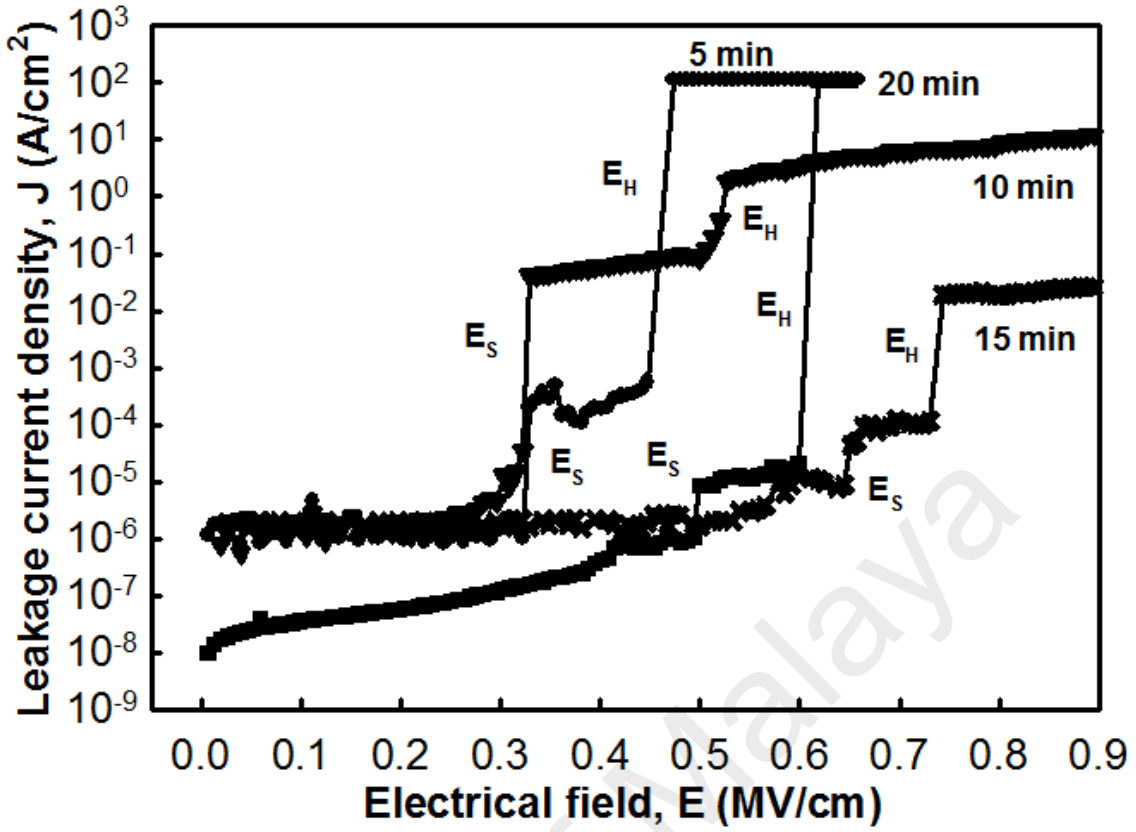

Figure 4.12: *J-E* characteristic of oxidized samples for various durations (5 min, 10 min, 15 min, and 20 min).

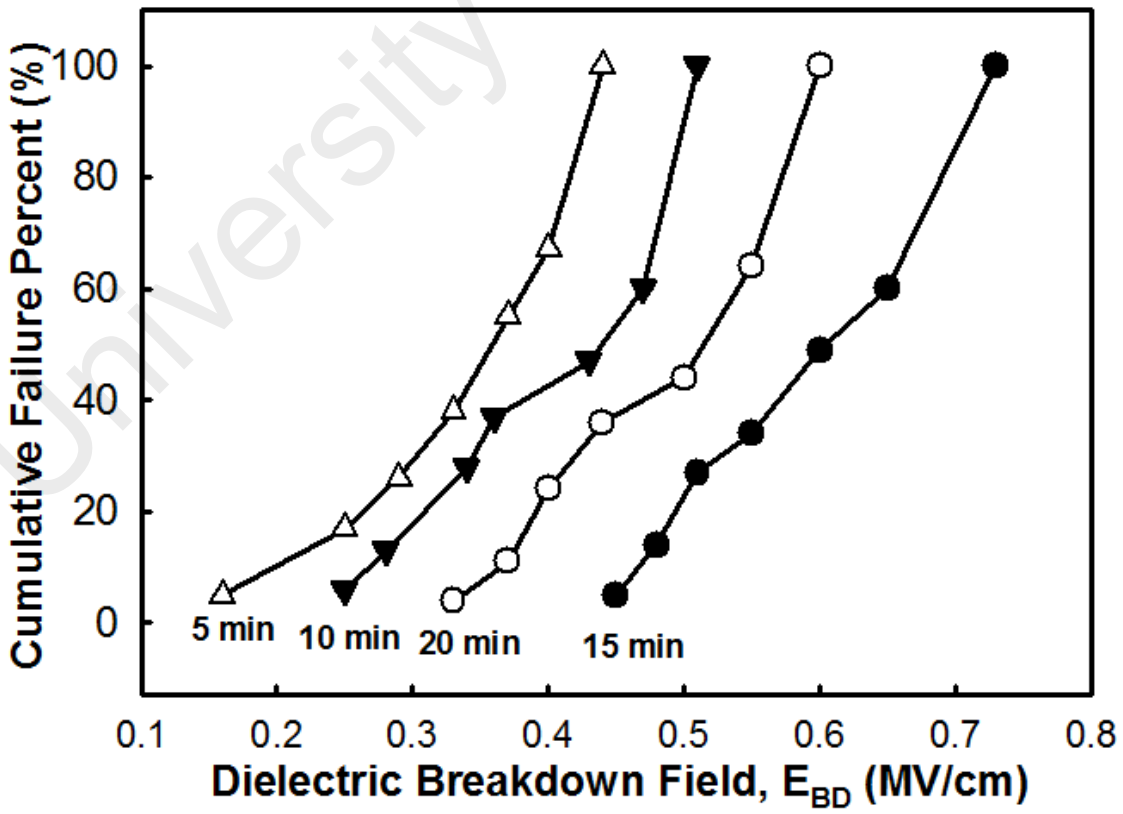

Figure 4.13: Cumulative failure percentage of dielectric breakdown field (E_{BD}) of oxidized samples for various durations (5 min, 10 min, 15 min, and 20 min).

The barrier height, $\emptyset_B$ of the conduction band edge between Si and the interfacial layer of oxide was extracted from the Fowler-Nordheim (FN) tunneling model. This model describes the flow of electron through a triangular potential barrier into the conduction band of an insulator. The FN tunneling can be defined as below (Y. H. Wong & Cheong, 2012a, 2012b):

$$J_{FN} = AE^2 \exp\left[\frac{-B}{E}\right] \quad \text{(Equation 4.1)}$$

where

$$A = \left[\frac{q^3}{8\pi h \emptyset_B}\right]\left[\frac{m}{m_{ox}}\right] \quad \text{(Equation 4.2)}$$

$$B = \frac{8\pi\left(m_{ox}{\emptyset_B}^3\right)^{1/2}}{3\text{qh}} \quad \text{(Equation 4.3)}$$

where, h is the Planck's constant (4.135 x 10^{-15} eV s), m_{ox} is the effective electron mass in the oxidized layer, and m is the free electron mass. A and B can be rewritten after replacing all constants into Eq. 4.2 and Eq. 4.3.

$$A = 1.54 \times 10^{-6}\left[\frac{m}{m_{ox}}\right]\left[\emptyset_B\right] \quad \text{(Equation 4.4)}$$

$$B = 6.83 \times 10^7\left[\frac{m_{ox}}{m}\right]\left[{\emptyset_B}^3\right]^{1/2} \quad \text{(Equation 4.5)}$$

By rearranging Eq. 4.1, we get

$$ln\left[\frac{J}{E^2}\right] = -B\left[\frac{1}{E}\right] + \ln A \quad \text{(Equation 4.6)}$$

Fig. 4.14 shows a FN plot of *ln* (J/E^2) versus 1/*E*. The gradient of the plot yields *B* and the *y*-intercept of the plot yields ln (*A*). In order to calculate $Ø_B$, the effective mass of high κ oxide was assumed to be 0.3*m* (Y. H. Wong & Cheong, 2012a, 2012b). The $Ø_B$ values range from 0.96 to 2.13 eV as shown in Fig. 4.15. The 15 min sample had the highest $Ø_B$ value (2.13 eV). The value (2.13 eV) was higher than previous reported values (0.85 eV) (Dakhel, 2004) but lower than values (2.34) (Kim, McIntyre, & Saraswat, 2003) and (2.88 – 2.92 eV) (V. A. Rozhkov, Trusova, & Berezhnoy, 1998) which were extracted from the photocurrent experiment.

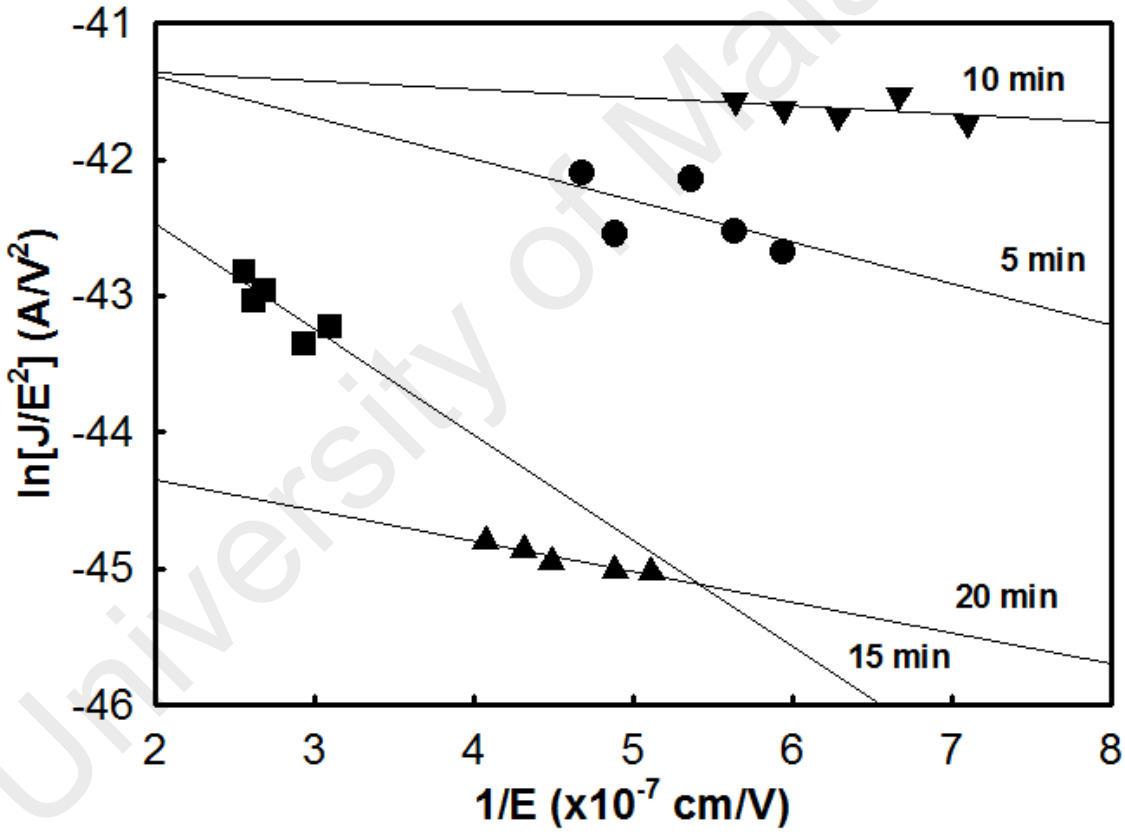

Figure 4.14: FN tunneling linear regression plot [*In* (J/E^2) versus *1/E*] of oxidized samples for various durations (5 min, 10 min, 15 min, and 20 min).

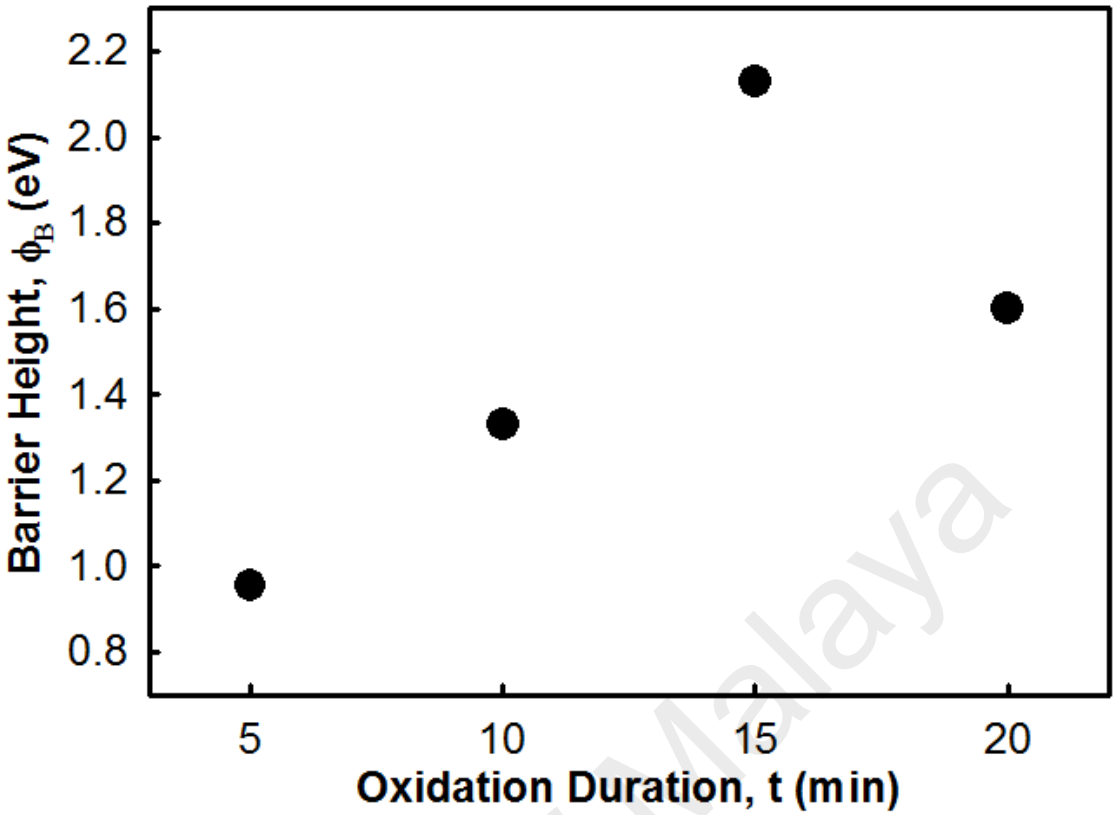

Figure 4.15: Barrier height values as a function of oxidation duration (5 min, 10 min, 15 min, and 20 min).

Fig. 4.16 shows three [(1) to (3)] major and five [(4) to (8)] trap-related possible electron conduction processes through the oxide material which was summarized by Yu *et al.* (Yu, Guan, & Wong, 2011). These are (1) the Schottky emission, (2) the Fowler-Nordheim (F-N) tunneling, (3) direct tunneling, (4) tunneling from cathode to traps, (5) emission from trap to conduction band or the Poole-Frenkel (P-F) emission, (6) F-N like tunneling from trap to conduction band, (7) trap to trap tunneling or the Mott hopping, and (8) tunneling from traps to anode. The trap-related electron conduction mechanism is also known as trap-assisted tunneling (TAT).

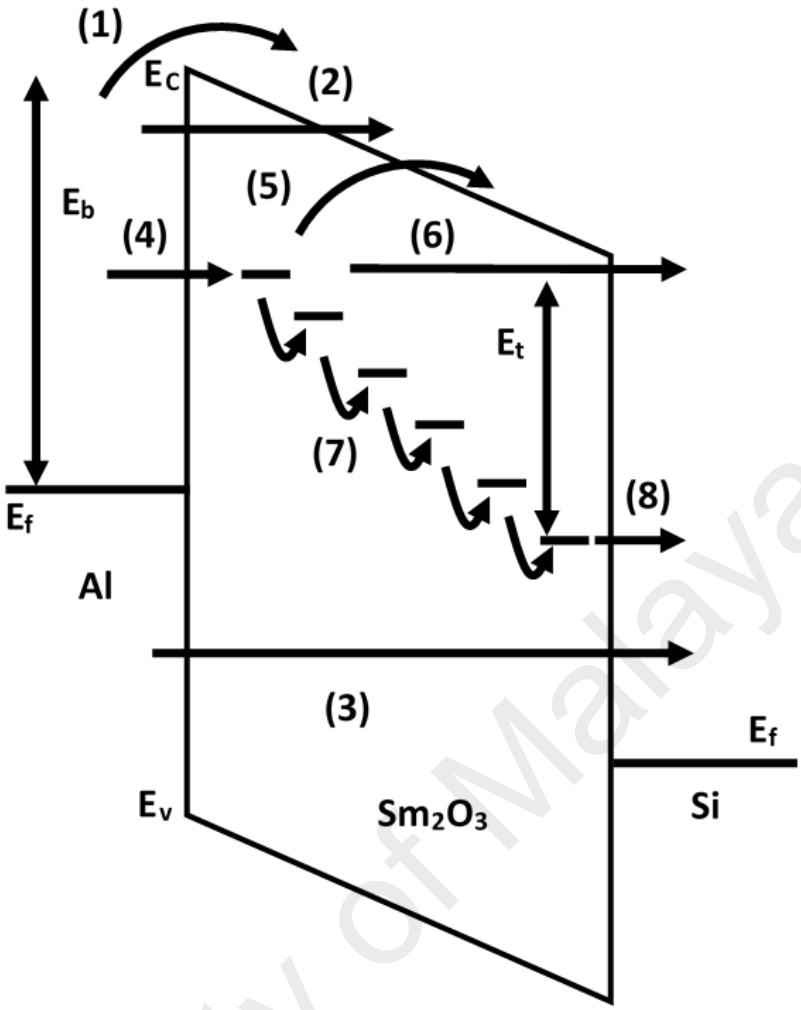

Figure 4.16: Eight possible electron conduction processes through the oxide material (Yu *et al.*, 2011).

Since our measured current was not a strong function of temperature and the thickness of the Sm_2O_3 film was about 150 nm, the Schottky emission and direct tunneling may be neglected. The F-N tunneling model was studied and the barrier height was extracted in the previous paragraph (Andersson, Pearce, & Spetz, 2013). Furthermore, a two-step breakdown was observed in all the investigated MOS capacitors. This left TAT as another possible mechanism of conduction. It is convenient to estimate trap energy ($Ø_t$) and trap density (N_t) by using a simplified tunneling current density equation (Cheong, Moon, Kim, Bahng, & Kim, 2010; Fleischer, Lai, & Cheng, 1992, 1993; X. R. Cheng, Cheng, & Liu, 1988). The traps measured from *J-E* curve were those traps contributing to TAT current while traps measured from *C-V* curve were the only charged traps that

can induce a voltage shift (Alers, Krisch, Monroe, Weir, & Chang, 1996). The simplified trap-assisted tunneling current density equation was defined as (Cheong *et al*., 2010; Fleischer *et al*., 1992, 1993; X. R. Cheng *et al*., 1988):

$$J = \frac{2C_t N_t q \emptyset_t \exp\left[(-A/E)\emptyset_t^{3/2}\right]}{3E} \qquad \text{(Equation 4.7)}$$

where C_t is the varying function of electron energy which approximate to 1, q is the electronic charge, and A is a constant equal to $4\sqrt{(2qm_o/3\hbar)}$. Further simplification leads to (Cheong *et al*., 2010; Fleischer *et al*., 1993):

$$\ln(JE) = \left(-A\emptyset_t^{3/2}\right)(1/E) + \ln(G) \qquad \text{(Equation 4.8)}$$

where $G = (2/3)(C_t N_t q \emptyset_t)$. Hence, by plotting *ln JE* versus 1/*E*, $\emptyset_t$ can be calculated from the slope and N_t can be calculated from the *y*-intercept value.

Fig. 4.17 shows the typical trap-assisted tunneling plot for investigated samples. A total of 30 points with ~ 0.9 of goodness of fit (r^2) were obtained. Fig. 4.18 shows the trap energy and trap density as a function of oxidation duration. The 15 min samples have the highest trap energy (0.0007485 eV) and lowest energy trap density (6.88 x 10^{21} cm^{-3}) as compared to other samples. This correspods to the relatively low leakage current density (as shown Fig. 4.12) as compared to others samples. However, the trap energy was lower than the trap energy of silicon nitride (~ 0.033 eV) (Yang, Wong, & Cheng, 1996), (~ 1.03 eV) (Perera, Ikeda, Hattori, & Kuroki, 2003), (~ 0.7 eV) (Fleischer, Lai, & Cheng, 1993), and ZrO_2 (~ 0.8 eV) (Houssa, Stesmans, & Heyns, 2001) reported by previous researchers because of their lower leakage current density (> 10^{-9} A cm^{-2}). Since the breakdown electrical field is located at a lower electrical field (< 4 MV cm^{-1}), hence the electrical conduction was dominated by shallow trap-assited tunneling (Yang, Wong,

& Cheng, 1996; Houng, Wang, & Chang, 1999; Perera, Ikeda, Hattori, & Kuroki, 2003). Beside that, the experimental and/or simulated energies of deep level trap at higher electrical field (> 4 MV cm^{-1}) of SiON were reported ranging from 1.6 eV to 2.87 eV by several researchers (Ramesh, Chandorkar, & Vasi, 1989; Fleischer, Lai, & Cheng, 1992; Cheng, Cheng, & Liu, 1988; Suzuki, Schroder, & Hayashi, 1986; Jimenez-Molinos, Palma, Gamiz, Banqueri, & Lopez-Villanueva, 2001).

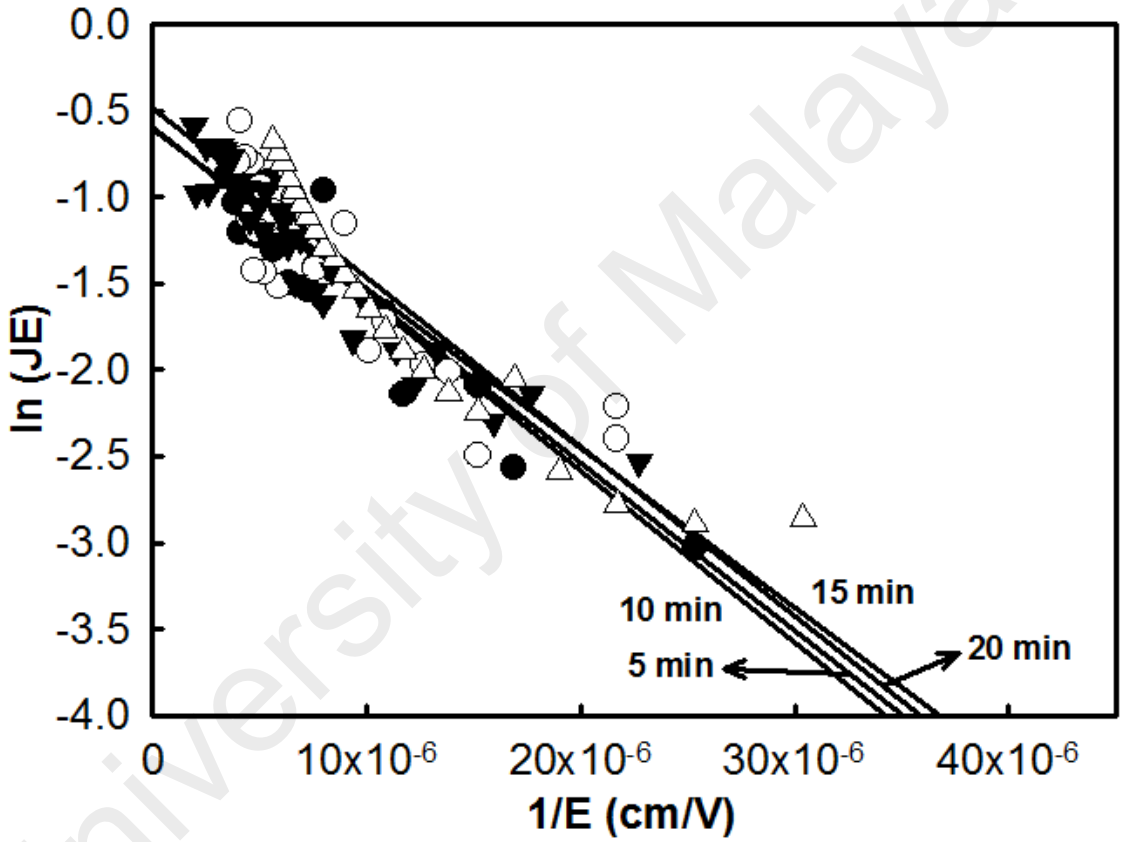

Figure 4.17: Typical trap-assisted tunneling plot of investigated samples for various durations (5 - 20 min).

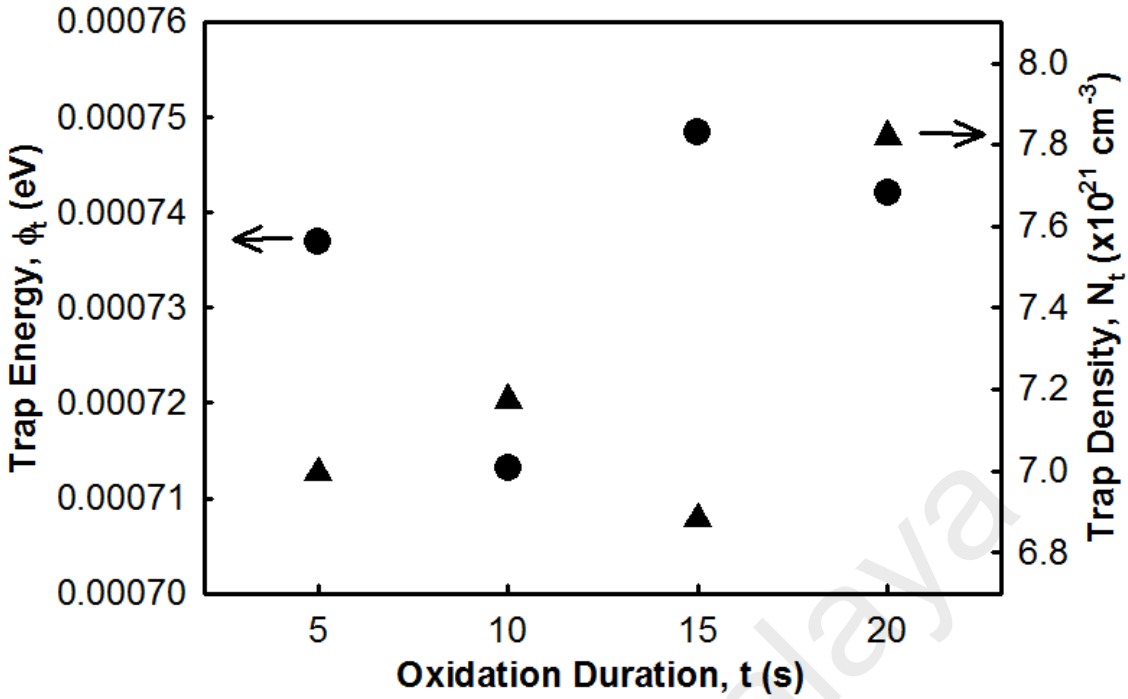

Figure 4.18: The trap energy and trap density of oxidized samples for various durations (5 - 20 min).

In this part, pure Sm metal thin film was sputtered on Si substrate and then oxidized by thermal oxidation process in oxygen ambient at 700 °C for various durations (5, 10, 15, and 20 min). The existence of polycrystalline Sm_2O_3 and interfacial layer was confirmed by the XRD, Raman, and EDX results. This finding was also supported by the FTIR results which indicate that the peaks of Sm - O and Si - Si bonding are either broadening and/or shifting. The crystallite size of 10 min sample has the smallest crystallite size according to both the W–H and Scherrer calculations. However, the 15 min sample has the smoothest surface, the highest breakdown voltage field of 0.71 MV cm^{-1} at ~ 10^{-4} A cm^{-2}, the highest barrier height of 2.13 eV, the highest trap energy of 0.0007485 eV, and the lowest trap density of 6.88 x 10^{21} cm^{-3} among the samples.

4.3 Effects of oxidation temperature on sputtered Sm thin film on Si substrate

4.3.1 Physical and chemical properties

4.3.1.1 XRD analysis

Fig. 4.19 shows the XRD patterns of the sputtered Sm thin film on Si substrate oxidized at different temperatures (600 °C, 700 °C, 800 °C, and 900 °C). Three strong peaks at 28°, 69°, and 76° were detected in all samples which matched the three different planes of cubic silicon which are c-Si (111), c-Si (004), and c-Si (331), respectively. These peaks were confirmed by Inorganic Crystal Structure Database (ICSD) with the reference code of 98-001-6569. The cubic structure of the Sm_2O_3 (c-Sm_2O_3) was revealed at various diffraction angles of 17.8°, 19.9°, 38.6°, 46°, 48°, 54°, 56°, 58.5°, 61°, 74.7°, and 75.5° corresponding to the (002), (112), (233), (152), (334), (154), (226), (444), (064), (138), and (257) planes, respectively. These peaks were confirmed by ICSD with the reference code of 98-004-0475. According to the XRD results, it was observed that the peaks at 38.6°, 46° and 58.5° became higher and sharper when the samples were oxidized at higher temperature as shown in Fig. 4.20. This implied that the crystallinity of the Sm_2O_3 increased with oxidation temperatures.

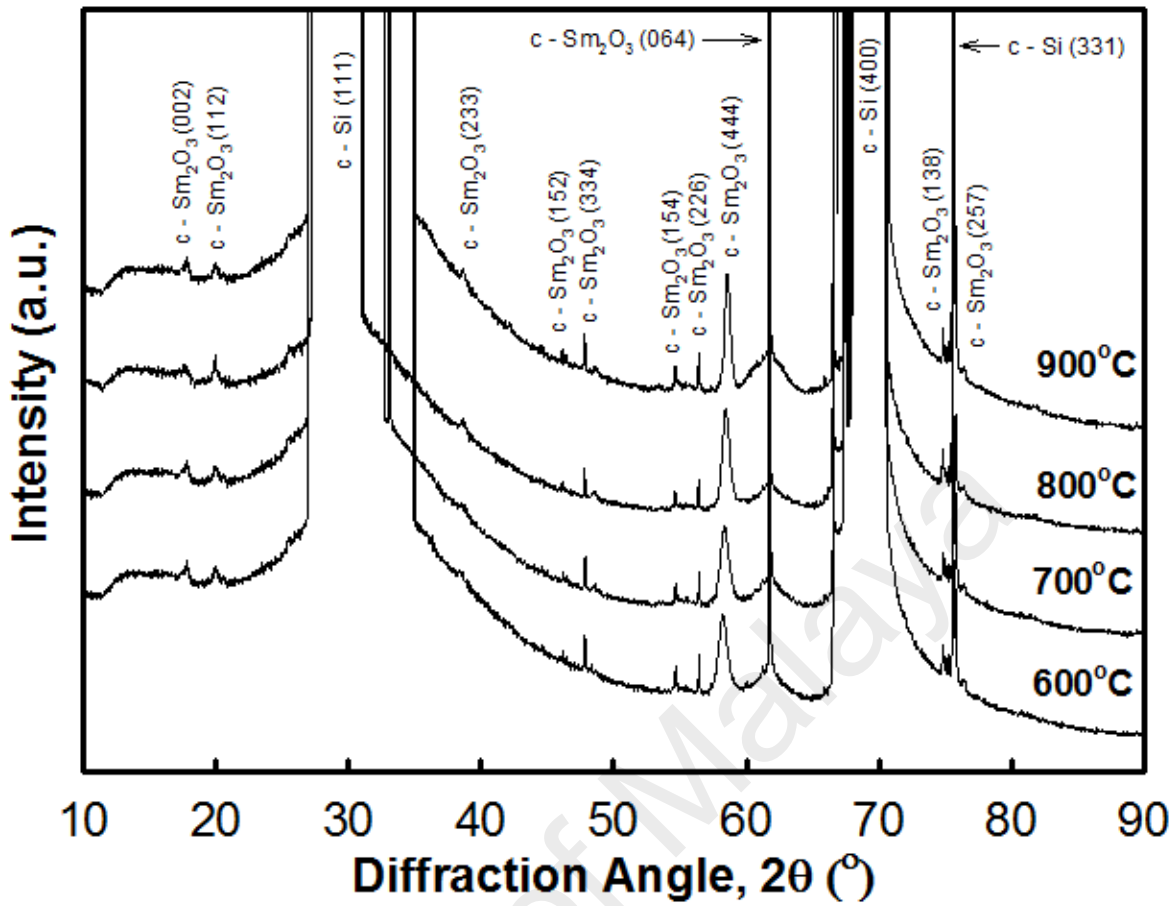

Figure 4.19: XRD patterns of oxidized samples at various temperatures (600 - 900°C).

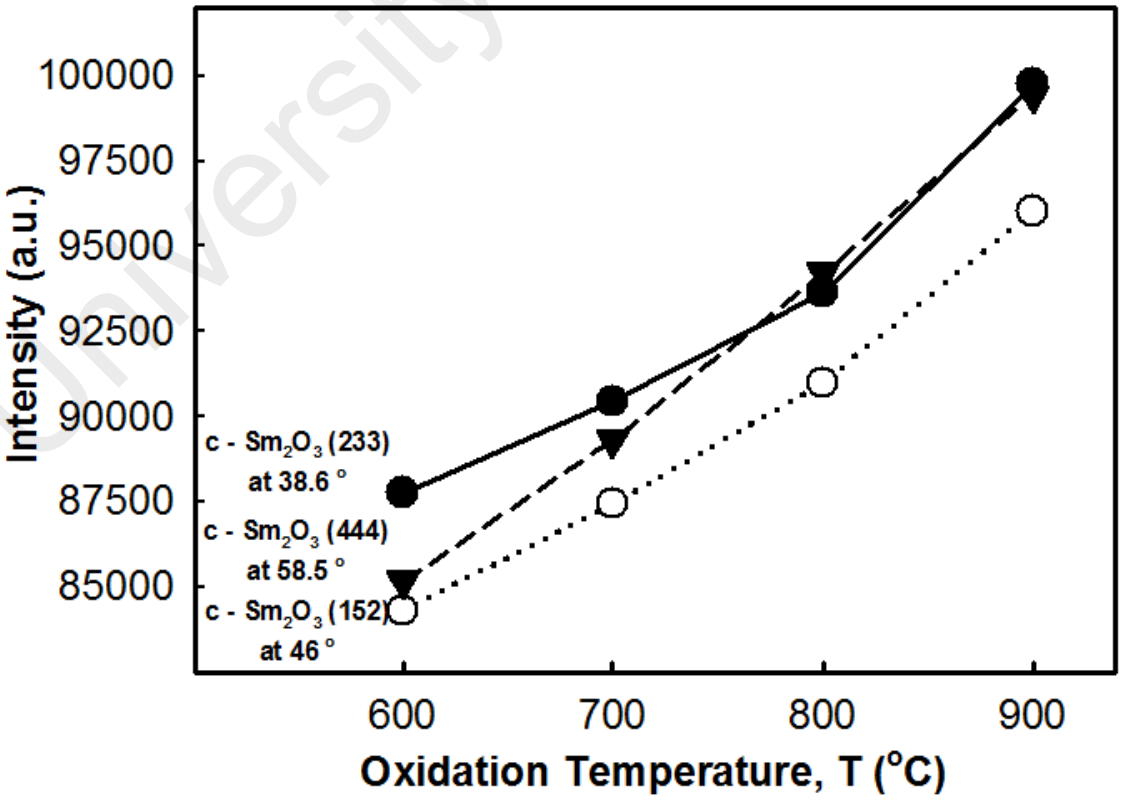

Figure 4.20: Intensities of Sm_2O_3 (233), (444), and (152) at 38.6°, 58.5°, and 46°, respectively as a function of oxidation temperatures (600 - 900°C).

From the Scherrer equation calculations, the average crystallite sizes of the Sm_2O_3 for 600 °C, 700 °C, 800 °C, and 900 °C were 12.2 nm, 11.6 nm, 16.1 nm, and 16.4 nm, respectively (Fig. 4.21). It was observed that crystallite sizes of 700 °C samples gave smaller differences or distribution of size. This means the crystallite size was more homogenous. Since the Scherrer equation only gives the lower bound of crystallite size and the microstrain was not taken into account, the W-H analysis was also conducted.

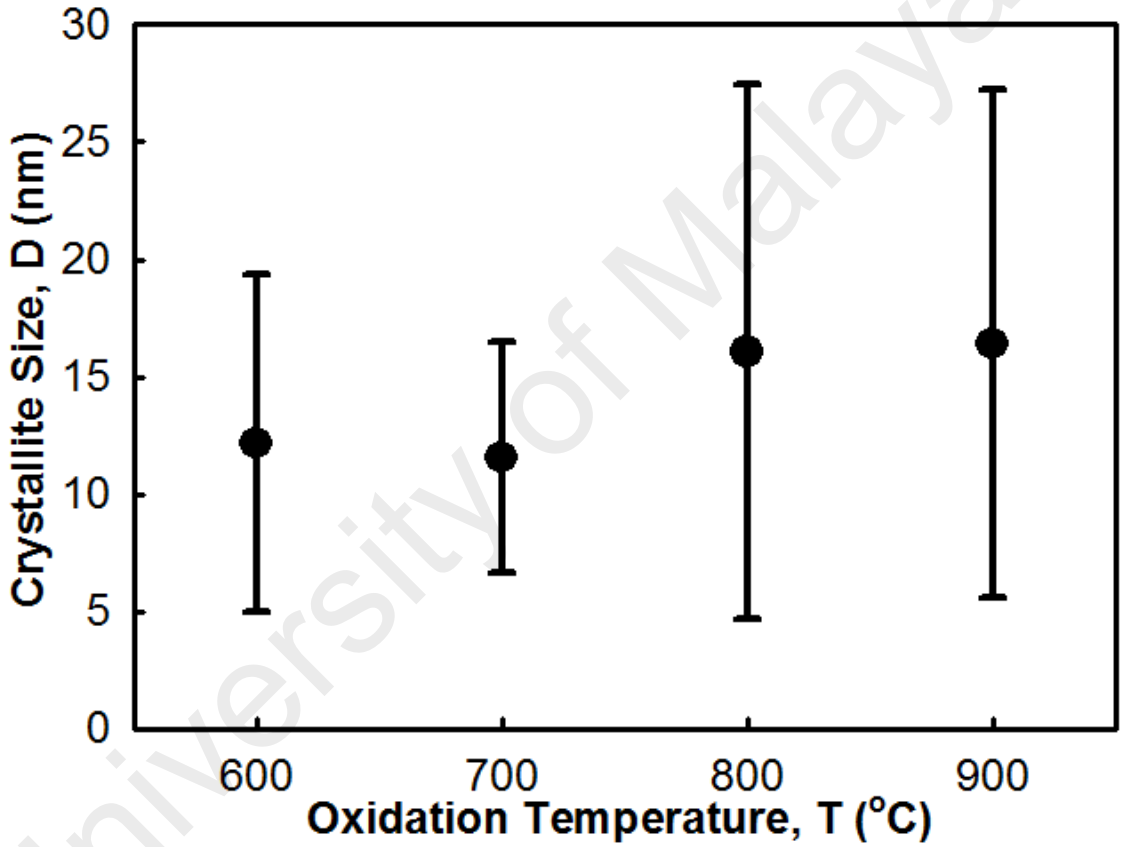

Figure 4.21: Calculated crystallite sizes of Sm_2O_3 by Scherrer equation as a function of oxidation temperature (600 - 900°C).

A $\beta_{hkl} \cos \theta$ versus 4 $\sin \theta$ graph (Fig. 4.22) was plotted based on Eq. 3.6. Based on the W-H analysis, the crystallite size of the Sm_2O_3 was increased from 9.32 nm to 65.77 nm while microstrain of the Sm_2O_3 was increased from 0.033 to 0.060 when the oxidation temperatures increased from 600 °C to 900 °C as shown in Fig. 4.23. The calculated crystallite sizes of Sm_2O_3 by both the Scherrer equation and the W-H analysis had the same trend which increased with the oxidation temperature.

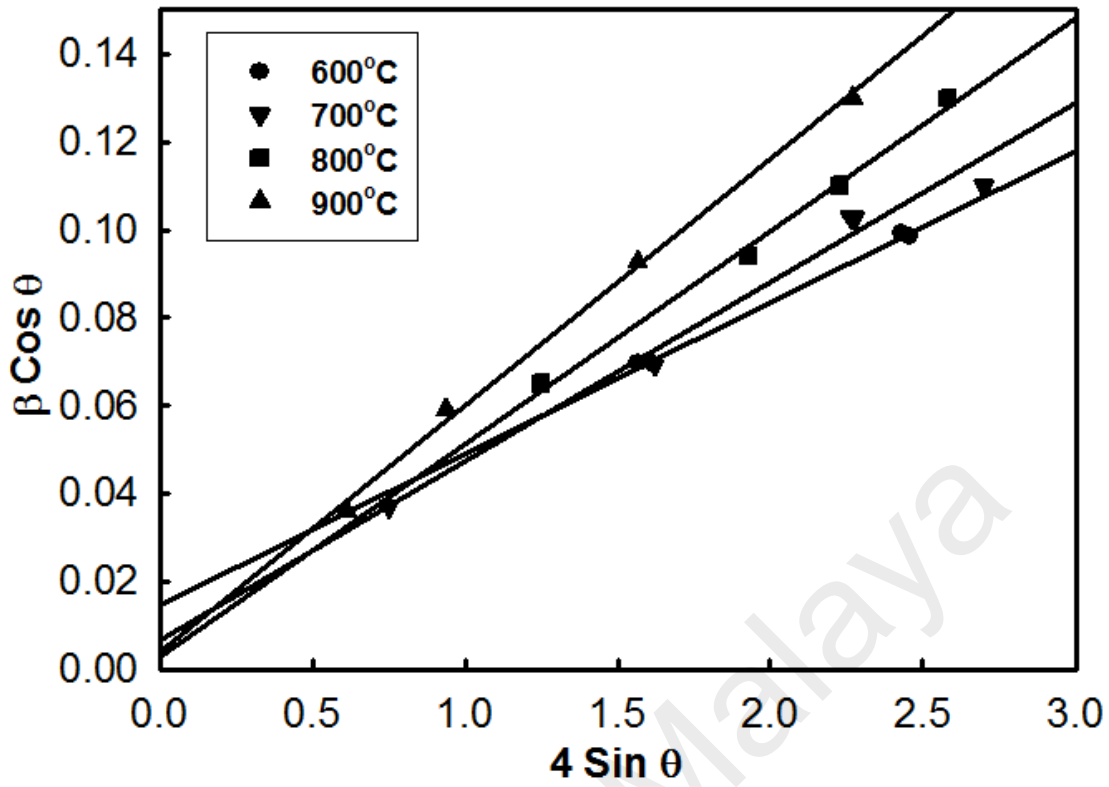

Figure 4.22: W-H plot of oxidized samples at various temperatures (600 - 900°C).

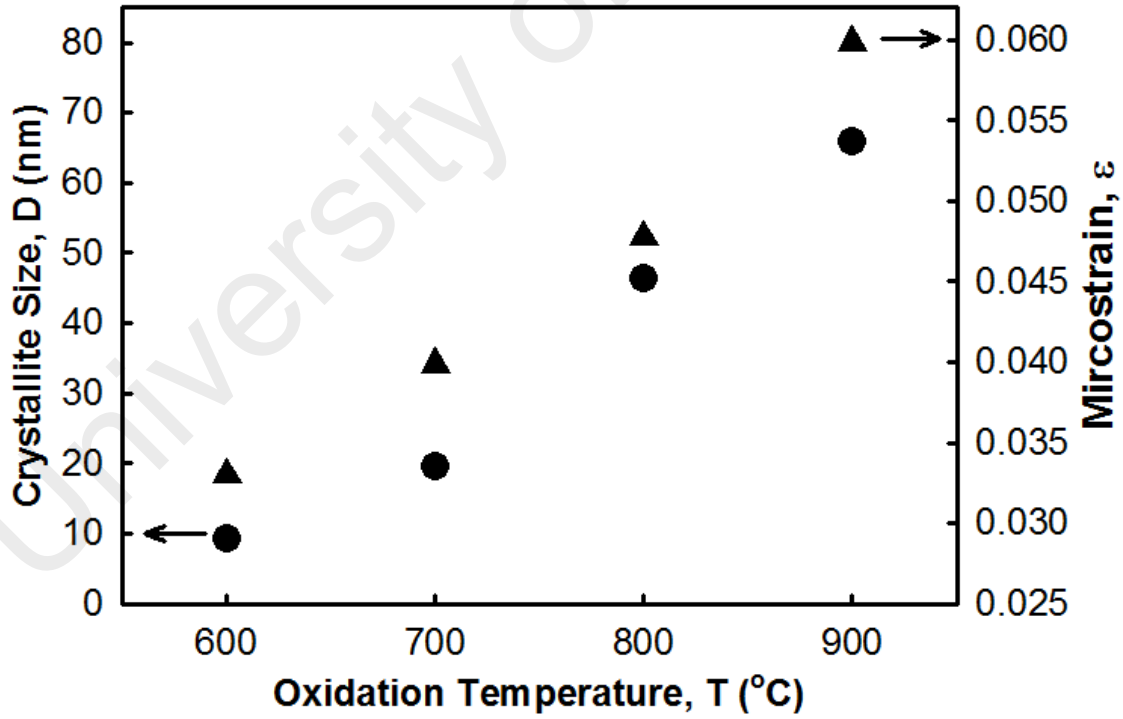

Figure 4.23: Relationship of calculated crystallite size and microstrain from W-H plot as a function of oxidation temperatures (600 - 900°C).

4.3.1.2 FTIR analysis

The FTIR analysis was used to determine the chemical functional groups in the samples. Fig. 4.24 shows the FTIR transmittance spectra (700-400 cm^{-1}) of Sm sputtered on Si substrates and the samples oxidized at different temperatures. The Si - Si vibration mode band was located at 567 cm^{-1} in all samples. The Si - Si peak was broadened as the oxidation temperature increased. For an oxidation temperature of 600 °C, the Sm - O vibration modes were detected at 409 cm^{-1} (Hussein *et al*., 2003), 418 cm^{-1} (Hussein *et al*., 2003; Ruiz-Gomez *et al*., 2014), 432 cm^{-1} (Hussein *et al*., 2003; Ismail, 1995), 439 cm^{-1} (Hussein *et al*., 2003; Ismail, 1995), 459 cm^{-1} (Hussein *et al*., 2003; Kusrini *et al*., 2014), 473 cm^{-1} (Kusrini *et al*., 2014; Ruiz-Gomez *et al*., 2014), 482 cm^{-1} (Hussein *et al*., 2003; Ruiz-Gomez *et al*., 2014), and 502 cm^{-1} (Hussein *et al*., 2003). However, the peaks of 700 °C, 800 °C, and 900 °C samples were shifted or broadened after the oxidation temperature was further increased. At 482 cm^{-1} and 502 cm^{-1}, the peaks of 700 °C, 800 °C, and 900 °C samples were broadened when the temperature increased.

At 473 cm^{-1}, all the peaks were broadened and their intensities were decreased as oxidation temperatures increased. At 459 cm^{-1}, the peak of 700 °C was shifted to a higher wavelength (462 cm^{-1}) compared to the 800 °C (461 cm^{-1}) sample and the 900 °C sample (460 cm^{-1}). For 432 cm^{-1} and 439 cm^{-1}, both peaks were combined into single peak (435 cm^{-1}) after further oxidation. However, the intensities of the peak decreased at 800 °C and almost disappeared at 900 °C. For 418 cm^{-1}, the peak of 700 °C sample was separated into two peaks while the intensities of 800 °C and 900 °C samples were decreased. At 409 cm^{-1}, the peaks of 700 °C, 800 °C, and 900 °C samples were shifted to 403 cm^{-1}, 410 cm^{-1}, and 407 cm^{-1}, respectively. It can be inferred that the broadening and shifting of peaks may be due to the formation or growth of interfacial layer.

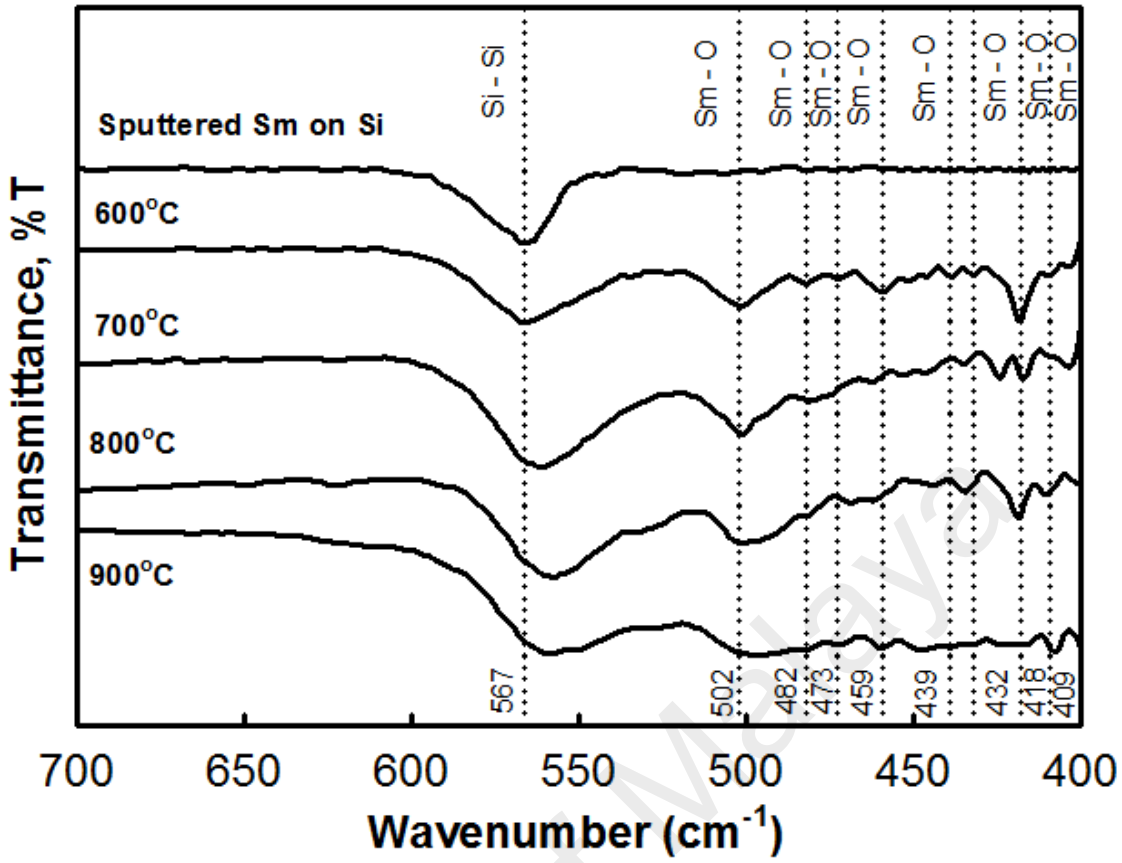

Figure 4.24: Transmittance spectra of oxidized samples at various temperatures (600 - 900°C).

4.3.1.3 Raman analysis

The Raman results for all oxidized samples were shown in Fig. 4.25. The peak at 520 cm^{-1} was thought to originate from the silicon substrate (Y. H. Wong & Cheong, 2011b). The peaks at 111 cm^{-1} (S. Jiang *et al*., 2013), 120 cm^{-1} (S. Jiang *et al*., 2013), 145 cm^{-1} (S. Jiang *et al*., 2013), 168 cm^{-1} (Mandal *et al*., 2014; S. Jiang *et al*., 2013), 177 cm^{-1} (S. Jiang *et al*., 2013), 238 cm^{-1} (Hongo *et al*., 2007; Mandal *et al*., 2014; S. Jiang *et al*., 2013), and 408 cm^{-1} (Hongo *et al*., 2007; Mandal *et al*., 2014; S. Jiang *et al*., 2013) were identified to be Sm_2O_3. For the unknown peaks at 245 and 477 cm^{-1}, their intensities increased when the oxidation temperature was increased owing to an increase of crystallinity (Fig. 4.26). Since they neither belong to Sm_2O_3 nor Si, they were inferred to originate from an interfacial layer inferred in the XRD and FTIR analysis.

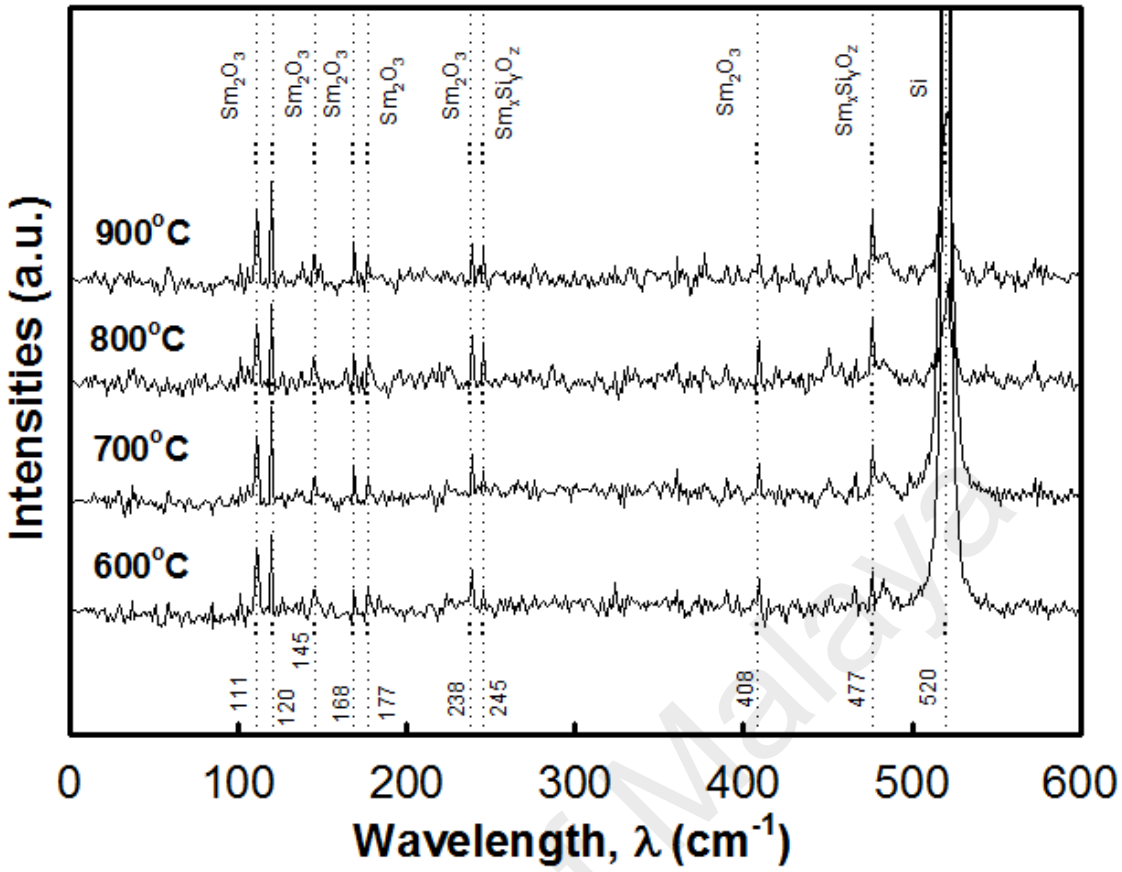

Figure 4.25: Raman spectra of oxidized samples at various temperatures (600 - 900°C).

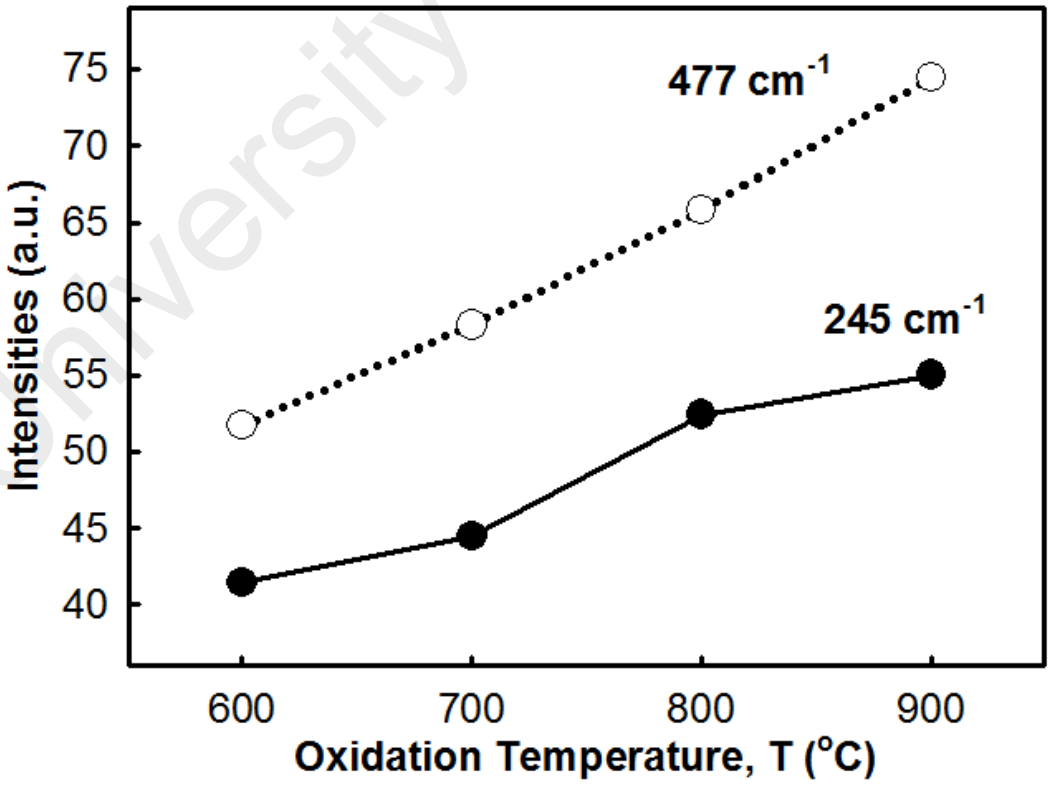

Figure 4.26: Intensities of IL at 245 cm^{-1} and 477 cm^{-1} as a function of oxidation temperature (600 - 900°C).

4.3.1.4 HRTEM and EDX analysis

Fig. 4.27 shows the cross sectional HRTEM images of the oxidized samples at different oxidation temperatures (600 °C - 900 °C). Magnified images of each of the oxidized samples were shown on the right hand side, respectively. It was observed that the oxide/semiconductor structure consists of four layers, i.e., Si substrate, interfacial layer-1 (IL-1), IL-2, and Sm_2O_3. The total oxide layer thickness of 600 °C, 700 °C, 800 °C, and 900 °C were 155.16 nm, 159.01 nm, 149.9 nm, and 163.08 nm, respectively. The thickness of IL-1 for 600 °C, 700 °C, 800 °C, and 900 °C samples were 2.02 nm, 1.69 nm, 2.97 nm, and 4.91 nm, respectively. The thickness of IL-2 for 600 °C, 700 °C, 800 °C, and 900 °C were 6.26 nm, 6.15 nm, 20.72 nm and 15.54 nm, respectively. The lattice fringes of Sm_2O_3 can be clearly seen with interplanar spacing (*d*) of 0.194 – 0.258 nm which was measured from the zoomed images (do not show here) and it was in agreement with the average *d* value (0.228 nm) of ICSD data of Sm_2O_3.

The polycrystalline structure of Sm_2O_3 and amorphous structure of IL-1 were revealed for all investigated samples. However, IL-2 is semi-polycrystalline and consists of both polycrystalline and amorphous regions for all samples. Hence, it was inferred that the two unknown peaks in Raman analysis were due to the presence of the semi-polycrystalline of interfacial layer. The total thickness of 800 °C sample was the thinnest (Fig. 4.28). However, its interfacial layer (IL-1+2) was thickest among the samples. For oxidation temperatures at 700 °C, both interfacial layers were the thinnest while the Sm_2O_3 film was the thickest among the samples (Fig. 4.28). The total thickness of interfacial layer increased dramatically at 800 °C and 900 °C of oxidation temperatures. It was because the oxygen atoms diffused to the Sm_2O_3/Si interface actively from crystal defects and nonstoichiometric compounds when the oxidation temperatures increased.

According to the EDX line scan, an interfacial layer was formed between Sm_2O_3 film and Si substrate (Fig. 4.29).

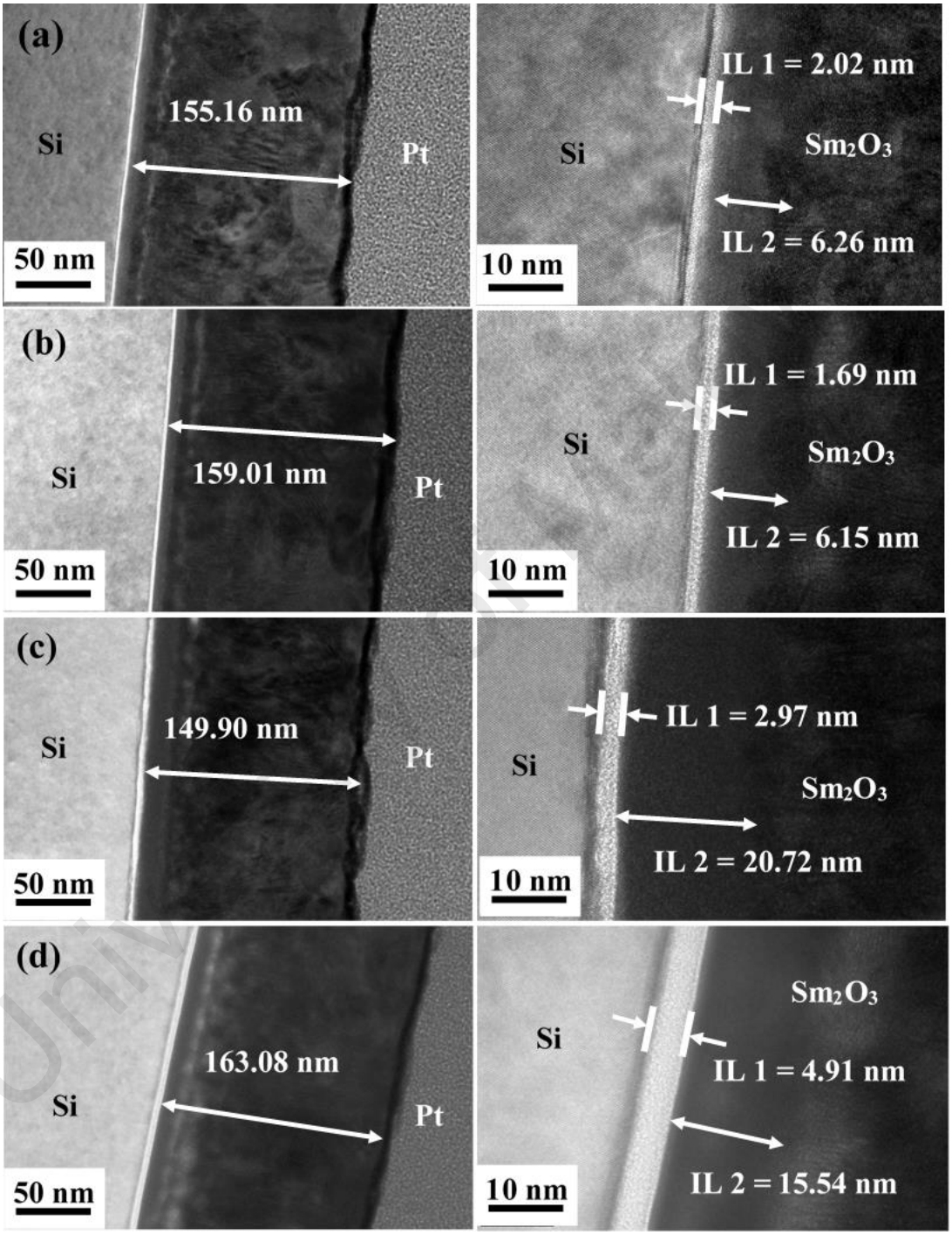

Figure 4.27: Cross sectional of HRTEM images of oxidized samples at various temperatures: (a) 600°C (b) 700°C (c) 800°C (d) 900°C. Magnification of each image is shown on the lower left side, respectively.

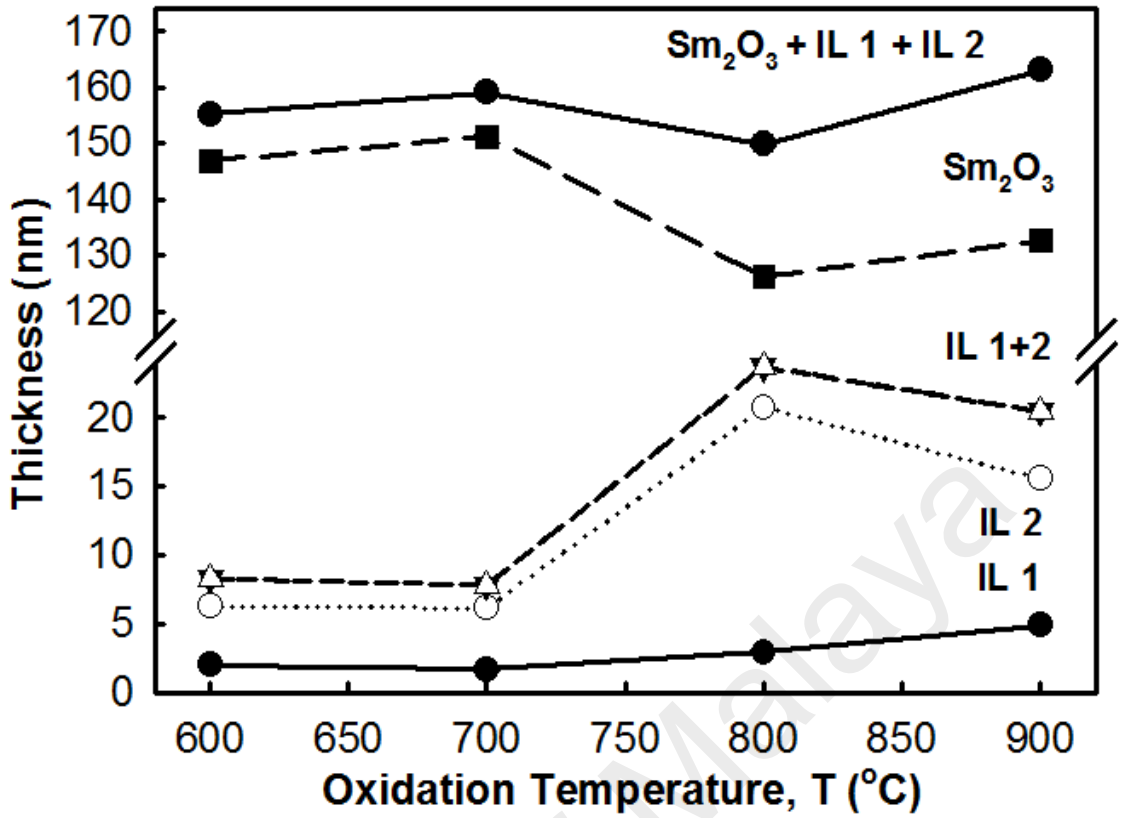

Figure 4.28: IL-1, IL-2, IL-1 + 2, Sm_2O_3, and total thickness of IL-1 and IL-2 as a function of oxidation temperature (600 - 900°C).

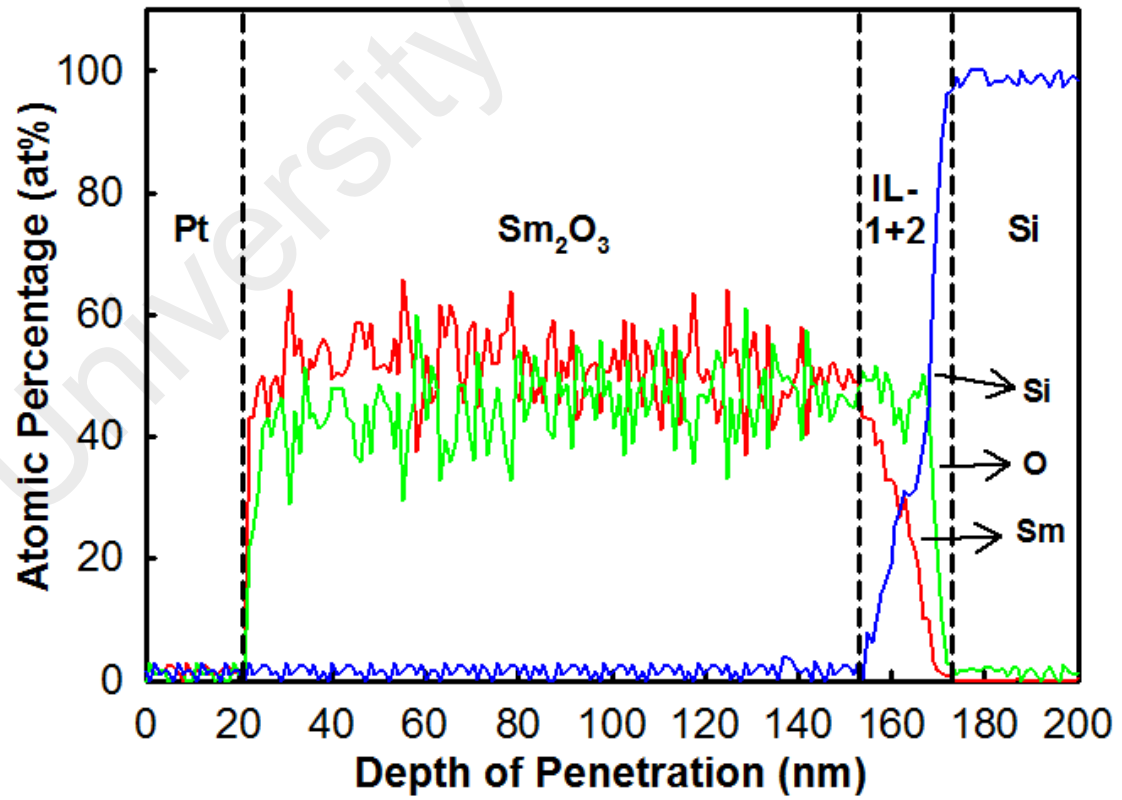

Figure 4.29: EDX compositions analysis of 700 °C samples.

4.3.1.5 Oxidation mechanism

Based on the EDX, XRD, FTIR, and Raman results, a sketched model is proposed in Fig. 4.30 (Venables, Spiller, & Hanbucken, 1984; Tu, Ottaviani, Thompson, & Mayer, 1982; Rochet, Agius, & Rigo, 1984; Zhang & Lagally, 1997; Massoud, Plummer, & Irene, 1985). At 600 °C, oxygen (O) reacts with Sm to form Sm_2O_3 (Rochet, Agius, & Rigo, 1984; Chao, Lin, & Macdonald, 1981). At the same time, Si also diffused into Sm_2O_3 to form an interfacial layer ($Sm_xSi_yO_z$) (Derrien & Commandre, 1982; Massoud, Plummer, & Irene, 1985). As shown in the EDX analysis, the Si-rich $Sm_xSi_yO_z$ layer (IL-1) is located near the Si substrate while Sm-rich $Sm_xSi_yO_z$ (IL-2) is located near the Sm_2O_3. This may attributed to concentration gradient of the composition. According to the HRTEM images, IL-2 is semi polycrystalline while IL-1 is amorphous. Some polycrystalline structures can be observed in the region between IL-2 and Sm_2O_3. At 700 °C, the growth rate of stable Sm_2O_3 was faster than $Sm_xSi_yO_z$. Thus, the thickest Sm_2O_3 was formed and the thinnest layer of both IL were observed. However, undesirable thick interfacial layer was formed aggressively when oxidation temperatures increased to 800 °C and 900 °C (Derrien & Commandre, 1982; Zhao, Wang, Lu, Palasantzas, & De Hosson, 1999). The reaction between Sm_2O_3 and Si occurred rapidly and formed thick $Sm_xSi_yO_z$ because of higher activation energy under higher temperature ambient (Jeurgens, Sloof, Tichelaar, & Mittemeijer, 2002; Chao, Lin, & Macdonald, 1981).

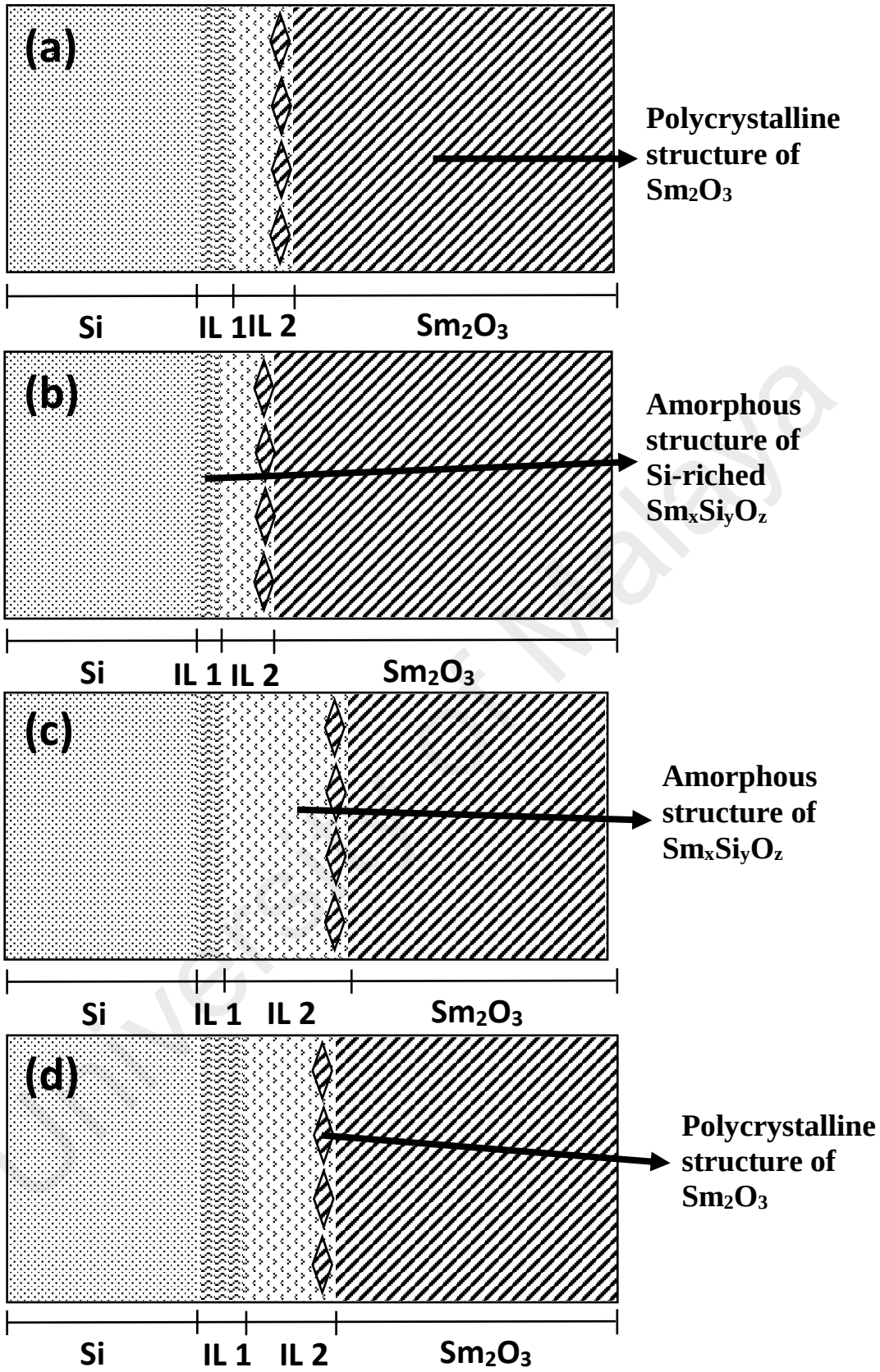

Figure 4.30: Sketched models of layer distribution at different oxidation temperatures: (a) 600°C (b) 700°C (c) 800°C (d) 900°C.

4.3.1.6 Arrhenius plot analysis

Fig. 4.31 shows the Arrhenius plot of IL-1, IL-2, IL-1+2, Sm_2O_3, and total (IL-1 + IL-2 + Sm_2O_3) growth in the O ambient. The IL-1, IL-2, IL-1+2, Sm_2O_3, and total growth rates were identified to be governed by:

$$t = t_0 \exp(\frac{-E_a}{kT}) \qquad \text{(Equation 4.9)}$$

where E_a is the reaction activation energy, k is the Boltzmann constant, t and t_o were the final and initial thickness of IL-1, IL-2, IL-1+2, Sm_2O_3, and total of IL-1,IL-2, and Sm_2O_3 respectively, at a given temperature, T in Kelvin. The calculated E_a for IL-1, IL-2, IL-1+2, Sm_2O_3, and total growth rates were 2.7 x 10^{-4} eV, 3.5 x 10^{-4} eV, 3.4 x 10^{-4} eV, -4.3 x 10^{-5} eV, and -8.6 x 10^{-6} eV, respectively. The positive values of E_a indicated the reaction rate increased when the oxidation temperature increased. It indicated the thickness of interfacial layers were increased as the oxidation temperatures increased. The negative values of E_a indicated the reaction rate decreased or densification occurred when the oxidation temperature increased. Besides that, the magnitude indicated the reaction tendency. It means a small magnitude indicated a fast growth while large magnitude indicated a slow growth.

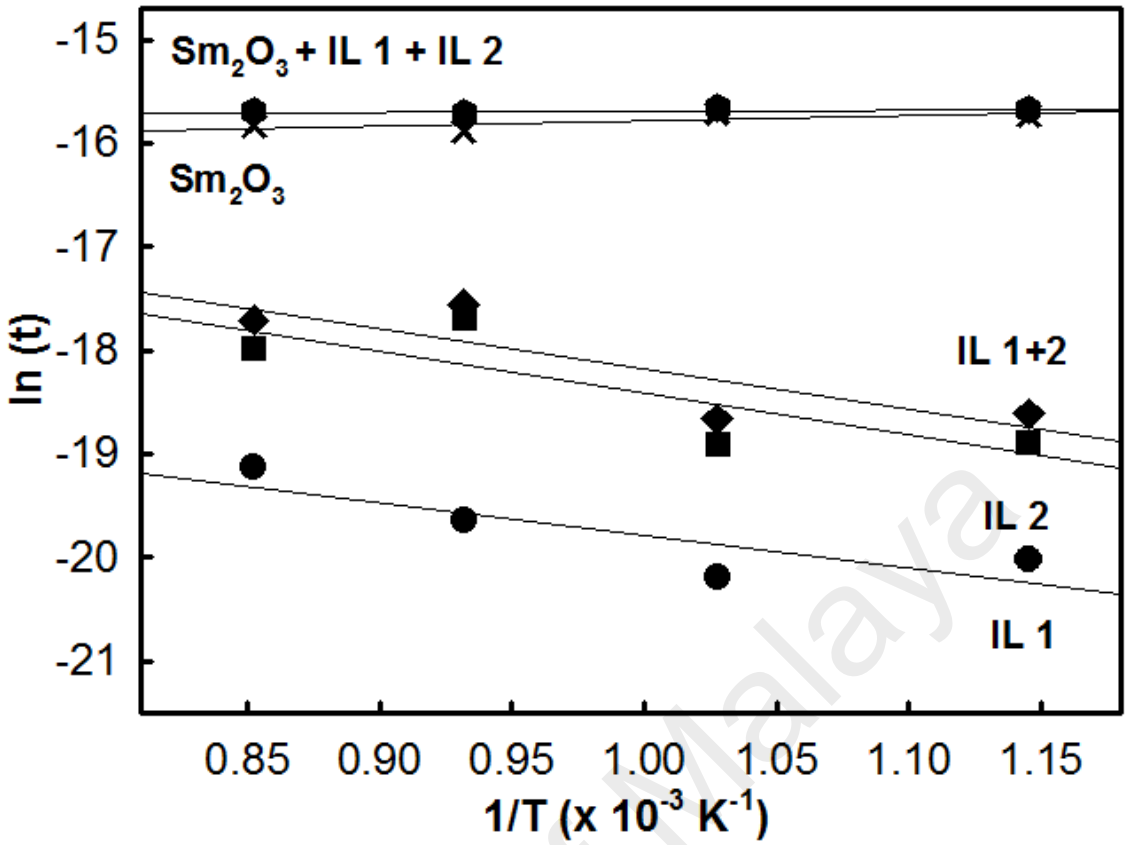

Figure 4.31: Arrhenius plots of IL-1, IL-2, IL-1 + 2, Sm_2O_3, and total of IL-1, IL-2 in O ambient.

4.3.1.7 AFM analysis

Fig. 4.32 shows the two-dimensional surface topography of oxidized samples by atomic microscopy force (AFM). The scanned area was 1 x 1 μm^2. The roughness of the surface decreased when the oxidation temperature increased from 600 °C to 700 °C but the roughness of the surface increased when oxidation temperature increased from 700 °C to 900 °C (Fig. 4.33). The rougher surface was because of higher growth rate at high temperature ambient (Bin Lee, Kwak, & Kim, 2003; K. S. Kim, Yoon, Lee, & Kim, 2001). This may also be due to misalignment of crystalline domains or consolidation of grains. Grain formation was most desirable at 700 °C but grain clustering occurred (dotted line in Fig. 4.32(c) & (d)) at higher temperatures (800 °C and 900 °C) (Chabinyc *et al.*, 2007). Similar phenomena were observed in previous work which reported their RMS decreased

initially and increased again when the annealing temperature increased (Chen, Hung, *et al.*, 2013; Pan & Huang, 2010).

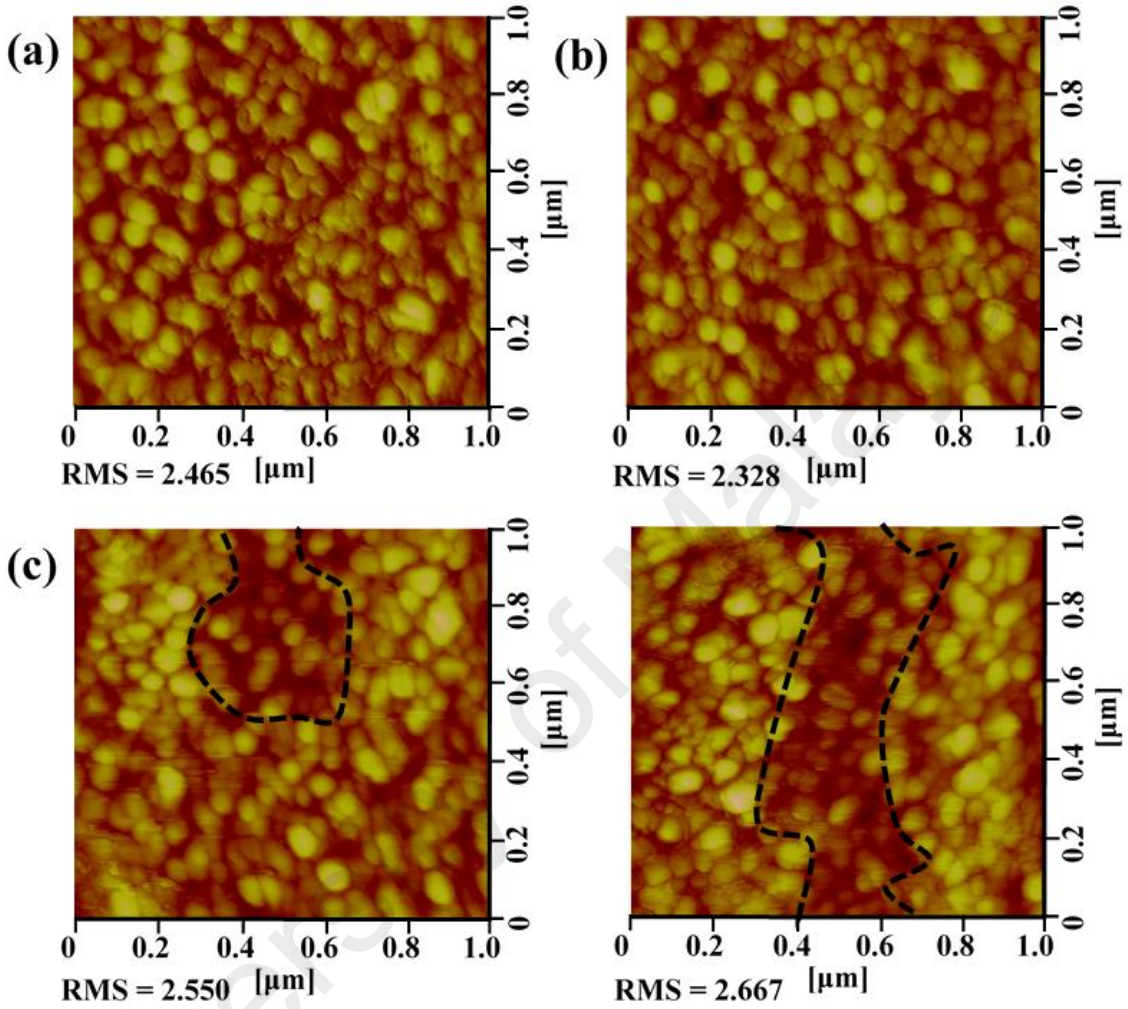

Figure 4.32: Two-dimensional surface topography of oxidized samples at various temperatures: (a) 600 °C (b) 700 °C (c) 800 °C (d) 900 °C.

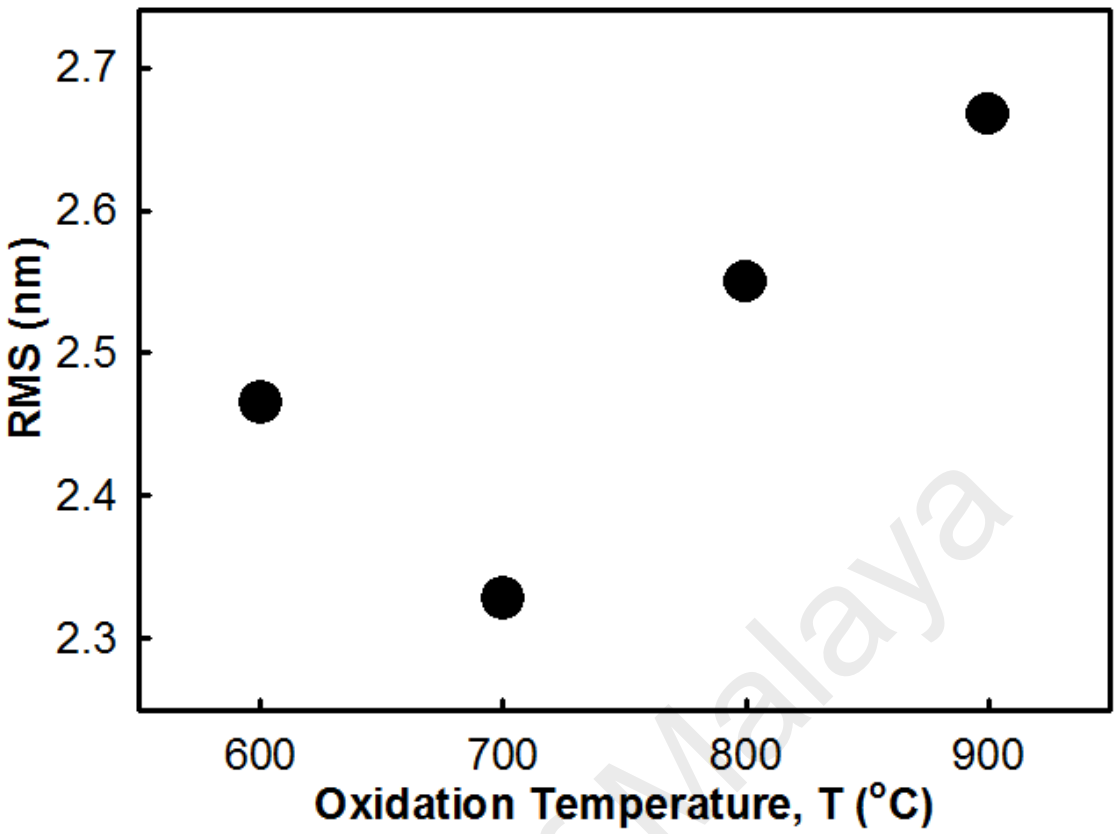

Figure 4.33: RMS values of oxidized samples at various temperatures (600 - 900°C).

4.3.2 Electrical properties

4.3.2.1 *J-E* characteristic

Fig. 4.34 shows the *J-E* characteristic of investigated samples. The *J-E* plot was transformed from *I-V* measurements. Samples oxidized at 600 °C and 700 °C had almost the same E_H. However, the *J* value was relatively lower for samples oxidized at 700 °C. The thickest IL in oxidized samples at 900 °C as shown in HRTEM analysis may downgrade its electrical breakdown field (Zhao, Wang, Lu, Palasantzas, & De Hosson, 1999). The roughness of the surface may contribute to the factors affecting the electrical breakdown field in samples (Tak, Kim, Park, Lee, & Lee, 2009; Zhao, Wang, Lu, Palasantzas, & De Hosson, 1999; Meuris *et al.*, 1992). The smoother samples (600 °C and 700 °C) have a higher electrical breakdown field than the rougher samples (800 °C and 900 °C). High roughness and large grain size may lead to faster electrical breakdown

field as compared to low roughness and small grain size because the grain boundaries were act as current travel paths. For smaller grain size, the current through the thick layer was much less than larger grain size (Meuris *et al.*, 1992; Zhao, Wang, Lu, Palasantzas, & De Hosson, 1999). From the *J-E* measurements, time-zero dielectric breakdown (TZBD) reliability tests were done at room temperature (25°C). The cumulative failure percentage of 100 capacitors are presented in Fig. 4.35. According to the plot, 700°C samples had the highest reliability.

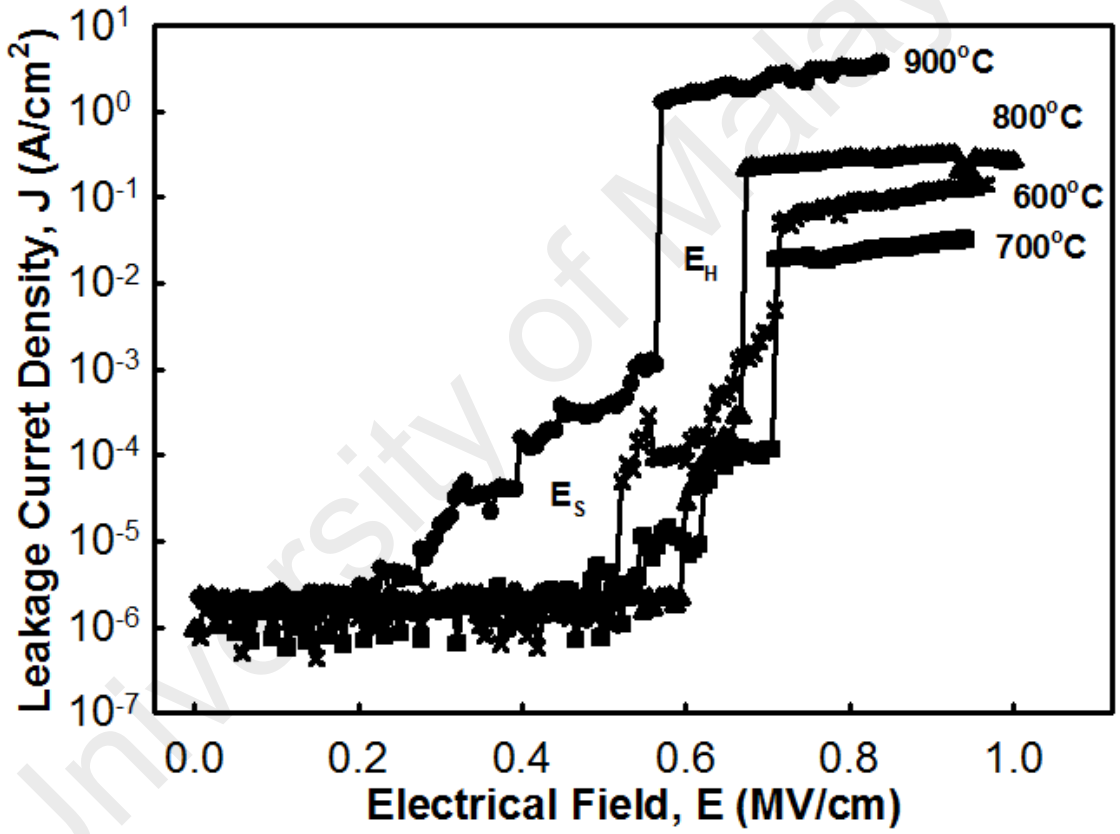

Figure 4.34: *J-E* characteristics of oxidized samples at various temperatures (600 - 900°C).

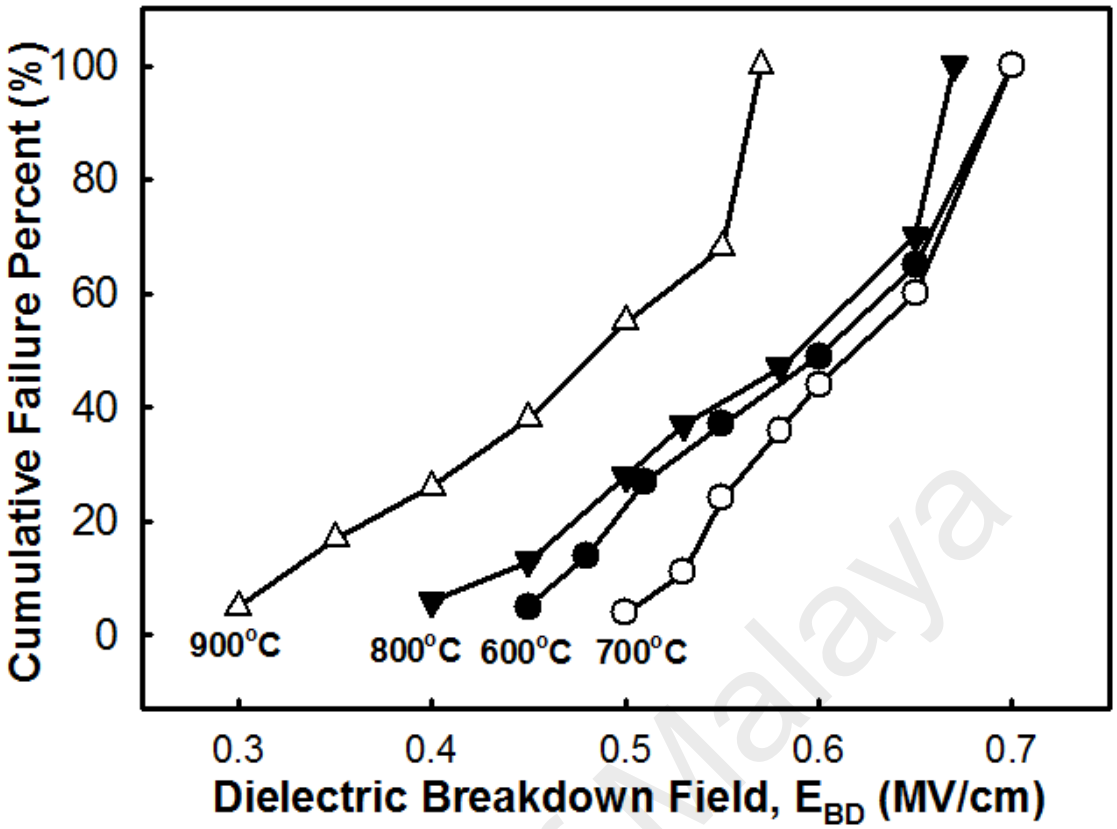

Figure 4.35: Cumulative failure percentage of dielectric breakdown field (E_{BD}) of oxidized samples at various temperatures (600 - 900°C).

The barrier height, $Ø_B$ of the conduction band edge between the Si and the interfacial layer was obtained using the Fowler-Nordheim (FN) tunneling model. The FN tunneling can be defined as in Eq. 4.6. Fig. 4.36 shows a linear FN plot of $In\ (J/E^2)$ versus $1/E$. The $Ø_B$ values ranged from 1.02 to 2.13 eV (Fig. 4.37). The oxidized samples at 700°C had the highest $Ø_B$ value (2.13 eV). The value (2.13 eV) was higher than previous reported value (0.85 eV) (Dakhel, 2004) but lower than values (2.34) (Kim, McIntyre, & Saraswat, 2003) and (2.88 – 2.92 eV) (V. A. Rozhkov *et al.*, 1998) which were extracted from photocurrent experiment.

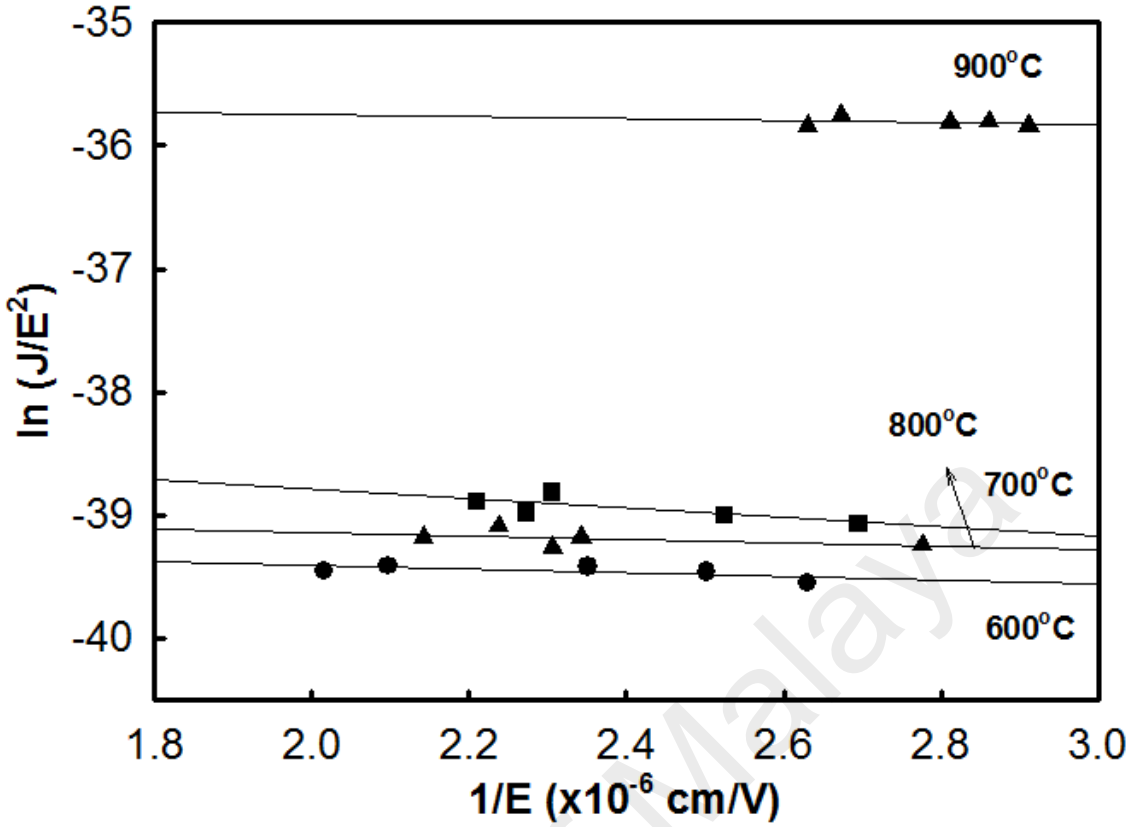

Figure 4.36: FN tunneling linear regression plot [*ln* (J/E^2) versus 1/*E*] of oxidized samples at various temperatures (600 - 900°C).

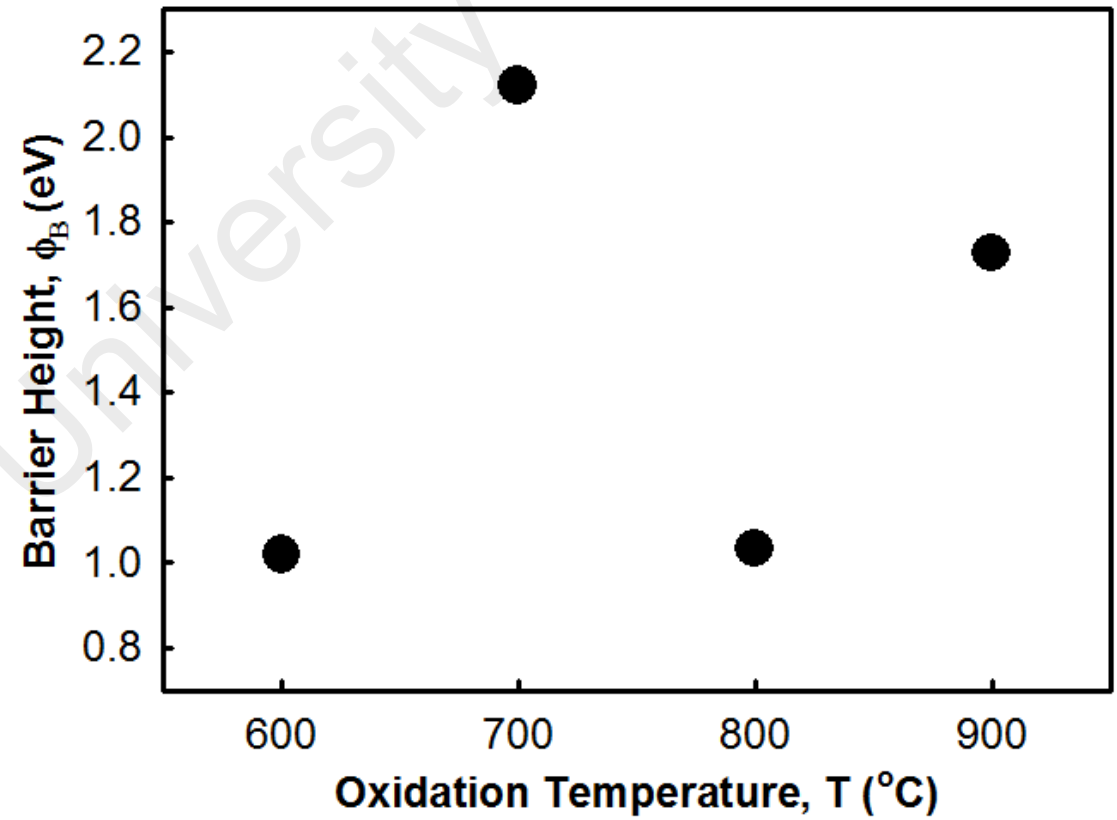

Figure 4.37: Barrier height values as a function of oxidation temperature (600 - 900°C).

Fig. 4.38 shows the typical trap-assisted tunneling plot for investigated samples. A total of 30 points with ~ 0.9 of goodness of fit (r^2) were obtained. Fig. 4.39 shows the trap energy and trap density as a function of oxidation temperature. The 700 ºC samples have the highest trap energy (0.0007485 eV) and lowest energy trap density (6.88 x 10^{21} cm^{-3}) as compared to others samples. This can explained to relatively lower leakage current density of 700 ºC samples (as shown Fig. 4.31. However, the trap energy was lower than the trap energy of silicon nitride (~ 0.033 eV) (Yang, Wong, & Cheng, 1996), (~ 1.03 eV) (Perera, Ikeda, Hattori, & Kuroki, 2003), (~ 0.7 eV) (Fleischer, Lai, & Cheng, 1993), and ZrO_2 (~ 0.8 eV) (Houssa, Stesmans, & Heyns, 2001) reported by previous researchers on the basis of their lower leakage current density (> 10^{-9} A cm^{-2}).

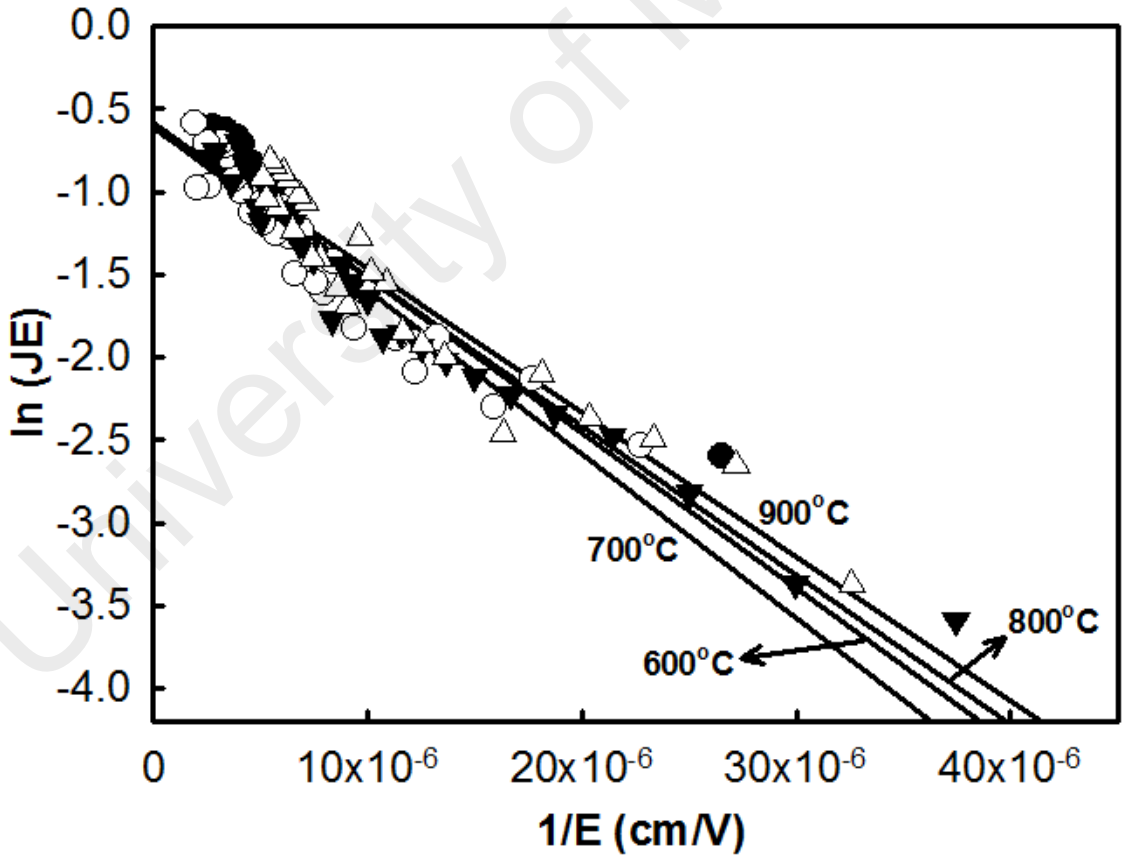

Figure 4.38: Typical trap-assisted tunneling plot of investigated samples at various temperatures (600 – 900 °C).

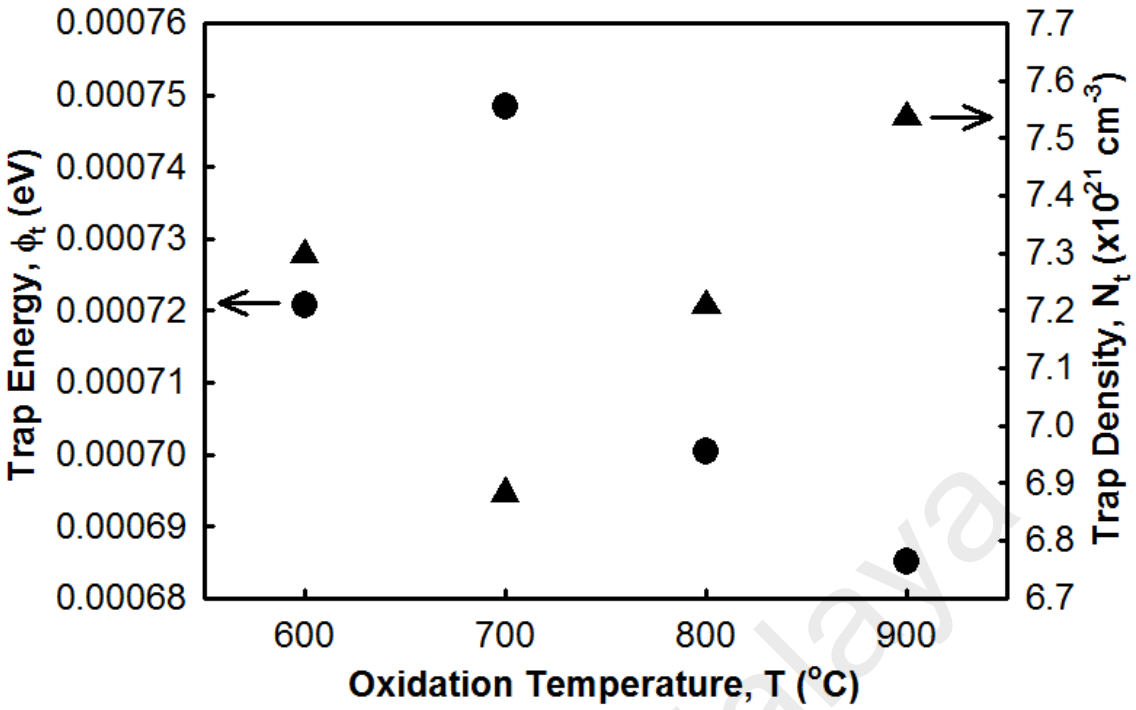

Figure 4.39: The trap energy and trap density of oxidized samples at various temperatures (600 – 900 °C).

4.3.2.2 *C-V* characteristic

Fig. 4.40 shows the typical high frequency (1 MHz) *C-V* curves measured at room temperature for samples thermally oxidized at various temperatures (600 ºC - 900 ºC). The gate bias was swept bi-directionally from + 1 to - 8 V. The highest and lowest capacitance at accumulation level of thermally oxidized samples were obtained at 700 ºC and 900 ºC, respectively. Based on previous reviews and studies (Kurniawan, Cheong, Razak, Lockman, & Ahmad, 2011; Wilk, Wallace, & Anthony, 2001; Y. H. Wong & Cheong, 2011a, 2012a, 2012b), the total capacitance (C_{total}) of the stacked layer was defined as below:

$$\frac{1}{C_{total}} = \frac{1}{C_{Sm_2O_3}} + \frac{1}{C_{IL}} \qquad \text{(Equation 4.10)}$$

where C_{Sm2O3} and C_{IL} were the capacitance of the Sm_2O_3 and the interface layer, respectively. The capacitance can be related to the existence of interface layers between

Sm_2O_3 and Si substrate. The C_{Sm2O3} and C_{IL} can be individually defined as (Kurniawan, Cheong, *et al*., 2011; Kurniawan, Wong, *et al*., 2011; Y. H. Wong & Cheong, 2011a, 2012a, 2012b)

$$C_{ox} = \frac{\kappa \varepsilon_o A}{t_{ox}} \qquad \text{(Equation 4.11)}$$

where C_{ox} is the capacitance of the oxide (Sm_2O_3 or interface layer), κ is the effective dielectric constant, ε_o is the permittivity of free space (8.85 x 10^{-12} F m^{-1}), A is the area of capacitor, and t_{ox} is the thickness of Sm_2O_3 or interface layer. The capacitance of the gate oxide was also strongly affected by κ and t_{ox} since A and ε_o were constant in this work. Hence, the capacitance was proportional to κ/t_{ox}.

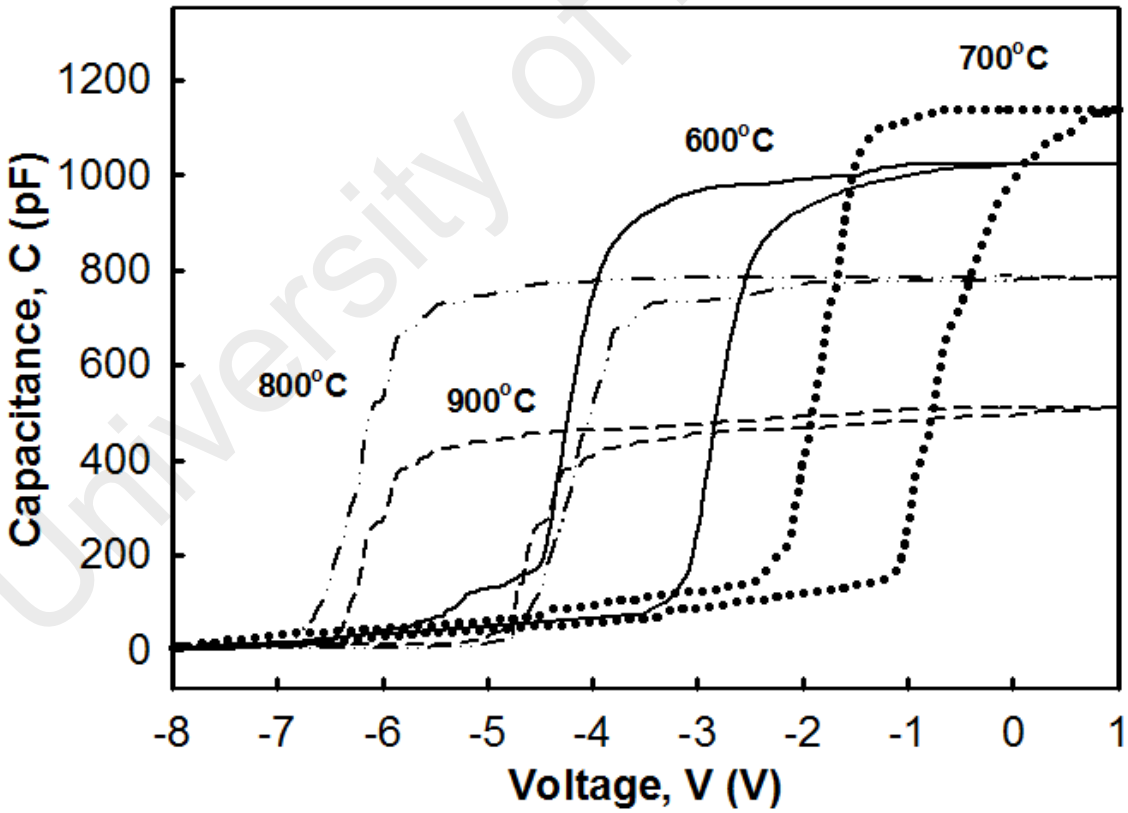

Figure 4.40: High frequency (1 MHz) *C-V* curves measured at room temperature for samples thermally oxidized at various temperatures (600 ºC - 900 ºC).

According to the thickness measurement from HRTEM images, the thicker IL (~20 nm) obtained at 800 ºC and 900 ºC samples had lower capacitances while thinner 600 ºC and 700 ºC (~ 9 nm) samples have higher capacitances. The capacitance degradation was also due to the rougher surface of 800 ºC and 900 ºC samples since surface roughness caused by process variation and inherited atomic level fluctuation (J. L. Zhang, Yuan, Ma, & Oates, 2001). By using the Eq. 4.11, the effective dielectric constant can be calculated. The relationship of the effective dielectric constant and oxidation temperature is shown in Fig. 4.41. The higher capacitance was attributed to a higher value of the effective dielectric constant.

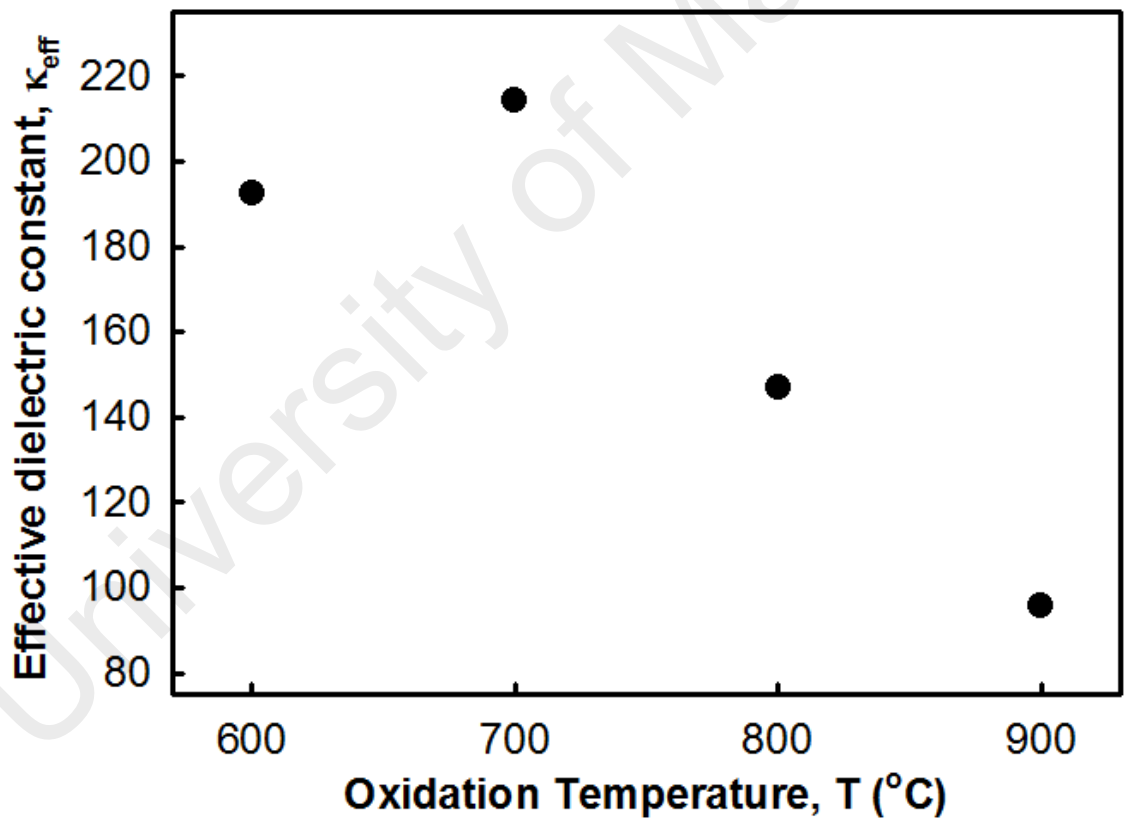

Figure 4.41: The effective dielectric constant of investigated samples as a function of oxidation temperature (600 ºC - 900 ºC).

In the *C-V* curves, a depletion region can be observed in the negative bias of all investigated capacitors which means that the flatband voltage (ΔV_{FB}) was shifted negatively and positive effective oxide charges (Q_{eff}) were accumulated during the thermal oxidation process. The Q_{eff} was calculated based on the equation below (Y. H. Wong & Cheong, 2011a, 2012a, 2012b):

$$Q_{eff} = \frac{\Delta V_{FB} C_{ox}}{qA} \qquad \text{(Equation 4.12)}$$

where q is the electronic charge. The calculated Q_{eff} for thermally oxidized samples is shown in Fig. 4.42. The lowest Q_{eff} (2.81 x 10^{13} cm^{-2}) was obtained by films oxidized at 700 ºC.

Hysteresis of *C-V* curves between forward and reverse bias were observed in all investigated samples. This phenomenon occurs due to slow traps located at some distance from the interface. The slow trap density (*STD*) can be defined as below: (Y. H. Wong & Cheong, 2011a, 2012a, 2012b)

$$STD = \frac{\Delta V C_{ox}}{qA} \qquad \text{(Equation 4.13)}$$

where ΔV was the difference between flatband voltage of the hysteresis curve. The films thermally oxidized at 700 ºC have the lowest *STD* value (0.566 x 10^{13} cm^{-2}) as shown in Fig. 4.42.

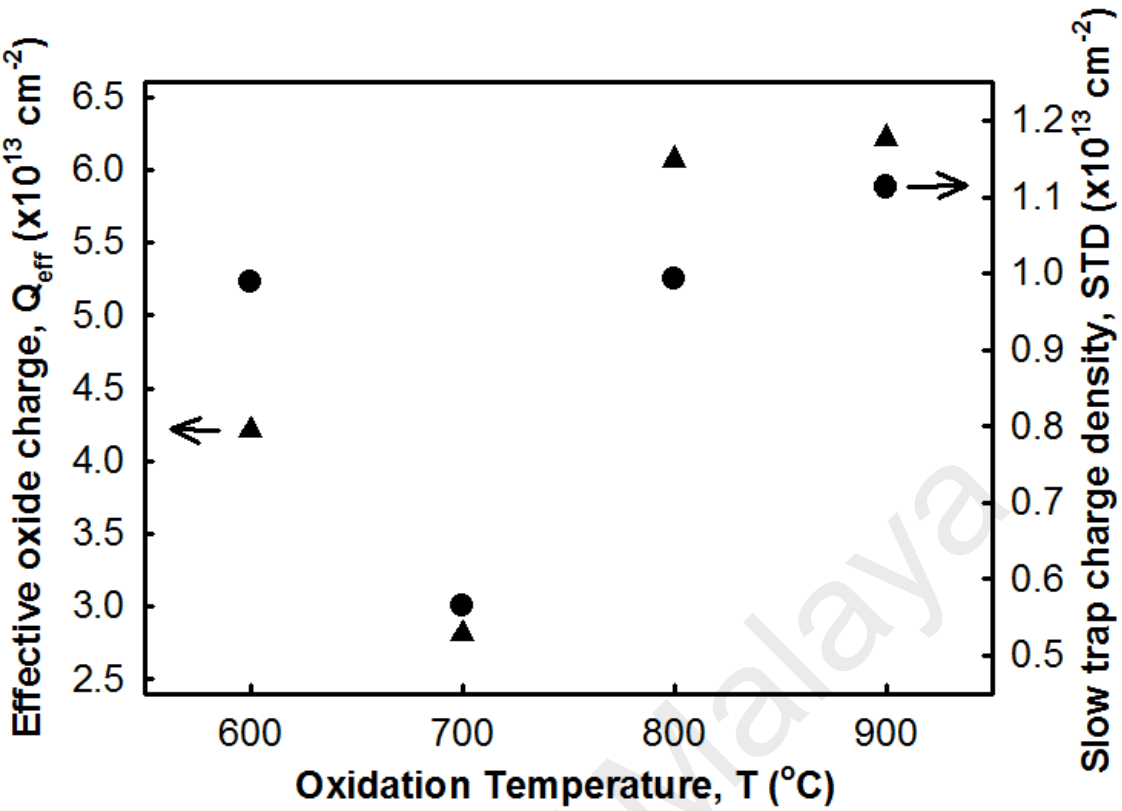

Figure 4.42: Effective oxide charge and slow trap charge density of oxidized samples at various temperatures (600 – 900 °C).

Fig. 4.43 shows the average interface trap density (D_{it}) as a function of energy level of the trap. The D_{it} was calculated using the Terman method (Y. H. Wong & Cheong, 2011a, 2012a, 2012b).

$$D_{it} = \frac{\Delta V_g C_{ox}}{\phi_s q A} \qquad \text{(Equation 4.14)}$$

where *Øs* is the surface potential of Si at a specific gate voltage, V_g. The surface potential of a particular capacitance was obtained from the ideal MOS capacitor. The gate voltage was obtained from experimental *C-V* curve which has the same capacitance as that of *Øs*. The steps were repeated until a relevant D_{it} versus $(E_C\text{-}E)$ curve was obtained as shown in Fig. 4.43. The films thermally oxidized at 700 ºC have the lowest D_{it} value (~ 10^{14} eV^{-1} cm^{-2}) at 0.06-0.27 eV of $(E_C\text{-}E)$. However, as compared to previous works (Pan & Huang, 2010), their leakage current density (~ 10^{-7} A cm^{-2}) was lower than our research

(~ 10^{-4} A cm^{-2}) as shown Fig. 4.34. This is attributed to the lower average interface trap density (~ 10^{12} eV^{-1} cm^{-2}) in their samples.

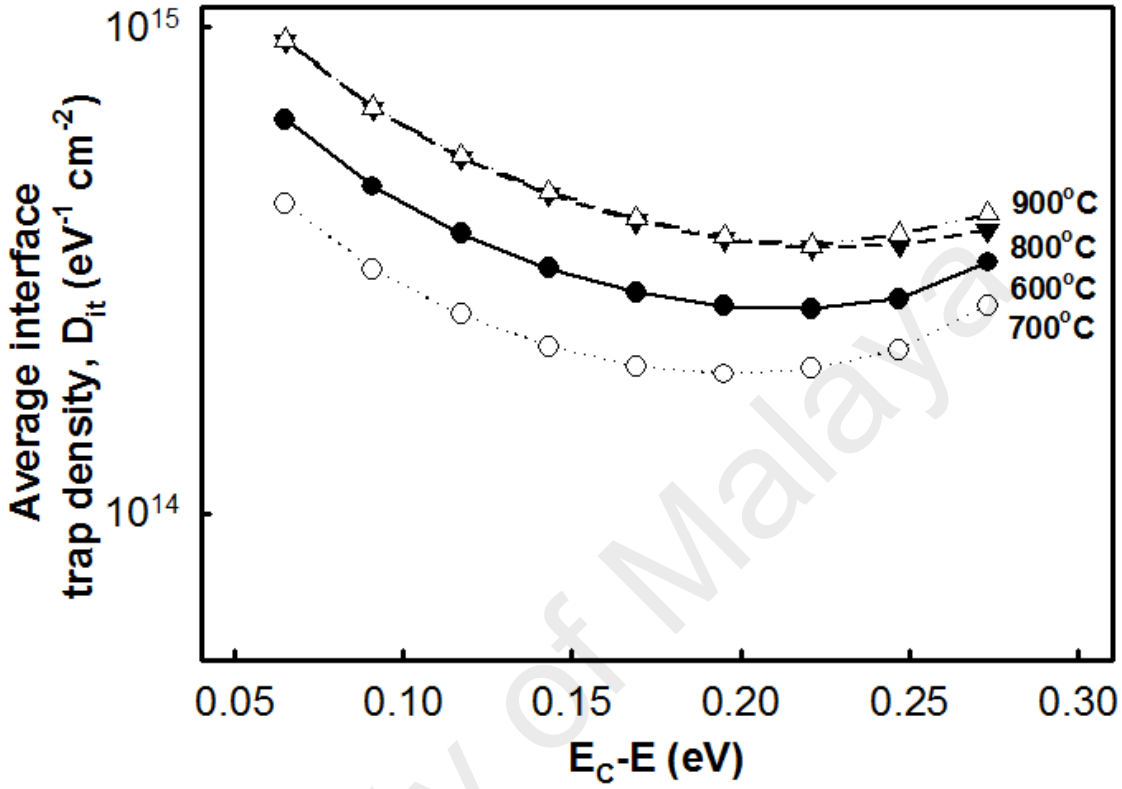

Figure 4.43: The average interface trap density as a function of oxidation temperature (600 – 900 °C).

By calculating the area under the D_{it} versus $(E_C\text{-}E)$ curve, the total interface trap density (D_{total}) of energy range $(E_C\text{-}E)$ can be determined (Y. H. Wong & Cheong, 2011a, 2012a, 2012b). Fig. 4.44 shows the total interface trap density (D_{total}) as a function of oxidation temperature (600 - 900 °C). The D_{total} exhibited a similar trend with the changes of Q_{eff} and *STD*. The films thermally oxidized at 700 ºC have the lowest D_{total} which was 0.73 x 10^{14} cm^{-2}.

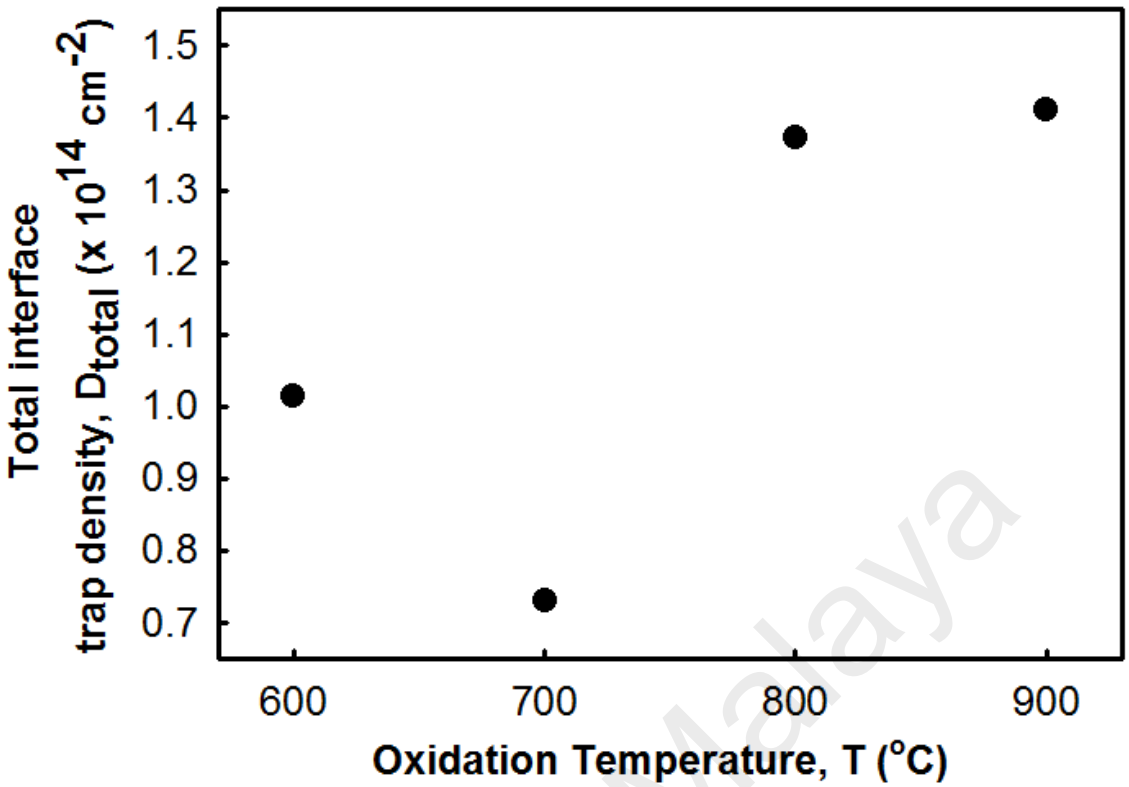

Figure 4.44: The total interface trap density as a function of oxidation temperature (600 - 900 °C).

In this part, the pure Sm metal film was sputtered on Si substrates and then thermally oxidized in oxygen ambient at various temperatures (600 °C to 900 °C) for 15 min. The existence of polycrystalline Sm_2O_3 and semi-polycrystalline interfacial layers were confirmed by the XRD, Raman, and EDX results, and supported by the FTIR results indicating the broadening and/or shifting of Sm - O and Si - Si bonding peaks. Based on these results, a sketched model was suggested. The crystallite sizes of the Sm_2O_3 which was calculated from the W–H plot and Scherrer equation exhibited similar trend. The sample oxidized at 700 °C had the thinnest interfacial layer and thickest Sm_2O_3 film as measured from the HRTEM images. According to the *C-V* and *J-E* measurements, the 700 °C sample which had smoother and uniform surface exhibited the best electrical results which had the highest κ_{eff} value of 214, the highest breakdown voltage field of 0.71 MV cm^{-1} at ~ 10^{-4} A cm^{-2}, the highest barrier height of 2.13 eV, the highest trap energy of 0.0007485 eV, and the lowest trap density of 6.88 x 10^{21} cm^{-3}. This is attributed to the thinnest interface layer between the Sm_2O_3 and Si substrate, the reduction in

effective oxide charge (2.81 x 10^{13} cm^{-2}), the slow trap charge density (5.56 x 10^{12} cm^{-2}), the average interface trap density (~ 10^{14} eV^{-1} cm^{-2}), and the total interface trap density (7.31 x 10^{13} cm^{-2}).

CHAPTER 5

RESULTS AND DISCUSSION: THERMAL OXYNITRIDATION

5.1 Introduction

This chapter presents and discusses the experimental results of physical, chemical, and electrical characterizations of thermally oxynitrided of sputtered Sm thin film on Si substrate. This chapter consists of two main parts: (i) effects of oxynitridation temperature for 15 min on sputtered Sm thin film on Si substrate and (ii) effects of oxynitridation duration at 700 ^{o}C on sputtered Sm thin film on Si substrate.

5.2 Effects of oxynitridation temperature on sputtered Sm thin film on Si substrate

5.2.1 Physical and chemical properties

5.2.1.1 XRD analysis

Fig. 5.1 shows the XRD patterns of the sputtered Sm thin film thermally oxynitrided on Si substrate at different temperatures (600 °C, 700 °C, 800 °C, and 900 °C). Four strong peaks at 33°, 61.9°, 69.6°, and 75.6° were detected in all samples which were matched with four different planes of cubic structure of silicon which are c-Si (111), c-Si (311), c-Si (400), and c-Si (331), respectively. These peaks were confirmed by Inorganic Crystal Structure Database (ICSD) with the reference code of 98-001-6569. The cubic structure of the Sm_2O_3 (c-Sm_2O_3) was revealed at various diffraction angles of 45.9°, 47.7°, 54.5°, 56.3°, 74.9°, and 76.3° corresponding to various planes of (152), (334), (154), (226), (004), and (257), respectively. These peaks were confirmed by ICSD with the reference code of 98-004-0475. There was no significant peak which belongs to Sm nitride. This may be due to either the low concentration of N or the high concentration of

Sm-N bond in amorphous structure of interfacial layer. As summarized in Fig. 5.2, the intensities of 47.7°, 54.5°, 56.3°, and 74.9° increased from 600 °C to 700 °C but decreased from 700 °C to 900 °C. As compared to oxidized samples, the number of peaks was smaller and the crystallinity of the Sm_2O_3 did not increase with oxidation temperature. It can be inferred that the thickness of the Sm_2O_3 was smaller than the oxidized sample and the reduction of the amount for the Sm_2O_3 compound due to the incorporation of nitrogen.

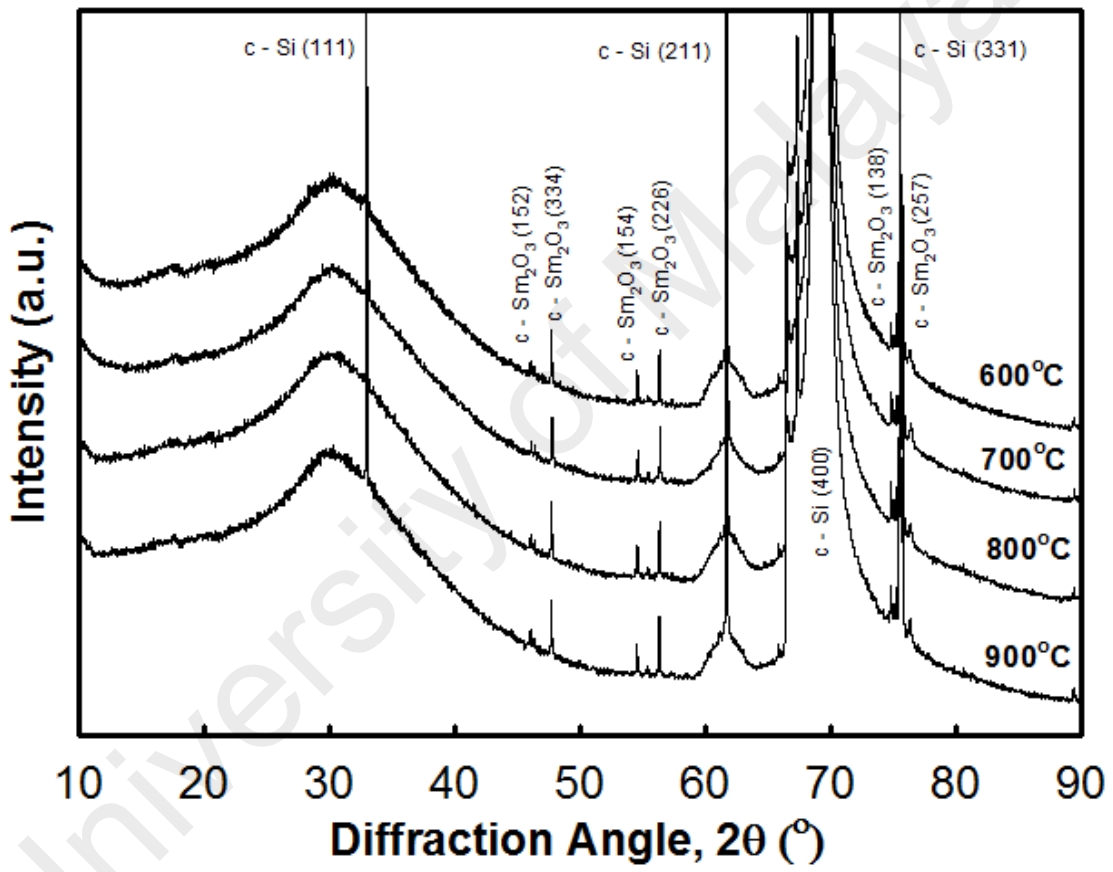

Figure 5.1: XRD patterns of thermally oxynitrided samples at various temperatures (600 – 900°C).

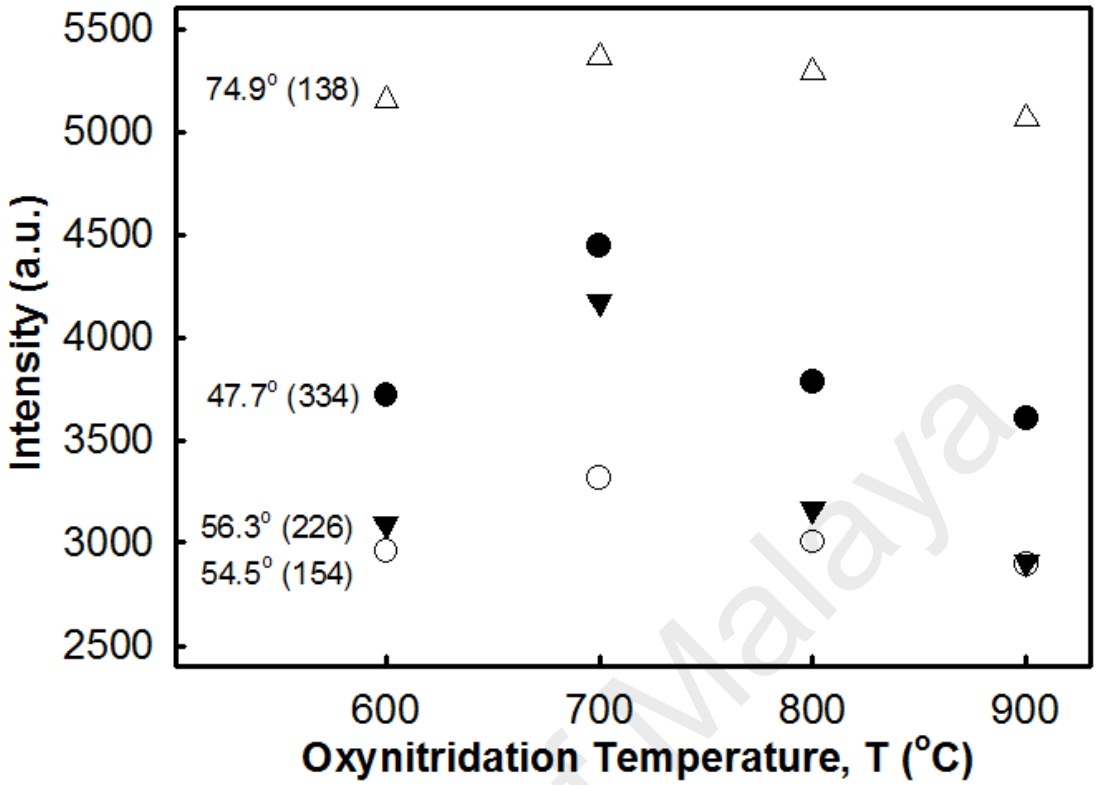

Figure 5.2: Intensities of the Sm_2O_3 (334), (154), (226), and (138) at 47.7°, 54.5°, 56.3°, and 74.9°, respectively as a function of oxynitridation temperatures (600 - 900°C).

By using the Scherrer equation, the crystallite sizes of the Sm_2O_3 averaged over various peak positions for 600 °C, 700 °C, 800 °C, and 900 °C were 38.24 nm, 30.76 nm, 31.40 nm, and 39.43 nm, respectively (Fig. 5.3). It was observed that crystallite sizes of 700 °C samples gave smaller differences or distribution of size. Since the Scherrer equation only gives lower bound of crystallite size and the microstrain was not taken into account, the W-H analysis was also conducted.

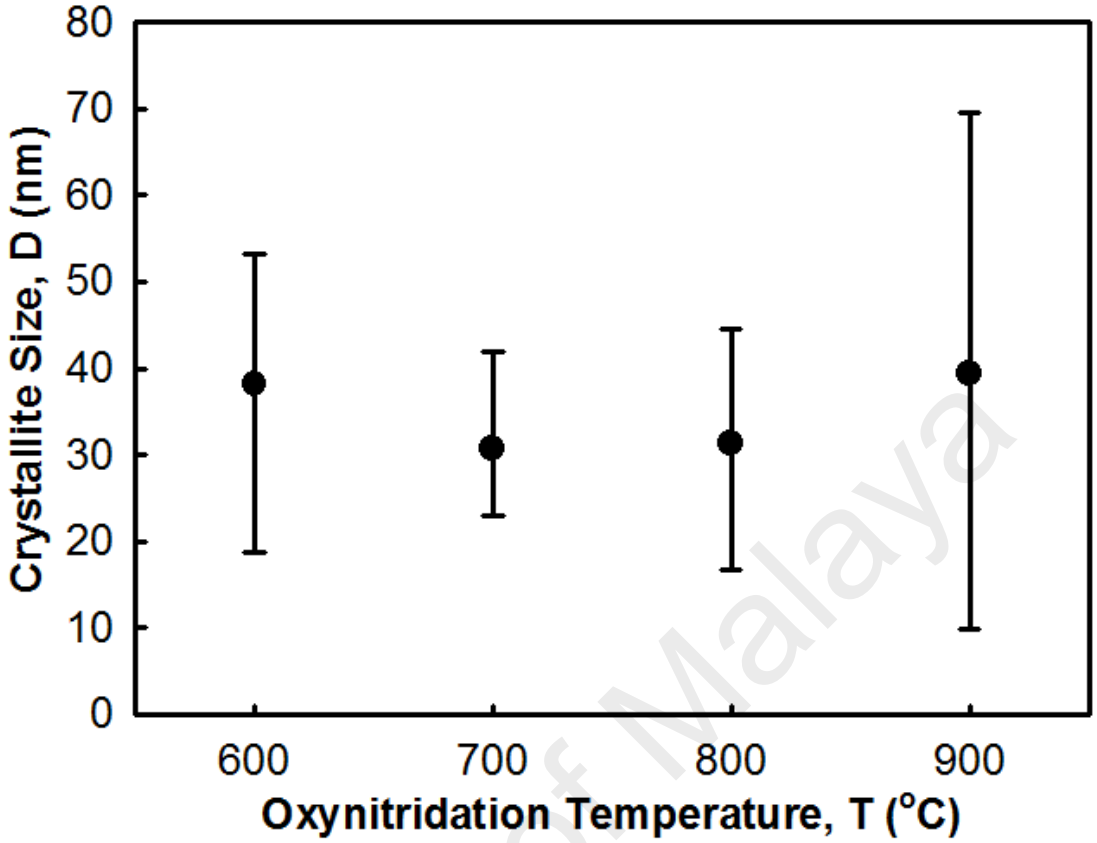

Figure 5.3: Calculated crystallite sizes by Scherrer equation of Sm_2O_3 as a function of oxynitridation temperatures (600 - 900°C).

A β_{hkl} cos θ versus 4 sin θ graph (Fig. 5.4) was plotted based on Eq. 3.6. Based on the W-H analysis, the crystallite sizes of the Sm_2O_3 ranged from 49.38 nm to 69.51 nm while microstrain of the Sm_2O_3 ranged from 0.01269 to 0.01614 as shown in Fig. 5.5. The crystallite size and microstrain did not increase with the oxynitridation temperature as compared to oxidized samples. The calculated crystallite size of the Sm_2O_3 by both the Scherrer equation and the W-H analysis had the same trend.

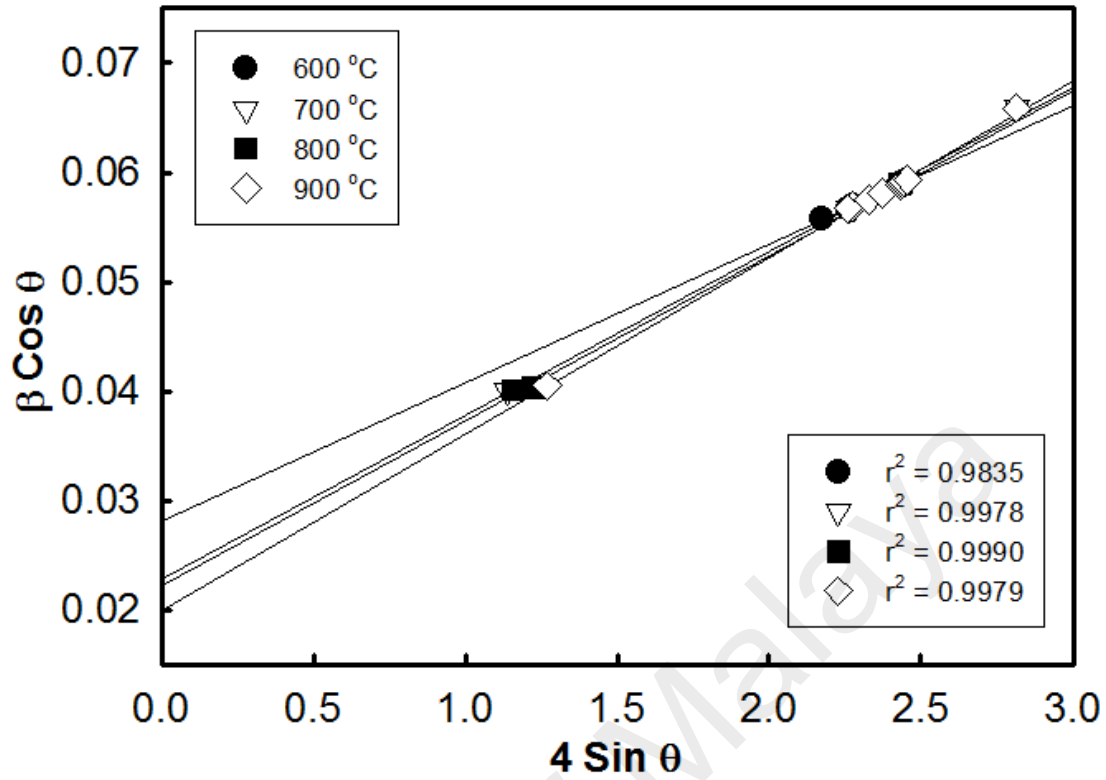

Figure 5.4: W-H plot of thermally oxynitrided samples at various temperatures (600 - 900°C).

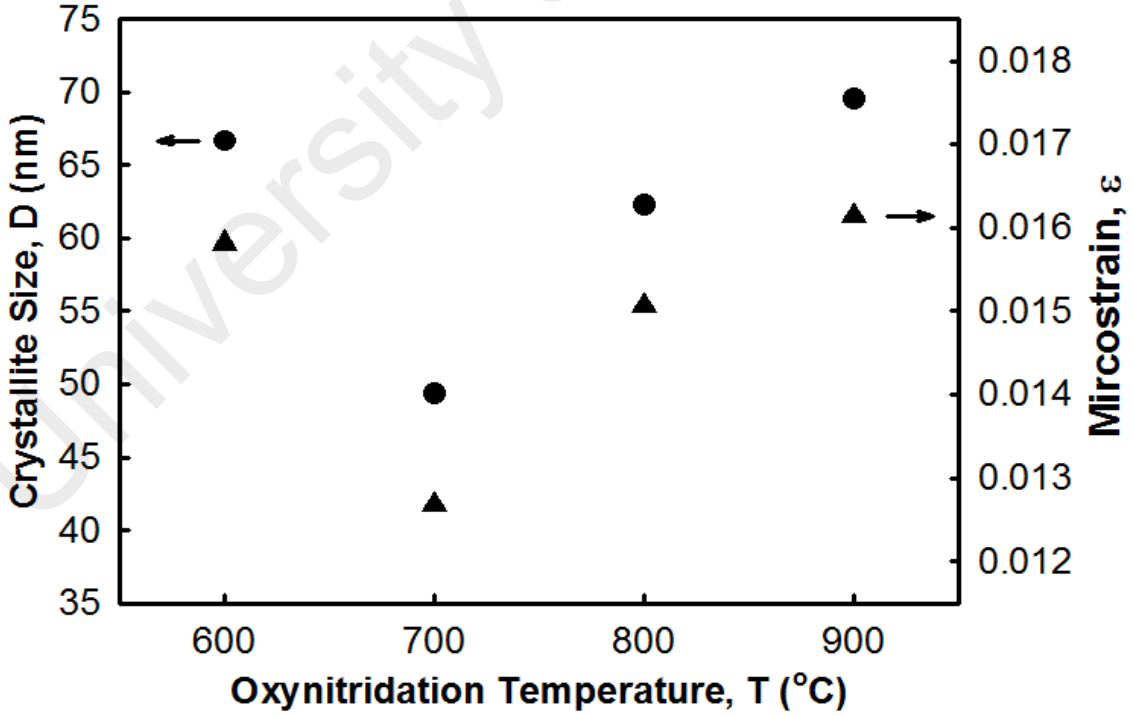

Figure 5.5: Relationship of calculated crystallite size and microstrain from W-H plot as a function of oxynitridation temperatures (600 – 900 °C).

5.2.1.2 XPS analysis

In order to investigate the surface composition and chemical bonding of thermally oxynitrided samples, all thermally oxynitrided samples were analyzed by both wide and narrow scan by XPS. According to the wide scan XPS, the core level spectra of Sm 3*d*, Si 2*p*, O 1*s*, and N 1*s* were detected in all thermally oxynitrided samples. Fig. 5.6 [(a)-(d)] shows the atomic percentage of the detected elements as functions of penetration depth and etching time for 600 °C to 900 °C of the thermally oxynitrided samples. The total thickness of 600 °C and 700 °C samples was lower than 800 °C and 900 °C samples. The atomic percentage of Sm, O, and N decreased when the etching time increased. An extremely high atomic percentage of Si indicated the appearance of Si substrate. Initially, the atomic percentage of Si was extremely small and then increased when the etching time was extended. This indicates the absence of Si at the outermost layer ($Sm_xO_yN_z$) but it was present at the interfacial layer ($Sm_aSi_bO_cN_d$). An interfacial layer ($Sm_aSi_bO_cN_d$) with a mixture of Sm, Si, O, and N was detected in between the outermost layer ($Sm_xO_yN_z$) and the Si substrate. A relatively low concentration (< 9 at %) of N was detected in all samples. Extensive analysis of the chemical compound of the interfacial layer ($Sm_aSi_bO_cN_d$) was done by a narrow scan XPS and is presented in the subsequent paragraph.

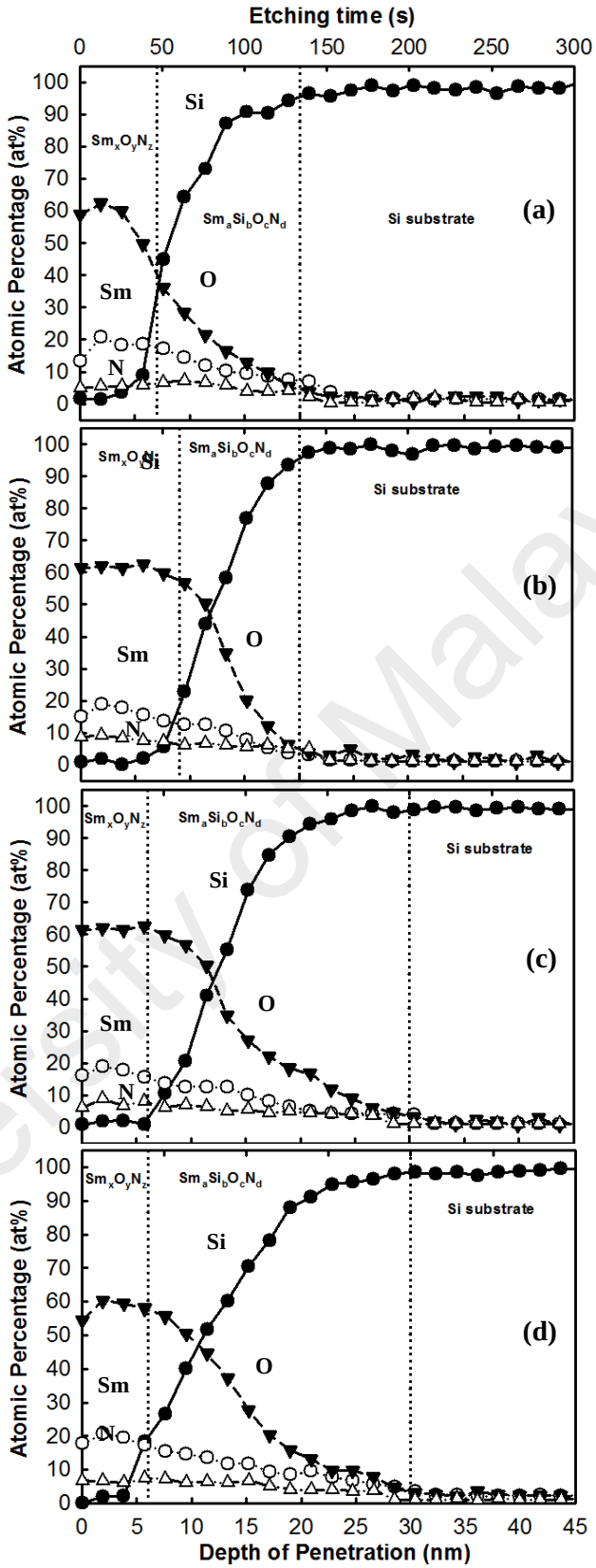

Figure 5.6: The atomic percentage of the Sm, Si, O, and N as functions of penetration depth and etching time: (a) 600 °C, (b) 700 °C, (c) 800 °C, and (d) 900 °C.

Fig. 5.7 [(a)-(d)] to Fig. 5.10 [(a)-(d)] show the narrow scan of each core level spectrum of Sm, O, Si, and N as a function of etching time for various oxynitridation temperatures (600 – 900 °C). The measured peaks (dotted line) were deconvoluted using non-linear Gaussian-Lorentzian functions (solid lines) by the CasaXPS software (version 2.3.16). The binding energy of Sm - O at the etching time of 0 s for 600 °C, 700 °C , 800 °C , and 900 °C samples were 1081 eV, 1081.25 eV, 1081.5 eV, and 1080.5 eV as shown in Fig. 5.7 [(a)-(d)] (Chen, Her, Mondal, Hung, & Pan, 2013; Chen, Hung, *et al*., 2013; D. G. Huang *et al*., 2009; Kao *et al*., 2010; Pan & Huang, 2010; Tang *et al*., 2013; Uwamino, Ishizuka, & Yamatera, 1984). The binding energies were shifted to higher binding energy (< 2 eV) when the etching time increased.

The Sm - Si - O bond (~ 1079 eV) was not detected at the etching time of 0 s in any thermally oxynitrided sample. However, the Sm - Si - O peak appeared and started to shift to higher binding energy when the etching time further increased. The intensity of the Sm - Si - O peak increased when the etching time was extended in all thermally oxynitrided samples. This proves that the outermost layer did not contain Si-related compounds but only the interfacial layer contains Si-related compounds. Besides that, the Sm - N bond (~ 1076 eV) was detected at all etching time in all thermally oxynitrided samples. The intensity of the Sm - N peak decreased when the etching time increased in all thermally oxynitrided samples. This trend can also be observed in Fig. 5.6 where the concentration of N decreased when the etching time increased. When the etching extended to Si substrate, the intensity of Sm 3*d* spectra decreased and disappeared.

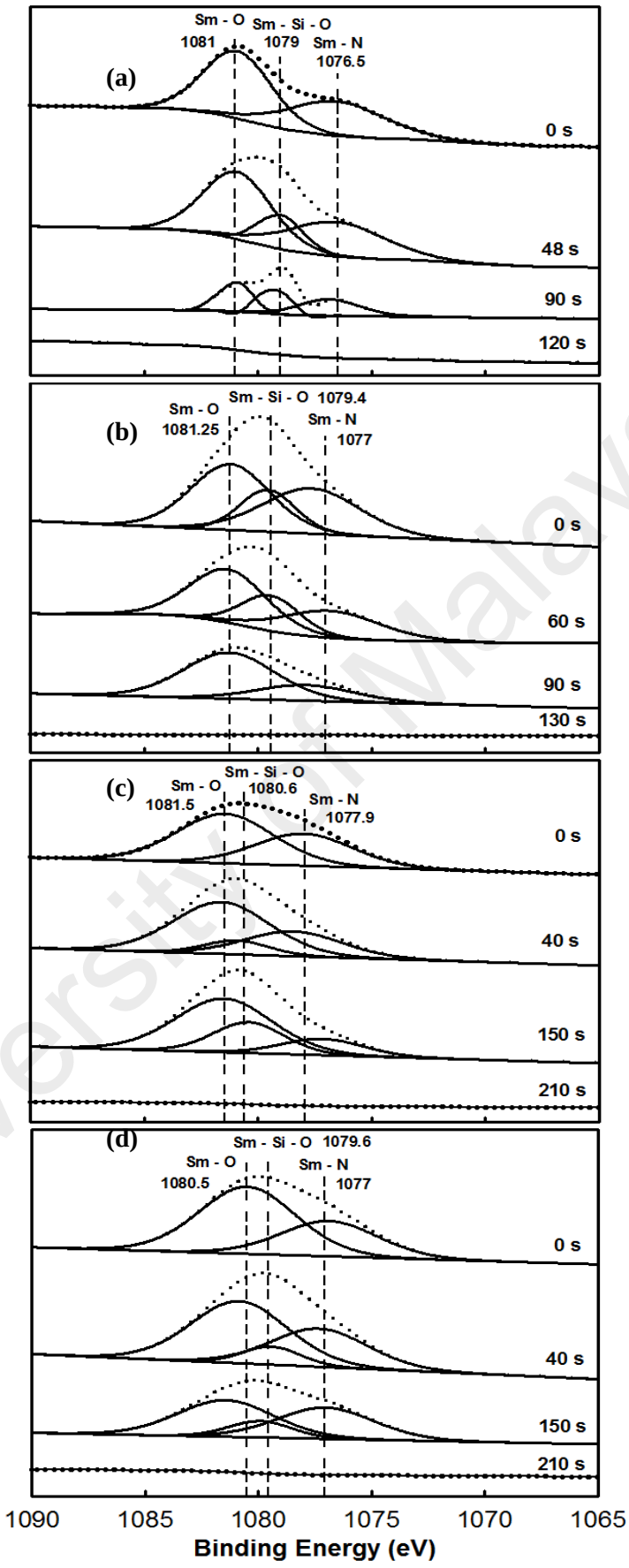

Figure 5.7: Variation of Sm 3*d* core level XPS spectra as a function of etching time at various oxynitridation temperatures: (a) 600 °C, (b) 700 °C, (c) 800 °C, and (d) 900 °C.

Fig. 5.8 [(a)-(d)] shows O 1*s* core level XPS spectra of samples thermally oxynitrided at various oxynitridation temperatures (600 – 900 °C). Both detected binding energies of 529 eV and 530 eV at etching time of 0 s were assigned to Sm - O bond (Chen, Her, *et al*., 2013; Chen, Hung, *et al*., 2013; Jeon & Hwang, 2003; Kao *et al*., 2010; Pan & Huang, 2010). However, the intensities of both Sm - O bonds decreased when the etching time increased. This inferred that the structural changes happened in the $Sm_xO_yN_z$/Si substrate system due to the formation of an interfacial layer since the binding energy was sensitive to the changes in local chemical environment (Brow & Pantano, 1986). Again, the Sm - Si - O bond (~ 531.1 eV) was not detected at the etching time of 0 s in all thermally oxynitrided samples but appeared when the etching time extended (Kao *et al*., 2010; Pan & Huang, 2010). This matched with the inference in the previous paragraph. When the etching extended to the Si substrate, the intensity of O 1*s* spectra decreased and disappeared.

Fig. 5.9 [(a)-(d)] shows Si 2*p* core level XPS spectra of samples thermally oxynitrided at various oxynitridation temperatures (600 – 900 °C). At the etching time of 0 s, no significant peak was recorded in all thermally oxynitrided samples. This indicated that the outermost layer did not contain Si-related compounds. When the etching time extended, three significant peaks were detected and located at ~ 99.3 eV, ~ 101.9 eV, and ~ 103.1 eV (Kao *et al.*, 2010; Pan & Huang, 2010; Y. H. Wong & Cheong, 2011b). These three peaks were assigned to Si - Si, Si - N, and Sm - Si – O bonds. The intensity of the Si - Si bond (~ 99.3 eV) increased significantly when the etching time was further extended (> 120 s). This extremely high intensity of peak originated from the Si substrate (Kao *et al.*, 2010; Pan & Huang, 2010). The Si - N and Sm - Si – O bonds were detected in all thermally oxynitrided samples and this is probably due to the formation of an interfacial layer as inferred in previous paragraph.

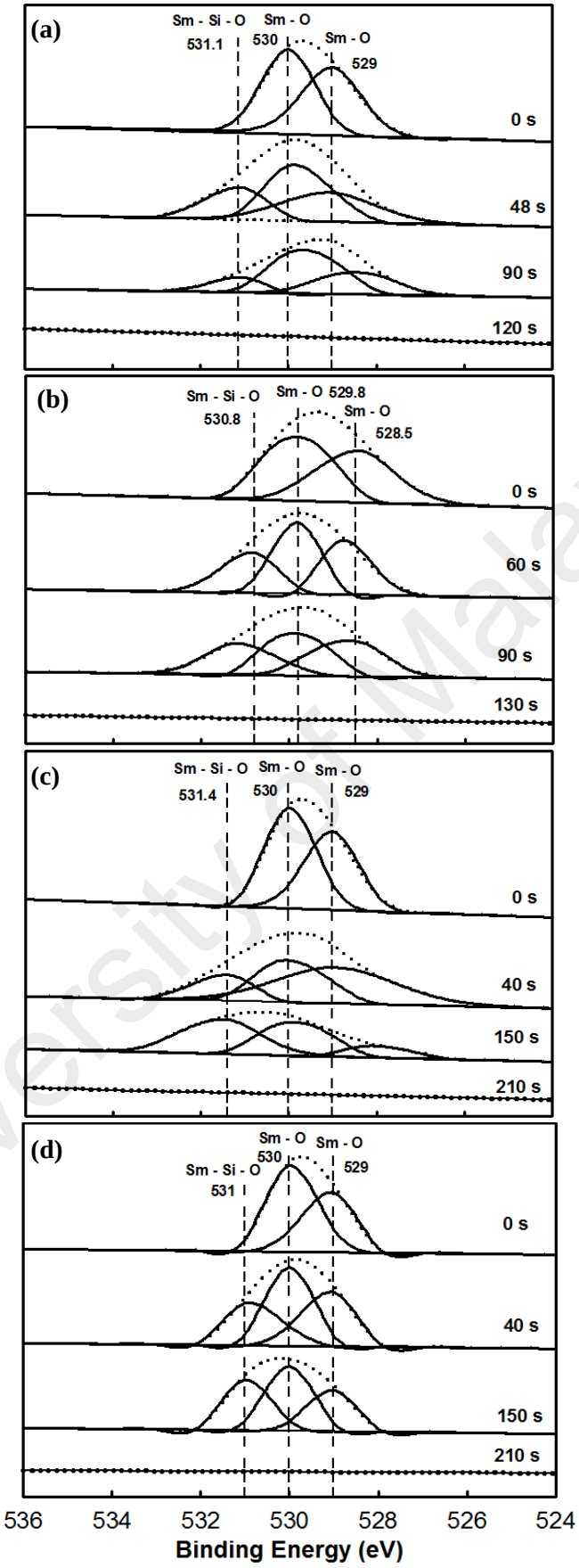

Figure 5.8: Variation of O 1*s* core level XPS spectra as a function of etching time at various oxynitridation temperatures: (a) 600 °C, (b) 700 °C, (c) 800 °C, and (d) 900 °C.

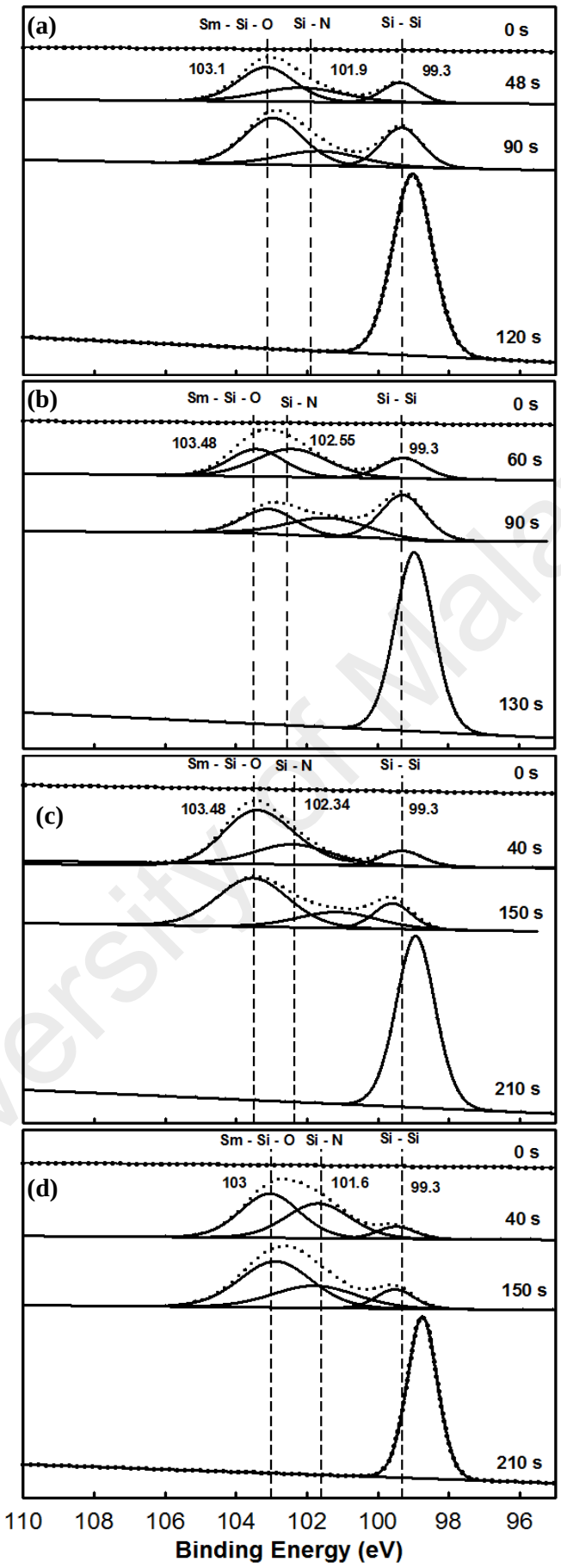

Figure 5.9: Variation of Si 2*p* core level XPS spectra as a function of etching time at various oxynitridation temperatures: (a) 600 °C, (b) 700 °C, (c) 800 °C, and (d) 900 °C.

Fig. 5.10 [(a)-(d)] shows N 1*s* core level XPS spectra of samples thermally oxynitrided at various oxynitridation temperatures (600 – 900 °C). Only the Sm - N bond (~ 400 eV) was recorded at the etching time of 0 s in all thermally oxynitrided samples (Barhai, Kumari, Banerjee, Pabi, & Mahapatra, 2010; ; D. G. Huang *et al.*, 2009; Futsuhara, Yoshioka, & Takai, 1998; Lippitz & Hubert, 2005; Tabet, Faiz, & Al-Oteibi, 2008). When the etching time was further extended, Si - N (~ 399 eV) was detected in all thermally oxynitrided samples (Hegde, Tobin, Reid, Maiti, & Ajuria, 1995; Shallenberger, Cole, & Novak, 1999; Y. H. Wong & Cheong, 2011b). The intensity of the Sm - N bond (~ 400 eV) decreased when the etching time increased which was consistent with the depth profile of thermally oxynitrided samples as shown in Fig. 5.6. When the etching extended to the Si substrate, the intensity of N 1*s* spectra decreased and disappeared.

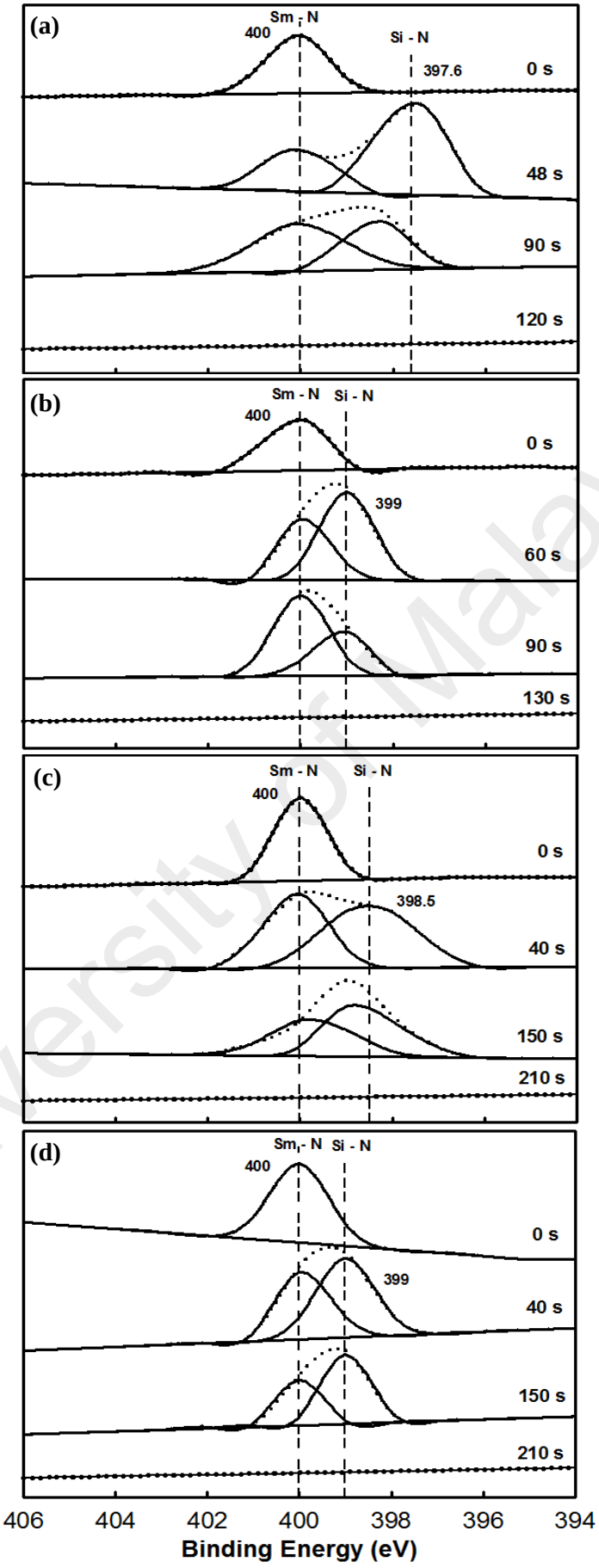

Figure 5.10: Variation of N 1*s* core level XPS spectra as a function of etching time at various oxynitridation temperatures: (a) 600 °C, (b) 700 °C, (c) 800 °C, and (d) 900 °C.

5.2.1.3 FTIR analysis

Fig. 5.11 shows the FTIR transmittance spectra (1200 - 400 cm^{-1}) of the samples thermally oxynitrided at different temperatures. The Si - Si vibration mode band was located at 600 cm^{-1} while the Si - O vibration mode band was located at 1050 cm^{-1} in all samples (Ansart, Ganda, Saporte, & Traverse, 1995; Y. H. Wong, Atuchin, Kruchinin, & Cheong, 2014; Y. H. Wong & Cheong, 2011b). The Si - Si peak broadened as the oxynitridation temperature increased. For oxynitridation temperature of 600 °C, the Sm - O vibration mode was detected at 430 cm^{-1} (Hussein *et al*., 2003; Ismail, 1995; Mandal *et al*., 2014; Ruiz-Gomez *et al*., 2014), 480 cm^{-1} (Ghosh *et al*., 2008; Hussein *et al*., 2003; Ruiz-Gomez *et al*., 2014), and 505 cm^{-1} (Hussein *et al*., 2003; Ismail, 1995). At 430 cm^{-1}, the intensity of the peak increased when the temperature increased from 600 °C to 700 °C. The increment of intensity is probably due to the increment of the crystallinity. However, the peak broadened and shifted when the temperature increased from 700 °C to 900 °C. For 480 cm^{-1} and 505 cm^{-1}, both peaks were combined into a single peak when temperature increased from 600 °C to 800 °C but start to broaden when the temperature increased to 900 °C. The peak at 672 cm^{-1} was assigned to the Sm – N vibration mode. The peak shifted when the temperature increased from 600 °C to 900 °C. The broadening and shifting of peaks may be due to the formation or growth of the interfacial layer as inferred from XRD and XPS analysis.

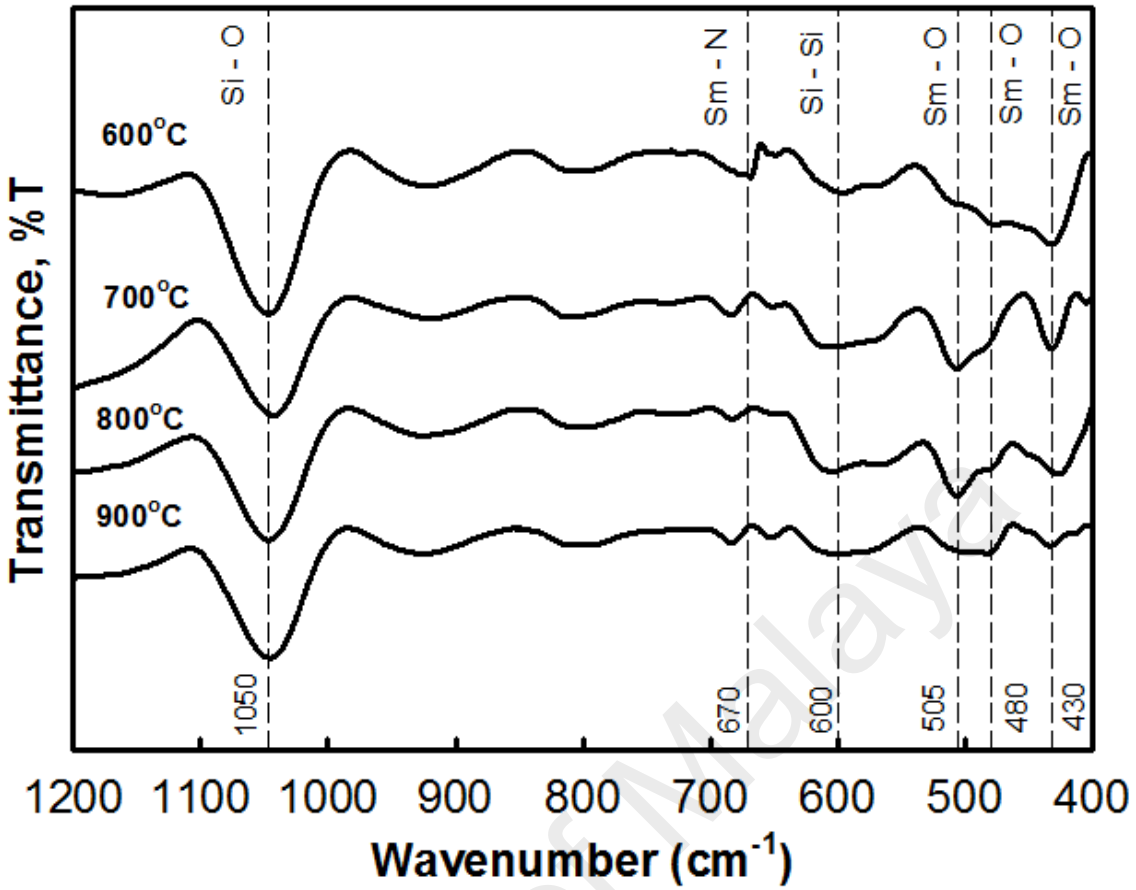

Figure 5.11: Transmittance spectra of thermally oxynitrided samples at various temperatures (600 - 900°C).

5.2.1.4 Raman analysis

Fig. 5.12 shows the Raman spectra for all samples thermally oxynitrided at various temperatures (600 - 900°C). The peak at 527 cm^{-1} was assigned to silicon substrate (N. Jiang, Georgiev, Wen, & Jayatissa, 2012; Y. H. Wong & Cheong, 2011b). The peaks at 310 cm^{-1} (S. Jiang *et al*., 2013), 441 cm^{-1} (Hongo *et al*., 2007; N. Jiang *et al*., 2012; S. Jiang *et al*., 2013), 628 cm^{-1} (S. Jiang *et al*., 2013), and 675 cm^{-1} (Hongo *et a*l., 2007; Mandal *et al*., 2014; N. Jiang *et al*., 2012; S. Jiang *et al*., 2013) were identified to be Sm_2O_3. The 700 °C sample had the highest intensity of these four peaks among the samples (Fig. 5.13). This is probably due to the increment of crystallinity as inferred in the XRD and FTIR analysis. According to this result, it was confirmed that polycrystalline Sm_2O_3 was formed and complemented with the XRD, XPS, and FTIR results.

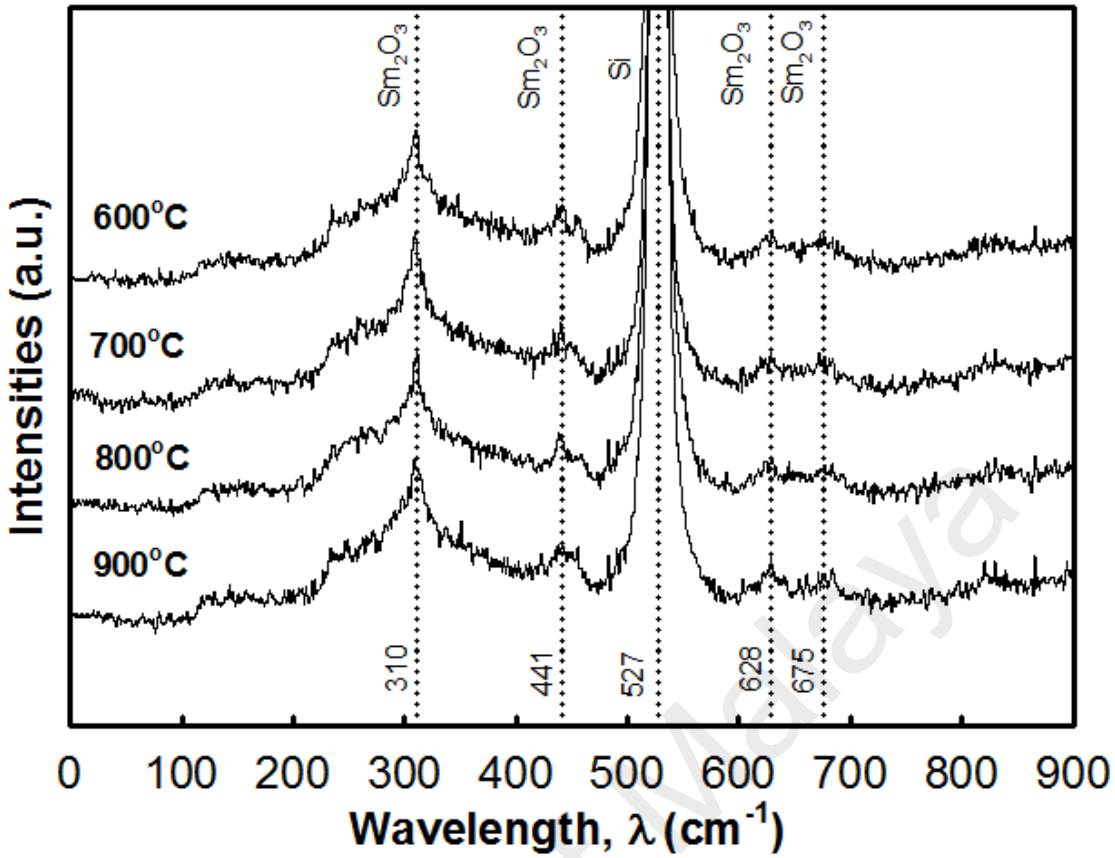

Figure 5.12: Raman spectra of thermally oxynitrided samples at various temperatures (600 - 900°C).

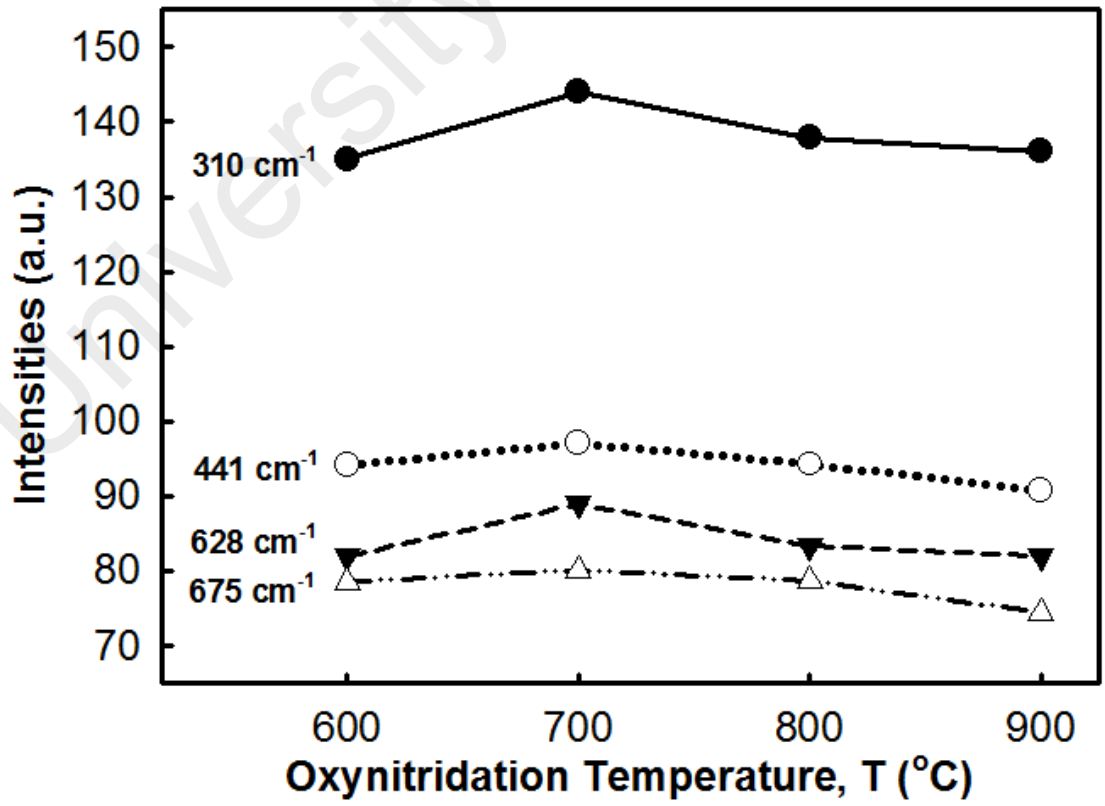

Figure 5.13: Intensities of Sm_2O_3 at 310 cm^{-1}, 441 cm^{-1}, 628 cm^{-1}, and 675 cm^{-1} as a function of oxynitridation temperatures (600 - 900°C).

5.2.1.5 HRTEM and EDX analysis

Fig. 5.14 shows the cross sectional of HRTEM images of the samples thermally oxynitrided at different oxynitridation temperatures (600 °C - 900 °C). It was observed that the oxynitride/semiconductor structure consists of three thin films: Si substrate, $Sm_aSi_bO_cN_d$, and $Sm_xO_yN_z$ films. The $Sm_xO_yN_z$ with polycrystalline structure and the $Sm_aSi_bO_cN_d$ with amorphous structure were observed. This result proves that the inference in the XRD, XPS, FTIR, and Raman analysis were true. The variation of the XRD, XPS, FTIR, and the Raman results were due to chemical and structural changes (formation of an interfacial layer) in the $Sm_xO_yN_z$/Si substrate system. As summarized in Fig. 5.15, the total thickness of Sm sputtered films thermally oxynitrided at 600 °C, 700 °C, 800 °C, and 900 °C were 18 nm, 19.6 nm, 31.8 nm, and 32.7 nm, respectively. The thickness of $Sm_aSi_bO_cN_d$ of 600 °C, 700 °C, 800 °C, and 900 °C samples were 11 nm, 10.6 nm, 25.55 nm and 26.7 nm, respectively. The thickness of $Sm_xO_yN_z$ of 600 °C, 700 °C, 800 °C, and 900 °C samples were 7 nm, 9 nm, 6.25 nm, and 6 nm, respectively. The lattice fringes of $Sm_xO_yN_z$ can be clearly seen with interplanar spacing (*d*) of 0.185 – 0.218 nm which was measured from the images. The range of values was relatively smaller than the oxidized samples (0.194 – 0.258 nm) and average *d* value (0.228 nm) of ICSD data of Sm_2O_3.This is probably due to a tighter and more linked structure produced in N contained ambient (Diot, Larcher, Marchand, Kempf, & Macaudiere, 2001; H. Wong & Gritsenko, 2002; Kumar, Sundaresan, & Rao, 2011; Lofaj, Satet, Hoffmann, & de Arellano Lopez, 2004).

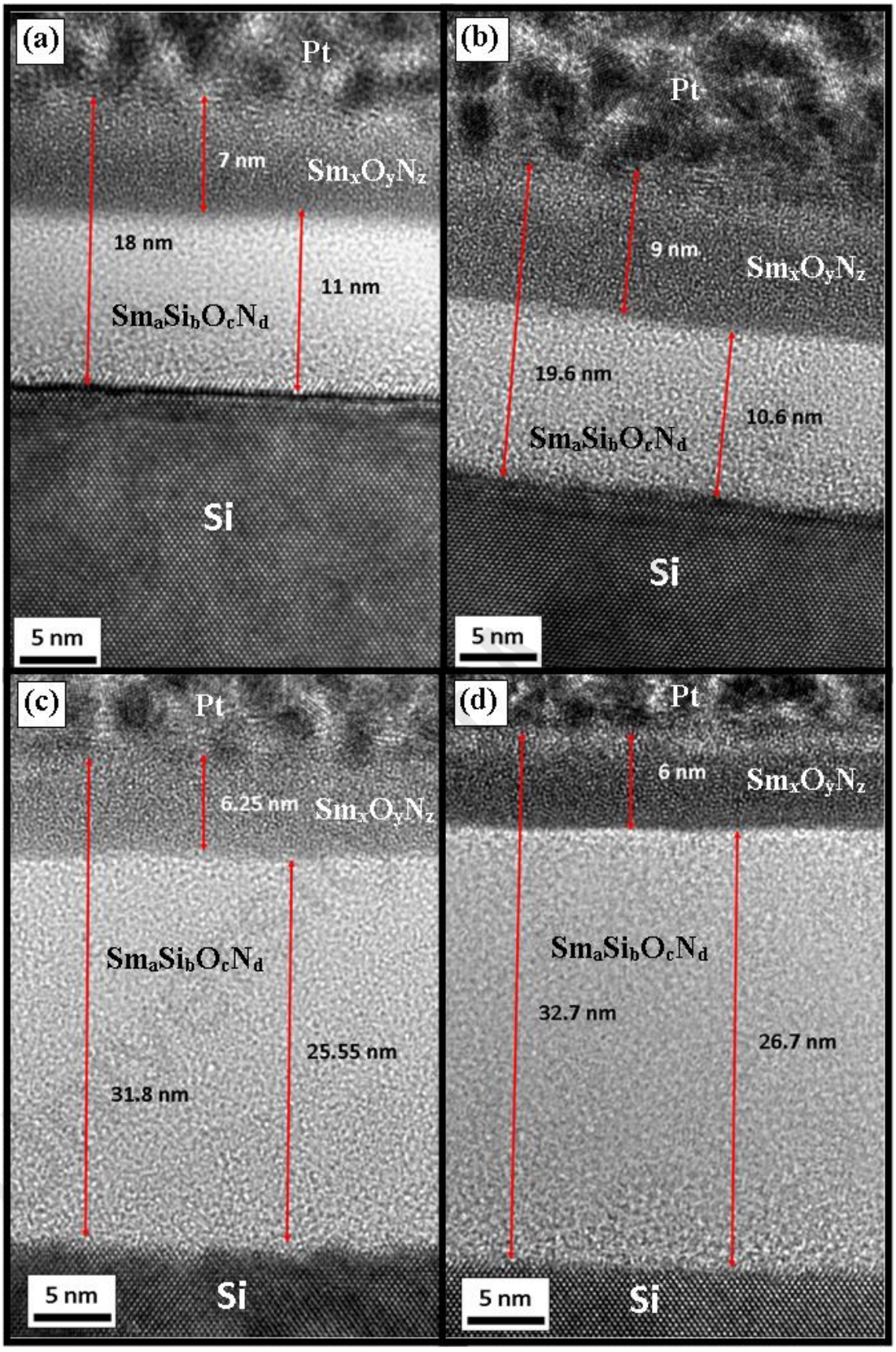

Figure 5.14: Cross sectional of HRTEM images of thermally oxynitrided samples at various temperatures: (a) 600°C (b) 700°C (c) 800°C (d) 900°C. Magnification of each image was shown on the left bottom side, respectively.

The 700 °C sample had the thickest $Sm_xO_yN_z$ film but the thinnest film of $Sm_aSi_bO_cN_d$. Hence, the inferences in the XRD, FTIR and Raman analysis were proved and supported. The higher crystallinity of $Sm_xO_yN_z$ film was due to thicker film of $Sm_xO_yN_z$. The presence of the film was also supported in the FTIR and XPS analysis. The total thickness of $Sm_aSi_bO_cN_d$ was increased dramatically at oxynitridation temperatures of 800 °C and 900 °C. It was because the oxygen atoms diffused to the $Sm_xO_yN_z$/Si interface actively from crystal defects and nonstoichiometric compounds when the oxidation temperatures increased. Fig. 5.16 shows the EDX line scan of composition analysis. It was observed that not only $Sm_xO_yN_z$ film was formed but also the Sm-Si-O-N interfacial layer between $Sm_xO_yN_z$ film and Si substrate. A small amount of N was detected.

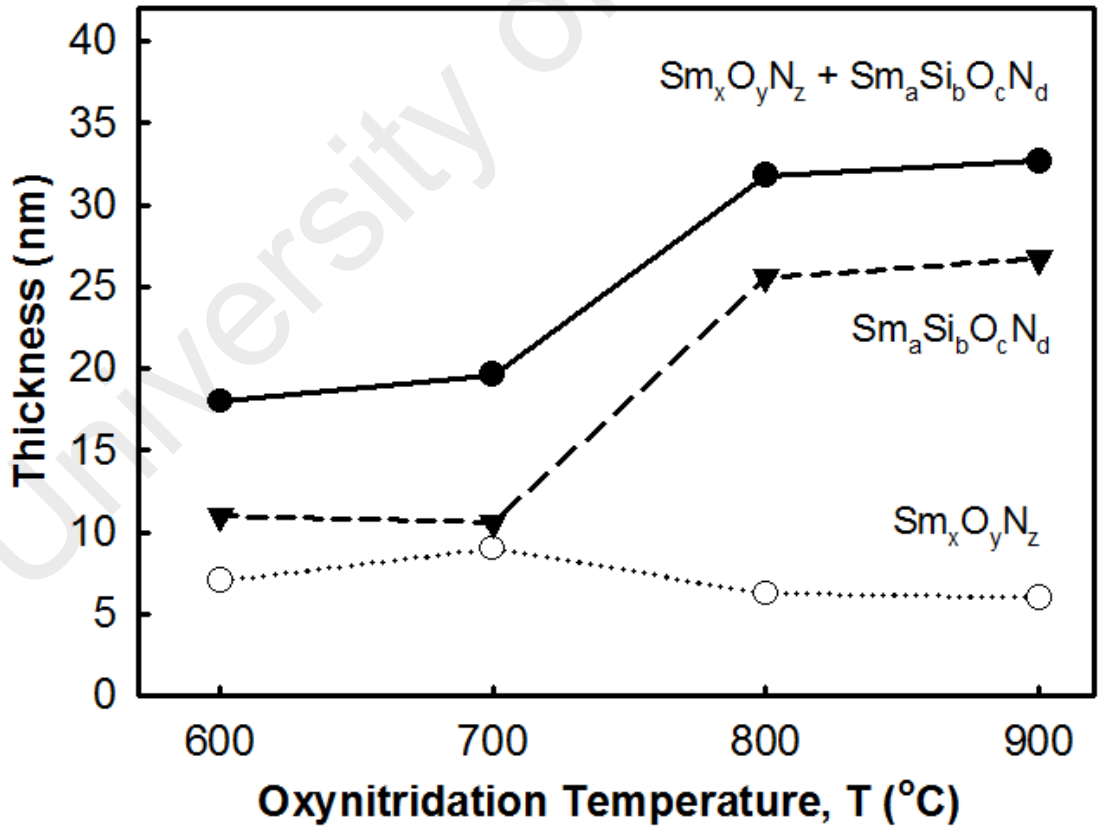

Figure 5.15: $Sm_xO_yN_z$, $Sm_aSi_bO_cN_d$ and total thickness of $Sm_aSi_bO_cN_d$, and $Sm_xO_yN_z$ as function of oxynitridation temperatures (600 - 900°C).

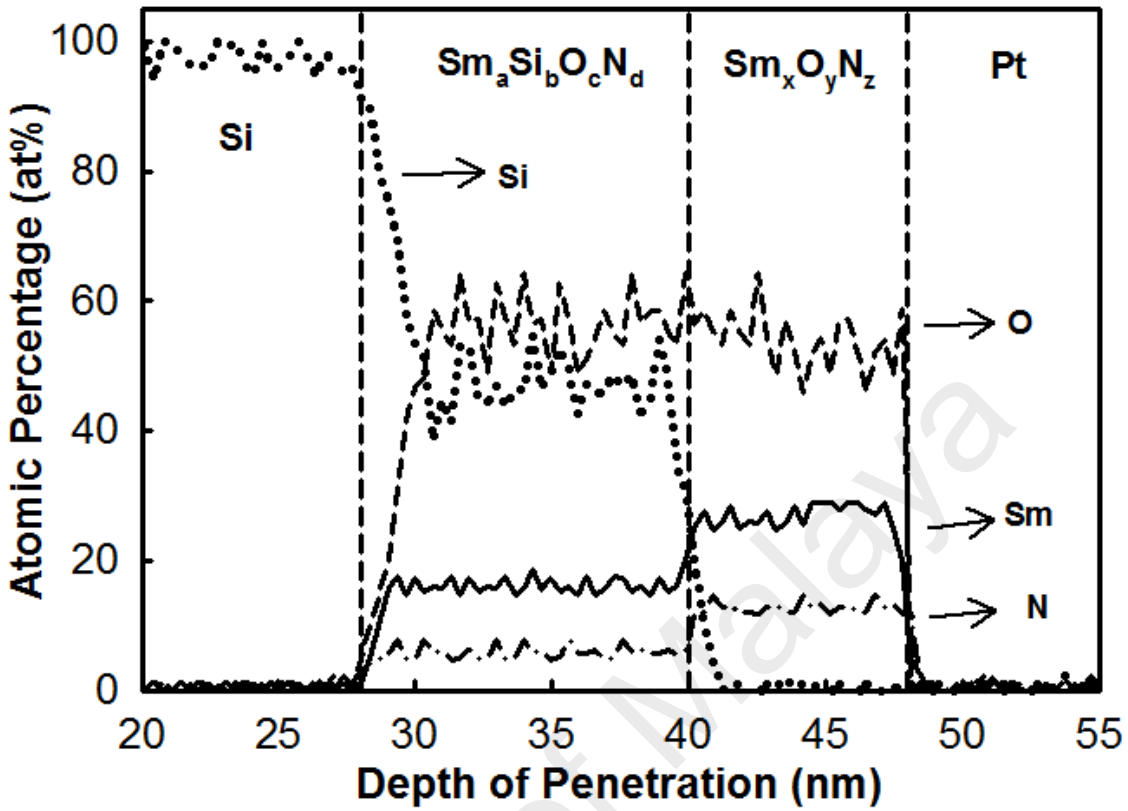

Figure 5.16: EDX compositions analysis of 700 °C samples.

5.2.1.6 Oxynitridation mechanism

A sketched model is proposed in Fig. 5.17 according to the results of the XRD, XPS, FTIR, Raman, HRTEM, and the EDX analysis (Venables, Spiller, & Hanbucken, 1984; Tu, Ottaviani, Thompson, & Mayer, 1982; Rochet, Agius, & Rigo, 1984; Zhang & Lagally, 1997; Massoud, Plummer, & Irene, 1985). Initially, oxygen (O) and nitrogen (N) reacted with Sm to form $Sm_xO_yN_z$. Since there was no free energy change-temperature dependence in the decomposition of N_2O into N and O compounds, the decomposition was spontaneous at all reaction temperatures. O atoms were easily absorbed by Sm atoms due to the hygroscopic nature of rare earth metals (Chin, Cheong, & Hassan, 2010; Jeon & Hwang, 2003). Concurrently, the N atoms also reacted with Sm or Sm_xO_y compounds to form SmN or $Sm_xO_yN_z$.

When the thickness of $Sm_xO_yN_z$ increased, less O and N atoms were able to diffuse in and the incomplete reaction of Sm, O and N occurred. This was supported by the decreasing of O and N concentrations in XPS depth profile as shown in Fig. 5.6. At the same time, Si also diffused into $Sm_xO_yN_z$ and reacted with the incomplete Sm - O – N compounds to form a more stable interfacial layer ($Sm_aSi_bO_cN_d$). As shown in the XPS and EDX analysis, the $Sm_aSi_bO_cN_d$ layer was located in between $Sm_xO_yN_z$ and Si substrate. According to the HRTEM images, $Sm_xO_yN_z$ exhibited polycrystalline structure while $Sm_aSi_bO_cN_d$ exhibited amorphous structure. At 700 °C, the growth rate of stable $Sm_xO_yN_z$ and $Sm_aSi_bO_cN_d$ were almost the same. Thus, the thickness of both $Sm_xO_yN_z$ and $Sm_aSi_bO_cN_d$ were similar. However, an undesirably thick $Sm_aSi_bO_cN_d$ was formed aggressively when oxynitridation temperature increased from 700 °C to 800 °C and 900 °C (Derrien & Commandre, 1982; Zhao, Wang, Lu, Palasantzas, & De Hosson, 1999). The reaction between $Sm_xO_yN_z$ and Si occurred rapidly to form thick $Sm_aSi_bO_cN_d$ because of higher activation energy under the higher temperature ambient (Jeurgens, Sloof, Tichelaar, & Mittemeijer, 2002; Chao, Lin, & Macdonald, 1981).

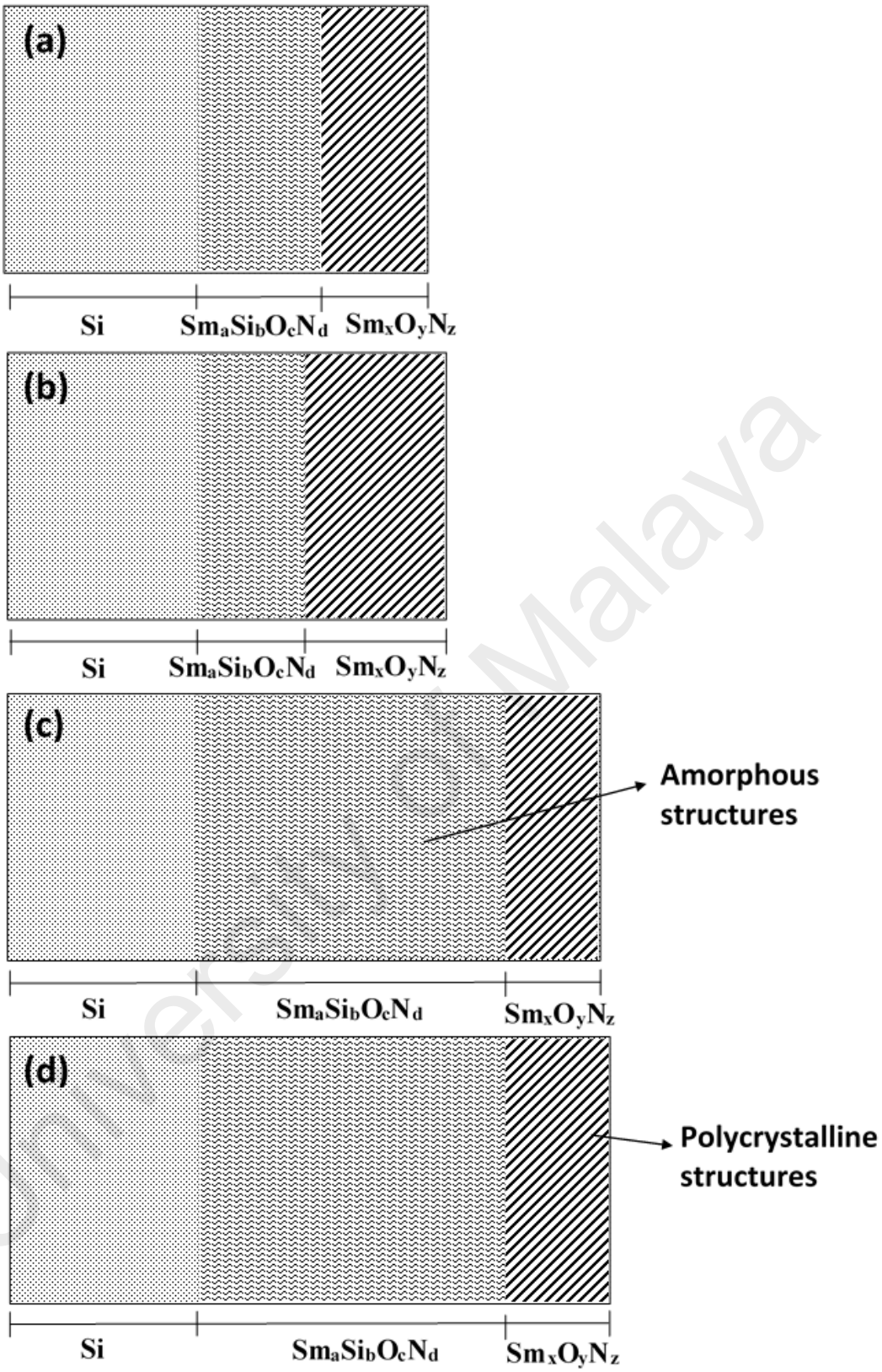

Figure 5.17: Sketched models of layers distributions after different oxynitridation temperatures: (a) 600°C (b) 700°C (c) 800°C (d) 900°C.

5.2.1.7 Arrhenius plot analysis

Fig. 5.18 shows the Arrhenius plot of $Sm_xO_yN_z$, $Sm_aSi_bO_cN_d$, and total ($Sm_xO_yN_z$ + $Sm_aSi_bO_cN_d$) growth in the N_2O ambient. The calculated E_a of $Sm_xO_yN_z$, $Sm_aSi_bO_cN_d$, and the total growth rate were 3.08 x 10^{-4} eV, -6.7 x 10^{-5} eV, and 2 x 10^{-4} eV, respectively. The positive value of E_a indicated the reaction rate increased when the oxynitridation temperature increased. It indicated the total thickness of $Sm_xO_yN_z$ and $Sm_aSi_bO_cN$ was increasing as the oxynitridation temperatures increased. The negative value of E_a indicated the reaction rate decreased or densification occurred when the oxynitridation temperature increased. Besides that, the magnitude indicated the reaction tendency. It means a small magnitude indicated a fast growth while large magnitude indicated a slow growth.

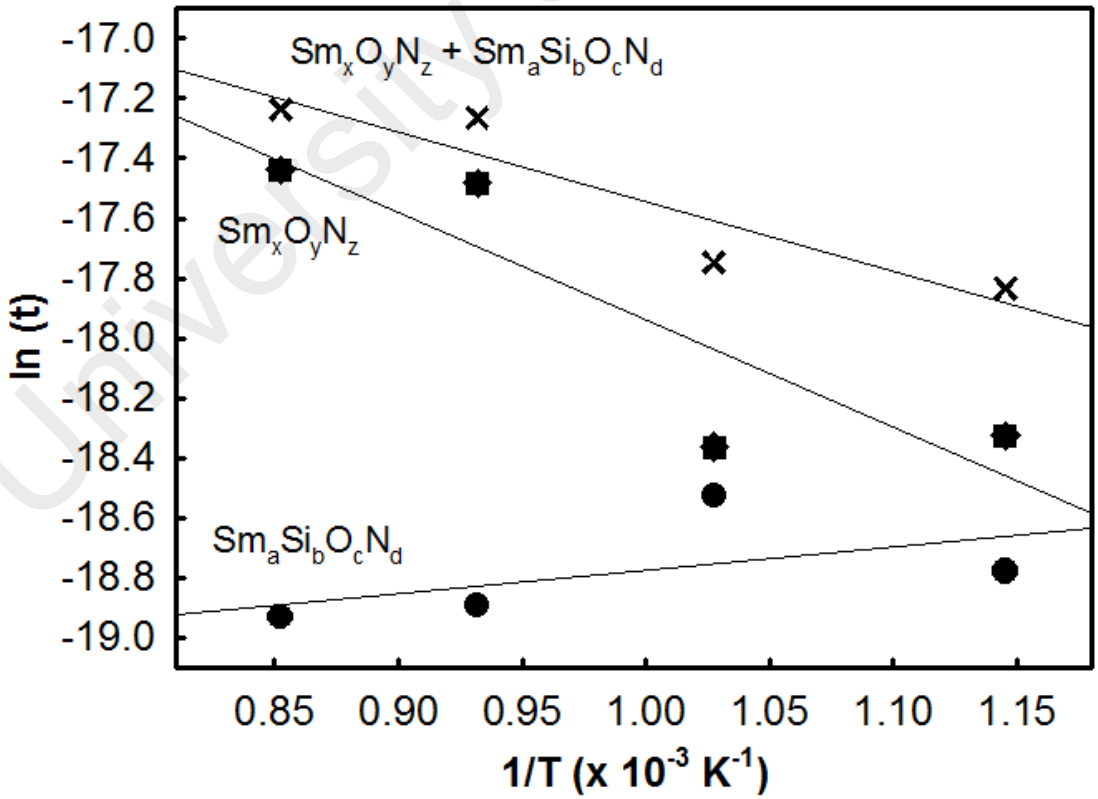

Figure 5.18: Arrhenius plots of $Sm_xO_yN_z$, $Sm_aSi_bO_cN_d$ and total thickness of $Sm_aSi_bO_cN_d$, and $Sm_xO_yN_z$ in N_2O ambient.

5.2.2 Electrical properties

5.2.2.1 *J-E* characteristic

Fig. 5.19 shows the *J-E* characteristic of investigated samples. The *J-E* plot was transformed from *I-V* measurements. Samples thermally oxynitrided at 700 °C have relatively high electrical breakdown field (3.9 MV cm^{-1}) and low leakage current density (~ 10^{-6} A cm^{-2}) as compared to others samples. The thick $Sm_aSi_bO_cN$ film of 800 °C and 900 °C as shown in the HRTEM analysis may downgrade the electrical breakdown field (Zhao, Wang, Lu, Palasantzas, & De Hosson, 1999). As compared to the oxidized samples, both the electrical breakdown field and leakage current density were improved by the incorporation of N (C. L. Cheng, Chang-Liao, & Wang, 2006; Tan, 2007). The enhancement and improvement on the electrical breakdown field and/or leakage current density were also observed as compared to previous works (Constantinescu *et al.*, 2012; Dakhel, 2004; Kaya, Yilmaz, Karacali, Cetinkaya, & Aktag, 2015; Paivasaari, Putkonen, & Niinisto, 2005; S. Y. Huang *et al.*, 2011). From the *J-E* measurements, time-zero dielectric breakdown (TZBD) reliability tests had been done at room temperature (25°C). The cumulative failure percentage of 100 capacitors is presented in Fig. 5.20. According to the plot, the 700°C samples have the highest reliability.

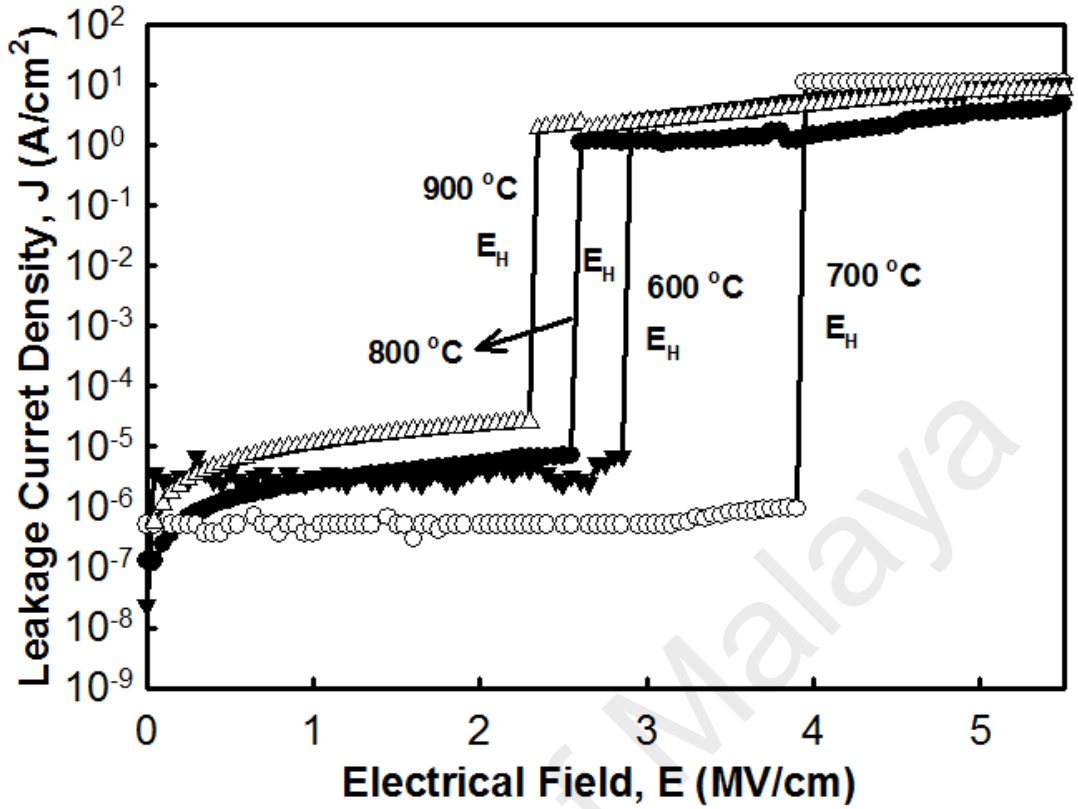

Figure 5.19: *J-E* characteristics of thermally oxynitrided samples at various temperatures (600 - 900°C).

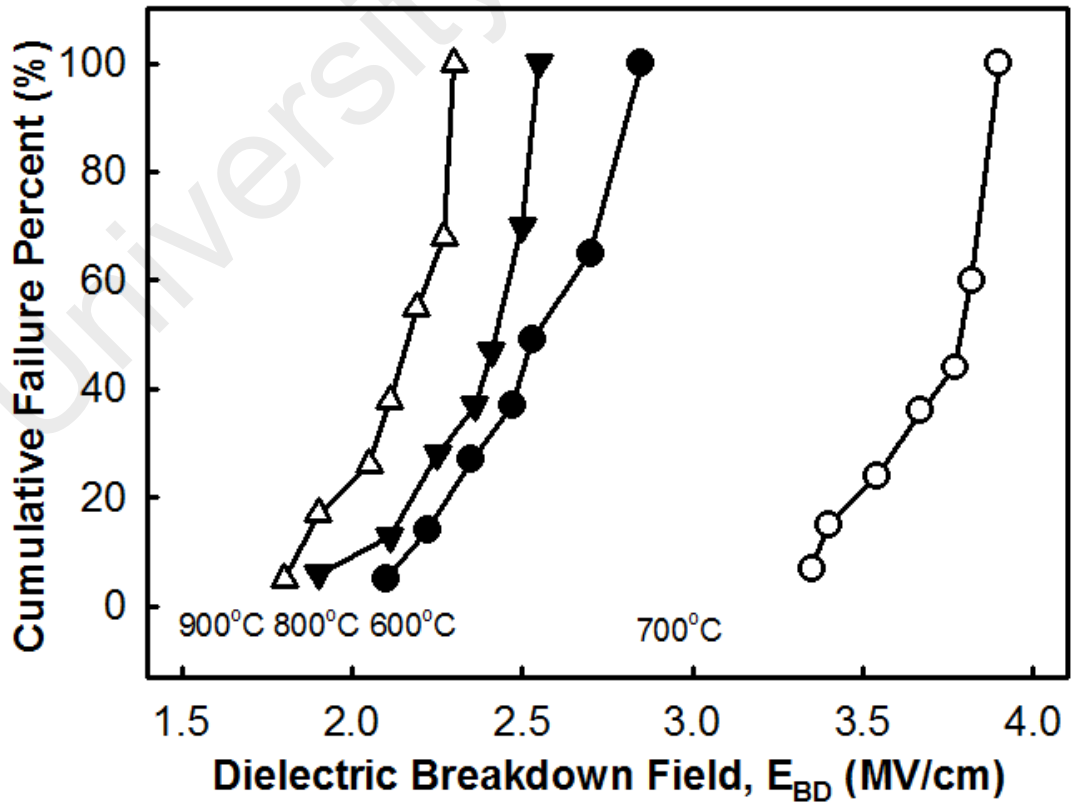

Figure 5.20: Cumulative failure percentage of dielectric breakdown field (E_{BD}) of thermally oxynitrided samples at various temperatures (600 - 900°C).

The barrier height, $Ø_B$ of conduction band edge between Si and the interfacial layer of oxide was obtained from the Fowler-Nordheim (FN) tunneling model. The FN tunneling refers to the flow of electron through a triangular potential barrier into the conduction band of an insulator. The FN tunneling can be defined as in Eq. 4.6. Fig. 5.21 shows a linear FN plot of $In\ (J/E^2)$ versus $1/E$. The $Ø_B$ values range from 3.14 to 6.33 eV (Fig. 5.22). The sample thermally oxynitrided at 700 °C possessed highest $Ø_B$ values (6.33 eV). The $Ø_B$ of $Sm_xO_yN_z$ was higher than $Ø_B$ of Sm_2O_3 as reported in previous works: 0.85 eV (Dakhel, 2004), 2.34 eV (Kim, McIntyre, & Saraswat, 2003), 2.88 – 2.92 eV (V. A. Rozhkov *et al.*, 1998), and also oxidized sample (2.13 eV) in the previous chapter.

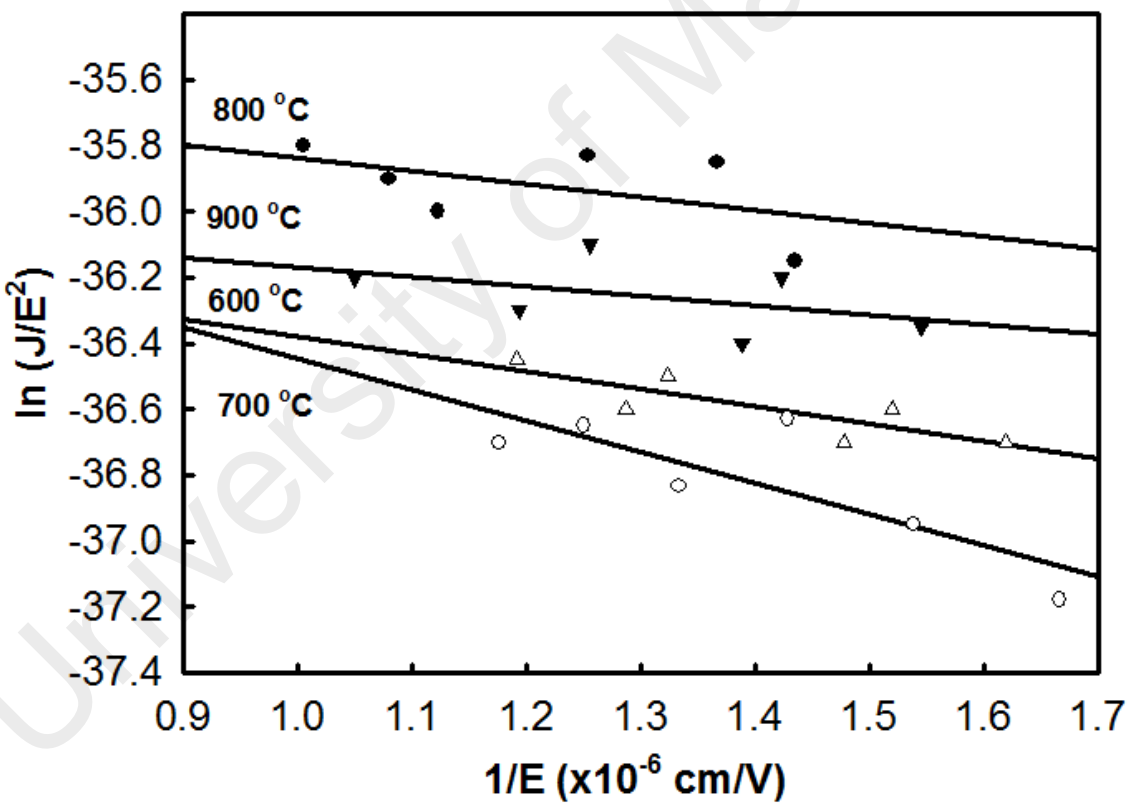

Figure 5.21: FN tunneling linear regression plot [$In\ (J/E^2)$ versus $1/E$] of thermally oxynitrided samples at various temperatures (600 - 900°C).

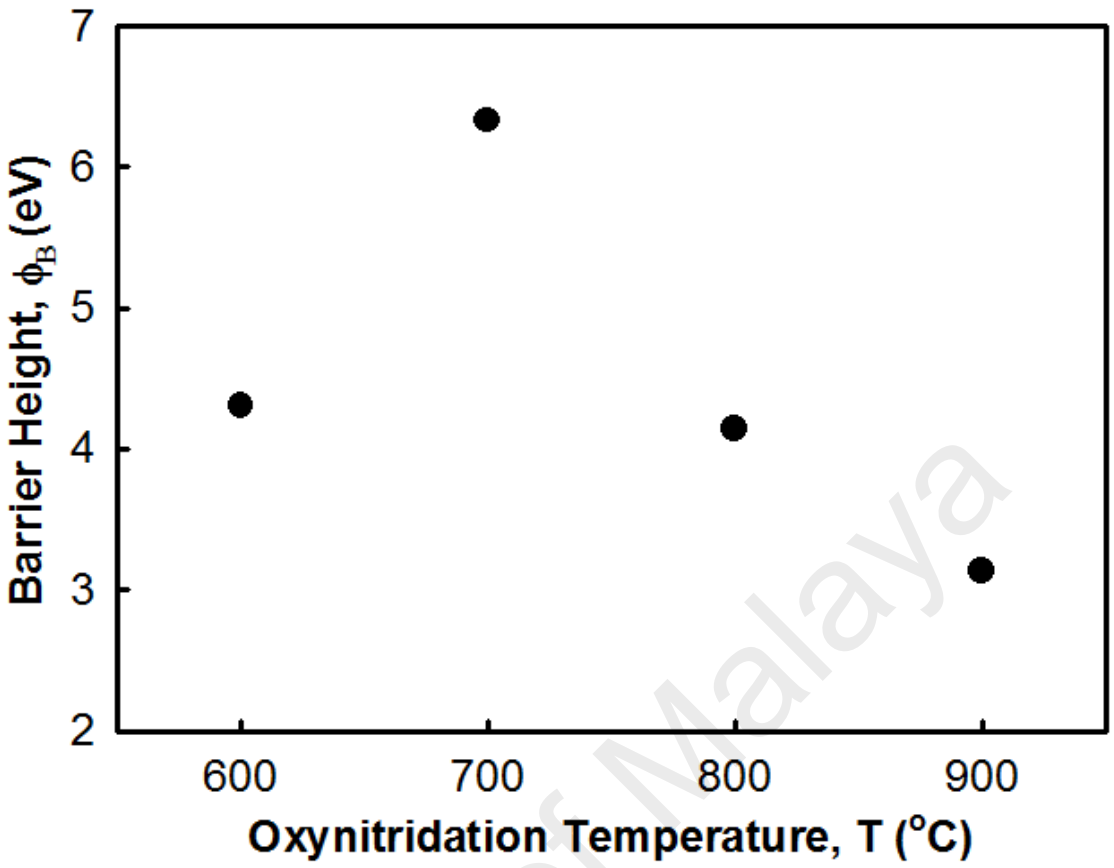

Figure 5.22: Barrier height values as a function of oxynitridation temperatures (600 - 900°C).

Fig. 5.23 shows the typical trap-assisted tunneling plot for investigated samples. A total of 30 points with goodness of fit (r^2) of ~ 0.9 were obtained. Fig. 5.24 shows the trap energy and trap density as a function of oxynitridation temperature. The 700 °C sample had the highest trap energy (0.005 eV) and the lowest energy trap density (5.657 x 10^{21} cm^{-3}) as compared to other samples. This explains that the 700 °C sample had the lowest leakage current density (as shown Fig. 5.19) as compared to others samples. However, the trap energy was lower than trap energy of silicon nitride (~ 0.033 eV) (Yang, Wong, & Cheng, 1996), (~ 1.03 eV) (Perera, Ikeda, Hattori, & Kuroki, 2003), (~ 0.7 eV) (Fleischer, Lai, & Cheng, 1993), and ZrO_2 (~ 0.8 eV) (Houssa, Stesmans, & Heyns, 2001) reported by previous researchers on the basis of their lower leakage current density (> 10^{-9} A cm^{-2}). Since the breakdown electrical field located at lower electrical field (< 4 MV cm^{-1}), hence the electrical conduction was dominated by shallow trap-

assited tunneling (Yang, Wong, & Cheng, 1996; Houng, Wang, & Chang, 1999; Perera, Ikeda, Hattori, & Kuroki, 2003). Beside that, the experimental and/or simulated energies of deep level traps at higher electrical fields (> 4 MV cm^{-1}) of SiON were reported ranging from 1.6 eV to 2.87 eV by several researchers (Ramesh, Chandorkar, & Vasi, 1989; Fleischer, Lai, & Cheng, 1992; Cheng, Cheng, & Liu, 1988; Suzuki, Schroder, & Hayashi, 1986; Jimenez-Molinos, Palma, Gamiz, Banqueri, & Lopez-Villanueva, 2001).

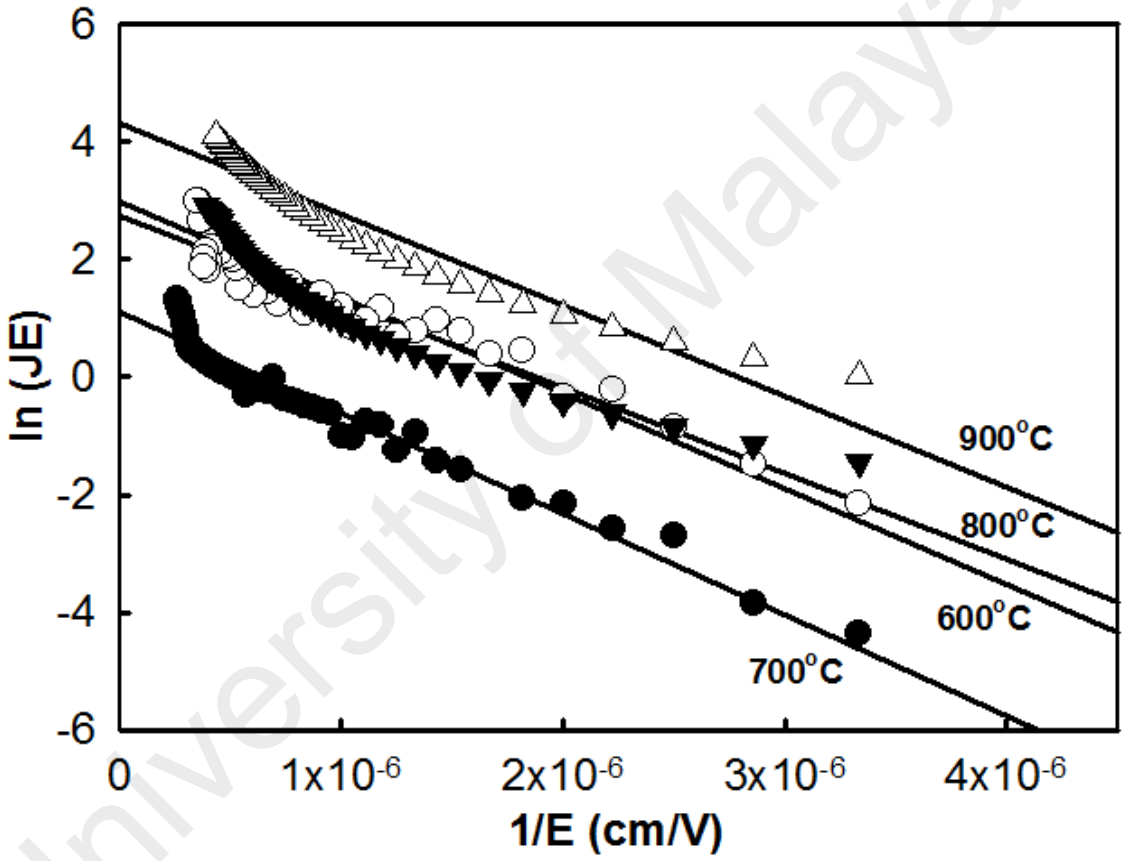

Figure 5.23: Typical trap-assisted tunneling plot of investigated samples at various temperatures (600 – 900 °C).

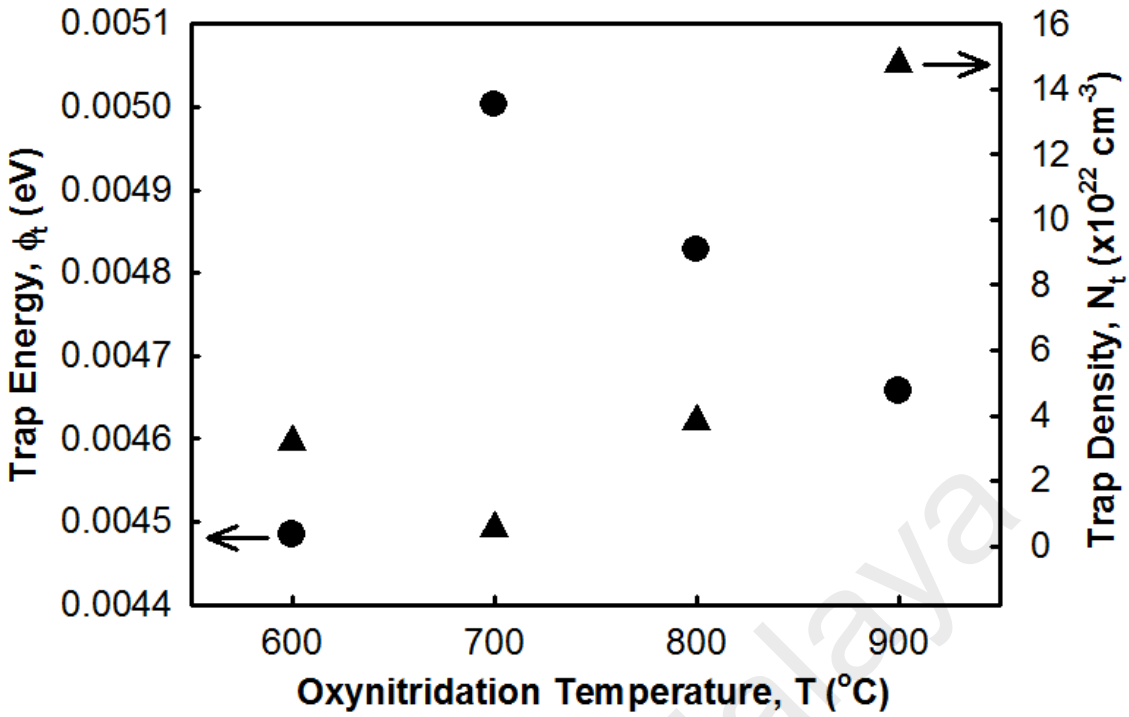

Figure 5.24: The trap energy and trap density of thermally oxynitrided samples at various temperatures (600 – 900 °C).

In this part, the structural, chemical, and electrical properties of sputtered Sm thin film thermally oxynitrided in N_2O ambient at various temperatures (600 – 900 °C) were presented. Polycrystalline Sm_2O_3 was detected in the XRD analysis, supported by the FTIR and Raman analysis. Both the Scherrer and W-H analysis have the same trend of crystallite size of Sm_2O_3. According to the XPS results, a $Sm_aSi_bO_cN_d$ film was stacked in between $Sm_xO_yN_z$ film and Si substrate. Sm-O, Sm-N, Si-N, Sm-Si-O, and Si-Si bonds were detected and matched the FTIR and Raman analysis. The HRTEM images and the EDX analysis prove that the oxynitride/semiconductor structure consists of three thin films: Si substrate, $Sm_aSi_bO_cN_d$, and $Sm_xO_yN_z$ films. In electrical characterization, the 700 °C sample have the best electrical breakdown field of 3.9 MV cm^{-1} at ~ 10^{-6} A cm^{-2}. This was attributed to the higher barrier height, trap energy, and lower trap density.

5.3 Effects of oxynitridation duration on sputtered Sm thin film on Si substrate

5.3.1 Physical and chemical properties

5.3.1.1 XRD analysis

Fig. 5.25 shows the XRD patterns of the thermally oxynitrided samples for different durations (5 min, 10 min, 15 min and 20 min). Four strong peaks at 33°, 61.9°, 69.6°, and 75.6° were detected in all samples which were matched with four different planes of cubic of silicon which were c-Si (111), c-Si (311), c-Si (400), and c-Si (331), respectively. These peaks were confirmed by Inorganic Crystal Structure Database (ICSD) with the reference code of 98-001-6569. The cubic phase of Sm_2O_3 (c-Sm_2O_3) was revealed at various diffraction angles of at 45.9°, 47.7°, 54.5°, 56.3°, 74.9°, and 76.3° corresponding to various planes of (152), (334), (154), (226), (004), and (257), respectively. These peaks were confirmed by the ICSD with the reference code of 98-004-0475. According to the XRD results, it was observed that the peak intensities at 47.7°, 54.5°, 56.3°, and 74.9° increased when oxynitridation duration increased from 5 min to 15 min but decreased from 15 min to 20 min as shown in Fig. 5.26. The intensity of Sm_2O_3 peaks decreased probably due to the excessive formation of an interfacial layer ($Sm_aSi_bO_cN_d$) which was caused by the diffusion of oxygen from $Sm_xO_yN_z$ film to Si substrate during extended time (20 min) (Lim *et al.*, 2011; S. Wang *et al*., 2015 Tamboli *et al*., 2010).

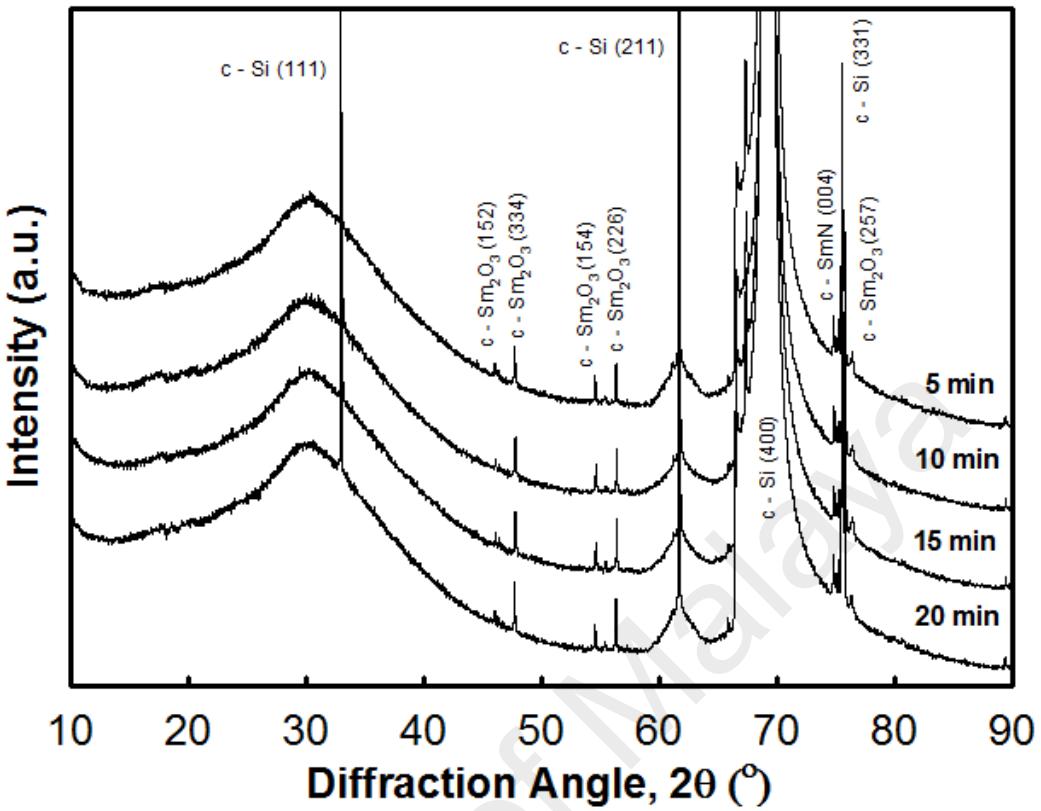

Figure 5.25: XRD patterns of thermally oxynitrided samples at various oxynitridation durations (5 min, 10 min, 15 min and 20 min).

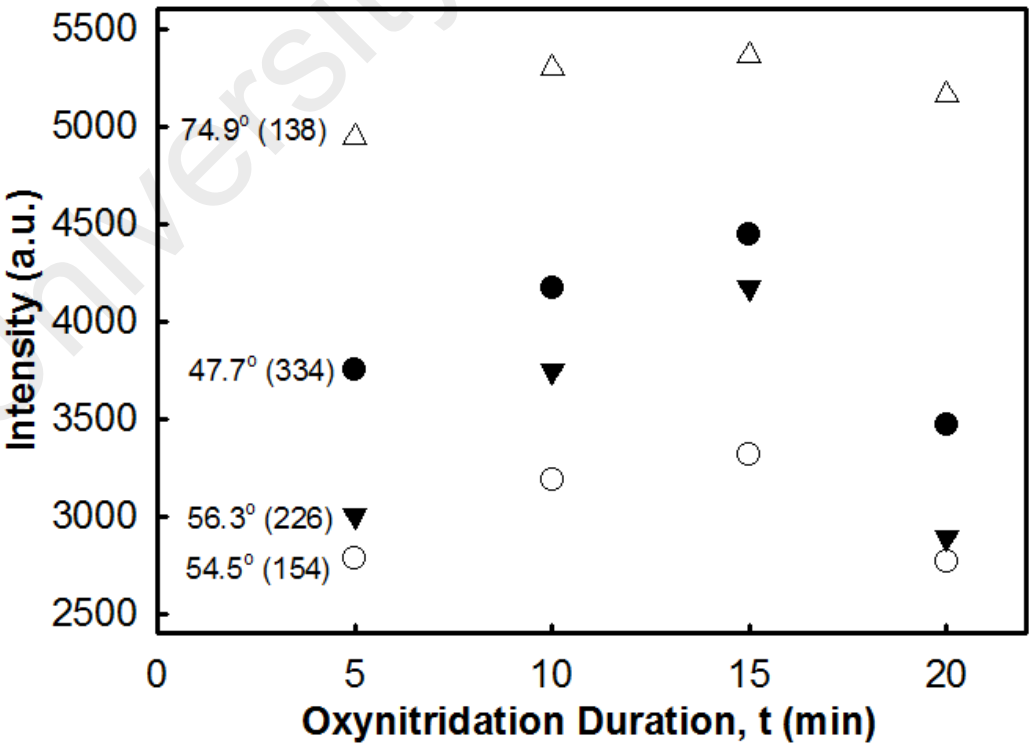

Figure 5.26: Intensities of Sm_2O_3 (334), (154), (226), and (138) at 47.7°, 54.5°, 56.3°, and 74.9°, respectively as a function of oxynitridation durations (5 min, 10 min, 15 min and 20 min).

Using the Scherrer equation, the crystallite sizes of Sm_2O_3 averaged over various peak positions for 5 min, 10 min, 15 min, and 20 min were 34.67 nm, 31.36 nm, 30.76 nm, and 33.17 nm, respectively (Fig. 5.27). Since the Scherrer equation only gives lower bound of crystallite size and the microstrain was not taken into account, the W-H analysis was also conducted.

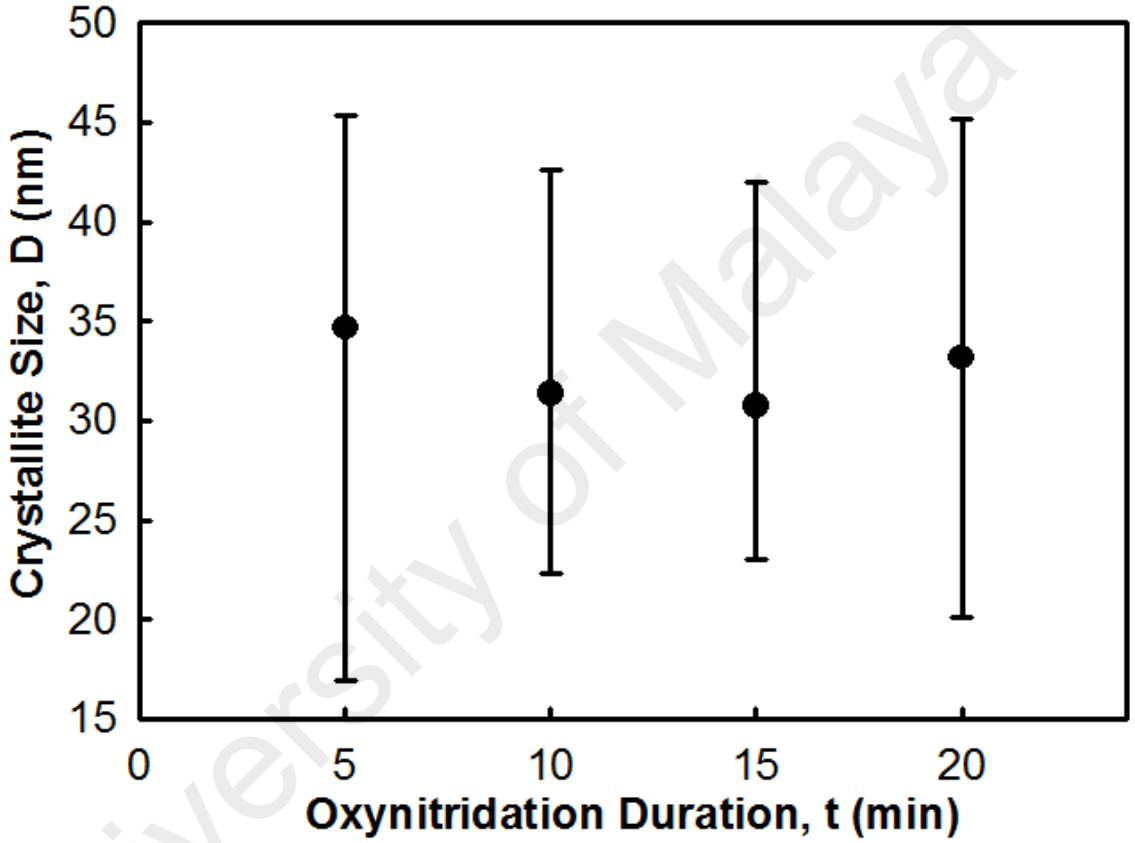

Figure 5.27: Calculated crystallite sizes by Scherrer equation of Sm_2O_3 as a function of oxynitridation durations (5 min, 10 min, 15 min, and 20 min).

A $\beta_{hkl} \cos \theta$ versus 4 $\sin \theta$ graph (Fig. 5.28) was plotted based on Eq. 3.6. Based on the W-H analysis, the crystallite size of Sm_2O_3 ranged from 49.38 nm to 66.13 nm while microstrain of Sm_2O_3 ranged from 0.0127 to 0.0164 as showed in Fig. 5.29. The 15 min sample had the smallest crystallite size and lowest microstrain. The calculated crystallite size of Sm_2O_3 by both the Scherrer equation and the W-H analysis had the same trend.

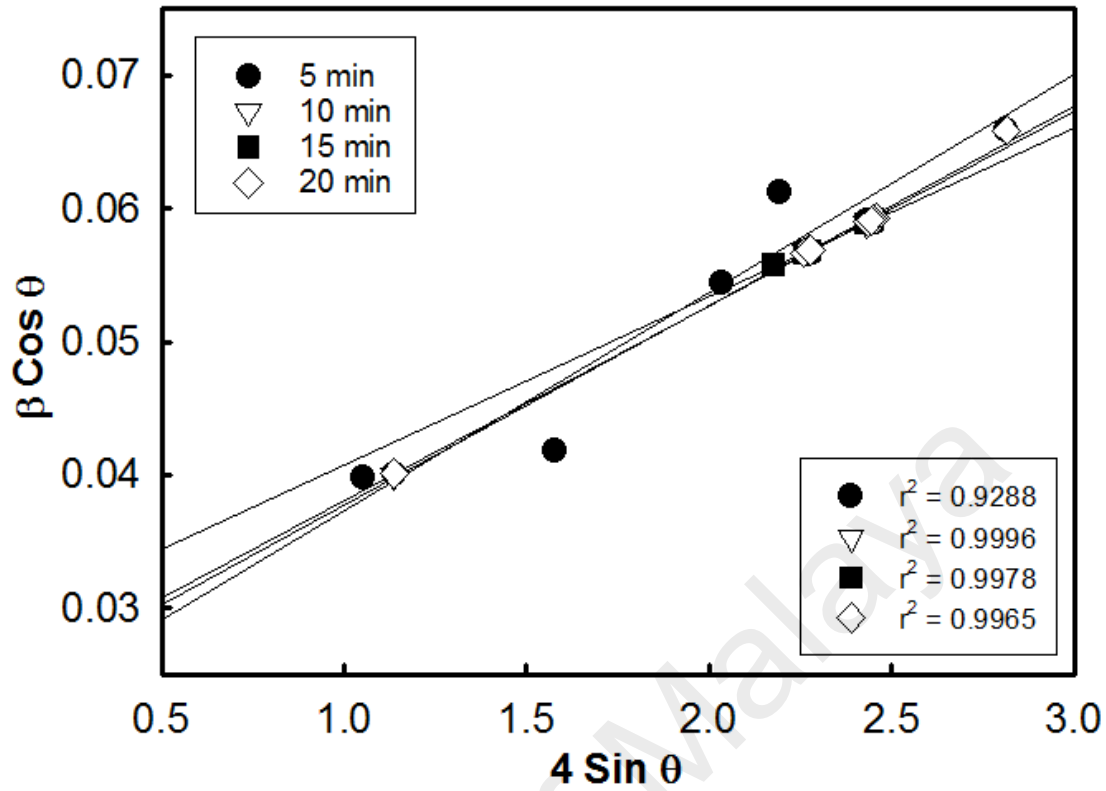

Figure 5.28: W-H plot of thermally oxynitrided samples for various oxynitridation durations (5 min, 10 min, 15 min and 20 min).

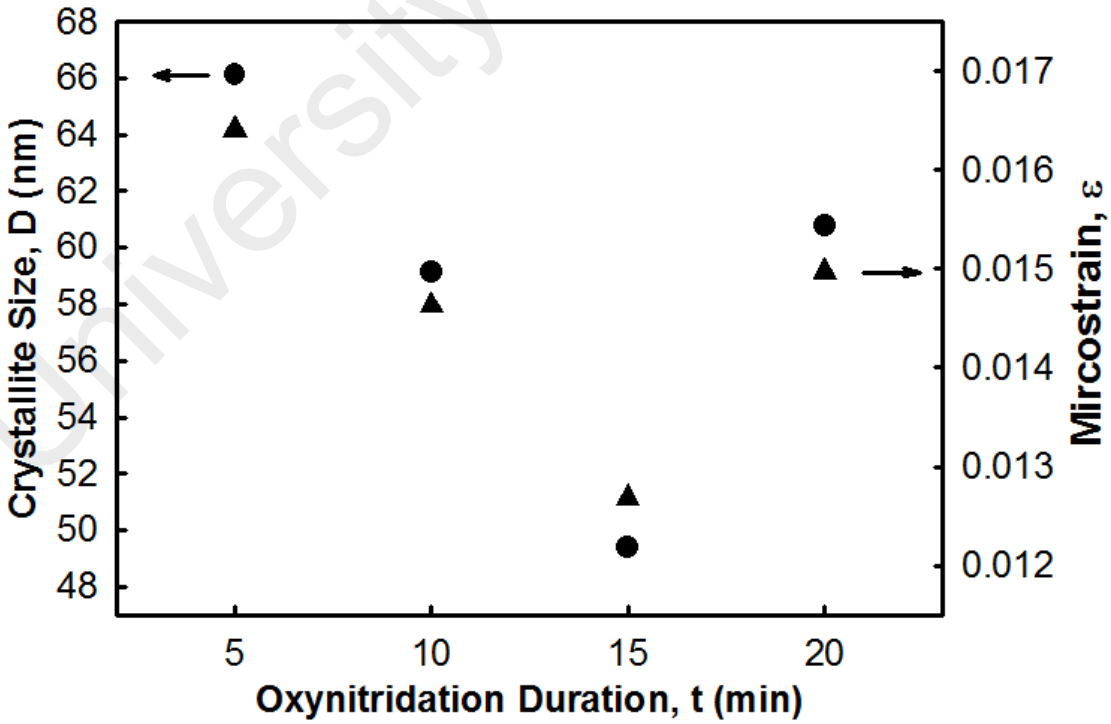

Figure 5.29: Relationship of calculated crystallite size and microstrain from W-H plot as a function of oxynitridation duration (5 min, 10 min, 15 min and 20 min).

5.3.1.2 FTIR analysis

Fig. 5.30 shows the FTIR transmittance spectra (1200 - 400 cm^{-1}) of samples thermally oxynitrided for different durations (5 - 20 min). Si - Si vibration mode band was located at 600 cm^{-1} while Si - O vibration mode band was located at 1050 cm^{-1} in all thermally oxynitrided samples (Ansart *et al*., 1995; Y. H. Wong *et al*., 2014; Y. H. Wong & Cheong, 2011b). The Si - Si peak broadened as oxynitridation duration increased. The 672 cm^{-1} was assigned to the Sm - N vibration mode. For the 5 min sample, Sm - O vibration mode was detected at 431 cm^{-1} (Hussein *et al*., 2003; Ismail, 1995; Mandal *et al*., 2014; Ruiz-Gomez *et al*., 2014) and 502 cm^{-1} (Hussein *et al*., 2003; Ismail, 1995). At 431 and 502 cm^{-1}, the peaks became sharper when the oxynitridation duration increased from 5 min to 15 min. However, the intensity of both peaks decreased when oxynitridation duration was further extended. This similar phenomenon also occurred in the XRD results. The broadening and the shifting of peaks can also be inferred as due to the formation or growth of interfacial layer ($Sm_aSi_bO_cN_d$) which matched with the inferences from the XRD results.

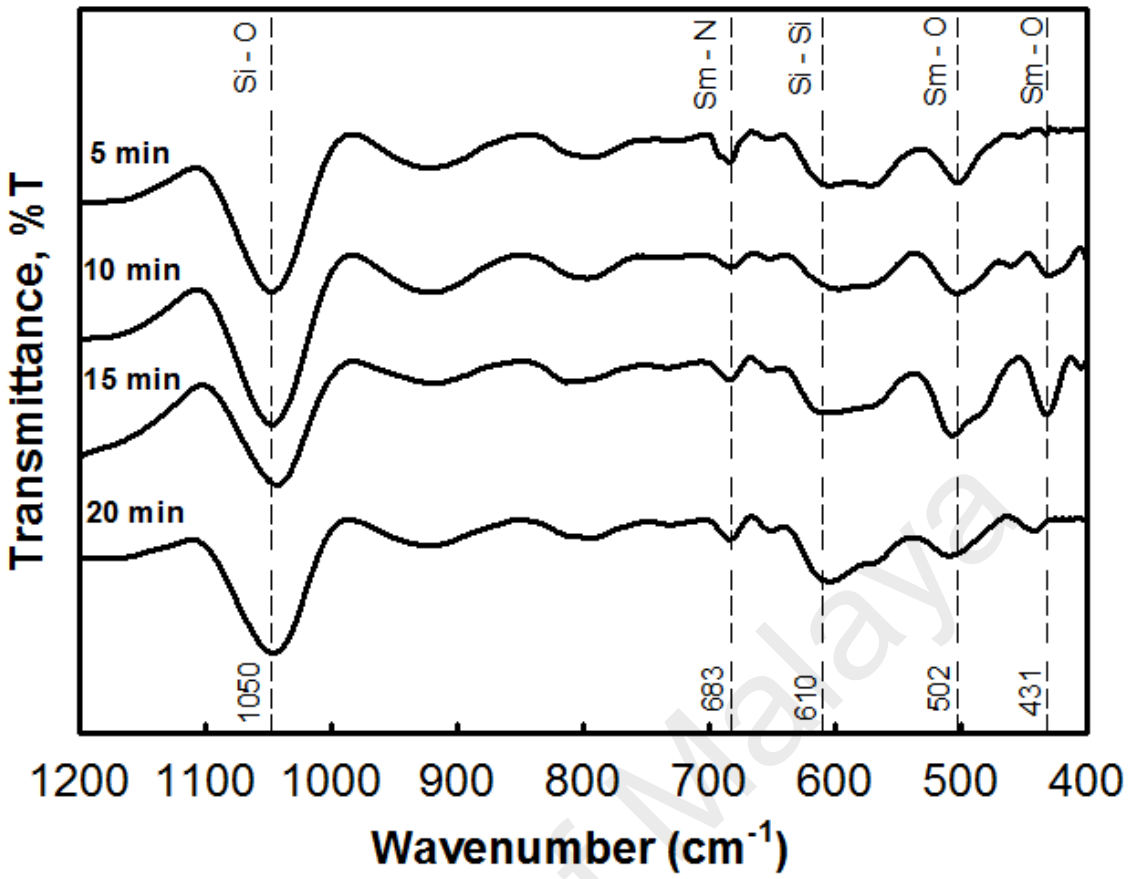

Figure 5.30: Transmittance spectra of thermally oxynitrided samples for various durations (5 min, 10 min, 15 min, and 20 min).

5.3.1.3 Raman analysis

The Raman results for all thermally oxynitrided samples are shown in Fig. 5.31. The peak at 527 cm^{-1} was assigned to silicon substrate (N. Jiang *et al*., 2012; Y. H. Wong & Cheong, 2011b). The peaks at 310 cm^{-1} (S. Jiang *et al*., 2013), 441 cm^{-1} (Hongo *et al*., 2007; N. Jiang *et al*., 2012; S. Jiang *et al*., 2013), 628 cm^{-1} (S. Jiang *et al*., 2013), and 675 cm^{-1} (Hongo *et al*., 2007; Mandal *et al*., 2014; N. Jiang *et al*., 2012; S. Jiang *et al*., 2013) were identified to be Sm_2O_3. Fig. 5.32 shows the intensities of Sm_2O_3 peaks and the 15 min sample had the highest intensity. The trend was similar to the XRD and FTIR results. According to this result, it was confirmed that polycrystalline Sm_2O_3 was formed and complemented with the XRD and FTIR results.

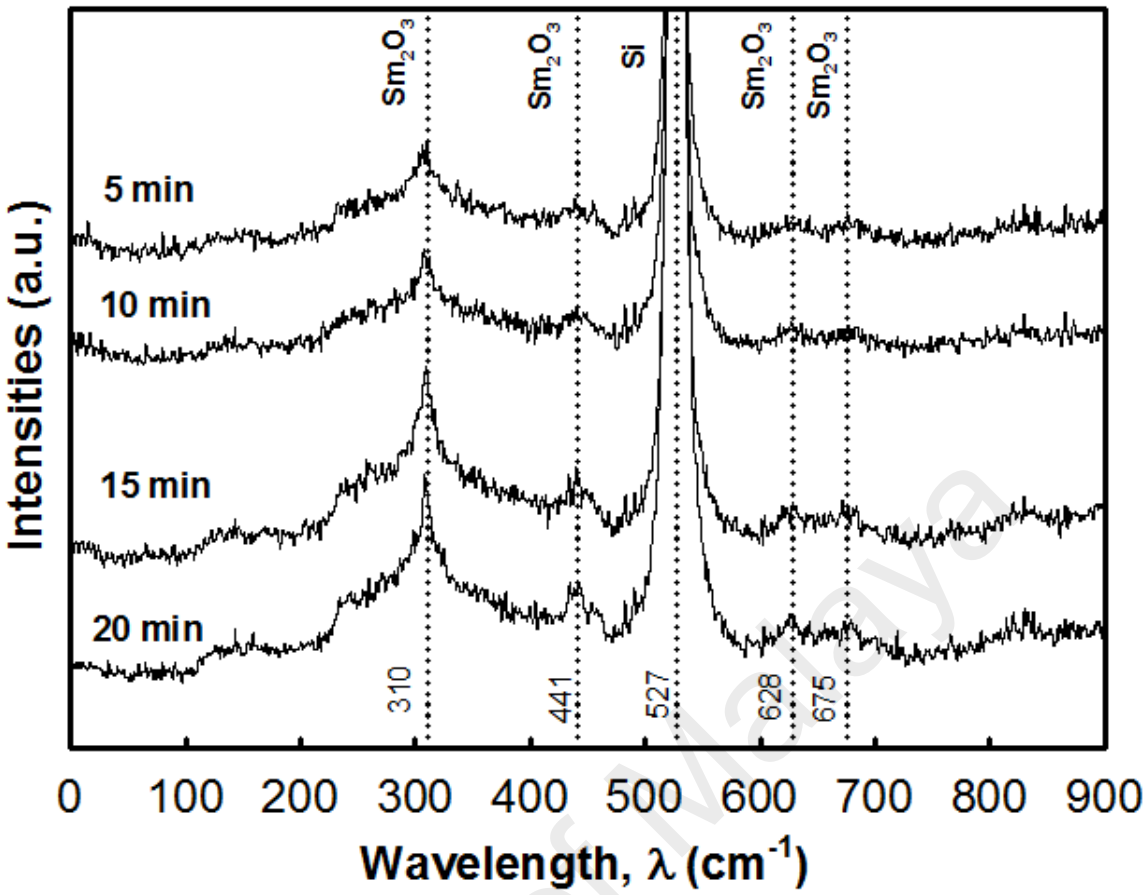

Figure 5.31: Raman spectra of thermally oxynitrided samples for various durations (5 min, 10 min, 15 min and 20 min).

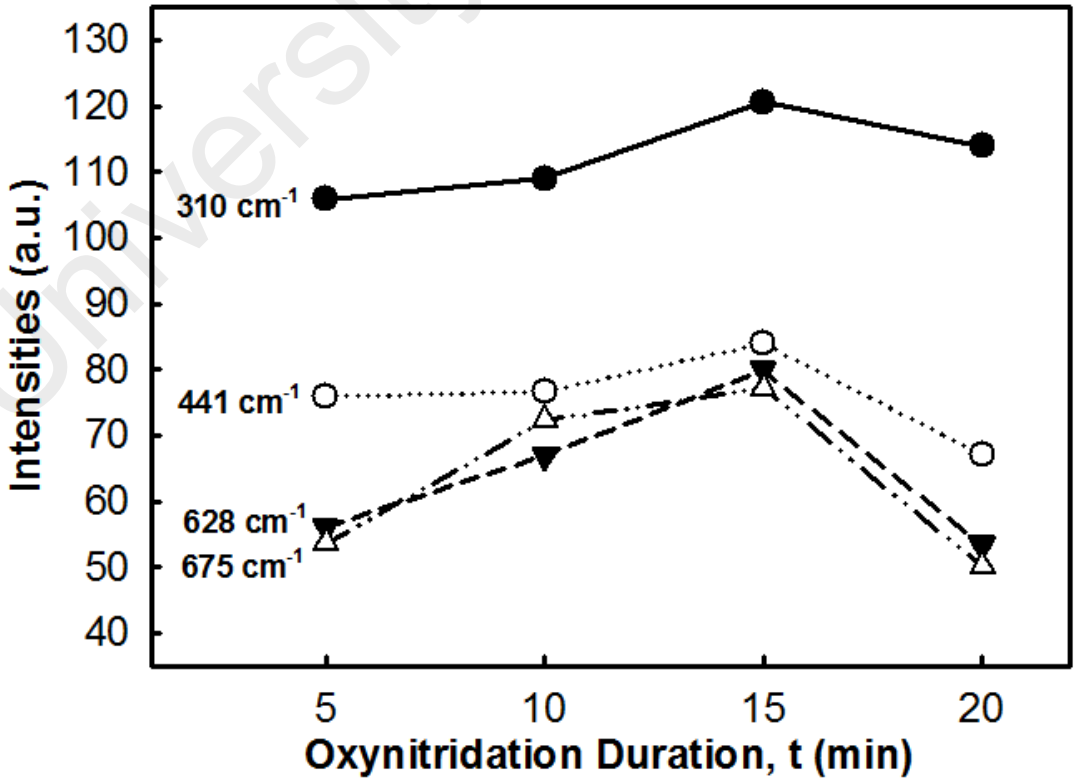

Figure 5.32: Intensities of Sm_2O_3 at 310 cm^{-1}, 441 cm^{-1}, 628 cm^{-1}, and 675 cm^{-1} as a function of oxynitridation duration (5 min, 10 min, 15 min and 20 min).

5.3.2 Electrical properties

5.3.2.1 *J-E* characteristic

Fig. 5.33 shows the *J-E* characteristic of investigated samples. The *J-E* plot was transformed from *I-V* measurements. The 15 min samples have a relatively high electrical breakdown field (3.9 MV cm^{-1}) and low leakage current density (~ 10^{-6} A cm^{-2}) as compared to others samples. The thicker $Sm_aSi_bO_cN_d$ film of the 20 min sample as inferred from the XRD, FTIR, and Raman analysis may downgrade the electrical breakdown field. As compared to the oxidized samples, both the electrical breakdown field and leakage current density were improved significantly by the incorporation of N (C. L. Cheng *et al*., 2006; Tan, 2007). The enhancement and improvement of the electrical breakdown field and/or leakage current density were also observed when compared to previous works (Constantinescu *et al*., 2012; Dakhel, 2004; Kaya, Yilmaz, Karacali, *et al.*, 2015; Paivasaari *et al*., 2005; S. Y. Huang *et al*., 2011). From the *J-E* measurements, time-zero dielectric breakdown (TZBD) reliability tests have been done at room temperature (25°C). The cumulative failure percentage of 100 capacitors is presented in Fig. 5.34. According to the plot, the 15 min sample had the highest reliability.

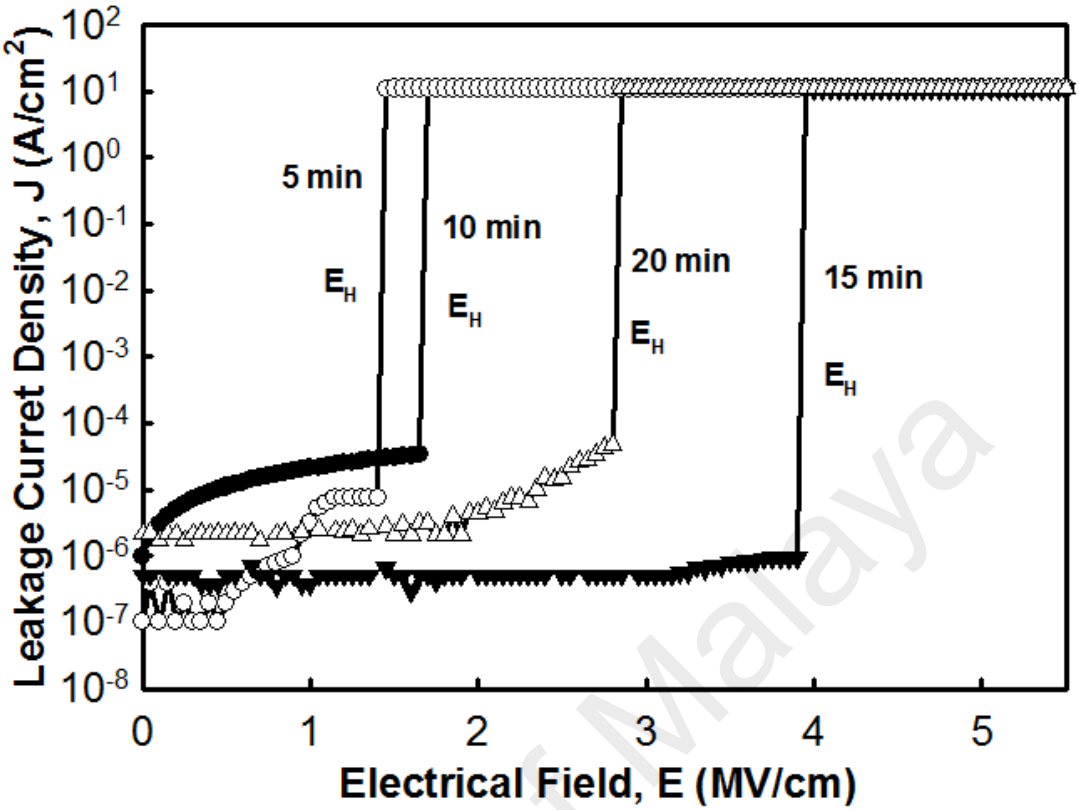

Figure 5.33: *J-E* characteristic of thermally oxynitrided samples for various durations (5 min, 10 min, 15 min and 20 min).

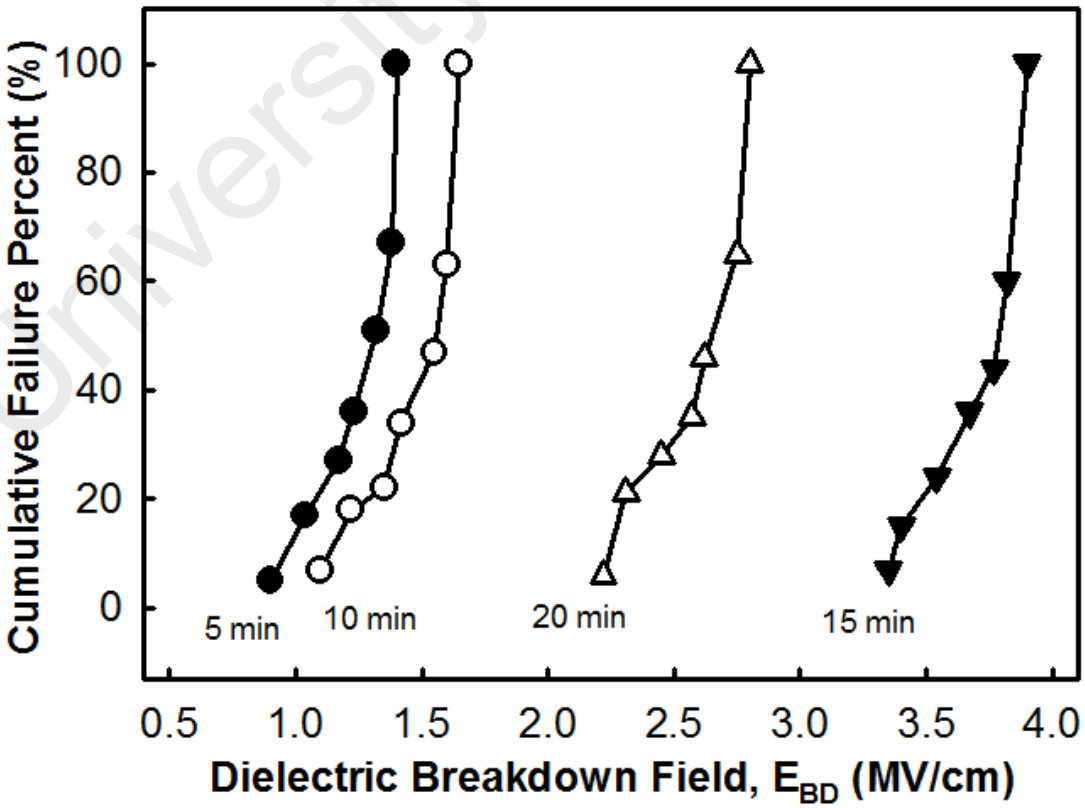

Figure 5.34: Cumulative failure percentage of dielectric breakdown field (E_{BD}) of thermally oxynitrided samples for various durations (5 min, 10 min, 15 min and 20 min).

The barrier height, $Ø_B$ of the conduction band edge between Si and the interfacial layer of oxide was extracted from the Fowler-Nordheim (FN) tunneling model. FN tunneling is refers to the flow of electrons through a triangular potential barrier into the conduction band of an insulator. FN tunneling is defined as in Eq. 4.6. Fig. 5.35 shows a linear FN plot of ln (J/E^2) versus $1/E$. The $Ø_B$ values ranged from 3.04 to 6.33 eV (Fig. 5.36). The 15 min sample possessed the highest $Ø_B$ value (6.33 eV). The $Ø_B$ of $Sm_xO_yN_z$ was higher than $Ø_B$ of Sm_2O_3 as reported in previous research: 0.85 eV (Dakhel, 2004), 2.34 eV (Kim, McIntyre, & Saraswat, 2003), 2.88 – 2.92 eV (V. A. Rozhkov *et al.*, 1998), and also oxidized sample (2.13 eV) in previous chapter.

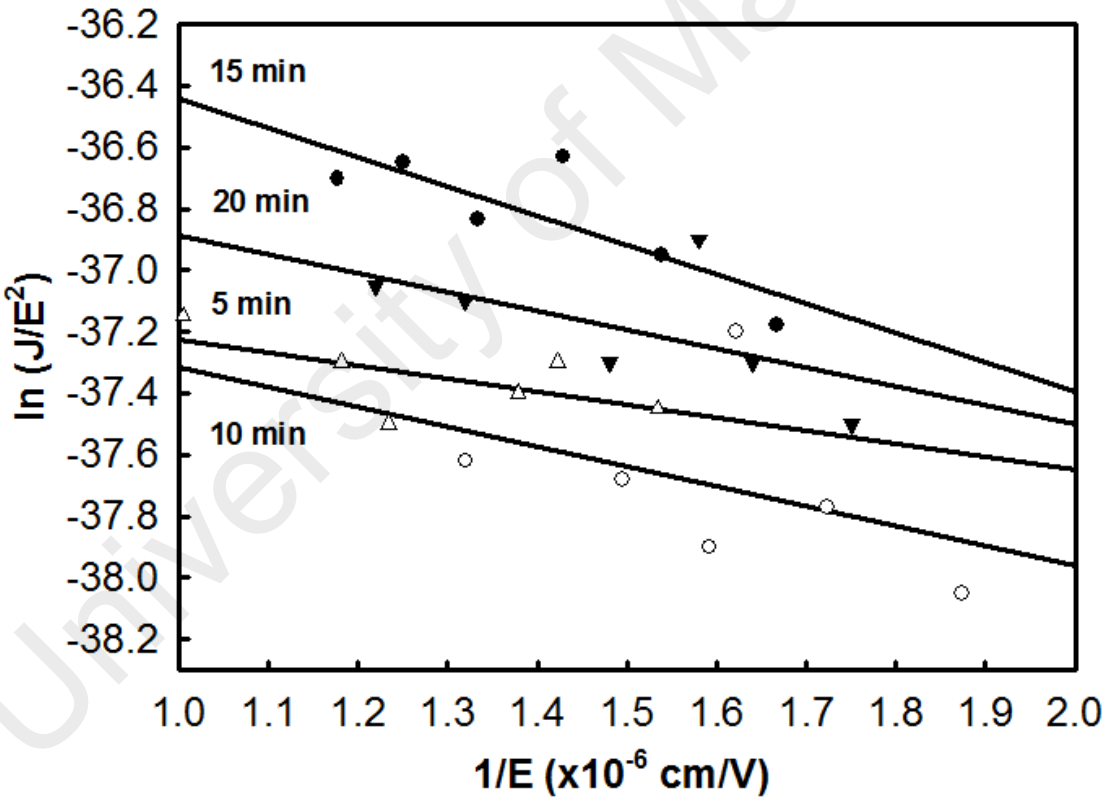

Figure 5.35: FN tunneling linear regression plot [*In* (J/E^2) versus $1/E$] of thermally oxynitrided samples for various durations (5 min, 10 min, 15 min, and 20 min).

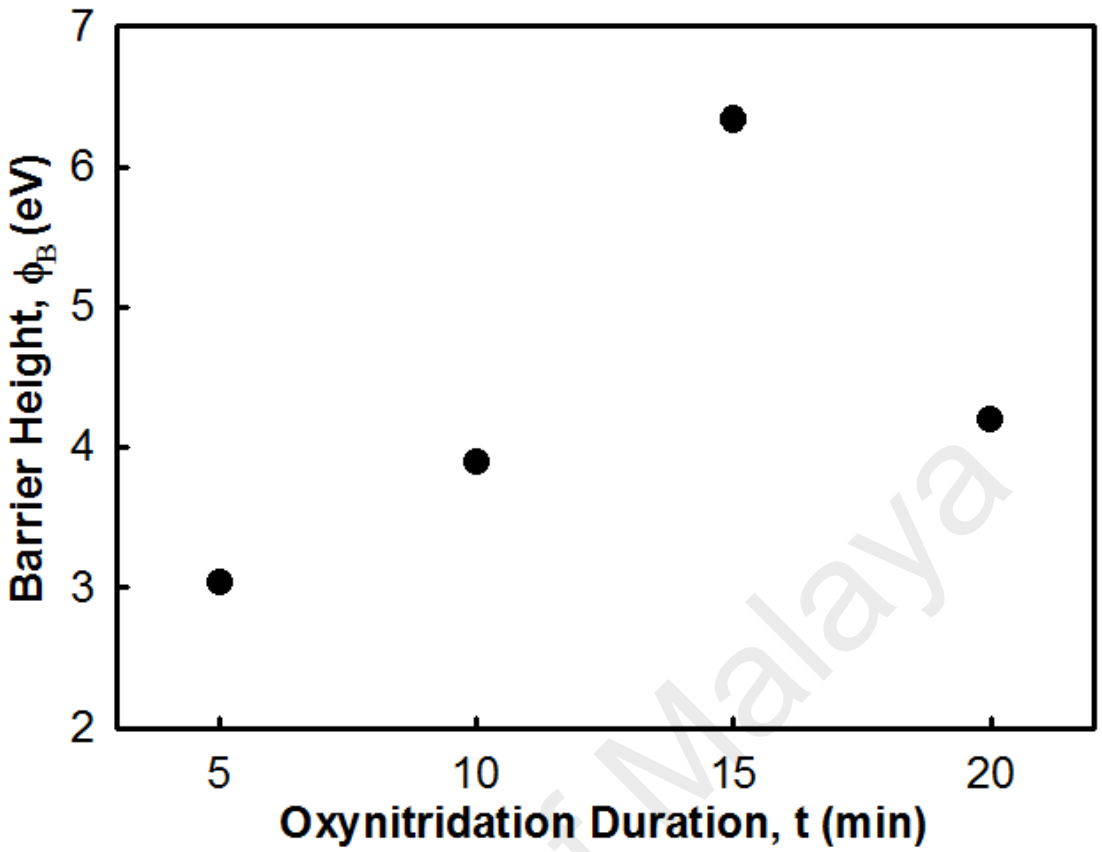

Figure 5.36: Barrier height values as a function of oxidation durations (5 min, 10 min, 15 min, and 20 min).

Fig. 5.37 shows the typical trap-assisted tunneling plot for investigated samples. A total of 30 points with goodness of fit (r^2) of ~ 0.9 were obtained. Fig. 5.38 shows the trap energy and trap density as a function of oxynitridation temperature. The 15 min sample had the highest trap energy (0.005 eV) and lowest energy trap density (5.657 x 10^{21} cm^{-3}) as compared to other samples. Hence, the 15 min sample had the lowest leakage current density (as shown Fig. 5.33) as compared to others samples. However, the trap energy was lower than the trap energy of silicon nitride (~ 0.033 eV) (Yang, Wong, & Cheng, 1996), (~ 1.03 eV) (Perera, Ikeda, Hattori, & Kuroki, 2003), (~ 0.7 eV) (Fleischer, Lai, & Cheng, 1993), and ZrO_2 (~ 0.8 eV) (Houssa, Stesmans, & Heyns, 2001) reported by previous researchers on the basis of their lower leakage current density (> 10^{-9} A cm^{-2}).

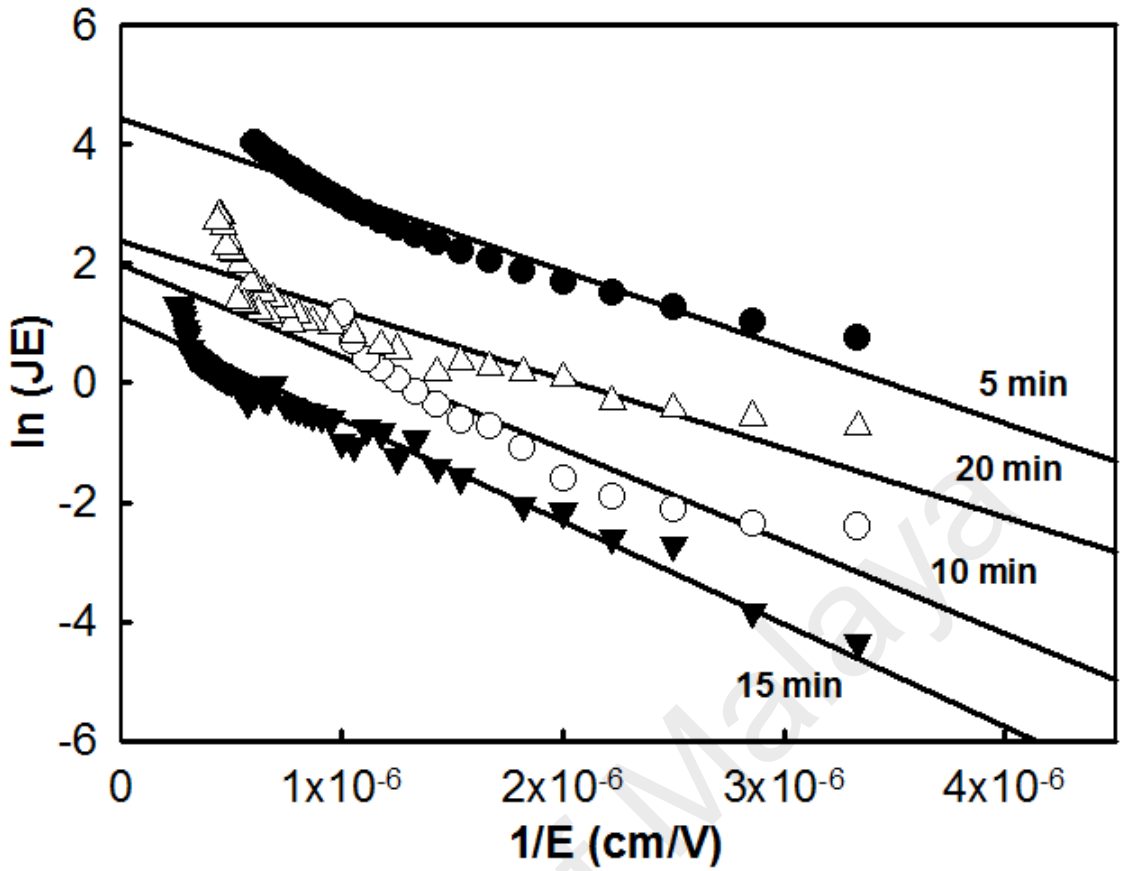

Figure 5.37: Typical trap-assisted tunneling plot of investigated samples at various oxynitridation durations (5 - 20 min).

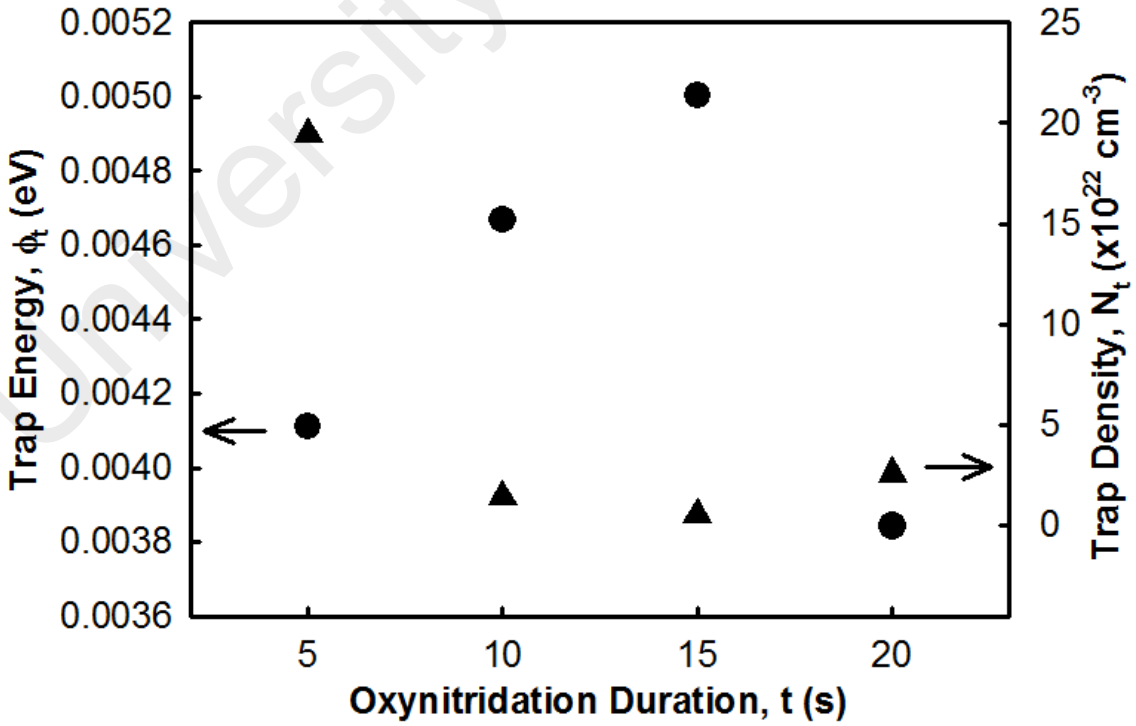

Figure 5.38: The trap energy and trap density of thermally oxynitrided samples for various oxynitridation durations (5 - 20 min).

In this part, the structural, chemical, and electrical properties of sputtered Sm thin films thermally oxynitrided in N_2O ambient for various oxynitridation durations (5 - 20 min) were present. Polycrystalline Sm_2O_3 was detected in the XRD analysis supported by the FTIR and Raman analysis. Both the Scherrer and W-H analysis have the same trend of crystallite size of Sm_2O_3. In the electrical characterization, the 15 min sample has the best electrical breakdown field of 3.9 MV cm^{-1} at ~ 10^{-6} A cm^{-2}. This was attributed to the higher barrier height, trap energy, and lower trap density.

5.4 Comparison of thermal oxidation and thermal oxynitridation of sputtered Sm thin film on Si substrate.

After both thermal oxidation and thermal oxynitridation of sputtered Sm thin film on Si substrate were conducted, the optimized parameters in terms of oxidation/ oxynitridation temperature and oxidation/oxynitridation duration were obtained. The optimized temperature and duration were summarized in Table 5.1. The optimized temperature and duration of both thermal oxidation and thermal oxynitridation were 700 °C and 15 min, respectively.

Table 5.1: The optimized temperature and duration of both thermal oxidation and thermal oxynitridation.

	Oxidation Ambient	**Optimized Temperature (°C)**	**Optimized Duration (min)**
Thermal Oxidation	O_2	700	15
Thermal Oxynitridation	N_2O	700	15

5.4.1 Physical and chemical properties

The physical and chemical properties of both thermal oxidation and thermal oxynitridation are summarized and compared in Table 5.2. It can be seen that the amount of Sm_2O_3 peaks in the XRD, FTIR, and Raman were reduced significantly after the incorporation of N. The crystallite size of Sm_2O_3 was increased while microstrain was reduced when thermally oxynitrided in N_2O ambient. According to the HRTEM images, an interfacial layer was observed after both thermal oxidation and thermal oxynitridation. A mixture of amorphous and semi-polycrystalline $Sm_xSi_yO_z$ was observed in thermal oxidation while amorphous $Sm_aSi_bO_cN_d$ was observed in thermal oxynitridation. Polycrystalline Sm_2O_3 and $Sm_xO_yN_z$ were both observed at outermost layer. The incorporation of N helped in enhancing the electrical performances.

Table 5.2: Comparison of physical and chemical properties of both thermal oxidized and thermal oxynitrided samples.

Characterization Method	Properties	Unit	Thermal Oxidation	Thermal Oxynitridation
XRD	Plane of Sm_2O_3	-	(002), (112), (233), (152), (334), (154), (226), (444), (064), (138), & (257)	(152), (334), (154), (226), (004), & (257)
	Amount of Sm_2O_3 peak	-	11	6
	Crystallite size (Scherrer Eq.)	nm	11.58	30.76
	Crystallite size (W-H plot)	nm	13.8	49.38
	Microstrain (W-H plot)	-	0.0364	0.01269
FTIR	Amount of Sm-O peak	-	9	3
Raman	Amount of Sm_2O_3 peak	-	7	4
HRTEM	Bulk	-	Sm_2O_3	$Sm_xO_yN_z$
	Thickness of bulk	nm	151.16	9
	Structure of bulk	-	Polycrystalline	Polycrystalline
	IL	-	$Sm_xSi_yO_z$	$Sm_aSi_bO_cN_d$
	Thickness of IL	nm	7.84	10.6
	Structure of IL	-	Semi-polycrystalline (IL 1) + amorphous (IL 2)	Amorphous
	Total thickness	nm	159	19.6

5.4.2 Electrical properties

Table 5.3 shows the comparison of electrical properties of both thermal oxidized and thermal oxynitrided samples in terms of *J-E* characteristic. The oxynitrided samples had higher electrical breakdown field as compared to the oxidized samples. Besides that, oxynitrided samples had a lower leakage current density. This may be due to the higher trap energy and lower trap density of oxynitrided sample. It proved that the incorporation of N improved and enhanced the electrical properties by the passivation of excessive interfacial carbon or silicon (Hoffmann & Schmeisser, 2006; Stathis & Zafar, 2006). The oxynitrided samples had a higher reliability and higher crystallization resistance as compared to oxidized samples owing to N in oxynitrided samples stabilized the oxygen ions (C. L. Cheng, Chang-Liao, Wang, & Wang, 2004; Zhang, Lu, Onodera, & Maeda, 2007). Oxynitride compounds are able to bridge oxides and nitrides and their interfaces to Si substrates (H. Wong & Gritsenko, 2002).

Table 5.3: Comparison of electrical properties of both thermal oxidized and thermal oxynitrided samples.

Characterization method	Properties	Unit	Thermal Oxidation	Thermal Oxynitridation
J-E	E_H	MV cm^{-1}	0.71	3.9
	J	A cm^{-2}	~ 10^{-4}	~ 10^{-6}
	Φ_B	eV	2.13	6.33
	Φ_t	eV	0.0007485	0.005
	N_t	cm^{-3}	6.88 x 10^{21}	5.657 x 10^{21}

CHAPTER 6

CONCLUSION AND FUTURE RECOMMENDATIONS

6.1 Conclusion

The Sm-oxide and Sm-oxynitride films had been successfully formed on Si substrate by thermal oxidation and thermal oxynitridation, respectively. The effects of thermal oxidation in O_2 gas ambient at different oxidation temperatures and durations on the physical and electrical properties of the oxidized sputtered Sm thin film on Si substrate were investigated. Apart from this, the effects of thermal oxynitridation in N_2O gas ambient at different oxynitridation temperatures and durations on the physical and electrical properties of the oxynitrided sputtered pure Sm thin film on Si substrate were also studied. According to the optimized parameters from both thermal oxidation and thermal oxynitridation processes, the oxidized and oxynitrided sputtered Sm thin film were compared. The electrical properties were improved significantly by the incorporation of N. As compared to previous works, the enhancement and improvement on the electrical breakdown field and leakage current density were observed. A sketched model related to oxidation and oxynitridation mechanisms were proposed to describe the formation of Sm-oxide and Sm-oxynitride.

6.1.1 Effects of oxidation duration and temperature on sputtered Sm thin film on Si substrate

Sm-oxide thin film has been successfully formed on Si substrate at various temperatures and durations. In this research, pure Sm metal film sputtered on Si substrate was oxidized by thermal oxidation process in oxygen ambient at 700 °C for various durations (5, 10, 15, and 20 min). The existence of polycrystalline Sm_2O_3 and interfacial

layer was confirmed by the XRD, Raman, and EDX results. It was also supported by the FTIR results which indicate that the peaks of Sm - O and Si - Si bonding are either broadening and/or shifting. The crystallite size of the 10 min sample has the smallest crystallite size in both the W–H and Scherrer calculations. However, the 15 min sample had the smoothest surface, highest breakdown voltage field of 0.71 MV cm^{-1} at ~ 10^{-4} A cm^{-2}, highest barrier height of 2.13 eV, highest trap energy of 0.000928 eV, and lowest trap density of 1.34 x 10^{22} cm^{-3} among the samples.

In addition, pure Sm metal film sputtered on Si substrates were oxidized by a thermal oxidation process in oxygen ambient at various temperatures (600 °C to 900 °C) for 15 min. The existence of polycrystalline Sm_2O_3 and semi-polycrystalline interfacial layers were confirmed by the XRD, Raman, and EDX results, and was also supported by the FTIR results indicating broadening and/or shifting of Sm - O and Si - Si bonding peaks. Based on these results, a sketched model was suggested. The crystallite sizes of Sm_2O_3 which was calculated from the W–H plot and Scherrer equation exhibited similar trend. The sample oxidized at 700 °C had the thinnest interfacial layer and thickest Sm_2O_3 film as measured from HRTEM images. According to the *C-V* and *J-E* measurements, the 700 °C sample which had smoother and uniform surface exhibited the best electrical results which had the highest κ_{eff} value of 214, the highest breakdown voltage field of 0.71 MV cm^{-1} at ~ 10^{-4} A cm^{-2}, highest barrier height of 2.13 eV, highest trap energy of 0.000928 eV, and lowest trap density of 1.34 x 10^{22} cm^{-3}. This is attributed to the thinnest interface layer between the Sm_2O_3 and Si substrate, reduction in effective oxide charge (2.81 x 10^{13} cm^{-2}), slow trap charge density (5.56 x 10^{12} cm^{-2}), average interface trap density (~ 10^{14} eV^{-1} cm^{-2}), and total interface trap density (7.31 x 10^{13} cm^{-2}).

6.1.2 Effects of oxynitridation temperature and duration on sputtered Sm thin film on Si substrate

Sm-oxynitride thin film had been successfully formed on Si substrate at various temperatures and durations. The structural, chemical, and electrical properties of sputtered Sm thin film thermally oxynitrided in N_2O ambient at various temperatures (600 – 900 °C) were present. The polycrystalline Sm_2O_3 was detected in XRD analysis and supported by the FTIR and Raman analysis. Both the Scherrer and W-H analysis have the same trend of crystallite size of Sm_2O_3. According to the XPS results, the $Sm_aSi_bO_cN_d$ film was stacked in between $Sm_xO_yN_z$ film and Si substrate. Sm-O, Sm-N, Si-N, Sm-Si-O, and Si-Si bonds were detected and matched with the FTIR and Raman analysis. The HRTEM images and EDX analysis proved that the oxynitride/semiconductor structure consists of three thin films, i.e., Si substrate, $Sm_aSi_bO_cN_d$, and $Sm_xO_yN_z$ films. In electrical characterization, the 700 °C sample have the best electrical breakdown field of 3.9 MV cm^{-1} at ~ 10^{-6} A cm^{-2}. This was attributed to the higher barrier height (6.33 eV), trap energy (0.005 eV), and lower trap density (5.657 x 10^{21} cm^{-3}).

Besides that, the structural, chemical, and electrical properties of sputtered Sm thin film thermally oxynitrided in N_2O ambient for various oxynitridation durations (5 - 20 min) were present. The polycrystalline of Sm_2O_3 was detected in the XRD analysis and supported by the FTIR and Raman analysis. Both the Scherrer and W-H analysis have the same trend of crystallite size of Sm_2O_3. In electrical characterization, the 15 min sample have the best electrical breakdown field of 3.9 MV cm^{-1} at ~ 10^{-6} A cm^{-2}. This was attributed to the higher barrier height (6.33 eV), trap energy (0.005 eV), and lower trap density (5.657 x 10^{21} cm^{-3}).

6.1.3 Comparison of thermal oxidation and thermal oxynitridation of sputtered Sm thin film on Si substrate.

According to the obtained results, the optimized temperature and duration of both thermal oxidation and thermal oxynitridation were 700 °C and 15 min, respectively. Both optimum samples were compared in terms of their physical, chemical, and electrical properties as described in section 5.4. The oxynitrided samples had higher electrical breakdown field as compared to the oxidized samples. Besides that, oxynitrided samples had lower leakage current density. It may be due to oxynitrided samples had higher trap energy and lower trap density as compared to the oxidized sample. It proved that the incorporation of N improved and enhanced the electrical properties by the passivation of excessive interfacial carbon or silicon (Hoffmann & Schmeisser, 2006; Stathis & Zafar, 2006).

6.1.4 Establish a possible mechanism model of oxidation and oxynitridation

According to the results of the XRD, FTIR, Raman, HRTEM, EDX, and/or XPS analysis, a sketched model was proposed for both thermal oxidation and thermal oxynitridation mechanisms. According to HRTEM images, four layers of the oxide/semiconductor stacking system was observed in the oxidized sample while three layers of the oxide/semiconductor stacking system was observed in the oxynitrided sample. For oxidizes sample, the IL-2 exhibited semi polycrystalline structure while the IL-1 exhibited amorphous structure. Some polycrystalline structures can be observed at the region between IL-2 and Sm_2O_3. For the oxynitrided sample, one layer of amorphous interfacial layer formed between Sm-oxynitride and Si substrate. At higher temperature, undesirably thick interfacial layers were formed due to higher activation energy under higher temperature ambient.

6.2 Recommendations for future research

The investigation in the present study exposed huge interesting areas that require further in-depth evaluation and future discovery. The following ideas are suggested for future research:

(i) The effects of thermal oxidation and/or thermal oxynitridation on the physical and electrical properties of the oxidized sputtered Sm thin film on SiC substrates can be investigated for high power applications.

(ii) It is worth to further investigate the effects of concentration of N_2O gas on the properties of sputtered Sm thin films on Si and/or SiC substrates.

(iii) The reliability of Sm-oxide and Sm-oxynitride can be further investigated by bias temperature instability (BTI) performance.

(iv) The leakage characteristics of the oxidized and oxynitrided Sm thin films can be estimated quantitatively by investigating the charge conduction mechanisms.

REFERENCES

Abrutis, A., Lukosius, M., Saltyte, Z., Galvelis, R., Baumann, P. K., Schumacher, M., & Lindner, J. (2008). Chemical vapour deposition of praseodymium oxide films on silicon: influence of temperature and oxygen pressure. *Thin Solid Films, 516*(15), 4758-4764. doi:10.1016/j.tsf.2007.08.097

Adelhelm, C., Pickert, T., Balden, M., Rasinski, M., Plocinski, T., Ziebert, C., . . . Maier, H. (2009). Monoclinic B-phase erbium sesquioxide (Er2O3) thin films by filtered cathodic arc deposition. *Scripta Materialia, 61*(8), 789-792. doi:10.1016/j.scriptamat.2009.06.031

Aditya, B. N., & Gupta, N. (2012). Material selection methodology for gate dielectric material in metal-oxide-semiconductor devices. *Materials & Design, 35*, 696-700. doi:10.1016/j.matdes.2011.10.015

Ahmet, P., Nakagawa, K., Kakushima, K., Nohira, H., Tsutsui, K., Sugii, N., . . . Iwai, H. (2008). Electrical characteristics of MOSFETs with La2O3/Y2O3 gate stack. *Microelectronics Reliability, 48*(11-12), 1769-1771.

Al-Kuhaili, M. F., & Durrani, S. M. A. (2007). Optical properties of erbium oxide thin films deposited by electron beam evaporation. *Thin Solid Films, 515*(5), 2885-2890. doi:10.1016/j.tsf.2006.08.048

Al-Kuhaili, M. F., & Durrani, S. M. A. (2014). Structural and optical properties of dysprosium oxide thin films. *Journal of Alloys and Compounds, 591*, 234-239. doi:10.1016/j.jallcom.2013.12.226

Alers, G. B., Fleming, R. M., Wong, Y. H., Dennis, B., Pinczuk, A., Redinbo, G., . . . Hasan, Z. (1998). Nitrogen plasma annealing for low temperature Ta2O5 films. *Applied Physics Letters, 72*(11), 1308-1310. doi:Doi 10.1063/1.120569

Andersson, M., Pearce, R., & Spetz, A. L. (2013). New generation SiC based field effect transistor gas sensors. *Sensors and Actuators B-Chemical, 179*, 95-106.

Andreeva, A. F. (1998). Preparation and properties of oxide films of the rare earth metals. *Powder Metallurgy and Metal Ceramics, 37*(1-2), 91-93. doi:Doi 10.1007/Bf02677236

Ansart, F., Ganda, H., Saporte, R., & Traverse, J. P. (1995). Study of the Oxidation of Aluminum Nitride Coatings at High-Temperature. *Thin Solid Films, 260*(1), 38-46. doi:Doi 10.1016/0040-6090(94)06480-6

Arden, W. (2006). Future semiconductor material requirements and innovations as projected in the ITRS 2005 roadmap. *Materials Science and Engineering B-Solid State Materials for Advanced Technology, 134*(2-3), 104-108. doi:10.1016/j.mseb.2006.07.004

Ashby, M. F. (1988). Materials Selection in Mechanical Design. *Journal of Metals, 40*(7), A1-A2.

Ashby, M. F. (1989). Materials Selection in Conceptual Design. *Materials Science and Technology, 5*(6), 517-525.

Ashby, M. F. (2000). Multi-objective optimization in material design and selection. *Acta Materialia, 48*(1), 359-369. doi:Doi 10.1016/S1359-6454(99)00304-3

Ashby, M. F., Brechet, Y., & Cebon, D. (2002). Selection strategies for materials and processes. *Advanced Engineering Materials, 4*(6), 327-334. doi:Doi 10.1002/1527-2648(20020605)4:6<327::Aid-Adem327>3.0.Co;2-N

Ashby, M. F., Brechet, Y. J. M., Cebon, D., & Salvo, L. (2004). Selection strategies for materials and processes. *Materials & Design, 25*(1), 51-67. doi:10.1016/S0261-3069(03)00159-6

Ashby, M. F., & Cebon, D. (1993). Materials Selection in Mechanical Design. *Journal De Physique Iv, 3*(C7), 1-9. doi:Doi 10.1051/Jp4:1993701

Ashby, M. F., Gibson, L. J., Wegst, U., & Olive, R. (1995). The Mechanical-Properties of Natural Materials .1. Material Property Charts. *Proceedings of the Royal Society-Mathematical and Physical Sciences, 450*(1938), 123-140. doi:DOI 10.1098/rspa.1995.0075

Atuchin, V. V., Kruchinin, V. N., Wong, Y. H., & Cheong, K. Y. (2013). Microstructural and optical properties of ZrON/Si thin films. *Materials Letters, 105*, 72-75. doi:10.1016/j.matlet.2013.03.100

Autran, J. L., Devine, R., Chaneliere, C., & Balland, B. (1997). Fabrication and characterization of Si-MOSFET's with PECVD amorphous Ta2O5 gate insulator. *Ieee Electron Device Letters, 18*(9), 447-449. doi:Doi 10.1109/55.622525

Balakrishnan, G., Sudhakara, P., Wasy, A., Ho, H. S., Shin, K. S., & Song, J. I. (2013). Epitaxial growth of cerium oxide thin films by pulsed laser deposition. *Thin Solid Films, 546*, 467-471. doi:10.1016/j.tsf.2013.06.048

Banakh, O., Csefalvay, C., Steinmann, P. A., Fenker, M., & Kappl, H. (2006). Evaluation of adhesion and tribological behaviour of tantalum oxynitride thin films deposited by reactive magnetron sputtering onto steel substrates. *Surface & Coatings Technology, 200*(22-23), 6500-6504. doi:10.1016/j.surfcoat.2005.11.079

Barhai, P. K., Kumari, N., Banerjee, I., Pabi, S. K., & Mahapatra, S. K. (2010). Study of the effect of plasma current density on the formation of titanium nitride and titanium oxynitride thin films prepared by reactive DC magnetron sputtering. *Vacuum, 84*(7), 896-901. doi:10.1016/j.vacuum.2009.12.004

Bernard, M. C., Goff, A. H. L., Thi, B. V., & Detorresi, S. C. (1993). Electrochromic Reactions in Manganese Oxides .1. Raman Analysis. *Journal of the Electrochemical Society, 140*(11), 3065-3070. doi:Doi 10.1149/1.2220986

Bethge, O., Zimmermann, C., Lutzer, B., Simsek, S., Smoliner, J., Stoger-Pollach, M., . . . Bertagnolli, E. (2014). Effective reduction of trap density at the Y2O3/Ge interface by rigorous high-temperature oxygen annealing. *Journal of Applied Physics, 116*(21). doi:Artn 21411110.1063/1.4903533

Bin Lee, J., Kwak, S. H., & Kim, H. J. (2003). Effects of surface roughness of substrates on the c-axis preferred orientation of ZnO films deposited by r.f. magnetron sputtering. *Thin Solid Films, 423*(2), 262-266.

Bhushan, B., & Dandavate, C. (2000). Thin-film friction and adhesion studies using atomic force microscopy. *Journal of Applied Physics, 87*(3), 1201-1210. doi:Doi 10.1063/1.371998

Brow, R. K., & Pantano, C. G. (1986). Compositionally Dependent Si 2p Binding-Energy Shifts in Silicon Oxynitride Thin-Films. *Journal of the American Ceramic Society, 69*(4), 314-316. doi:DOI 10.1111/j.1151-2916.1986.tb04738.x

Buchanan, D. A. (1999). Scaling the gate dielectric: Materials, integration, and reliability. *Ibm Journal of Research and Development, 43*(3), 245-264.

Carr, E. C., & Buhrman, R. A. (1993). Role of Interfacial Nitrogen in Improving Thin Silicon-Oxides Grown in N2o. *Applied Physics Letters, 63*(1), 54-56. doi:Doi 10.1063/1.109749

Carr, E. C., Ellis, K. A., & Buhrman, R. A. (1995). N-Depth Profiles in Thin Sio2 Grown or Processed in N2o - the Role of Atomic Oxygen. *Applied Physics Letters, 66*(12), 1492-1494. doi:Doi 10.1063/1.113665

Casady, J. B., & Johnson, R. W. (1996). Status of silicon carbide (SiC) as a wide-bandgap semiconductor for high-temperature applications: A review. *Solid-State Electronics, 39*(10), 1409-1422.

Castan, H., Garcia, H., Duenas, S., Bailon, L., Miranda, E., Kukli, K., . . . Leskela, M. (2015). Conduction and stability of holmium titanium oxide thin films grown by atomic layer deposition. *Thin Solid Films, 591*, 55-59. doi:10.1016/j.tsf.2015.08.027

Cebon, D., & Ashby, M. F. (2006). Engineering materials informatics. *Mrs Bulletin, 31*(12), 1004-1012. doi:Doi 10.1557/Mrs2006.229

Chabinyc, M. L., Lujan, R., Endicott, F., Toney, M. F., McCulloch, I., & Heeney, M. (2007). Effects of the surface roughness of plastic-compatible inorganic dielectrics on polymeric thin film transistors. *Applied Physics Letters, 90*(23). doi:Artn 23350810.1063/1.2746955

Chalker, P. R. (1999). Wide bandgap semiconductor materials for high temperature electronics. *Thin Solid Films, 343*, 616-622.

Chan, T. K., Darmawan, P., Ho, C. S., Malar, P., Lee, P. S., & Osipowicz, T. (2008). Interface strain study of thin Lu2O3/Si using HRBS. *Nuclear Instruments & Methods in Physics Research Section B-Beam Interactions with Materials and Atoms, 266*(8), 1486-1489. doi:10.1016/j.nimb.2007.12.090

Chang, S. Y., Jeong, M. I., Chandra, S. V. J., Lee, Y. B., Hong, H. B., Reddy, V. R., & Choi, C. J. (2008). Thermal stability of high-k Er-silicate gate dielectric formed by interfacial reaction between Er and SiO2 films. *Materials Science in Semiconductor Processing, 11*(4), 122-125. doi:10.1016/j.mssp.2009.06.001

Chao, C. Y., Lin, L. F., & Macdonald, D. D. (1981). A Point-Defect Model for Anodic Passive Films .1. Film Growth-Kinetics. *Journal of the Electrochemical Society, 128*(6), 1187-1194. doi:Doi 10.1149/1.2127591

Chappe, J. M., Martin, N., Lintymer, J., Sthal, F., Terwagne, G., & Takadoum, J. (2007). Titanium oxynitride thin films sputter deposited by the reactive gas pulsing process. *Applied Surface Science, 253*(12), 5312-5316. doi:10.1016/j.apsusc.2006.12.004

Chappe, J. M., Martin, N., Pierson, J. F., Terwagne, G., Lintymer, J., Gavoille, J., & Takadoum, J. (2004). Influence of substrate temperature on titanium oxynitride thin films prepared by reactive sputtering. *Applied Surface Science, 225*(1-4), 29-38. doi:10.1016/j.apsusc.2003.09.028

Chen, D. X., Habu, D., Masubuchi, Y., Torii, S., Kamiyama, T., & Kikkawa, S. (2016). Partial nitrogen loss in SrTaO2N and LaTiO2N oxynitride perovskites. *Solid State Sciences, 54*, 2-6. doi:10.1016/j.solidstatesciences.2015.08.018

Chen, F. H., Her, J. L., Mondal, S., Hung, M. N., & Pan, T. M. (2013). Impact of Ti doping in Sm2O3 dielectric on electrical characteristics of a-InGaZnO thin-film transistors. *Applied Physics Letters, 102*(19). doi:Artn 19351510.1063/1.4807014

Chen, F. H., Her, J. L., Shao, Y. H., Li, W. C., Matsuda, Y. H., & Pan, T. M. (2013). Structural and electrical characteristics of high-kappa ErTixOy gate dielectrics on InGaZnO thin-film transistors. *Thin Solid Films, 539*, 251-255. doi:10.1016/j.tsf.2013.04.139

Chen, F. H., Hung, M. N., Yang, J. F., Kuo, S. Y., Her, J. L., Matsuda, Y. H., & Pan, T. M. (2013). Effect of surface roughness on electrical characteristics in amorphous InGaZnO thin-film transistors with high-kappa Sm2O3 dielectrics. *Journal of Physics and Chemistry of Solids, 74*(4), 570-574. doi:DOI 10.1016/j.jpcs.2012.12.006

Chen, S., Liu, Z. T., Feng, L. P., Che, X. S., & Zhao, X. R. (2013). The dielectric properties enhancement due to Yb incorporation into HfO2. *Applied Physics Letters, 103*(13). doi:Artn 13290210.1063/1.4821850

Chen, S., Liu, Z. T., Feng, L. P., Che, X. S., & Zhao, X. R. (2014). Effect of ytterbium inclusion in hafnium oxide on the structural and electrical properties of the high-k gate dielectric. *Journal of Rare Earths, 32*(6), 580-584. doi:10.1016/S1002-0721(14)60111-3

Chen, X. Y., Song, L. X., You, L. J., & Zhao, L. L. (2013). Incorporation effect of Y2O3 on the structure and optical properties of HfO2 thin films. *Applied Surface Science, 271*, 248-252. doi:10.1016/j.apsusc.2013.01.168

Chen, Y. W., Lai, C. M., Cheng, L. W., Hsu, C. H., & Hsu, C. W. (2012). Further work function and interface quality improvement on Al2O3 capped high-k/metal gate p-type metal-oxide-semiconductor field-effect-transistors by incorporation of fluorine. *Thin Solid Films, 520*(13), 4482-4485. doi:10.1016/j.tsf.2012.02.087

Cheng, C. L., Chang-Liao, K. S., Wang, P. L., & Wang, T. K. (2004). Physical and reliability characteristics of metal-oxide-semiconductor devices with HfOxNy gate dielectrics on different surface-oriented substrates. *Japanese Journal of Applied Physics Part 2-Letters & Express Letters, 43*(5a), L599-L601. doi:10.1143/Jjap.43.L599

Cheng, C. L., Chang-Liao, K. S., & Wang, T. K. (2006). Improved electrical and surface characteristics of metal-oxide-semiconductor device with gate hafnium oxynitride by chemical dry etching. *Solid-State Electronics, 50*(2), 103-108. doi:10.1016/j.sse.2005.12.001

Cheng, J. B., Li, A. D., Shao, Q. Y., Ling, H. Q., Wu, D., Wang, Y., . . . Ming, N. B. (2004). Growth and characteristics of La2O3 gate dielectric prepared by low pressure metalorganic chemical vapor deposition. *Applied Surface Science, 233*(1-4), 91-98. doi:10.1016/j.apsusc.2004.03.232

Cheng, X. H., Xu, D. P., Song, Z. R., He, D. W., Yu, Y. H., Zhao, Q. T., & Shen, D. S. (2009). Characterization of gadolinium oxide film by pulse laser deposition. *Applied Surface Science, 256*(3), 921-923. doi:10.1016/j.apsusc.2009.08.086

Cheng, X. R., Cheng, Y. C., & Liu, B. Y. (1988). Nitridation-Enhanced Conductivity Behavior and Current Transport Mechanism in Thin Thermally Nitrided Sio2. *Journal of Applied Physics, 63*(3), 797-802. doi:Doi 10.1063/1.340072

Cheng, X. R., Qi, Z. M., Zhang, G. B., Zhou, H. J., Zhang, W. P., & Yin, M. (2009). Growth and characterization of Y2O3 thin films. *Physica B-Condensed Matter, 404*(1), 146-149. doi:10.1016/j.physb.2008.10.022

Cheng, X. R., Qi, Z. M., Zhang, H. J., Zhang, G. B., & Pan, G. Q. (2012). Growth and interface of amorphous La2Hf2O7/Si thin film. *Journal of Rare Earths, 30*(2), 189-192. doi:10.1016/S1002-0721(12)60020-9

Cheong, K. Y., Moon, J., Kim, H. J., Bahng, W., & Kim, N. K. (2010). Metal-oxide-semiconductor characteristics of thermally grown nitrided SiO2 thin film on 4H-SiC in various N2O ambient. *Thin Solid Films, 518*(12), 3255-3259. doi:10.1016/j.tsf.2009.11.003

Chew, C. C., Goh, K. H., Gorji, M. S., Tan, C. G., Ramesh, S., & Wong, Y. H. (2016). Breakdown field enhancement of Si-based MOS capacitor by post-deposition annealing of the reactive sputtered ZrOxNy gate oxide. *Applied Physics a-Materials Science & Processing, 122*(2). doi:ARTN 6610.1007/s00339-016-9624-7

Chin, W. C., Cheong, K. Y., & Hassan, Z. (2010). Sm2O3 gate dielectric on Si substrate. *Materials Science in Semiconductor Processing, 13*(5-6), 303-314.

Cho, M. H., Chang, H. S., Cho, Y. J., Moon, D. W., Min, K. H., Sinclair, R., . . . Lee, N. I. (2004). Change in the chemical state and thermal stability of HfO2 by the incorporation of Al2O3. *Applied Physics Letters, 84*(4), 571-573. doi:10.1063/1.1633976

Cho, M. H., Ko, D. H., Choi, Y. K., Lyo, I. W., Jeong, K., & Whang, C. N. (2002). Epitaxial Y2O3 film growth on an oxidized Si surface. *Thin Solid Films, 402*(1-2), 38-42. doi:Doi 10.1016/S0040-6090(01)01625-X

Choi, S. C., Cho, M. H., Whangbo, S. W., Whang, C. N., Hong, C. E., Kim, N. Y., . . . Lee, M. Y. (1997). Heteroepitaxial growth of Y2O3 films on Si(100) by reactive ionized cluster beam deposition. *Nuclear Instruments & Methods in Physics Research Section B-Beam Interactions with Materials and Atoms, 121*(1-4), 170-174. doi:Doi 10.1016/S0168-583x(96)00589-7

Choi, S. C., Cho, M. H., Whangbo, S. W., Whang, C. N., Kang, S. B., Lee, S. I., & Lee, M. Y. (1997). Epitaxial growth of Y2O3 films on Si(100) without an interfacial oxide layer. *Applied Physics Letters, 71*(7), 903-905. doi:Doi 10.1063/1.119683

Cico, K., Kuzmik, J., Gregusova, D., Stoklas, R., Lalinsky, T., Georgakilas, A., . . . Frohlich, K. (2007). Optimization and performance of Al2O3/GaN metal-oxide-semiconductor structures. *Microelectronics Reliability, 47*(4-5), 790-793. doi:10.1016/j.microrel.2007.01.010

Constantinescu, C., Ion, V., Galca, A. C., & Dinescu, M. (2012). Morphological, optical and electrical properties of samarium oxide thin films. *Thin Solid Films, 520*(20), 6393-6397. doi:DOI 10.1016/j.tsf.2012.06.049

Cristea, D., Crisan, A., Cretu, N., Borges, J., Lopes, C., Cunha, L., . . . Munteanu, D. (2015). Structure dependent resistivity and dielectric characteristics of tantalum oxynitride thin films produced by magnetron sputtering. *Applied Surface Science, 354*, 298-305. doi:10.1016/j.apsusc.2015.06.167

Cuesta, A., Dhamelincourt, P., Laureyns, J., Martinez-Alonso, A., & Tascon, J. M. D. (1998). Comparative performance of X-ray diffraction and Raman microprobe techniques for the study of carbon materials. *Journal of Materials Chemistry, 8*(12), 2875-2879. doi:DOI 10.1039/a805841e

Dakhel, A. A. (2004a). Dielectric and optical properties of samarium oxide thin films. *Journal of Alloys and Compounds, 365*(1-2), 233-239.

Dakhel, A. A. (2004b). Dielectric properties of europium-indium oxide solid solution films prepared on Si (100) substrates. *Journal of Physics and Chemistry of Solids, 65*(11), 1765-1771. doi:10.1016/j.jpcs.2004.06.001

Dakhel, A. A. (2004c). Electrical and transport properties of europium-indium oxide films prepared on Si(100) substrates. *Physica B-Condensed Matter, 353*(3-4), 255-262. doi:10.1016/j.physb.2004.10.006

Dakhel, A. A. (2004d). Electrical conduction processes in neodymium oxide thin films prepared on Si(100) substrates. *Journal of Alloys and Compounds, 376*(1-2), 38-42. doi:10.1016/j.jallcom.2004.01.009

Dakhel, A. A. (2004e). Optical and dielectric properties of gadolinium-indium oxide films prepared on Si (100) substrate. *Chemical Physics Letters, 393*(4-6), 528-534. doi:10.1016/j.cplett.2004.06.094

Dakhel, A. A. (2005a). The ac conductivity and dielectric properties of Europium-Indium oxide films prepared on silicon (100) substrate. *Thin Solid Films, 476*(2), 366-372. doi:10.1016/j.tsf.2004.10.007

Dakhel, A. A. (2005b). The annealing effect for structural, optical and electrical properties of dysprosium-manganese oxide films grown on Si substrate. *Solid-State Electronics, 49*(12), 1996-2001. doi:10.1016/j.sse.2005.09.016

Dakhel, A. A. (2005c). DC conduction properties of Gadolinium-Indium oxide films deposited on Si(100). *Solid-State Electronics, 49*(4), 562-566. doi:10.1016/j.sse.2004.11.014

Dakhel, A. A. (2005d). DC conduction properties of oxidised erbium films deposited on Si(100) substrates. *Journal of Alloys and Compounds, 396*(1-2), 74-78. doi:10.1016/j.jallcom.2005.01.007

Dakhel, A. A. (2006a). Characterisation of oxidised erbium films deposited on Si(100) substrates. *Materials Chemistry and Physics, 100*(2-3), 366-371. doi:10.1016/j.matchemphys.2006.01.005

Dakhel, A. A. (2006b). DC electrical measurements on gadolinium-erbium oxide films prepared on Si (100) substrates. *Current Applied Physics, 6*(1), 32-36. doi:10.1016/j.cap.2004.10.005

Dakhel, A. A. (2006c). Study of do conduction mechanisms in dysprosium-manganese oxide insulator thin films grown on Si substrates. *Microelectronics Reliability, 46*(8), 1303-1308. doi:10.1016/j.microrel.2005.11.001

Dakhel, A. A. (2006d). Temperature and frequency dependent dielectric properties of dysprosium oxide grown on Si(p) substrates. *Journal of Alloys and Compounds, 422*(1-2), 1-5. doi:10.1016/j.jallcom.2005.11.040

Dakhel, A. A. (2008). Charge trapping and ac-electrical conduction in nanocrystalline erbiurn manganate film on Si substrate. *Journal of Alloys and Compounds, 458*(1-2), 77-82. doi:10.1016/j.jallcom.2007.04.050

Dakhel, A. A. (2009). Annealing effect on the structural, optical and electrical properties of Yb-Mn oxide thin films. *Journal of Alloys and Compounds, 476*(1-2), 28-32. doi:10.1016/j.jallcom.2008.09.095

Dakhel, A. A. (2010). Effect of ytterbium doping on the optical and electrical properties of intrinsic In2O3 thin films. *Microelectronics Reliability, 50*(2), 211-216. doi:10.1016/j.microrel.2009.11.007

Danterroches, C. (1984). High-Resolution Tem Study of the Si(001)/Sio2 Interface. *Journal De Microscopie Et De Spectroscopie Electroniques, 9*(3), 147-&.

Darmawan, P., Yuan, C. L., & Lee, P. S. (2006). Trap-controlled behavior in ultrathin Lu2O3 high-k gate dielectrics. *Solid State Communications, 138*(12), 571-573. doi:10.1016/j.ssc.2006.05.003

Depas, M., Nigam, T., & Heyns, M. M. (1996). Soft breakdown of ultra-thin gate oxide layers. *Ieee Transactions on Electron Devices, 43*(9), 1499-1504. doi:Doi 10.1109/16.535341

Derrien, J., & Commandre, M. (1982). Sio2 Ultra Thin-Film Growth-Kinetics as Investigated by Surface Techniques. *Surface Science, 118*(1-2), 32-46. doi:Doi 10.1016/0039-6028(82)90011-5

Diot, N., Larcher, O., Marchand, R., Kempf, J. Y., & Macaudiere, P. (2001). Rare-earth and tungsten oxynitrides with a defect fluorite-type structure as new pigments. *Journal of Alloys and Compounds, 323*, 45-48. doi:Doi 10.1016/S0925-8388(01)00999-9

Durand, C., Dubourdieu, C., Vallee, C., Gautier, E., Ducroquet, F., Jalabert, D., . . . Joubert, O. (2005). Structural and electrical characterizations of yttrium oxide films after postannealing treatments. *Journal of the Electrochemical Society, 152*(12), F217-F225. doi:10.1149/1.2109487

Elford, A., & Mawby, P. A. (1999). The numerical modelling of silicon carbide high power semiconductor devices. *Microelectronics Journal, 30*(6), 527-534.

Ellis, K. A., & Buhrman, R. A. (1996). Furnace gas-phase chemistry of silicon oxynitridation in N2O. *Applied Physics Letters, 68*(12), 1696-1698. doi:Doi 10.1063/1.115909

Engstrom, O., Raeissi, B., Hall, S., Buiu, O., Lemme, M. C., Gottlob, H. D. B., . . . Cherkaoui, K. (2007). Navigation aids in the search for future high-k dielectrics: Physical and electrical trends. *Solid-State Electronics, 51*(4), 622-626. doi:10.1016/j.sse.2007.02.021

Enta, Y., Suto, K., Takeda, S., Kato, H., & Sakisaka, Y. (2006). Oxynitridation of Si(100) surface with thermally excited N2O gas. *Thin Solid Films, 500*(1-2), 129-132. doi:10.1016/j.tsf.2005.11.058

Escoubas, S., Brillet, H., Mesarotti, T., Raymond, G., Thomas, O., & Morin, P. (2008). Local strains induced in silicon channel by a periodic array of nitride capped poly lines investigated by high resolution X-ray diffraction. *Materials Science and Engineering B-Advanced Functional Solid-State Materials, 154*, 129-132. doi:10.1016/j.mseb.2008.08.016

Evangelou, E. K., Wiemer, C., Fanciulli, M., Sethu, M., & Cranton, W. (2003). Electrical and structural characteristics of yttrium oxide films deposited by rf-magnetron sputtering on n-Si. *Journal of Applied Physics, 94*(1), 318-325. doi:10.1063/1.1580644

Fadley, C. S. (2010). X-ray photoelectron spectroscopy: Progress and perspectives. *Journal of Electron Spectroscopy and Related Phenomena, 178*, 2-32. doi:10.1016/j.elspec.2010.01.006

Fang, Z. W., Williams, P. A., Odedra, R., Jeon, H., & Potter, R. J. (2012). Gadolinium nitride films deposited using a PEALD based process. *Journal of Crystal Growth, 338*(1), 111-117. doi:10.1016/j.jcrysgro.2011.10.049

Feng, X., Wong, H., Yang, B. L., Dong, S. R., Iwai, H., & Kakushima, K. (2014). On the current conduction mechanisms of CeO2/La2O3 stacked gate dielectric. *Microelectronics Reliability, 54*(6-7), 1133-1136. doi:10.1016/j.microrel.2013.12.014

Fenker, M., Kappl, H., Banakh, O., Martin, N., & Pierson, J. F. (2006). Investigation of Niobium oxynitride thin films deposited by reactive magnetron sputtering. *Surface & Coatings Technology, 201*(7), 4152-4157. doi:10.1016/j.surfcoat.2006.08.104

Fernandes, P. A., Salome, P. M. P., & da Cunha, A. F. (2009). Growth and Raman scattering characterization of Cu2ZnSnS4 thin films. *Thin Solid Films, 517*(7), 2519-2523. doi:10.1016/j.tsf.2008.11.031

Field, F., Kirchain, R., & Roth, R. (2007). Process cost modeling: Strategic engineering and economic evaluation of materials technologies. *Jom, 59*(10), 21-32. doi:DOI 10.1007/s11837-007-0126-0

Fleischer, S., Lai, P. T., & Cheng, Y. C. (1992). Simplified Closed-Form Trap-Assisted Tunneling Model Applied to Nitrided Oxide Dielectric Capacitors. *Journal of Applied Physics, 72*(12), 5711-5715. doi:Doi 10.1063/1.351923

Fleischer, S., Lai, P. T., & Cheng, Y. C. (1993). A New Method for Extracting the Trap Energy in Insulators. *Journal of Applied Physics, 73*(7), 3348-3351. doi:Doi 10.1063/1.352934

Frohlich, K., Luptak, R., Dobrocka, E., Husekova, K., Cico, K., Rosova, A., . . . Espinos, J. P. (2006). Characterization of rare earth oxides based MOSFET gate stacks prepared by metal-organic chemical vapour deposition. *Materials Science in Semiconductor Processing, 9*(6), 1065-1072. doi:10.1016/j.mssp.2006.10.025

Fuchs, E. R. H., Field, F. R., Roth, R., & Kirchain, R. E. (2008). Strategic materials selection in the automobile body: Economic opportunities for polymer composite design. *Composites Science and Technology, 68*(9), 1989-2002. doi:10.1016/j.compscitech.2008.01.015

Futsuhara, M., Yoshioka, K., & Takai, O. (1998). Optical properties of zinc oxynitride thin films. *Thin Solid Films, 317*(1-2), 322-325. doi:Doi 10.1016/S0040-6090(97)00646-9

Gaboriaud, R. J., Pailloux, F., Guerin, P., & Paumier, F. (2001). Yttrium sesquioxide, Y2O3, thin films deposited on Si by ion beam sputtering: microstructure and dielectric properties. *Thin Solid Films, 400*(1-2), 106-110. doi:Doi 10.1016/S0040-6090(01)01468-7

Gaboriaud, R. J., Paumier, F., Pailloux, F., & Guerin, P. (2004). Y2O3 thin films: internal stress and microstructure. *Materials Science and Engineering B-Solid State Materials for Advanced Technology, 109*(1-3), 34-38. doi:10.1016/j.mseb.2003.10.023

Gao, J., He, G., Sun, Z. Q., Chen, H. S., Zheng, C. Y., Jin, P., . . . Liu, M. (2016). Modification of electrical properties and carrier transportation mechanism of ALD-derived HfO2/Si gate stacks by Al2O3 incorporation. *Journal of Alloys and Compounds, 667*, 352-358. doi:10.1016/j.jallcom.2016.01.171

George, S. M., Sneh, O., Dillon, A. C., Wise, M. L., Ott, A. W., Okada, L. A., & Way, J. D. (1994). Atomic Layer Controlled Deposition of Sio2 and Al2o3 Using Abab - Binary Reaction Sequence Chemistry. *Applied Surface Science, 82-3*, 460-467. doi:Doi 10.1016/0169-4332(94)90259-3

Ghosh, S. N., Parm, I. O., Dhungel, S. K., Jang, K. S., Jeong, S. W., Yoo, J., Yi, J. (2008). Field-induced surface passivation of p-type silicon by using AlON films. *Renewable Energy, 33*(2), 320-325. doi:10.1016/j.renene.2007.05.030

Gillen, R., & Robertson, J. (2013). Electronic structure of lanthanide oxide high K gate oxides. *Microelectronic Engineering, 109*, 72-74.

Gordon, R. G., Becker, J., Hausmann, D., & Suh, S. (2001). Vapor deposition of metal oxides and silicates: Possible gate insulators for future microelectronics. *Chemistry of Materials, 13*(8), 2463-2464. doi:DOI 10.1021/cm010145k

Gottlob, H. D. B., Echtermeyer, T., Mollenhauer, T., Efavi, J. K., Schmidt, M., Wahlbrink, T., . . . Fissel, A. (2006). CMOS integration of epitaxial Gd(2)O(3) high-k gate dielectrics. *Solid-State Electronics, 50*(6), 979-985. doi:10.1016/j.sse.2006.04.018

Grave, D. A., Hughes, Z. R., Robinson, J. A., Medill, T. P., Hollander, M. J., Stump, A. L., Wolfe, D. E. (2012). Process-structure-property relations of micron thick Gd2O3 films deposited by reactive electron-beam physical vapor deposition (EB-PVD). *Surface & Coatings Technology, 206*(13), 3094-3103. doi:10.1016/j.surfcoat.2011.12.031

Grill, A., & Neumayer, D. A. (2003). Structure of low dielectric constant to extreme low dielectric constant SiCOH films: Fourier transform infrared spectroscopy characterization. *Journal of Applied Physics, 94*(10), 6697-6707. doi:10.1063/1.1618358

Guisbiers, G., Herth, E., Legrand, B., Rolland, N., Lasri, T., & Buchaillot, L. (2010). Materials selection procedure for RF-MEMS. *Microelectronic Engineering, 87*(9), 1792-1795. doi:10.1016/j.mee.2009.10.016

Guo, H., Yang, X. D., Xiao, T., Zhang, W. P., Lou, L. R., & Mugnier, J. (2004). Structure and optical properties of sol-gel derived Gd2O3 waveguide films. *Applied Surface Science, 230*(1-4), 215-221. doi:10.1016/j.apsusc.2004.02.032

Gupta, A., Toby, S., Gusev, E. P., Lu, H. C., Li, Y., Green, M. L., . . . Garfunkel, E. (1998). Nitrous oxide gas phase chemistry during silicon oxynitride film growth. *Progress in Surface Science, 59*(1-4), 103-115. doi:Doi 10.1016/S0079-6816(98)00039-2

Gusev, E. P., Cartier, E., Buchanan, D. A., Gribelyuk, M., Copel, M., Okorn-Schmidt, H., & D'Emic, C. (2001). Ultrathin high-K metal oxides on silicon: processing, characterization and integration issues. *Microelectronic Engineering, 59*(1-4), 341-349. doi:Doi 10.1016/S0167-9317(01)00667-0

Gusev, E. P., Lu, H. C., Garfunkel, E., Gustafsson, T., Green, M. L., Brasen, D., & Lennard, W. N. (1998). Nitrogen engineering of ultrathin oxynitrides by a thermal NO/O(2)/NO process. *Journal of Applied Physics, 84*(5), 2980-2982. doi:Doi 10.1063/1.368435

Gusev, E. P., Lu, H. C., Gustafsson, T., Garfunkel, E., Green, M. L., & Brasen, D. (1997). The composition of ultrathin silicon oxynitrides thermally grown in nitric oxide. *Journal of Applied Physics, 82*(2), 896-898. doi:Doi 10.1063/1.365858

Hardy, A., Adelmann, C., Van Elshocht, S., Van den Rul, H., Van Bael, M. K., De Gendt, S., Mullens, J. (2009). Study of interfacial reactions and phase stabilization of mixed Sc, Dy, Hf high-k oxides by attenuated total reflectance infrared spectroscopy. *Applied Surface Science, 255*(17), 7812-7817. doi:10.1016/j.apsusc.2009.04.184

He, G., Zhu, L. Q., Sun, Z. Q., Wan, Q., & Zhang, L. D. (2011). Integrations and challenges of novel high-k gate stacks in advanced CMOS technology. *Progress in Materials Science, 56*(5), 475-572.

Hegde, R. I., Maiti, B., & Tobin, P. J. (1997). Growth and film characteristics of N2O and NO oxynitride gate and tunnel dielectrics. *Journal of the Electrochemical Society, 144*(3), 1081-1086. doi:Doi 10.1149/1.1837535

Hegde, R. I., Tobin, P. J., Reid, K. G., Maiti, B., & Ajuria, S. A. (1995). Growth and Surface-Chemistry of Oxynitride Gate Dielectric Using Nitric-Oxide. *Applied Physics Letters, 66*(21), 2882-2884. doi:Doi 10.1063/1.113461

Heiba, Z. K., & Mohamed, B. M. (2015). Structural and magnetic properties of Mn doped Ho2O3 nanocrystalline. *Journal of Molecular Structure, 1102*, 135-140. doi:10.1016/j.molstruc.2015.08.048

Henkel, C., Abermann, S., Bethge, O., Pozzovivo, G., Klang, P., Stoger-Pollach, M., & Bertagnolli, E. (2011). Schottky barrier SOI-MOSFETs with high-k La2O3/ZrO2 gate dielectrics. *Microelectronic Engineering, 88*(3), 262-267.

Her, J. L., Pan, T. M., Liu, J. H., Wang, H. J., Chen, C. H., & Koyama, K. (2014). Electrical characteristics of GdTiO3 gate dielectric for amorphous InGaZnO thin-film transistors. *Thin Solid Films, 569*, 6-9. doi:10.1016/j.tsf.2014.08.021

Herrmann, M., Forter-Barth, U., Kempa, P. B., & Krober, H. (2009). Particle Characterization by X-ray Powder Diffraction. *Chemical Engineering & Technology, 32*(7), 1067-1072. doi:10.1002/ceat.200900069

Hirose, M., Mizubayashi, W., Khairurrijal, Ikeda, M., Murakami, H., Kohno, A., . . . Miyazaki, S. (2000). Ultrathin gate dielectrics for silicon nanodevices. *Superlattices and Microstructures, 27*(5-6), 383-393. doi:DOI 10.1006/spmi.2000.0861

Hoffmann, P., & Schmeisser, D. (2006). Improvement of nitrogen incorporation into oxynitrides on 4H-SiC(0001). *Nuclear Instruments & Methods in Physics Research Section B-Beam Interactions with Materials and Atoms, 246*(1), 85-89. doi:10.1016/j.nimb.2005.12.019

Hongo, T., Kondo, K. I., Nakamura, K. G., & Atou, T. (2007). High pressure Raman spectroscopic study of structural phase transition in samarium oxide. *Journal of Materials Science, 42*(8), 2582-2585. doi:10.1007/s10853-006-1417-5

Houng, M. P., Wang, Y. H., & Chang, W. J. (1999). Current transport mechanism in trapped oxides: A generalized trap-assisted tunneling model. *Journal of Applied Physics, 86*(3), 1488-1491. doi:Doi 10.1063/1.370918

Houssa, M., Pantisano, L., Ragnarsson, L. A., Degraeve, R., Schram, T., Pourtois, G., . . . Heyns, M. M. (2006). Electrical properties of high-kappa gate dielectrics: Challenges, current issues, and possible solutions. *Materials Science & Engineering R-Reports, 51*(4-6), 37-85. doi:10.1016/j.mser.2006.04.001

Houssa, M., Stesmans, A., & Heyns, M. M. (2001). Model for the trap-assisted tunnelling current through very thin SiO2/ZrO2 gate dielectric stacks. *Semiconductor Science and Technology, 16*(6), 427-432. doi:Doi 10.1088/0268-1242/16/6/302

Hsu, C. T., Su, Y. K., & Yokoyama, M. (1992). High Dielectric-Constant of Rf-Sputtered Hfo2 Thin-Films. *Japanese Journal of Applied Physics Part 1-Regular Papers Brief Communications & Review Papers, 31*(8), 2501-2504. doi:Doi 10.1143/Jjap.31.2501

Huang, D. G., Liao, S. J., Zhou, W. B., Quan, S. Q., Liu, L., He, Z. J., & Wan, J. B. (2009). Synthesis of samarium- and nitrogen-co-doped TiO2 by modified hydrothermal method and its photocatalytic performance for the degradation of 4-chlorophenol. *Journal of Physics and Chemistry of Solids, 70*(5), 853-859. doi:10.1016/j.jpcs.2009.04.005

Huang, S. Y., Chang, T. C., Chen, M. C., Chen, S. C., Lo, H. P., Huang, H. C., Tsai, M. J. (2011). Resistive switching characteristics of Sm2O3 thin films for nonvolatile memory applications. *Solid-State Electronics, 63*(1), 189-191. doi:DOI 10.1016/j.sse.2011.04.012

Huang, W., Min, Y. L., Ru, G. P., Jiang, Y. L., Qu, X. P., & Li, B. Z. (2008). Effect of erbium interlayer on nickel silicide formation on Si(100). *Applied Surface Science, 254*(7), 2120-2123. doi:10.1016/j.apsusc.2007.08.081

Hubbard, K. J., & Schlom, D. G. (1996). Thermodynamic stability of binary oxides in contact with silicon. *Journal of Materials Research, 11*(11), 2757-2776. doi:Doi 10.1557/Jmr.1996.0350

Hussein, G. A. M., Buttrey, D. J., DeSanto, P., Abd-Elgaber, A. A., Roshdy, H., & Myhoub, A. Y. Z. (2003). Formation and characterization of samarium oxide generated from different precursors. *Thermochimica Acta, 402*(1-2), 27-36.

Hwang, C. S., & Kim, H. J. (1993). Deposition and Characterization of Zro2 Thin-Films on Silicon Substrate by Mocvd. *Journal of Materials Research, 8*(6), 1361-1367. doi:Doi 10.1557/Jmr.1993.1361

Ioannou-Sougleridis, V., Constantoudis, V., Alexe, M., Scholz, R., Vellianitis, G., & Dimoulas, A. (2004). Effects on surface morphology of epitaxial Y2O3 layers on Si(001) after postgrowth annealing. *Thin Solid Films, 468*(1-2), 303-309. doi:10.1016/j.tsf.2004.05.076

Ismail, H. M. (1995). Assessment of Textural Consequences on Products of Thermal-Decomposition of Samarium Acetylacetonate. *Colloids and Surfaces a-Physicochemical and Engineering Aspects, 97*(3), 247-254. doi:Doi 10.1016/0927-7757(95)03083-P

Jeon, S., & Hwang, H. S. (2003). Effect of hygroscopic nature on the electrical characteristics of lanthanide oxides (Pr2O3, Sm2O3, Gd2O3, and Dy2O3). *Journal of Applied Physics, 93*(10), 6393-6395. doi:10.1063/1.1569028

Jeurgens, L. P. H., Sloof, W. G., Tichelaar, F. D., & Mittemeijer, E. J. (2002). Growth kinetics and mechanisms of aluminum-oxide films formed by thermal oxidation of aluminum. *Journal of Applied Physics, 92*(3), 1649-1656. doi:10.1063/1.1491591

Ji, T., Cui, J., Fang, Z. B., Nie, T. X., Fan, Y. L., Li, X. L., Jiang, Z. M. (2011). Single crystalline Tm2O3 films grown on Si (0 0 1) by atomic oxygen assisted molecular beam epitaxy. *Journal of Crystal Growth, 321*(1), 171-175. doi:10.1016/j.jcrysgro.2011.02.038

Jiang, N., Georgiev, D. G., Wen, T., & Jayatissa, A. H. (2012). Reactive radio frequency sputtering deposition and characterization of zinc nitride and oxynitride thin films. *Thin Solid Films, 520*(6), 1698-1704. doi:10.1016/j.tsf.2011.08.038

Jiang, S., Liu, J., Lin, C. L., Li, X. D., & Li, Y. C. (2013). High-pressure x-ray diffraction and Raman spectroscopy of phase transitions in Sm2O3. *Journal of Applied Physics, 113*(11). doi:Artn 11350210.1063/1.4795504

Jimenez-Molinos, F., Palma, A., Gamiz, F., Banqueri, J., & Lopez-Villanueva, J. A. (2001). Physical model for trap-assisted inelastic tunneling in metal-oxide-semiconductor structures. *Journal of Applied Physics, 90*(7), 3396-3404.

Jo, S. J., Ha, J. S., Park, N. K., Kang, D. K., & Kim, B. H. (2006). 5 nm thick lanthanum oxide thin films grown on Si(100) by atomic layer deposition: The effect of post-annealing on the electrical properties. *Thin Solid Films, 513*(1-2), 253-257. doi:10.1016/j.tsf.2006.01.008

Joshi, A. B., Ahn, J., & Kwong, D. L. (1993). Oxynitride Gate Dielectrics for P(+)-Polysilicon Gate Mos Devices. *Ieee Electron Device Letters, 14*(12), 560-562. doi:Doi 10.1109/55.260789

Kakushima, K., Tachi, K., Ahmet, P., Tsutsui, K., Sugii, N., Hattori, T., & Iwai, H. (2010). Advantage of further scaling in gate dielectrics below 0.5 nm of equivalent oxide thickness with La(2)O(3) gate dielectrics. *Microelectronics Reliability, 50*(6), 790-793.

Kalkur, T. S., & Lu, Y. C. (1992). Electrical Characteristics of Zro2-Based Metal-Insulator Semiconductor Structures on P-Si. *Thin Solid Films, 207*(1-2), 193-196. doi:Doi 10.1016/0040-6090(92)90122-R

Kao, C. H., Chan, T. C., Chen, K. S., Chung, Y. T., & Luo, W. S. (2010). Physical and electrical characteristics of the high-k Nd2O3 polyoxide deposited on polycrystalline silicon. *Microelectronics Reliability, 50*(5), 709-712. doi:10.1016/j.microrel.2010.02.005

Kao, C. H., Chen, C. C., & Lin, C. J. (2015). Comparison of gadolinium oxide trapping layers in flash memory applications. *Vacuum, 118*, 74-79. doi:10.1016/j.vacuum.2015.02.033

Kao, C. H., Chen, H., Chen, K. S., Huang, C. Y., Huang, C. H., Ou, J. C., Kuo, L. T. (2010). Study on polysilicon extended gate field effect transistor with samarium oxide sensing membrane *IEEE*.

Kao, C. H., Chen, H., Chen, S. Z., Hung, S. H., Chen, C. Y., He, Y. Y., . . . Lin, M. H. (2015). Effects of annealing on CeO2-based flash memories. *Vacuum, 118*, 69-73. doi:10.1016/j.vacuum.2015.01.024

Kao, C. H., Chen, H., & Huang, C. Y. (2013). Effects of Ti addition and annealing on high-k Gd2O3 sensing membranes on polycrystalline silicon for extended-gate field-effect transistor applications. *Applied Surface Science, 286*, 328-333. doi:10.1016/j.apsusc.2013.09.080

Kao, C. H., Chen, H., Liao, Y. C., Deng, J. Z., Chu, Y. C., Chen, Y. T., & Chang, H. (2014). Comparison of high-kappa Nd2O3 and NdTiO3 dielectrics deposited on polycrystalline silicon substrates. *Thin Solid Films, 570*, 412-416. doi:10.1016/j.tsf.2014.03.017

Kao, C. H., Chen, H., Liu, C. C., Chen, C. Y., Chen, Y. T., & Chu, Y. C. (2014). Electrical, material and multianalyte-sensitive characteristics of thermal CeO2/SiO2-stacked oxide capacitors. *Thin Solid Films, 570*, 552-557. doi:10.1016/j.tsf.2014.02.037

Kao, C. H., Chen, H., Pan, Y. T., Chiu, J. S., & Lu, T. C. (2012). The characteristics of the high-K Er2O3 (erbium oxide) dielectrics deposited on polycrystalline silicon. *Solid State Communications, 152*(6), 504-508. doi:10.1016/j.ssc.2011.12.042

Kao, C. H., Liu, K. C., Lee, M. H., Cheng, S. N., Huang, C. H., & Lin, W. K. (2012). High dielectric constant terbium oxide (Tb2O3) dielectric deposited on strained-Si:C. *Thin Solid Films, 520*(8), 3402-3405. doi:10.1016/j.tsf.2011.10.173

Karimi, H., Zhang, Y. T., Cui, S., Ma, R. H., Li, G., Wang, Q. N., . . . Fan, X. P. (2014). Spectroscopic properties of Eu-doped oxynitride glass-ceramics for white light LEDs. *Journal of Non-Crystalline Solids, 406*, 119-126. doi:10.1016/j.jnoncrysol.2014.10.003

Kato, K., Sakashita, M., Takeuchi, W., Taoka, N., Nakatsuka, O., & Zaima, S. (2014). Importance of control of oxidant partial pressure on structural and electrical properties of Pr-oxide films. *Thin Solid Films, 557*, 276-281. doi:10.1016/j.tsf.2013.10.088

Kato, K., Toyota, H., Jin, Y., & Ono, T. (2008). Characterization of tantalum oxy-nitrides deposited by ECR sputtering. *Vacuum, 83*(3), 592-595. doi:10.1016/j.vacuum.2008.04.045

Kawanago, T., Suzuki, T., Lee, Y., Kakushima, K., Ahmet, P., Tsutsui, K., . . . Iwai, H. (2012). Compensation of oxygen defects in La-silicate gate dielectrics for improving effective mobility in high-k/metal gate MOSFET using oxygen annealing process. *Solid-State Electronics, 68*, 68-72. doi:10.1016/j.sse.2011.10.006

Kaya, S., Yilmaz, E., Kahraman, A., & Karacali, H. (2015). Frequency dependent gamma-ray irradiation response of Sm2O3 MOS capacitors. *Nuclear Instruments & Methods in Physics Research Section B-Beam Interactions with Materials and Atoms, 358*, 188-193. doi:10.1016/j.nimb.2015.06.037

Kaya, S., Yilmaz, E., Karacali, H., Cetinkaya, A. O., & Aktag, A. (2015). Samarium oxide thin films deposited by reactive sputtering: Effects of sputtering power and substrate temperature on microstructure, morphology and electrical properties. *Materials Science in Semiconductor Processing, 33*, 42-48. doi:10.1016/j.mssp.2015.01.035

Kerr, L. L., Li, X. N., Canepa, M., & Sommer, A. J. (2007). Raman analysis of nitrogen doped ZnO. *Thin Solid Films, 515*(13), 5282-5286. doi:10.1016/j.tsf.2006.12.186

Kim, D. K., Lee, H., Kim, D., & Kim, Y. K. (2005). Electrical and mechanical properties of tantalum nitride thin films deposited by reactive sputtering. *Journal of Crystal Growth, 283*(3-4), 404-408. doi:10.1016/j.jcrysgro.2005.06.017

Kim, H., McIntyre, P. C., & Saraswat, K. C. (2003). Effects of crystallization on the electrical properties of ultrathin HfO2 dielectrics grown by atomic layer deposition. *Applied Physics Letters, 82*(1), 106-108. doi:10.1063/1.1533117

Kim, H. D., & Roh, Y. (2006). A study on interface layer with annealing conditions of ZrO2/ZrSixOy high-k gate oxide. *Journal of the Korean Physical Society, 49*, S755-S759.

Kim, H. T., Mun, T., Park, C., Jin, S. W., & Park, H. Y. (2013). Characteristics of lithium phosphorous oxynitride thin films deposited by metal-organic chemical vapor deposition technique. *Journal of Power Sources, 244*, 641-645. doi:10.1016/j.jpowsour.2012.12.109

Kim, J. B., Fuentes-Hernandez, C., Potscavage, W. J., Zhang, X. H., & Kippelen, B. (2009). Low-voltage InGaZnO thin-film transistors with Al2O3 gate insulator grown by atomic layer deposition. *Applied Physics Letters, 94*(14). doi:Artn 14210710.1063/1.3118575

Kim, K. S., Yoon, S. Y., Lee, W. J., & Kim, K. H. (2001). Surface morphologies and electrical properties of antimony-doped tin oxide films deposited by plasma-enhanced chemical vapor deposition. *Surface & Coatings Technology, 138*(2-3), 229-236. doi:Doi 10.1016/S0257-8972(00)01114-2

Kim, K. W., Jung, S. D., Kim, D. S., Im, K. S., Kang, H. S., Lee, J. H., . . . Cristoloveanu, S. (2011). Charge trapping and interface characteristics in normally-off Al2O3/GaN-MOSFETs. *Microelectronic Engineering, 88*(7), 1225-1227. doi:10.1016/j.mee.2011.03.116

Kim, W. H., Maeng, W. J., Moon, K. J., Myoung, J. M., & Kim, H. (2010). Growth characteristics and electrical properties of La2O3 gate oxides grown by thermal and plasma-enhanced atomic layer deposition. *Thin Solid Films, 519*(1), 362-366.

Kogler, R., Mucklich, A., Eichhorn, F., Schell, N., Skorupa, W., & Christensen, J. S. (2007). Praseodymium compound formation in silicon by ion beam synthesis. *Vacuum, 81*(10), 1318-1322. doi:10.1016/j.vacuum.2007.01.037

Kosola, A., Paivasaari, J., Putkonen, M., & Niinisto, L. (2005). Neodymium oxide and neodymium aluminate thin films by atomic layer deposition. *Thin Solid Films, 479*(1-2), 152-159. doi:10.1016/j.tsf.2004.10.004

Kuei, P. Y., & Hu, C. C. (2008). Gadolinium oxide high-k gate dielectrics prepared by anodic oxidation. *Applied Surface Science, 254*(17), 5487-5491. doi:10.1016/j.apsusc.2008.02.115

Kukli, K., Kemell, M., Dimri, M. C., Puukilainen, E., Tamm, A., Stern, R., . . . Leskela, M. (2014). Holmium titanium oxide thin films grown by atomic layer deposition. *Thin Solid Films, 565*, 261-266. doi:10.1016/j.tsf.2014.06.028

Kukli, K., Ritala, M., Leskela, M., Sundqvist, J., Oberbeck, L., Heitmann, J., . . . Aidla, A. (2007). Influence of TiO2 incorporation in HfO2 and Al2O3 based capacitor dielectrics. *Thin Solid Films, 515*(16), 6447-6451. doi:10.1016/j.tsf.2006.11.049

Kumar, N., Sundaresan, A., & Rao, C. N. R. (2011). Rare earth niobium oxynitrides, LnNbON(2-delta) (Ln = Y, La, Pr, Nd, Gd, Dy): Synthesis, structure and properties. *Materials Research Bulletin, 46*(11), 2021-2024. doi:10.1016/j.materresbull.2011.07.009

Kuo, C. T., Kwor, R., & Jones, K. M. (1992). Study of Sputtered Hfo2 Thin-Films on Silicon. *Thin Solid Films, 213*(2), 257-264. doi:Doi 10.1016/0040-6090(92)90291-I

Kurniawan, T., Cheong, K. Y., Razak, K. A., Lockman, Z., & Ahmad, N. (2011). Oxidation of sputtered Zr thin film on Si substrate. *Journal of Materials Science-Materials in Electronics, 22*(2), 143-150. doi:10.1007/s10854-010-0103-1

Kurniawan, T., Wong, Y. H., Cheong, K. Y., Moon, J. H., Bahng, W., Razak, K. A., Kim, N. K. (2011). Effects of post-oxidation annealing temperature on ZrO2 thin film deposited on 4H-SiC substrate. *Materials Science in Semiconductor Processing, 14*(1), 13-17. doi:10.1016/j.mssp.2010.12.011

Kusrini, E., Arbianti, R., Sofyan, N., Abdullah, M. A. A., & Andriani, F. (2014). Modification of chitosan by using samarium for potential use in drug delivery system. *Spectrochimica Acta Part a-Molecular and Biomolecular Spectroscopy, 120*, 77-83. doi:10.1016/j.saa.2013.09.132

Kwo, J., Hong, M., Kortan, A. R., Queeney, K. L., Chabal, Y. J., Opila, R. L., . . . Rosamilia, J. M. (2001). Properties of high kappa gate dielectrics Gd2O3 and Y2O3 for Si. *Journal of Applied Physics, 89*(7), 3920-3927. doi:Doi 10.1063/1.1352688

Kwon, K. H., Lee, C. K., Yang, J. K., Choi, S. G., Chang, H. J., Jeon, H., & Park, H. H. (2008). Effective formation of interface controlled Y2O3 thin film on Si(100) in a metal-(ferroelectric)-insulator-semiconductor structure. *Microelectronic Engineering, 85*(8), 1781-1785. doi:10.1016/j.mee.2008.05.004

Lawniczak-Jablonska, K., Babushkina, N. V., Dynowska, E., Malyshev, S. A., Romanova, L. I., Zhygulin, D. V., & Laiho, T. (2006). Surface morphology of DyxOy films grown on Si. *Applied Surface Science, 253*(2), 639-645. doi:10.1016/j.apsusc.2005.12.150

Lee, J. S., Kim, W. H., Oh, I. K., Kim, M. K., Lee, G., Lee, C. W., . . . Kim, H. (2014). Atomic layer deposition of Y2O3 and yttrium-doped HfO2 using a newly synthesized Y(iPrCp)(2)(N-iPr-amd) precursor for a high permittivity gate dielectric. *Applied Surface Science, 297*, 16-21. doi:10.1016/j.apsusc.2014.01.032

Lee, T., Choi, K., Ando, T., Park, D. G., Gribelyuk, M. A., Kwon, U., & Banerjee, S. K. (2011). Mechanism of V-FB/V-TH shift in Dysprosium incorporated HfO2 gate dielectric n-Type Metal-Oxide-Semiconductor devices. *Journal of Vacuum Science & Technology B, 29*(2). doi:Artn 02120910.1116/1.3562974

Lee, W. J., Cho, M. H., Kim, Y. K., Baeck, J. H., Jeong, I. S., Jeong, K., . . . Ko, D. H. (2010). Changes in Gd2O3 films grown on Si(100) as a function of nitridation temperature and Zr incorporation. *Thin Solid Films, 518*(6), 1682-1688. doi:10.1016/j.tsf.2009.11.071

Leong, M., Doris, B., Kedzierski, J., Rim, K., & Yang, M. (2004). Siticon device scaling to the sub-10-nm regime. *Science, 306*(5704), 2057-2060. doi:10.1126/science.1100731

Leskela, M., Kukli, K., & Ritala, M. (2006). Rare-earth oxide thin films for gate dielectrics in microelectronics. *Journal of Alloys and Compounds, 418*(1-2), 27-34.

Leskela, M., & Ritala, M. (2003). Rare-earth oxide thin films as gate oxides in MOSFET transistors. *Journal of Solid State Chemistry, 171*(1-2), 170-174. doi:10.1016/S0022-4596(02)00204-9

Lespade, P., Marchand, A., Couzi, M., & Cruege, F. (1984). Characterization of Carbon Materials with Raman Microspectrometry. *Carbon, 22*(4-5), 375-385. doi:Doi 10.1016/0008-6223(84)90009-5

Levasseur, A., Vinatier, P., & Gonbeau, D. (1999). X-ray photoelectron spectroscopy: A powerful tool for a better characterization of thin film materials. *Bulletin of Materials Science, 22*(3), 607-614. doi:Doi 10.1007/Bf02749975

Lim, W. F., Cheong, K. Y., & Lockman, Z. (2011). Effects of post-deposition annealing temperature and time on physical properties of metal-organic decomposed lanthanum cerium oxide thin film. *Thin Solid Films, 519*(15), 5139-5145. doi:10.1016/j.tsf.2011.01.072

Lin, C. C., Wu, Y. H., Wu, C. Y., & Lee, C. W. (2014). Formation of amorphous Yb2O3/crystalline ZrTiO4 gate stack and its application in n-MOSFET with sub-nm EOT. *Applied Surface Science, 299*, 47-51. doi:10.1016/j.apsusc.2014.01.182

Lin, C. H., Kang, J. F., Han, D. D., Tian, D. Y., Wang, W., Zhang, J. H., . . . Han, R. Q. (2003). Electrical properties of Al2O3 gate dielectrics. *Microelectronic Engineering, 66*(1-4), 830-834.

Lin, K. C., Juan, P. C., Liu, C. H., Wang, M. C., & Chou, C. H. (2015). Leakage current mechanism and effect of Y2O3 doped with Zr high-K gate dielectrics. *Microelectronics Reliability, 55*(11), 2198-2202. doi:10.1016/j.microrel.2015.07.045

Lippitz, A., & Hubert, T. (2005). XPS investigations of chromium nitride thin films. *Surface & Coatings Technology, 200*(1-4), 250-253. doi:10.1016/j.surfcoat.2005.02.091

Litta, E. D., Hellstrom, P. E., Henkel, C., & Ostling, M. (2014). Electrical characterization of thulium silicate interfacial layers for integration in high-k/metal gate CMOS technology. *Solid-State Electronics, 98*, 20-25. doi:10.1016/j.sse.2014.04.004

Litta, E. D., Hellstrom, P. E., & Ostling, M. (2015). Threshold voltage control in TmSiO/HfO2 high-k/metal gate MOSFETs. *Solid-State Electronics, 108*, 24-29. doi:10.1016/j.sse.2014.12.008

Lo Nigro, R., Toro, R. G., Malandrino, G., Fiorenza, P., Raineri, V., & Fragala, I. L. (2005). Effects of deposition temperature on the microstructural and electrical properties of praseodymium oxide-based films. *Materials Science and Engineering B-Solid State Materials for Advanced Technology, 118*(1-3), 117-121. doi:10.1016/j.mseb.2004.12.022

Lo Nigro, R., Toro, R. G., Malandrino, G., Fragala, I. L., Raineri, V., & Fiorenza, P. (2006). Praseodymium based high-k dielectrics grown on Si and SiC substrates. *Materials Science in Semiconductor Processing, 9*(6), 1073-1078. doi:10.1016/j.mssp.2006.10.026

Lo Nigro, R., Toro, R. G., Malandrino, G., Raineri, V., & Fragala, I. L. (2005). Effects of the thermal annealing processes on praseodymium oxide based films grown on silicon substrates. *Materials Science and Engineering B-Solid State Materials for Advanced Technology, 118*(1-3), 192-196. doi:10.1016/j.mseb.2004.12.027

Lo, S. H., Buchanan, D. A., & Taur, Y. (1999). Modeling and characterization of quantization, polysilicon depletion, and direct tunneling effects in MOSFETs with ultrathin oxides. *Ibm Journal of Research and Development, 43*(3), 327-337.

Lo, S. H., Buchanan, D. A., Taur, Y., & Wang, W. (1997). Quantum-mechanical modeling of electron tunneling current from the inversion layer of ultra-thin-oxide nMOSFET's. *Ieee Electron Device Letters, 18*(5), 209-211. doi:Doi 10.1109/55.568766

Lofaj, F., Satet, R., Hoffmann, M. J., & de Arellano Lopez, A. R. (2004). Thermal expansion and glass transition temperature of the rare-earth doped oxynitride glasses. *Journal of the European Ceramic Society, 24*(12), 3377-3385. doi:10.1016/j.jeurceramsoc.2003.10.012

Logothetidis, S., Patsalas, P., Evangelou, E. K., Konofaos, N., Tsiaoussis, I., & Frangis, N. (2004). Dielectric properties and electronic transitions of porous and nanostructured cerium oxide films. *Materials Science and Engineering B-Solid State Materials for Advanced Technology, 109*(1-3), 69-73. doi:10.1016/j.mseb.2003.10.048

Lu, H. C., Gusev, E. P., Gustafsson, T., Brasen, D., Green, M. L., & Garfunkel, E. (1997). Compositional and mechanistic aspects of ultrathin oxynitride film growth on Si(100). *Microelectronic Engineering, 36*(1-4), 29-32. doi:Doi 10.1016/S0167-9317(97)00010-5

Lu, H. C., Gusev, E. P., Gustafsson, T., & Garfunkel, E. (1997). Effect of near-interfacial nitrogen on the oxidation behavior of ultrathin silicon oxynitrides. *Journal of Applied Physics, 81*(10), 6992-6995. doi:Doi 10.1063/1.365264

Lu, Z. H., Hussey, R. J., Graham, M. J., Cao, R., & Tay, S. P. (1996). Rapid thermal N2O oxynitride an Si(100). *Journal of Vacuum Science & Technology B, 14*(4), 2882-2887. doi:Doi 10.1116/1.588929

Lu, Z. H., Tay, S. P., Cao, R., & Pianetta, P. (1995). The Effect of Rapid Thermal N2o Nitridation on the Oxide/Si(100) Interface Structure. *Applied Physics Letters, 67*(19), 2836-2838. doi:Doi 10.1063/1.114801

Lucovsky, G., Niimi, H., Koh, K., & Green, M. L. (1998). Monolayer nitrogen atom incorporation at buried Si-SiO2 interfaces: Preparation by remote plasma oxidation/nitridation and characterization by on-line auger electron spectroscopy. *Surface Review and Letters, 5*(1), 167-173. doi:Doi 10.1142/S0218625x98000323

Lucovsky, G., Niimi, H., Wu, Y., Parker, C. R., & Hauser, J. R. (1998). Optimization of nitrided gate dielectrics by plasma-assisted and rapid thermal processing. *Journal of Vacuum Science & Technology A, 16*(3), 1721-1729. doi:Doi 10.1116/1.581291

Luptak, R., Frohlich, K., Rosova, A., Husekova, K., Tapajna, M., Machajdik, D., . . . Mansilla, C. (2005). Growth of gadolinium oxide films for advanced MOS structure. *Microelectronic Engineering, 80*, 154-157. doi:10.1016/j.mee.2005.04.059

Ma, Z. J., Chen, J. C., Liu, Z. H., Krick, J. T., Cheng, Y. C., Hu, C., & Ko, P. K. (1994). Suppression of Boron Penetration in P+ Polysilicon Gate P-Mosfets Using Low-Temperature Gate-Oxide N2o Anneal. *Ieee Electron Device Letters, 15*(3), 109-111. doi:Doi 10.1109/55.285386

Maleto, M. I., Solovjeva, L. I., Turevskaya, E. P., Vorotilov, K. A., & Yanovskaya, M. I. (1994). Alkoxy-Derived Y2o3-Stabilized Zro2 Thin-Films. *Thin Solid Films, 249*(1), 1-5. doi:Doi 10.1016/0040-6090(94)90076-0

Mamatrishat, M., Kouda, M., Kakushima, K., Nohira, H., Ahmet, P., Kataoka, Y., . . . Iwai, H. (2012). Valence number transition and silicate formation of cerium oxide films on Si(100). *Vacuum, 86*(10), 1513-1516. doi:10.1016/j.vacuum.2012.02.050

Mandal, J., Sarkar, B. J., Deb, A. K., & Chakrabarti, P. K. (2014). Magnetic phase transition of nanocrystalline Fe-doped samarium oxide (Sm1.90Fe0.10O3). *Journal of Magnetism and Magnetic Materials, 371*, 35-42. doi:10.1016/j.jmmm.2014.06.068

Mane, A. U., Wenger, C., Lupina, G., Schroeder, T., Lippert, G., Sorge, R., . . . Mussig, H. J. (2005). Process integration of Pr-based high-k gate dielectrics. *Microelectronic Engineering, 82*(2), 148-153. doi:10.1016/j.mee.2005.07.004

Massoud, H. Z., Plummer, J. D., & Irene, E. A. (1985). Thermal-Oxidation of Silicon in Dry Oxygen - Growth-Rate Enhancement in the Thin Regime .2. Physical-Mechanisms. *Journal of the Electrochemical Society, 132*(11), 2693-2700. doi:Doi 10.1149/1.2113649

Masubuchi, Y., Kawamura, F., Taniguchi, T., & Kikkawa, S. (2015). High pressure densification and dielectric properties of perovskite-type oxynitride SrTaO2N. *Journal of the European Ceramic Society, 35*(4), 1191-1197. doi:10.1016/j.jeurceramsoc.2014.10.028

Meuris, M., Verhaverbeke, S., Mertens, P. W., Heyns, M. M., Hellemans, L., Bruynseraede, Y., & Philipossian, A. (1992). The Relationship of the Silicon Surface-Roughness and Gate Oxide Integrity in Nh4oh/H2o2 Mixtures. *Japanese Journal of Applied Physics Part 2-Letters, 31*(11a), L1514-L1517.

Mian, C. S., & Flora, I. S. Y. (1999). Nitrogen in ultra-thin gate oxides: its profile and functions. *Solid-State Electronics, 43*(11), 1997-2003.

Mishra, M., Kuppusami, P., Ramya, S., Ganesan, V., Singh, A., Thirumurugesan, R., & Mohandas, E. (2015). Microstructure and optical properties of Gd2O3 thin films prepared by pulsed laser deposition. *Surface & Coatings Technology, 262*, 56-63. doi:10.1016/j.surfcoat.2014.12.012

Mittemeijer, E. J., & Welzel, U. (2008). The "state of the art" of the diffraction analysis of crystallite size and lattice strain. *Zeitschrift Fur Kristallographie, 223*(9), 552-560. doi:10.1524/zkri.2008.1213

Miyazaki, S. (2002). Characterization of high-k gate dielectric/silicon interfaces. *Applied Surface Science, 190*(1-4), 66-74.

Momose, H. S., Morimoto, T., Ozawa, Y., Yamabe, K., & Iwai, H. (1994). Electrical Characteristics of Rapid Thermal Nitrided-Oxide Gate N-Mosfets and P-Mosfets with Less-Than 1 Atom-Percent Nitrogen Concentration. *Ieee Transactions on Electron Devices, 41*(4), 546-552. doi:Doi 10.1109/16.278508

Mote, V. D., Purushotham, Y., & Dole, B. N. (2011). Structural and morphological studies on Mn substituted ZnO nanometer-sized crystals. *Crystal Research and Technology, 46*(7), 705-710. doi:10.1002/crat.201100107

Muller, D. A., Sorsch, T., Moccio, S., Baumann, F. H., Evans-Lutterodt, K., & Timp, G. (1999). The electronic structure at the atomic scale of ultrathin gate oxides. *Nature, 399*(6738), 758-761. doi:Doi 10.1038/21602

Mussig, H. J., Dabrowski, J., Ignatovich, K., Liu, J. P., Zavodinsky, V., & Osten, H. J. (2002). Initial stages of praseodymium oxide film formation on Si(001). *Surface Science, 504*(1-3), 159-166. doi:Pii S0039-6028(01)01961-6

Neumayer, D. A., & Cartier, E. (2001). Materials characterization of ZrO2-SiO2 and HfO2-SiO2 binary oxides deposited by chemical solution deposition. *Journal of Applied Physics, 90*(4), 1801-1808. doi:Doi 10.1063/1.1382851

Ng, J. A., Kuroki, Y., Sugii, N., Kakushima, K., Ohmi, S. I., Tsutsui, K., . . . Wong, H. (2005). Effects of low temperature annealing on the ultrathin La2O3 gate dielectric; comparison of post deposition annealing and post metallization annealing. *Microelectronic Engineering, 80*, 206-209.

Nunez, O. R., Tarango, A. J. M., Murphy, N. R., Phinney, L. C., Hossain, K., & Ramana, C. V. (2015). Physical characterization of sputter-deposited amorphous tungsten oxynitride thin films. *Thin Solid Films, 596*, 160-166. doi:10.1016/j.tsf.2015.08.066

Ohmi, S. I., Kobayashi, C., Aizawa, K., Yamamoto, S. I., Tokumitsu, E., Ishiwara, H., & Iwai, H. (2000). High quality ultrathin La2O3 Films for high-k gate insulator.

Onisawa, K., Fuyama, M., Tamura, K., Taguchi, K., Nakayama, T., & Ono, Y. A. (1990). Dielectric-Properties of Rf-Sputtered Y2o3 Thin-Films. *Journal of Applied Physics, 68*(2), 719-723. doi:Doi 10.1063/1.346804

Opila, R. L., Chang, J. P., Du, M., Bevk, J., Ma, Y., Weldon, M., Gurevich, A. (1999). X-ray photoelectron study of gate oxides and nitrides. *Solid State Phenomena, 65-6*, 257-260.

Osten, H. J., Bugiel, E., & Fissel, A. (2003). Epitaxial praseodymium oxide: a new high-K dielectric. *Solid-State Electronics, 47*(12), 2161-2165. doi:10.1016/S0038-1101(03)00190-4

Osten, H. J., Liu, J. P., Bugiel, E., Mussig, H. J., & Zaumseil, P. (2001). Epitaxial growth of praseodymium oxide on silicon. *Materials Science and Engineering B-Solid State Materials for Advanced Technology, 87*(3), 297-302. doi:Doi 10.1016/S0921-5107(01)00728-0

Osten, H. J., Liu, J. P., Bugiel, E., Mussig, H. J., & Zaumseil, P. (2002). Growth of crystalline praseodymium oxide on silicon. *Journal of Crystal Growth, 235*(1-4), 229-234. doi:Doi 10.1016/S0022-0248(01)01777-8

Osten, H. J., Liu, J. P., Mussig, H. J., & Zaumseil, P. (2001). Epitaxial, high-K dielectrics on silicon: the example of praseodymium oxide. *Microelectronics Reliability, 41*(7), 991-994. doi:Doi 10.1016/S0026-2714(01)00054-3

Pagliuca, F., Luches, P., & Valeri, S. (2013). Interfacial interaction between cerium oxide and silicon surfaces. *Surface Science, 607*, 164-169. doi:10.1016/j.susc.2012.09.002

Paivasaari, J., Putkonen, M., & Niinisto, L. (2005). A comparative study on lanthanide oxide thin films grown by atomic layer deposition. *Thin Solid Films, 472*(1-2), 275-281. doi:10.1016/j.tsf.2004.06.160

Paivasaari, J., Putkonen, M., Sajavaara, T., & Niinisto, L. (2004). Atomic layer deposition of rare earth oxides: erbium oxide thin films from beta-diketonate and ozone precursors. *Journal of Alloys and Compounds, 374*(1-2), 124-128. doi:10.1016/j.jallcom.2003.11.149

Pampillon, M. A., Feijoo, P. C., Andres, E. S., Lucia, M. L., del Prado, A., & Toledano-Luque, M. (2011). Anomalous thermal oxidation of gadolinium thin films deposited on silicon by high pressure sputtering. *Microelectronic Engineering, 88*(9), 2991-2996. doi:10.1016/j.mee.2011.04.058

Pampillon, M. A., Feijoo, P. C., & San Andres, E. (2013). Electrical characterization of gadolinium oxide deposited by high pressure sputtering with in situ plasma oxidation. *Microelectronic Engineering, 109*, 236-239. doi:10.1016/j.mee.2013.03.094

Pan, T. M., Chang, W. T., & Chiu, F. C. (2010). Structural and electrical properties of thin Ho2O3 gate dielectrics. *Thin Solid Films, 519*(2), 923-927. doi:10.1016/j.tsf.2010.09.002

Pan, T. M., Chang, W. T., & Chiu, F. C. (2011). Structural properties and electrical characteristics of high-k Dy2O3 gate dielectrics. *Applied Surface Science, 257*(9), 3964-3968. doi:10.1016/j.apsusc.2010.11.144

Pan, T. M., Chen, F. H., & Jung, J. S. (2012). Structural and electrical characteristics of a high-k Lu2O3 charge trapping layer for nonvolatile memory application. *Materials Chemistry and Physics, 133*(2-3), 1066-1070. doi:10.1016/j.matchemphys.2012.02.017

Pan, T. M., & Huang, C. C. (2010). Effects of oxygen content and postdeposition annealing on the physical and electrical properties of thin Sm2O3 gate dielectrics. *Applied Surface Science, 256*(23), 7186-7193.

Pan, T. M., Huang, C. C., You, S. X., & Yeh, C. C. (2008). Effect of Annealing on the Structural and Electrical Properties of High-k Sm(2)O(3) Dielectrics. *Electrochemical and Solid State Letters, 11*(12), G62-G65.

Pan, T. M., & Huang, M. D. (2011). Structural properties and sensing characteristics of high-k Ho2O3 sensing film-based electrolyte-insulator-semiconductor. *Materials Chemistry and Physics, 129*(3), 919-924. doi:10.1016/j.matchemphys.2011.05.032

Pan, T. M., & Huang, W. S. (2009). Physical and electrical characteristics of a high-k Yb2O3 gate dielectric. *Applied Surface Science, 255*(9), 4979-4982. doi:10.1016/j.apsusc.2008.12.048

Pan, T. M., Jung, J. S., & Chen, F. H. (2010). Metal-oxide-high-k-oxide-silicon memory structure incorporating a Tb2O3 charge trapping layer. *Applied Physics Letters, 97*(1). doi:Artn 01290610.1063/1.3462321

Pan, T. M., & Lee, J. D. (2007). Physical and electrical properties of yttrium oxide gate dielectrics on si substrate with NH3 plasma treatment. *Journal of the Electrochemical Society, 154*(8), H698-H703. doi:10.1149/1.2742808

Pan, T. M., & Li, Z. H. (2010). High-performance CF4 plasma treated polycrystalline silicon thin-film transistors using a high-k Tb2O3 gate dielectric. *Applied Physics Letters, 96*(11). doi:Artn 11350410.1063/1.3357428

Pan, T. M., Li, Z. H., & Deng, C. K. (2010). Effects of CF4 Plasma Treatment on the Electrical Characteristics of Poly-Silicon TFTs Using a Tb2O3 Gate Dielectric. *Ieee Transactions on Electron Devices, 57*(7), 1519-1526. doi:10.1109/Ted.2010.2047904

Pan, T. M., Lin, J. C., Wu, M. H., & Lai, C. S. (2009). Study of high-k Er(2)O(3) thin layers as ISFET sensitive insulator surface for pH detection. *Sensors and Actuators B-Chemical, 138*(2), 619-624. doi:10.1016/j.snb.2009.01.051

Pan, T. M., & Lu, C. H. (2011). Effect of postdeposition annealing on the structural and electrical properties of thin Dy2TiO5 dielectrics. *Thin Solid Films, 519*(22), 8149-8153. doi:10.1016/j.tsf.2011.06.039

Pan, T. M., & Yen, L. C. (2010a). Influence of postdeposition annealing on structural properties and electrical characteristics of thin Tm2O3 and Tm2Ti2O7 dielectrics. *Applied Surface Science, 256*(9), 2786-2791. doi:10.1016/j.apsusc.2009.11.029

Pan, T. M., & Yen, L. C. (2010b). Structural properties and electrical characteristics of high-k Tm2Ti2O7 gate dielectrics. *Applied Surface Science, 256*(6), 1845-1848. doi:10.1016/j.apsusc.2009.10.017

Parate, O., & Gupta, N. (2011). Material selection for electrostatic microactuators using Ashby approach. *Materials & Design, 32*(3), 1577-1581. doi:10.1016/j.matdes.2010.09.012

Park, S. I., Ok, I., Kim, H. S., Zhu, F., Zhang, M. H., Yum, J. H., . . . Lee, J. C. (2007). Optimization of electrical characteristics of TiO2-incorporated HfO2 n-type doped gallium arsenide metal oxide semiconductor capacitor with silicon interface passivation layer. *Applied Physics Letters, 91*(8). doi:Artn 08290810.1063/1.2775048

Paumier, F., Gaboriaud, R. J., & Kaul, A. R. (2002). Yttrium oxide thin films: chemistry-stoichiometry- strain and microstructure. *Crystal Engineering, 5*(3-4), 169-175. doi:10.1016/S1463-0184(02)00026-6

Perera, R., Ikeda, A., Hattori, R., & Kuroki, Y. (2003). Trap assisted leakage current conduction in thin silicon oxynitride films grown by rapid thermal oxidation combined microwave excited plasma nitridation. *Microelectronic Engineering, 65*(4), 357-370. doi:10.1016/S0167-9317(02)01025-0

Pfiester, J. R., Baker, F. K., Mele, T. C., Tseng, H. H., Tobin, P. J., Hayden, J. D., . . . Parrillo, L. C. (1990). The Effects of Boron Penetration on P+ Polysilicon Gated Pmos Devices. *Ieee Transactions on Electron Devices, 37*(8), 1842-1851. doi:Doi 10.1109/16.57135

Pisecny, P., Husekova, K., Frohlich, K., Harmatha, L., Soltys, J., Machajdik, D., . . . Jakabovic, J. (2004). Growth of lanthanum oxide films for application as a gate dielectric in CMOS technology. *Materials Science in Semiconductor Processing, 7*(4-6), 231-236. doi:10.1016/j.mssp.2004.09.020

Plummer, J. D., & Griffin, P. B. (2001). Material and process limits in silicon VLSI technology. *Proceedings of the Ieee, 89*(3), 240-258. doi:Doi 10.1109/5.915373

Pratap, R., & Arunkumar, A. (2007). Material selection for MEMS devices. *Indian Journal of Pure & Applied Physics, 45*(4), 358-367.

Quah, H. J., & Cheong, K. Y. (2011). Deposition and post-deposition annealing of thin Y2O3 film on n-type Si in argon ambient. *Materials Chemistry and Physics, 130*(3), 1007-1015. doi:10.1016/j.matchemphys.2011.08.024

Quah, H. J., & Cheong, K. Y. (2014). Characterization of ultrathin Al2O3 gate oxide deposited by RF-magnetron sputtering on gallium nitride epilayer on sapphire substrate. *Materials Chemistry and Physics, 148*(3), 592-604. doi:10.1016/j.matchemphys.2014.08.022

Queralt, X., Ferrater, C., Sanchez, F., Aguiar, R., Palau, J., & Varela, M. (1995). Erbium Oxide Thin-Films on Si(100) Obtained by Laser-Ablation and Electron-Beam Evaporation. *Applied Surface Science, 86*(1-4), 95-98. doi:Doi 10.1016/0169-4332(94)00383-1

Quinn, D. J., Spearing, S. M., Ashby, M. F., & Fleck, N. A. (2006). A systematic approach to process selection in MEMS. *Journal of Microelectromechanical Systems, 15*(5), 1039-1050. doi:10.1109/Jmems.2006.880292

Ramesh, K., Chandorkar, A. N., & Vasi, J. (1989). Electron Trapping and Detrapping in Thermally Nitrided Silicon Dioxide. *Journal of Applied Physics, 65*(10), 3958-3962. doi:Doi 10.1063/1.343362

Ranuarez, J. C., Deen, M. J., & Chen, C. H. (2006). A review of gate tunneling current in MOS devices. *Microelectronics Reliability, 46*(12), 1939-1956. doi:10.1016/j.microrel.2005.12.006

Rao, R. V. (2006). A material selection model using graph theory and matrix approach. *Materials Science and Engineering a-Structural Materials Properties Microstructure and Processing, 431*(1-2), 248-255. doi:10.1016/j.msea.2006.06.006

Rao, R. V. (2008a). A decision making methodology for material selection using an improved compromise ranking method. *Materials & Design, 29*(10), 1949-1954. doi:10.1016/j.matdes.2008.04.019

Rao, R. V. (2008b). Evaluation of environmentally conscious manufacturing programs using multiple attribute decision-making methods. *Proceedings of the Institution of Mechanical Engineers Part B-Journal of Engineering Manufacture, 222*(3), 441-451. doi:10.1243/09544054jem981

Rao, R. V., & Patel, B. K. (2010a). Decision making in the manufacturing environment using an improved PROMETHEE method. *International Journal of Production Research, 48*(16), 4665-4682. doi:Pii 91323915210.1080/00207540903049415

Rao, R. V., & Patel, B. K. (2010b). A subjective and objective integrated multiple attribute decision making method for material selection. *Materials & Design, 31*(10), 4738-4747. doi:10.1016/j.matdes.2010.05.014

Reddy, G. P., & Gupta, N. (2010). Material selection for microelectronic heat sinks: An application of the Ashby approach. *Materials & Design, 31*(1), 113-117. doi:10.1016/j.matdes.2009.07.013

Robertson, J. (2000). Band offsets of wide-band-gap oxides and implications for future electronic devices. *Journal of Vacuum Science & Technology B, 18*(3), 1785-1791. doi:Doi 10.1116/1.591472

Robertson, J. (2004). High dielectric constant oxides. *European Physical Journal-Applied Physics, 28*(3), 265-291.

Robertson, J., & Wallace, R. M. (2015). High-K materials and metal gates for CMOS applications. *Materials Science & Engineering R-Reports, 88*, 1-41. doi:10.1016/j.mser.2014.11.001

Rochet, F., Agius, B., & Rigo, S. (1984). An O-18 Study of the Oxidation Mechanism of Silicon in Dry Oxygen. *Journal of the Electrochemical Society, 131*(4), 914-923. doi:Doi 10.1149/1.2115727

Roeckerath, M., Heeg, T., Lopes, J. M. J., Schubert, J., Mantl, S., Besmehn, A., . . . Niinisto, L. (2008). Characterization of lanthanum lutetium oxide thin films grown by atomic layer deposition as an alternative gate dielectric. *Thin Solid Films, 517*(1), 201-203. doi:10.1016/j.tsf.2008.08.064

Rozhkov, V. A., Goncharov, V. P., & Trusova, A. Y. (1995). Electrical and photoelectrical properties of MIS structures with rare earthoxide fllms as insulator *Conduction and Breakdown in Solid Dielectrics*.

Rozhkov, V. A., Trusova, A. Y., & Berezhnoy, I. G. (1998). Silicon MIS structures using samarium oxide films. *Thin Solid Films, 325*(1-2), 151-155.

Rugar, D., & Hansma, P. (1990). Atomic Force Microscopy. *Physics Today, 43*(10), 23-30. doi:Doi 10.1063/1.881238

Ruiz-Gomez, M. A., Gomez-Solis, C., Zarazua-Morin, M. E., Tones-Martinez, L. M., Juarez-Ramirez, I., Sanchez-Martinez, D., & Figueroa-Torres, M. Z. (2014). Innovative solvo-combustion route for the rapid synthesis of MoO3 and Sm2O3 materials. *Ceramics International, 40*(1), 1893-1899. doi:10.1016/j.ceramint.2013.07.095

Santra, K., Chatterjee, P., & Sen Gupta, S. P. (2002). Voigt modelling of size-strain analysis: Application to alpha-Al2O3 prepared by combustion technique. *Bulletin of Materials Science, 25*(3), 251-257. doi:Doi 10.1007/Bf02711163

Sato, S., Tachi, K., Kakushima, K., Ahmet, P., Tsutsui, K., Sugii, N., . . . Iwai, H. (2007). Thermal-stability improvement of LaON thin film formed using nitrogen radicals. *Microelectronic Engineering, 84*(9-10), 1894-1897. doi:10.1016/j.mee.2007.04.088

Schamm, S., Scarel, G., & Fanciulli, M. (2007). Local structure, composition and electronic properties of rare earth oxide thin films studied using advanced transmission electron microscopy techniques (TEM-EELS). *Rare Earth Oxide Thin Films: Growth , Characterization , and Applications, 106*, 153-177.

Schmitt, J., & Flemming, H. C. (1998). FTIR-spectroscopy in microbial and material analysis. *International Biodeterioration & Biodegradation, 41*(1), 1-11. doi:Doi 10.1016/S0964-8305(98)80002-4

Sen, B., Wong, H., Molina, J., Iwai, H., Ng, J. A., Kakushima, K., & Sarkar, C. K. (2007). Trapping characteristics of lanthanum oxide gate dielectric film explored from temperature dependent current-voltage and capacitance-voltage measurements. *Solid-State Electronics, 51*(3), 475-480. doi:10.1016/j.sse.2007.01.032

Shalini, K., & Shivashankar, S. A. (2005). Oriented growth of thin films of samarium oxide by MOCVD. *Bulletin of Materials Science, 28*(1), 49-54.

Shallenberger, J. R., Cole, D. A., & Novak, S. W. (1999). Characterization of silicon oxynitride thin films by x-ray photoelectron spectroscopy. *Journal of Vacuum Science & Technology a-Vacuum Surfaces and Films, 17*(4), 1086-1090. doi:Doi 10.1116/1.582038

Shao, Q. Y., Li, A. D., Ling, H. Q., Wu, D., Wang, Y., Feng, Y., . . . Ming, N. B. (2003). Growth and characterization of Al2O3 gate dielectric films by low-pressure metalorganic chemical vapor deposition. *Microelectronic Engineering, 66*(1-4), 842-848. doi:10.1016/S0167-9317(02)01009-2

Sharma, A., Tripathi, S., & Shripathi, T. (2009). X-ray photoelectron study of annealed Co thin film on Si surface. *Applied Surface Science, 256*(2), 530-535. doi:10.1016/j.apsusc.2009.08.007

Shi, L., Yuan, Y., Liang, X. F., Xia, Y. D., Yin, J., & Liu, Z. G. (2007). Microstructure and dielectric properties of La2O3 doped amorphous SiO2 films as gate dielectric material. *Applied Surface Science, 253*, 3731–3735.

Sinclair, R. (1985). High-Resolution Tem of Semiconductor Interfaces. *Journal of Metals, 37*(11), A92-A92.

Singh, M. P., Shalini, K., Shivashankar, S. A., Deepak, G. C., Bhat, N., & Shripathi, T. (2008). Microstructure, crystallinity, and properties of low-pressure MOCVD-grown europium oxide films. *Materials Chemistry and Physics, 110*(2-3), 337-343. doi:10.1016/j.matchemphys.2008.02.017

Son, K. A., Mao, A. Y., Sun, Y. M., Kim, B. Y., Liu, F., Kamath, A., . . . Vrtis, R. N. (1998). Chemical vapor deposition of ultrathin Ta2O5 films using Ta[N(CH3)(2)](5). *Applied Physics Letters, 72*(10), 1187-1189. doi:Doi 10.1063/1.121009

Spearing, S. M. (2000). Materials issues in microelectromechanical systems (MEMS). *Acta Materialia, 48*(1), 179-196. doi:Doi 10.1016/S1359-6454(99)00294-3

Srikar, V. T., & Spearing, S. M. (2003). Materials selection in micromechanical design: An application of the Ashby approach. *Journal of Microelectromechanical Systems, 12*(1), 3-10. doi:10.1109/Jems.2002.807466

Srivastava, A., & Malhotra, Y. (2011). Study of Lanthanum incorporated HfO2 nano-scale high-kappa dielectric using Dense Plasma Focus for metal-insulator-metal capacitor applications. *Recent Researches in Telecommunications, Informatics, Electronics & Signal Processing*, 159-161.

Srivastava, A., Mangla, O., & Gupta, V. (2015). Study of La-Incorporated HfO2 MIM Structure Fabricated Using PLD System for Analog/Mixed Signal Applications. *Ieee Transactions on Nanotechnology, 14*(4), 612-618. doi:10.1109/Tnano.2015.2422754

Stathis, J. H., & Zafar, S. (2006). The negative bias temperature instability in MOS devices: A review. *Microelectronics Reliability, 46*(2-4), 270-286. doi:DOI 10.1016/j.microrel.2005.08.001

Suzuki, E., Schroder, D. K., & Hayashi, Y. (1986). Carrier Conduction in Ultrathin Nitrided Oxide-Films. *Journal of Applied Physics, 60*(10), 3616-3621. doi:Doi 10.1063/1.337568

Tabet, N., Faiz, M., & Al-Oteibi, A. (2008). XPS study of nitrogen-implanted ZnO thin films obtained by DC-Magnetron reactive plasma. *Journal of Electron Spectroscopy and Related Phenomena, 163*(1-3), 15-18. doi:10.1016/j.elspec.2007.11.003

Tak, Y. H., Kim, K. B., Park, H. G., Lee, K. H., & Lee, J. L. (2009). Criteria for ITO (indium-tin-oxide) thin film as the bottom electrode of an organic light emitting diode (vol 411, pg 12, 2002). *Thin Solid Films, 517*(15), 4490-4490. doi:10.1016/j.tsf.2008.12.032

Tamboli, S. H., Puri, V., & Puri, R. K. (2010). Adhesion and stress of magnesium oxide thin films: Effect of thickness, oxidation temperature and duration. *Applied Surface Science, 256*(14), 4582-4585. doi:10.1016/j.apsusc.2010.02.052

Tan, S. Y. (2007). Challenges and performance limitations of high-k and oxynitride gate dielectrics for 90/65 nm CMOS technology. *Microelectronics Journal, 38*(6-7), 783-786. doi:10.1016/j.mejo.2007.04.012

Tang, J. T., Chen, X. M., Liu, Y., Gong, W., Peng, Z. S., Cai, T. J., Deng, Q. (2013). Samarium-doped mesoporous TiO2 nanoparticles with improved photocatalytic performance for elimination of gaseous organic pollutants. *Solid State Sciences, 15*, 129-136. doi:10.1016/j.solidstatesciences.2012.10.001

Tang, M. H., Zhou, Y. C., Zheng, X. J., Yan, Z., Cheng, C. P., Ye, Z., & Hu, Z. S. (2006). Characterization of ultra-thin Y2O3 films as insulator of MFISFET structure. *Transactions of Nonferrous Metals Society of China, 16*, S63-S66. doi:Doi 10.1016/S1003-6326(06)60143-X

Terasawa, N., Akimoto, K., Mizuno, Y., Ichimiya, A., Sumitani, K., Takahashi, T., Toriumi, A. (2005). Crystallization process of high-k gate dielectrics studied by surface X-ray diffraction. *Applied Surface Science, 244*(1-4), 16-20. doi:10.1016/j.apsusc.2004.09.12

Tessier, F., Maillard, P., Orhan, E., & Chevire, F. (2010). Study of the R-(Zr,W)-(O,N) (R = Y, Nd, Sm, Gd, Yb) oxynitride system. *Materials Research Bulletin, 45*(2), 97-102. doi:10.1016/j.materresbull.2009.10.003

Thomas, R., Saavedra-Arias, J. J., Karan, N. K., Murari, N. M., Katiyar, R. S., Ehrhart, P., & Waser, R. (2008). Thin films of high-k dysprosium scandate prepared by metal organic chemical vapor deposition for metal-insulator-metal capacitor applications. *Solid State Communications, 147*(7-8), 332-335. doi:10.1016/j.ssc.2008.05.014

Ting, C. C., Li, W. Y., Wang, C. H., & Yong, H. E. (2014). Structural and electrical properties of the europium-doped indium zinc oxide thin film transistors. *Thin Solid Films, 562*, 625-631. doi:10.1016/j.tsf.2014.04.052

Triyoso, D. H., Gilmer, D. C., Jiang, J., & Droopad, R. (2008). Characteristics of thin lanthanum lutetium oxide high-k dielectrics. *Microelectronic Engineering, 85*(8), 1732-1735. doi:10.1016/j.mee.2008.04.041

Tseng, H. C., Chang, T. C., Huang, J. J., Chen, Y. T., Yang, P. C., Huang, H. C., . . . Tsai, M. J. (2011). Resistive switching characteristics of ytterbium oxide thin film for nonvolatile memory application. *Thin Solid Films, 520*(5), 1656-1659. doi:10.1016/j.tsf.2011.07.026

Tu, K. N., Ottaviani, G., Thompson, R. D., & Mayer, J. W. (1982). Thermal-Stability and Growth-Kinetics of Co2si and Cosi in Thin-Film Reactions. *Journal of Applied Physics, 53*(6), 4406-4410. doi:Doi 10.1063/1.331223

Uwamino, Y., Ishizuka, T., & Yamatera, H. (1984). X-Ray Photoelectron-Spectroscopy of Rare-Earth Compounds. *Journal of Electron Spectroscopy and Related Phenomena, 34*(1), 67-78. doi:Doi 10.1016/0368-2048(84)80060-2

Vali, R., & Hosseini, S. M. (2004). First-principles study of structural, dynamical, and dielectric properties of A-La2O3. *Computational Materials Science, 31*(1-2), 125-130.

Venables, J. A., Spiller, G. D. T., & Hanbucken, M. (1984). Nucleation and Growth of Thin-Films. *Reports on Progress in Physics, 47*(4), 399-459. doi:Doi 10.1088/0034-4885/47/4/002

Venkateswarlu, K., Bose, A. C., & Rameshbabu, N. (2010). X-ray peak broadening studies of nanocrystalline hydroxyapatite by Williamson-Hall analysis. *Physica B-Condensed Matter, 405*(20), 4256-4261. doi:10.1016/j.physb.2010.07.020

Vives, S., Gaffet, E., & Meunier, C. (2004). X-ray diffraction line profile analysis of iron ball milled powders. *Materials Science and Engineering a-Structural Materials Properties Microstructure and Processing, 366*(2), 229-238. doi:10.1016/S0921-5093(03)00572-0

Wang, D. W., Tsau, L. M., Wang, K. L., & Chow, P. (1995). Nanofabrication of Thin Chromium Film Deposited on Si(100) Surfaces by Tip Induced Anodization in Atomic-Force Microscopy. *Applied Physics Letters, 67*(9), 1295-1297. doi:Doi 10.1063/1.114402

Wang, J. J., Fang, Z. B., Ji, T., Ren, W. Y., Zhu, Y. Y., & He, G. (2012). Band offsets of epitaxial Tm2O3 high-k dielectric films on Si substrates by X-ray photoelectron spectroscopy. *Applied Surface Science, 258*(16), 6107-6110. doi:10.1016/j.apsusc.2012.03.013

Wang, J. J., Ji, T., Zhu, Y. Y., Fang, Z. B., & Ren, W. Y. (2012). Band gap and structure characterization of Tm2O3 films. *Journal of Rare Earths, 30*(3), 233-235. doi:10.1016/S1002-0721(12)60029-5

Wang, S., Liao, Z. H., Liu, Y. H., & Liu, W. Q. (2015). Influence of thermal oxidation duration on the microstructure and fretting wear behavior of Ti6Al4V alloy. *Materials Chemistry and Physics, 159*, 139-151. doi:10.1016/j.matchemphys.2015.03.063

Wang, Z. M., Wu, J. X., Fang, Q., & Zhang, J. Y. (2004). Photoemission study of high-k praseodymium silicates formed by annealing of ultrathin Pr2O3 on SiO2/Si. *Thin Solid Films, 462*, 118-122. doi:10.1016/j.tsf.2004.05.012

Watahiki, T., Tinkham, B. P., Jenichen, B., Braun, W., & Ploog, K. H. (2007). Growth of praseodymium oxide and silicate for high-kappa dielectrics by molecular beam epitaxy. *Journal of Crystal Growth, 301*, 381-385. doi:10.1016/j.jcrysgro.2006.11.094

Watahiki, T., Tinkham, B. P., Jenichen, B., Shayduk, R., Braun, W., & Ploog, K. H. (2008). Praseodymium silicide formation at the Pr(2)O(3)/Si interface. *Applied Surface Science, 255*(3), 758-760. doi:10.1016/j.apsusc.2008.07.063

Watts, J. F. (1994). X-Ray Photoelectron-Spectroscopy. *Vacuum, 45*(6-7), 653-671. doi:Doi 10.1016/0042-207x(94)90107-4

Wilk, G. D., Wallace, R. M., & Anthony, J. M. (2001). High-kappa gate dielectrics: Current status and materials properties considerations. *Journal of Applied Physics, 89*(10), 5243-5275.

Wolfframm, D., Ratzke, M., Kouteva-Arguirova, S., & Reif, J. (2002). Praseodymium oxide growth on Si(100) by pulsed-laser deposition. *Materials Science in Semiconductor Processing, 5*(4-5), 429-434. doi:10.1016/S1369-8001(02)00127-0

Wong, H., & Gritsenko, V. A. (2002). Defects in silicon oxynitride gate dielectric films. *Microelectronics Reliability, 42*(4-5), 597-605. doi:Pii S0026-2714(02)00005-7Doi 10.1016/S0026-2714(02)00005-7

Wong, H., Yang, B. L., Kakushima, K., Ahmet, P., & Iwai, H. (2012a). Effects of aluminum doping on lanthanum oxide gate dielectric films. *Vacuum, 86*(7), 929-932. doi:10.1016/j.vacuum.2011.06.023

Wong, H., Yang, B. L., Kakushima, K., Ahmet, P., & Iwai, H. (2012b). Properties of CeOx/La2O3 gate dielectric and its effects on the MOS transistor characteristics. *Vacuum, 86*(7), 990-993.

Wong, Y. H., Atuchin, V. V., Kruchinin, V. N., & Cheong, K. Y. (2014). Physical and dispersive optical characteristics of ZrON/Si thin-film system. *Applied Physics a-Materials Science & Processing, 115*(3), 1069-1072. doi:10.1007/s00339-013-7947-1

Wong, Y. H., & Cheong, K. Y. (2010). ZrO2 thin films on Si substrate. *Journal of Materials Science-Materials in Electronics, 21*(10), 980-993.

Wong, Y. H., & Cheong, K. Y. (2011a). Electrical Characteristics of Oxidized/Nitrided Zr Thin Film on Si. *Journal of the Electrochemical Society, 158*(12), H1270-H1278. doi:10.1149/2.106112jes

Wong, Y. H., & Cheong, K. Y. (2011b). Thermal oxidation and nitridation of sputtered Zr thin film on Si via N2O gas. *Journal of Alloys and Compounds, 509*(35), 8728-8737. doi:10.1016/j.jallcom.2011.06.041

Wong, Y. H., & Cheong, K. Y. (2012a). Metal-Oxide-Semiconductor Characteristics of Zr-Oxynitride Thin Film on 4H-SiC Substrate. *Journal of the Electrochemical Society, 159*(3), H293-H299. doi:10.1149/2.081203jes

Wong, Y. H., & Cheong, K. Y. (2012b). Properties of thermally oxidized and nitrided Zr-oxynitride thin film on 4H-SiC in diluted N2O ambient. *Materials Chemistry and Physics, 136*(2-3), 624-637. doi:10.1016/j.matchemphys.2012.07.035

Wong, Y. H., & Cheong, K. Y. (2013). Comparison of oxidized/nitrided Zr thin films on Si and SiC substrates. *Ceramics International, 39*, S475-S479. doi:10.1016/j.ceramint.2012.10.117

Wu, M. H., Cheng, C. H., Lai, C. S., & Pan, T. M. (2009). Structural properties and sensing performance of high-k Sm2O3 membrane-based electrolyte-insulator-semiconductor for pH and urea detection. *Sensors and Actuators B-Chemical, 138*(1), 221-227.

Wu, X., Landheer, D., Quance, T., Graham, M. J., & Botton, G. A. (2002). Structural comparison of gadolinium and lanthanum silicate films on Si(100) by HRTEM, EELS and SAED. *Applied Surface Science, 200*(1-4), 15-20. doi:Pii S0169-4332(02)00888-7

Wu, Y. P., Zhu, S. F., Liu, T. W., Li, F. F., Zhang, Y. Z., Rao, Y. C., & Zhang, Y. B. (2014). Preparation and properties of erbium oxide films deposited by radio frequency magnetron sputtering. *Applied Surface Science, 307*, 615-620. doi:10.1016/j.apsusc.2014.04.086

Xu, R. S., Tao, Q., Yang, Y., & Takoudis, C. G. (2012). Atomic layer deposition and characterization of stoichiometric erbium oxide thin dielectrics on Si(100) using (CpMe)(3)Er precursor and ozone. *Applied Surface Science, 258*(22), 8514-8520. doi:10.1016/j.apsusc.2012.05.019

Yamamoto, T., Momida, H., Hamada, T., Uda, T., & Ohno, T. (2005). First-principles study of dielectric properties of cerium oxide. *Thin Solid Films, 486*(1-2), 136-140. doi:10.1016/j.tsf.2004.11.240

Yang, B. L., Wong, H., & Cheng, Y. C. (1996). Modelling of trap-assisted electronic conduction in thin thermally nitrided oxide films. *Solid-State Electronics, 39*(3), 385-390. doi:Doi 10.1016/0038-1101(95)00134-4

Yang, B. L., Wong, H., Kakushima, K., & Iwai, H. (2012). Improving the electrical characteristics of MOS transistors with CeO2/La2O3 stacked gate dielectric. *Microelectronics Reliability, 52*(8), 1613-1616.

Yang, C., Fan, H. Q., Qju, S. J., Xi, Y. X., & Fu, Y. F. (2009). Microstructure and dielectric properties of La2O3 films prepared by ion beam assistant electron-beam evaporation. *Journal of Non-Crystalline Solids, 355*(1), 33-37.

Yu, S. M., Guan, X. M., & Wong, H. S. P. (2011). Conduction mechanism of TiN/HfOx/Pt resistive switching memory: A trap-assisted-tunneling model. *Applied Physics Letters, 99*(6). doi:Artn 063507 10.1063/1.3624472

Yu, Z., Liang, L. Y., Liu, Z. M., Xu, W. Y., Sun, X. L., & Cao, H. T. (2011). Effects of sputtering pressure and post-metallization annealing on the physical properties of rf-sputtered Y2O3 films. *Journal of Alloys and Compounds, 509*(19), 5810-5815. doi:10.1016/j.jallcom.2011.02.127

Yue, S. J., Wei, F., Wang, Y., Yang, Z. M., Tu, H. L., & Du, J. (2008). Phase control of magnetron sputtering deposited Gd2O3 thin films as high-kappa gate dielectrics. *Journal of Rare Earths, 26*(3), 371-374. doi:Doi 10.1016/S1002-0721(08)60098-8

Zak, A. K., Majid, W. H. A., Abrishami, M. E., & Yousefi, R. (2011). X-ray analysis of ZnO nanoparticles by Williamson-Hall and size-strain plot methods. *Solid State Sciences, 13*(1), 251-256. doi:10.1016/j.solidstatesciences.2010.11.024

Zhang, J. L., Yuan, J. S., Ma, Y., & Oates, A. S. (2001). Modeling of direct tunneling and surface roughness effects on C-V characteristics of ultra-thin gate MOS capacitors. *Solid-State Electronics, 45*(2), 373-377. doi:Doi 10.1016/S0038-1101(00)00234-3

Zhang, Z. Y., & Lagally, M. G. (1997). Atomistic processes in the early stages of thin-film growth. *Science, 276*(5311), 377-383. doi:DOI 10.1126/science.276.5311.377

Zhang, Y., Lu, H., Onodera, K., & Maeda, R. (2007). Development of hafnium oxynitride dielectrics for radio-frequency-microelectromechanical system capacitive switches. *Sensors and Actuators a-Physical, 139*(1-2), 337-342. doi:10.1016/j.sna.2007.02.005

Zhao, X. Y., Wang, X. L., Lin, H., & Wang, Z. Q. (2008). Average electronegativity, electronic polarizability and optical basicity of lanthanide oxides for different coordination numbers. *Physica B-Condensed Matter, 403*(10-11), 1787-1792. doi:10.1016/j.physb.2007.10.005

Zhao, Y. P., Wang, G. C., Lu, T. M., Palasantzas, G., & De Hosson, J. T. M. (1999). Surface-roughness effect on capacitance and leakage current of an insulating film. *Physical Review B, 60*(12), 9157-9164. doi:DOI 10.1103/PhysRevB.60.9157

Zhou, J. P., Chai, C. L., Yang, S. Y., Liu, Z. K., Song, S. L., Li, Y. L., & Chen, N. F. (2004). Properties of high k gate dielectric gadolinium oxide deposited on Si(100) by dual ion beam deposition (DIBD). *Journal of Crystal Growth, 270*(1-2), 21-29. doi:10.1016/j.jcrysgro.2004.05.114

Zhu, Y. Y., Fang, Z. B., & Liu, Y. S. (2010). Structural and optical properties of Er2O3 films. *Journal of Rare Earths, 28*(5), 752-755. doi:10.1016/S1002-0721(09)60194-0

Zhu, Y. Y., Fang, Z. B., Xu, R., Chen, J., Cao, H. J., & Li, H. Y. (2011). Study on vacuum ultraviolet spectra of amorphous Er2O3 films on Si(001) substrates. *Journal of Rare Earths, 29*(9), 888-890. doi:10.1016/S1002-0721(10)60561-3

LIST OF PUBLICATIONS AND PAPERS PRESENTED

K.H. Goh, A.S.M.A. Haseeb, and Y.H. Wong, *Physical and electrical properties of thermal oxidized Sm_2O_3 gate oxide thin film on Si substrate: Influence of oxidation durations.* Thin Solid Films, 2016. 606: p. 80-86. (Published)

K.H. Goh, A.S.M.A. Haseeb, and Y.H. Wong, *Effect of Oxidation Temperature on Physical and Electrical Properties of Sm_2O_3 Thin Film on Si Substrate*. Journal of Electronic Materials, 2016. p. 1-11. (Published)

C.C. Chew, K.H. Goh, M.S. Gorji, C.G. Tan, S. Ramesh, and Y.H. Wong, *Breakdown field enhancement of Si-based MOS capacitor by post-deposition annealing of the reactive sputtered ZrO_xN_y gate oxide.* Applied Physics A-Materials Science & Processing, 2016. 122(2). (Published)

K.H. Goh, A.S.M.A. Haseeb, and Y.H. Wong, *Trap-Assisted Tunneling Mechanism, Capacitance-Voltage Characteristics, and Surface Properties of Sm_2O_3 Thin Film on Si Substrate*. Journal of Materials Science: Materials in Electronics, 2016. (Accepted)

C.Y. Lee, K.H. Goh, and Y.H. Wong, *Influence of Applied Voltage on the Physical and Electrical Properties of Anodic Sm_2O_3 Thin Films on Si in 0.01 M NaOH Solution*. Micro & Nano Letters (2016). (Accepted)

K.H. Goh, A.S.M.A. Haseeb, Y. H. Wong, *Electrical, Microstructural, and Surface Roughness Study of Thermally Oxidized Metallic Sm Thin Film on Si Substrate.* 37th International Electronic Manufacturing Technology (IEMT) Conference, Georgetown, Penang, Malaysia, 20 Sep - 22 Sep 2016. (Published)

K.H. Goh, A.S.M.A., Haseeb and Y. H., Wong, *Effects of Oxidation Temperatures on Physical and Electrical Properties of Sm_2O_3 Gate Oxide Thin Film on Si Substrate*, International Conference on the Science and Engineering of Materials (ICoSEM), Kuala Lumpur, Malaysia, 16-19 Nov 2015. (Attended)